POLITECNICO DI MILANO
DEPARTMENT OF MECHANICAL ENGINEERING

A New Damage Detection Technique

Cheng Liangliang

Ph.D. Thesis in Mechanical Engineering
XXIX Cycle

POLITECNICO DI MILANO
DEPARTMENT OF MECHANICAL ENGINEERING
DOCTORAL PROGRAMME IN MECHANICAL ENGINEERING

A New Damage Detection Technique

Doctoral Dissertation of:
Cheng Liangliang

Supervisors:
Prof. Cigada Alfredo
Prof. Busca Giorgio

Tutor:
Prof. Pennachi Paolo Emilio Lino Maria

2017 - XXIX cycle

Abstract

Many infrastructures and mechanical structures are inevitable to suffer damage along with aging, which has drawn a lot of attention during the research of last decades in terms of the damage localization and quantification of engineering structures for health evaluation. Damage identification based on vibration-based data has been developed rapidly, since the change of physical structure naturally causes a change of system property such as natural frequency, modal damping and mode shape. There exists a variety of vibration-based methodologies for damage detection: by means of the change of natural frequency, the change of mode shape, the change of frequency response function and the change of transmissibility function, and so on. Among these methodologies, measuring the change of transmissibility function is preferable since it not only has a better sensitivity to the damage but also none prior information of the system loading is required.

Transmissibility function as one of the most popular methods widely applied for identifying damage. Moreover, it is traditionally defined as response spectrum ratio between two degrees of freedom. During the recent decades, more damage indicators based on transmissibility function have been proposed and their results of damage identification have proved the excellent performance of this approach in terms of the sensitivity than the classical frequency response function (FRF). The author also points out the significance of poles and zeros to localize damage in the dynamic system. More recently, it has been proved that the value of transmissibility function converges to the mode shape ratio when frequency bandwidth is restricted to the system's poles.

The convenience and effectiveness of using transmissibility in practice is the basis of making it selected as the main research object in this work. A new conception, namely strain transmissibility function, has been proposed in this study due to the fact that strain is more sensitive regarding to damage in comparison with displacement, which could be proved through the related sensitivity analysis. In addition, the

accuracy of damage localisation also relies on the number of sensors. Especially when dynamic test is performed on large structures such as bridges, tunnels and buildings, it is extremely difficult to reach the target of full coverage on the objects. Also, usually a large number of sensors are need and then the idea is impracticable mainly for economic reasons. Fortunately, distributed fiber optics techniques have kept developing rather maturely and they have been applied into various domains which can measure continuously strain and temperature along the structure layout. During the validation of the feasibility of the proposed new conception and approach, a series of simulation studies and the related experiments based on distributed fiber optics have been carried out.

However, many researchers mainly concentrate on linear damage case where damage can be considered as the linear reduction of mass and stiffness, apparently, their methodology is unable to detect the change caused by the nonlinear damage. Damage scenarios in engineering structures are manifested as nonlinear behaviours in many cases, which could be deemed as the potential security hazard. Certain types of damage in MDOF systems create a significant nonlinear change instead of a linear one, such as breathing crack (Bilinear stiffness), post-buckled structures (Duffing nonlinearity) and rattling joints (The system with discontinuity), etc. Therefore, the study on nonlinear damage identification is of great importance.

Another part of this study focuses on nonlinear damage identification based on the conception of nonlinear output frequency response function (NOFRF). The highlight of this work is the extension of the NOFRF approach to the general input condition and corresponding simulation on a MDOF system clearly demonstrates its availability. In particular, this work also discovers and proves the relationship between NOFRF-based transmissibility function and Output-based transmissibility function under general input condition, which offers a more convenient and reliable strategy for detecting and localizing damaged components, on account of various damaged scenarios, including existence of single damaged component and multiple damaged components. In addition, various loading scenarios are taken into consideration as well, including single-point loading, multiple-point loading and distributed uniformed loading.

Declaration

The author hereby declares that this dissertation is a record of work carried out in the Department of Mechanical Engineering at Politecnico di Milano during the period of October 2013 to April 2017. This dissertation is original in content except where otherwise stated.

Cheng Liangliang

April 2017

Acknowledgements

First of all, I would like to express my deepest thanks to my supervisor Prof. Alfredo Cigada and Giorgio Busca for their excellent guidance and encouragement to provide me sufficient support throughout these years. It was honored to be one of their students.

I am sincerely grateful to the Prof. Ziqiang Lang, who has offered me a great opportunity research period in University of Sheffield. Even if I just spent few months there, it made a significant enhancement on my research work.

Special thanks go to Prof. Michele Gasparetto, Stefano Manzoni, Giovanni Moschioni, Marco Tarabini, Emanuele Zappa, who provided me a lot of help during my research activities.

I would like to thank to my friend, Yunpeng Zhu, in University of Sheffield, who often discussed with me and provided me useful suggestions when I was confronted with difficulties in my research.

I would like to thank my intimate colleagues, Alessio Datteo, Silvio Giancola, Rui Liu, Ambra Vandone, Marta Berardengo, Alberto Lavatelli and Ali Siami, who have shared with the wonderful research period in the research group of measurement.

I am grateful to my friends, Wenshan Fang, Peixue, Menglu Liao, Fan Yang and Huilong Yu, whom I enjoyed my spare time together.

Thanks to the all the member staff in the experimental lab (C4), who very kindly helped me with my experiment setups, and special thanks go to the administrative and support staff, Marcella Netti and Silvia Barattieri.

In the last but not the least, I would like to say thank you to my family, my father, my mother and my sister. They keep giving me the encouragement and home-support during these years.

Contents

CHAPTER 1

Introduction

1.1 Overview

This chapter deals with a systematic literature review about structural damage identification concerning the field of Structural Health Monitoring (SHM). Due to the continuously increasing demand on damage identification for engineering infrastructures, the methods about vibration-based structural damage identification have drawn the attentions of many researchers. A brief review on above-mentioned methods is given. Afterwards, on the account of the rapid development of distributed fiber optics technology that show many distinct advantages, the potentials applied to SHM have been keeping investigated. A literature review of distributed fiber optics is presented later on, which involves the recent engineering applications. Finally, it clarifies the research objectives and the novel contributions of this thesis.

1.2 Structural Health Monitoring

The security issues of aerospace, civil and mechanical engineering infrastructures are increasingly catching the sight of many researches, because most of civil, mechanical and aerospace structures are

vulnerable to damage due to human factors, natural disasters, prolonged fatigue and corrosion which makes SHM become strongly motivated. Damage is defined as changes of material or geometric characteristics, also including changes of boundary conditions and system connectivity. Loads of available effective non-destructive tools and researches have been emerged over the past 30 years, and damage identification becomes the coral basis of SHM.

1.2.1 The conception of SHM

The process of implementing a damage identification strategy for aerospace, civil and mechanical engineering infrastructure is referred to as structural health monitoring (SHM)[1]. The basic idea is to infer changes in structural properties and predict structural damage by measuring the response of the structure before and after abnormal loads, or to detect long-term structural degradation through continuous monitoring. For civil engineering structures, the SHM system can monitor structural damage under earthquake or explosion, or monitor health status of the structures for a long term under the surrounding environment and human activities. This information can provide an important reference for the structural safety assessment and can also be used for the maintenance of the structures and the assessment of their remaining life.

SHM system generally consists of four main subsystems[2]: 1. Sensor system; 2. Signal acquisition and processing system; 3. Signal communication and transmission system; 4. Signal analysis and monitoring system.

SHM technology is based on the measurement results from the same location of structures at different time stages to identify the health state of the structures, so historical data is critical, and the accuracy of recognition depends strongly on the sensors and the interpretation algorithms. It can be said, structural health monitoring is likely to be widely used offline, static, passive damage monitoring, into online, dynamic, real-time monitoring and control. However, current SHM systems to ensure the safety operation of bridges as the goal still need to be developed compared to the anticipation due to the main reason that the current SHM systems are devoting at damage detection after the existence of damage rather than damage prognosis. Therefore, damage

detection and damage prognosis can be composed of two main research topics of SHM and there is inherent difference between them: Damage detection is carried out based on the deterministic monitoring data[3-5], while damage prognosis is to predict the possible damage in the future based on historical monitoring data. The main purpose of damage prognosis is to remind the owner taking necessary technical measures to reduce the structural damage or prevent possible catastrophic damage before damage occurrence[6-8].

1.2.2 Model-based and data-driven approach

Due to the higher performance and increasing demand for structural health monitoring system, damage detection has become more and more important with aiming to increase the safety and reliability of the structures. Early fault diagnosis can help to avoid abnormal events and reduce the loss of productivity, which in turn can be beneficial to avoid the main system failures and disasters. Therefore, fault diagnosis is a major research topic, attracted by industry practitioners and academic researchers. There is a lot of literature about the process of fault diagnosis from analysis methods to artificial intelligence and statistical methods. From the viewpoint of modeling, some methods need precise process models, semi quantitative or qualitative models. On the other hand, some methods don't depend on any models, only rely on the time history data. The fault diagnosis methods from [9], [10] and [11] can be required is divided into two categories, model-based and data-driven methods regarding to the prior process knowledge.
Model-based methods can be divided into qualitative[12, 13] and quantitative[9, 10, 14, 15] methods, given the provided prior knowledge, which is usually developed based on some basic understanding of the process of physics. In the quantitative model, the understanding of this model can be read from the relationship between system input and output function. As for qualitative model, qualitative functions can be used to describe the system. Data-driven methods take the availability of a large amount of time history data, which can be converted and presented as a priori knowledge to different ways of diagnosis system. Feature extraction can be made from those time history data in order to diagnose faults. The feature extraction process can be defined as quantitative or qualitative methods as well. In the quantitative feature

extraction, it can be divided into the methods based on statistical or non-statistical way.

Model-based method is mainly discussed in the finite element model development. After the initial development of the finite element model, the experimental data is used to update the dynamic characteristics of system matrix (mass, stiffness and damping), to make the model more accurate which is able to represent the experimental structure. Then making use of the measured structure data collected to perform damage identification through the inverse problem[16].

Data-driven approach, as another hot topic of damage detection, has been continuously developing. The data-driven approaches do not need prior knowledge of the process, but aim at investigating the hidden information in the data through various data analysis and processing methods based on the historical process data, and obtaining the different data characteristic patterns under the normal operational condition and the damaged situation, thereby determining the operational status of the process. Because the data-driven method only relies on the time history data, it is general-purpose and suitable for the fault detection and diagnosis of various structures and devices. In the meantime, through the various data processing and analysis methods (such as multivariate statistical methods, cluster analysis, spectral analysis, wavelet analysis, etc.) to extract the feature from the data in order to identify the damage. Data-driven can be categorized into linear regression method[17], artificial neural network method[18-20], support vector machine method[21-23], fuzzy modeling methods[24-26]. The main advantage of data-driven methods is that it does not need to set up a complex mathematical model, which reduces the workload of theory and calculation, and avoids the error caused by modeling. And high-dimensional data can be condensed into low-dimensional data to be analyzed[27]. But from another point of view, it is too dependent on the accuracy of vibration measurement signals. Measurement error and measurement noise will have a great impact on the recognition results. The most critical point is that data-driven methods are not directly related to the physical parameters of the structure itself, so it is difficult to achieve quantitative identification of structural damage.

1.2.3 Applications of SHM system

Many infrastructures like towers, high-rise buildings and bridge structures must have been regularly assessed in order to achieve safety, maintenance, and obtain economic benefits. The structure maintenance and monitoring of the condition of the structure becomes a great challenge. The structural health monitoring (SHM) in recent decades in civil engineering, aerospace engineering, machinery and many other fields has aroused great concern. For an example, a variety of sensors have been installed in Akashi Kaikyo Bridge[28], as the world longest suspension bridge, in order to confirm the design assumptions and relevant parameter values of the bridge under strong wind and earthquake. Sensor devices like anemometers which are aiming to determine the wind characteristics of the bridge, seismometers, accelerometers are used to verity the dynamic behavior under earthquake, velocity gauges, girder edge displacement gauges, tuned mass damper (TMD) displacement gauges, thermometers and GPS. Three bridges of the Korea Expressway Corporation in Korea[29] have been chosen as a Korea-US joint research, various smart sensors and sensor configuration have been adopted such as piezoelectric sensors, wireless sensors, and also vision-based monitoring system, attempting to validate their independent research and development on the smart sensors, sensing monitoring system and data processing algorithms. Take another example, the Canton Tower in Guangzhou[30], China, with a total height of 600m, is a circular gradient grid structure. SHM system has been applied into this tower, with implementing 800 sensors to cover the complete tower itself, which contains 6 modules: Sensory system, Signal acquisition and transmission system, Signal processing and control system, Data management system and Maintenance system. In order to employ the SHM system, ambient vibration under different conditional stages has been carried out for a long term monitoring. FEM-based mode update has been accomplished by comparing the experimental modal analysis. Also the relative modal parameters of the tower have been successfully identified.

1.3 Vibration-based structural damage identification

With the advancement of science and technology, modern space structure is inclined to be large-scale and complexed due to the demand for industrial development, as well as the future development of mankind. However, these structures will be damaged under some environmental conditions which will change the characteristics of the structure, and lead to a greater structural damage accumulation. And eventually it will bring about sudden failure of the structure, so that the safety of the structure is being threatened. Therefore, structural damage identification has become the focus of attention of scholars all over the world. Especially, structural damage diagnosis based on structural vibration response and system dynamic characteristic parameters has become a focus of research in recent decades. And structural damage identification based on non-destructive testing methods is a current hot and difficult research. Nowadays non-destructive identification technology is widely used in the aerospace industry, power plant equipment, construction, metallurgy and machinery manufacturing etc. The basic idea is: damage can cause changes in the structures of the physical parameters (mass, stiffness, etc.), the modal parameters of the structures (modal frequencies, mode shapes, modal damping, etc.) will change accordingly, thus damage can be determined based on these variables.

According to different technical levels, the damage identification and quality assessment of engineering structures can be divided into four levels[31]:

1) Whether the structure is expected to be damaged;
2) To determine the location of damage;
3) To determine the degree of damage;
4) Life expectancy after the structural damage.

The following part demonstrates various vibration-based methods on damage identification briefly.

1.3.1 Based on the change of natural frequencies[32-37]

Natural frequency is a function of structural stiffness and mass. An occurrence of damage to the structures will lead to a change of natural frequencies. For the actual engineering structures, the natural frequencies are easy to be measured and not related with the measurement position. The error of the frequency measurement is smaller than that of the vibration mode and the damping measurement. But it is not enough to provide sufficient information for damage identification. The advantage of using natural frequencies to detect damage is that the natural frequencies are easy to be obtained and the measurement accuracy is high. But natural frequencies of structural sometimes are not very sensitive to early damage, usually only existence of damage can be found, and the damage location cannot be determined due to that a damage at different locations can cause the same amount of frequency change. Some investigations have been published in relative articles, which claimed that damage identification based on natural frequencies can be merely feasible for some particular structures. The application on complexed structures is still a challenge and it needs to be developed.

1.3.2 Based on the change of mode shapes[38-45]

Structural damage will result in changes in mode shape, and mode shape contains the location information, hence the methods based on the vibration mode shape can not only identify the damage but locate the damage. The basic idea is to identify the mode shape before and after damage, and compare the difference for each measurement point which is capable to recognize and localize the damage. In addition, MAC and COMAC criteria could be useful damage indicators as well. Apart from the change of mode shape, the slope and curvature of mode shape could be used to damage identification based on the fact that the small perturbation caused by the damage on the mode shape will be amplified, resulting in a significant change in the slope and the curvature of the mode shape. Therefore, the slope and the curvature of the mode shape is more sensitive in terms of damage compared to mode shape itself. However, the measurement error of eigenvectors is rather larger than that of eigenvalues. The effectiveness of the mode shape based method

depends on the accuracy of the identified modes, and the accuracy of the modes is related to the quality of the test data and the number of measurement points. And the quality of test data relies on the instruments and the corresponding methods Generally the accelerometers and other traditional sensors have been applied into acquire the response, also there emerges some advanced test methods, such as laser Doppler vibrometer, Spot pattern interferometer, fiber optics, etc.

1.3.3 Based on the change of flexibility[46-54]

Under the condition that the modal normalization, the flexibility matrix is a function of the reciprocal of the frequency and the mode shape. As the frequency increases, the reciprocal effects of the high frequency in the compliance matrix are negligible, so that a matrix with good accuracy can be obtained as long as the first few lower order modal parameters and frequencies are measured. The largest element in each column of the difference matrix is obtained from the difference matrix of the two flexibility matrixes before and after damage, and the position of the damage can be found by checking the largest element in each column. Pandey and Biswas proposed a structure damage method based on flexibility matrix difference, and it is shown that the flexibility matrix difference is quite effective in locating and identifying the damage. Toksoy and Aktan[52] proposed a method to evaluate bridge condition based on modal flexibility obtained from measured processing data, and it has been applied into a three-span high way bridge. Moreover, Li Yongmei *et al.*[53] proposed a structure damage identification method based on flexibility difference curvature, and it is proved that only low modal orders are effective enough to be considered into assess the structural health conditions. Catbas *et al.*[54] further extended the application of modal flexibility and derived a practical approach to obtain modal flexibility from real modal tests data.

1.3.4 Based on the change of FRF[55-59]

When natural frequency or mode shape are considered as the basis for damage identification, the primary step is to identify the natural frequencies or mode shapes of the structure by means of modal identification methods, which is time-consuming and introduces

parameter identification errors. And even, when the damage occurs near the node of a certain mode, the changes of modal parameters, such as the natural frequency and mode shape, are very small before and after the structural damage, thus the structural damage cannot be identified based on those modal parameters. Therefore, using frequency response function considered as raw data without data post-processing could be a greater approach for damage detection.
Based on the similar assumption of detecting the damage in accordance with the greatest change of mode shape, a new conception called "operational mode shape" could be utilized and applied into the damage detection, through finding the greatest change of operational mode shape during the selected frequency range. There are various existing methods for damage detection, which are based on FRF-operational mode shape, FRF-operational mode shape slope, FRF-operational mode shape curvature and its square. An issue needs to be noted, true damage location might be masked when a broader frequency range is considered into the selection for damage indicator calculation, due to the reason that the differences between undamaged and damaged frequency response functions where are near around resonances and anti-resonances are going to be larger, which could cover the true damage location if a false damage location is identified under those frequencies. Therefore, a new conception of occurrence has been put forward in order to lower the possibility of identifying false damage locations, based on the idea that the location can be found where the maximum difference between undamaged and damaged frequency response functions under each frequency line. And occurrence will be counted and summed so as to locate the damage.

1.3.5 Based on the change of transmissibility function[60-69]

Transmissibility function as one of most popular methods widely applied for identifying damage has been proposed firstly in[60]. And it is traditionally defined as response spectrum ratio between two degrees of freedom. During the recent decades, more damage indicators based on transmissibility function have been proposed[60-62] and demonstrated their excellent performance in terms of damage identification, owing to the fact that transmissibility is more sensitive to local damage compared to FRF, which has been discussed in[65], and it points out the

significance of poles and zeros to localize damage in the dynamic system. More recently, it has proved that the value of transmissibility function converges to the mode shape ratio when frequency bandwidth is restricted to the system's poles. Even though the methods based on transmissibility don't need any mathematical model or a priori knowledge, and can effectively identify early structural damage, the number and position of the measurement points have a great influence on the damage identification accuracy[70].

However, many researches mainly concentrate on linear damage case where damage can be considered as the linear reduction of mass and stiffness, and it has been proved to be insensitive in terms of nonlinear damage. Few researches concentrate on the nonlinear damage situation based on the conception of transmissibility so far. It is worthy to mention that Timothy J. Johnson[65] introduced nonlinear component in MDOF system by utilizing cubic nonlinear stiffness on the spring. Lang[66] firstly proposed the damage index for detecting nonlinear component based on nonlinear output frequency response function under harmonic excitation, which has been proved effectively by mathematical derivation and relevant numerical simulations. Zhao and Lang[69] have recently proposed a new method based on transmissibility at super-harmonic frequencies for identifying nonlinear components, that does not need the identification of NOFRFs, in other words, input signal doesn't need to be measurable.

1.4 Fiber optics

Fiber optic transmission and sensing are two important areas of fiber technology[71]. Fiber-optic sensor is widely used because of its rapid development and application. Fiber-optic sensor has strong potentiality of anti-electromagnetic interference, high sensitivity, good electrical insulation, safe and reliable, corrosion-resistant. It can be applied in many fields such as industry, agriculture, biomedicine, national defense and so on, which could be reckoned as an innovational measurement placement instead of the traditional detection technology and instrumentation.

Its enhancement on measurement technology and instrumentation can be reflected as the following aspects[71-74]: (1) High sensitivity. Because

light is an electromagnetic wave with a very short wavelength, its optical length could be obtained through its light phase. The optical fiber interferometer, for example, because the diameter of fiber optics is very small, when the fiber is subject to a small mechanical external force or temperature changes, its optical length will change, that causes a large phase change. (2) Anti-electromagnetic interference, electrical insulation, corrosion resistance, intrinsically safe. As the optical fiber sensor is the use of optical transmission of information, also optical fiber is electrically insulated, corrosion-resistant transmission medium, and safe and reliable, which makes it effectively use for strong electromagnetic interference, flammable, explosive and other harsh environments. (3) High measurement speed. Light is the fastest and can transmit two-dimensional information, it can be used for high-speed measurements. Signal analysis of radar requires a very high detection rate, the application of electronic methods is difficult to achieve, while the use of high-speed spectrum analysis based on light diffraction phenomenon can be resolved. (4) Huge information capacity. In addition, fiber optic sensor also has a light weight, small size, able-curved, wide range of objects, reusability, and low cost. The optical fiber sensor has so many advantages, making its application is very extensive, involving petrochemical, power, medical, civil engineering and many other fields. So it will have a huge role in promoting on the development of science and technology, industrial and agricultural production and national defense construction.

1.4.1 Fiber optics sensing technologies

A typical fiber optic transmission configuration is shown in Fig. 1-1, which mainly contains five components and operate the process of transmitting the information.

1) A converter should be used in order to transform electric signal into a signal which could be recognized by light source.
2) A light emitter should be needed to transmit the light into fiber optics.
3) The light signal should go through the fiber optic until it reaches the end of the fiber optics.
4) It is a must to have a light detector, which is able to detect the light signal and reconvert the light signal into electric signal at the end of

the fiber optics.

5) A converter is needed to reconvert the light signal back to the electric signal and complete the whole transmission process.

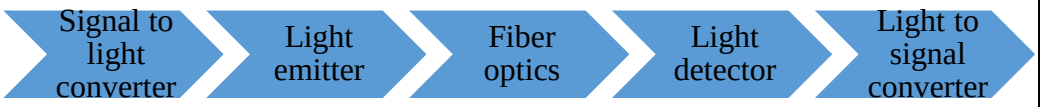

Fig. 1-1 Configuration of a typical fiber optics transmission process

The basic composition of a cross-sectional typical fiber optics is shown in Fig. 1-2, which are the core, the cladding and the coating. The optic fibers are usually made by transparent materials such as glass, and it is the core which surrounded by another cylindrical layer called cladding. And the outer layer is aiming to protect the fiber and provide stronger durability. Generally speaking, the diameter of the optical fiber is rather thin, like 0.1-0.3 mm. However, these parameters are not fixed and able to be adjusted according to the particular demands.

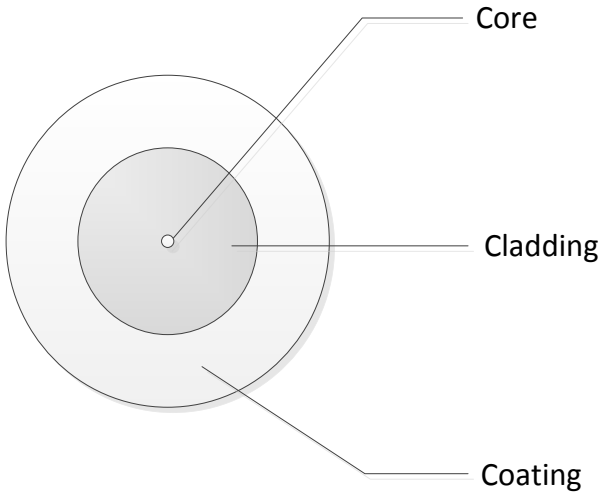

Fig. 1-2 The basic composition of a typical fiber optics

There are several existing fiber optics sensing technologies in recent days, and they have been already applied into commercial purpose. In

general, they can be classified into three types: grating-based sensors, distributed sensors and interferometric sensors[75]. There are loads of fiber optics applied into real industrial engineering field. An overview of the types of fiber optics based on the sensing technologies has been listed in Fig. 1-3.

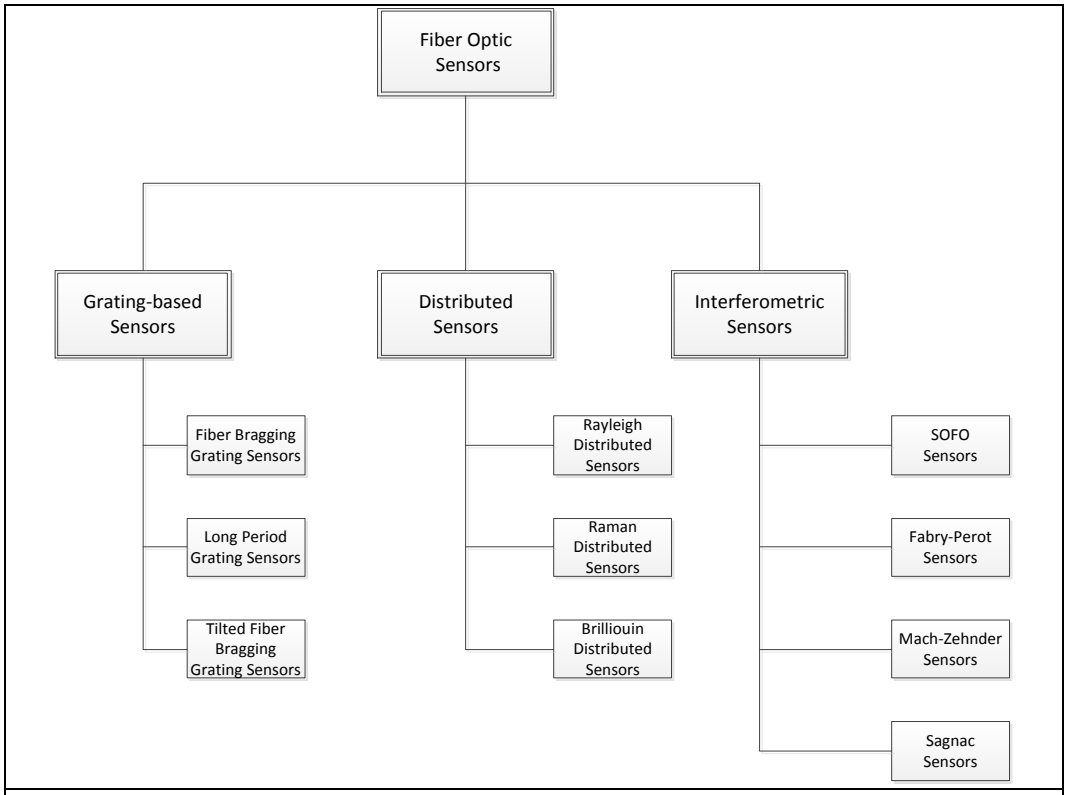

Fig. 1-3 A list of the types of fiber optics (adapted from [75])

1.4.1.1 Grating-based sensors

Fiber Bragg Grating sensor is a nonlinear optical fiber sensor of wavelength modulation type[76]. It has been considered as the most mature fiber optics sensor, which have been already applied into many industrial fields. A basic functional principle of FBG can be found in Fig. 1-4.

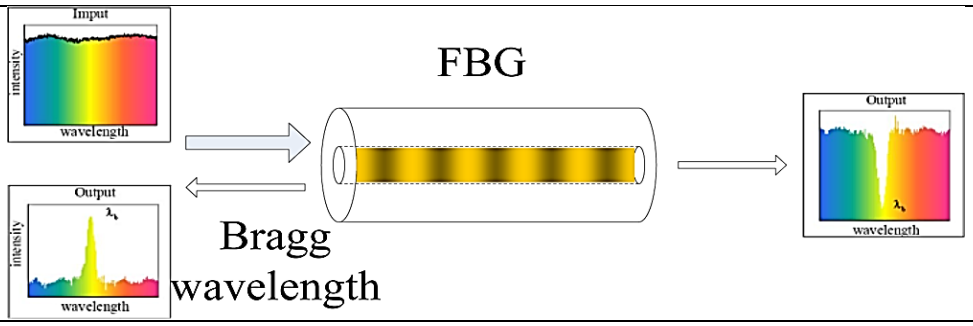

Fig. 1-4 Functional principle of FBG sensor (adapted from [75])

The fiber Bragg grating sensor is one of the most widely used fiber optic sensor, which can change the wavelength of the reflected light according to the change of ambient temperature and / or strain[77, 78]. Fiber Bragg Grating is based on holographic interference or phase mask method, which makes a small piece of light-sensitive optical fiber exposed to a period distribution of light intensity. Thus the optical refractive index of the optical fiber is permanently changed depending on the intensity of the light to be irradiated. This method of periodic changes in refractive index of light is called Fiber Bragg Grating.

When a beam of light with a broad spectrum is propagated to the fiber Bragg grating, each fraction of the fiber after the change in refractive index reflects only a specific wavelength of light, called the Bragg wavelength, as shown in the following equation(1-1). This characteristic makes the fiber Bragg grating reflect only a specific wavelength of light, and other wavelengths of light will be spread.

$\lambda_b = 2n\Lambda$	(1-1)

In equation, λ_b is the Bragg wavelength, n is the effective refractive index of fiber core and Λ is the interval between gratings is called the grating period.

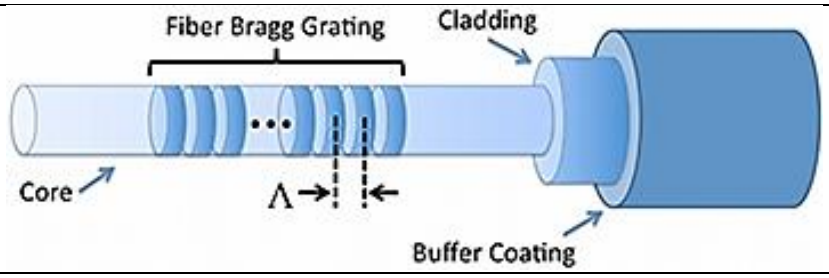

Fig. 1-5 A perspective view of a fiber Bragg grating

Strain and temperature will affect the effective refractive index n and the grating period Λ of fiber Bragg grating, which results in the change of grating reflected light wavelength. The change of the reflection wavelength of fiber Bragg grating with strain and temperature can be approximated by the relation in equation(1-2):

$$\frac{\Delta\lambda}{\lambda_0} = (1-p_e)*\varepsilon + (\alpha_\Lambda + \alpha_n)*\Delta T \qquad (1\text{-}2)$$

In equation, where $\Delta\lambda$ is the change of reflected wavelength and λ_0 is the initial reflected wavelength.

The term $(1-p_e)*\varepsilon$ indicates the effect of strain change on the reflection wavelength. Where p_e is the strain optical sensitivity coefficient, and ε is the change of strain effected by grating. The term $(\alpha_\Lambda + \alpha_n)*\Delta T$ indicates the effect of temperature change on the wavelength. Where α_Λ is the thermal expansion coefficient and α_n is the temperature optical sensitivity coefficient. The coefficient α_Λ reflects the optical refractive index due to temperature changes and the coefficient α_n reflects the same temperature changes caused by the grating cycle change.

Because the fiber Bragg grating will be affected by strain and temperature changes at the same time, it is necessary to consider both of these factors during the calculation of reflection wavelength changes, but also to analyze them separately. When performing temperature measurements, the fiber Bragg grating must be kept completely free of strain. You can use the FBG temperature sensor that is specifically packaged for this purpose. This kind of sensor ensures that the properties of the fiber Bragg grating inside the package are not coupled

to any external bending, stretching, squeezing or twisting strain. In this case, the thermal expansion coefficient α_Λ of the glass is usually negligible in practical use. Therefore, the change in the reflection wavelength due to the temperature change can be mainly determined by the temperature optical sensitivity coefficient α_n of the optical fiber.

Fiber Bragg grating strain gauges are more complicated in some way because temperature and strain affect both the reflected wavelengths of the sensor. In order to perform the measurements correctly, the influence of the temperature on the fiber Bragg grating must be compensated during the test. In order to achieve this compensation, you can use a FBG strain sensor with good thermal contact FBG temperature sensor to complete. After obtaining the test results, simply subtracting the wavelength change measured by the FBG temperature sensor from the wavelength change measured by the FBG strain sensor can eliminate the second expression to the right of the plus sign from equation(1-2) and this compensates for the effect of temperature changes during strain tests.

In addition to be used widely in strain and temperature monitoring applications, a new signal detection technology has been discovered based on acoustic or ultrasonic signals[79, 80], which could be effectively applied into structural health monitoring. The coral change for this technology is traditional PZT sensors have been placed by FBG sensors to collect acoustic or ultrasonic signals, which makes wring issue more simple. Full scale monitoring is on high demand for large infrastructures, FBG sensors are capable to meet this need by using the multiplexing technology.

1.4.1.2 Distributed sensors

Distributed fiber-optic sensor is arranged along the field, the field distribution and time-varying information can be measured and monitored by using the unique detection technology along the fiber transmission path along. They can provide a real distributed way to monitor the structures along the entire fiber. Due to the large amount of information obtained at the same time, the cost of unit information is greatly reduced, so that a high cost performance can be obtained. It is a very promising sensor which can be competitive with point sensing

sensors, so in recent years more and more attention has been caught on the research of distributed fiber optics sensors. The basic principle of distributed fiber optics is shown in Fig. 1-1.

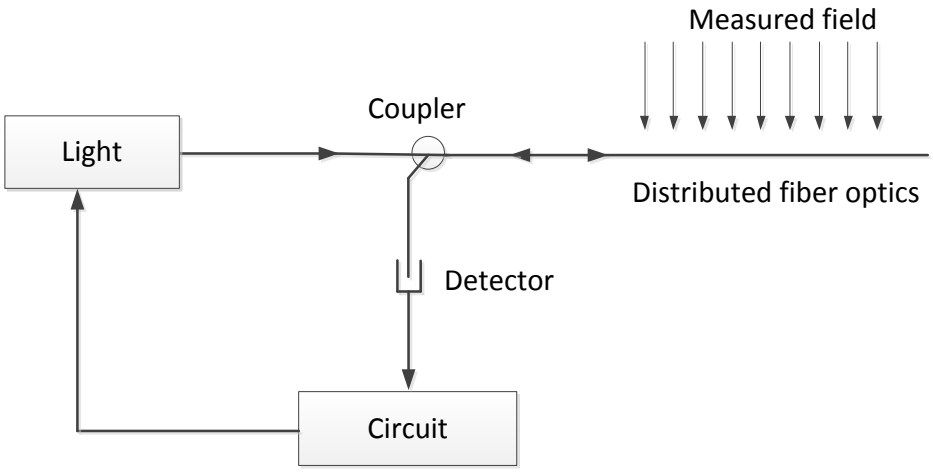

Fig. 1-6 Basic principle of distributed fiber optics

There are three main classification based on two different sensing technologies: OTDR, OFDR and POTDR, namely optical time domain reflectometry, optical frequency domain reflectometry and polarization optical time domain reflectometry respectively. Optical time domain reflectometry technology emerged at the beginning of 1980, aiming to test the optical cables for the use of telecommunications. In the OTDR technique[75, 81-83], a short light pulse is emitted into the fiber, and then the photodetector processes the amount of light which is backscattered as the beam propagates along the fiber.

Generally speaking, light transmission in the fiber will occur three types of scattering, including Rayleigh scattering caused by the changes in the refractive index of fiber, optical phonon-induced Raman scattering, and Brillouin scattering caused by acoustic phonon[84]. Rayleigh scattering is an inherent property of optical fibers. When light waves propagate during the fiber, they encounter linear scattering due to the random fluctuation of refractive index n of the fiber core. Brillouin scattering is the result of the interaction of incident light with acoustic or propagating

pressure waves, which is equivalent to a dense grating moving at a constant velocity (and with a certain frequency). Therefore, the Brillouin scattering can be regarded as the scattering of the incident light on the moving grating, and the Doppler effect makes the frequency of the scattered light different from that of the incident light. When the scattered light, incident light and pressure wave under specific frequency meet the phase matching conditions (for grating, is corresponding to meet the Bragg (Bragg diffraction conditions)), the scattered light intensity is the maximum under this frequency.

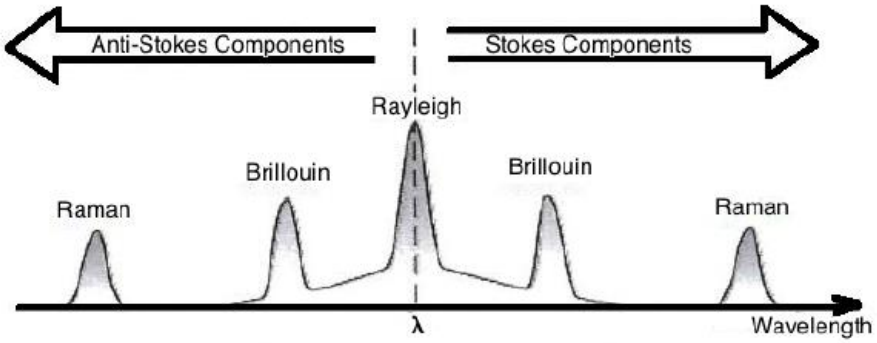

Fig. 1-7 Backscattering spectrum (adapted from [84])

Raman scattering is the phenomenon that a photon of the incident light is scattered into another low-frequency photon by an acoustical photon, and the acoustical phonon completes the transition between its two vibrational states. Raman scattering depends on the temperature of the fiber which has been found in[85, 86] so as to develop various unique technique of measurement. Raman scattered light contains Stokes light and anti-Stokes light. As shown in Fig. 1-7, Rayleigh scattering does not change its wavelength, while Raman scattering and Brillouin scattering are the information carried by the inelastic scattering of light and matter. And their scattering wavelength is shifted with respect to the incident wavelength.

And it is worthy to mention that Rayleigh scattering, as a quasi-elastic or linear phenomenon, mostly relies on any external physical field. And

Rayleigh-based distributed fiber optics is used to measure propagation effects, which contains attenuation and gain, phase interference and polarization variation. However, Raman and Brillouin-based distributed fiber optics are influenced by the propagation effects as well, but it can be neglected due to the direct relation with the measurement parameters.

Table. 1-1 concludes the characteristics and applications of the distributed fiber optics based on OTDR technology.

Table. 1-1 The characteristics and applications of the distributed fiber optics based on OTDR technology

Technology	Advantages	Shortcomings	Main applications
OTDR	Continuously shows the variation of the loss of the entire fiber line relative to the distance. Non-destructive measurement, multi-function, easy to use	There is always a blind spot. The attenuation values measured at both ends of the fiber are usually different, usually the average value is taken.	For the detection of fiber damage points
BOTDR	For a single distribution of the measurement parameters have a high accuracy and spatial	Because the Brillouin frequency shift is very small, and its line width is very narrow, which requires the laser has a very high frequency stability	Stress and temperature monitoring

	resolution	and a very narrow (about kHz) adjustable line width, the optical filter also has high requirements. The system is complex and expensive to manufacture and use. The current focus is on temperature and stress sensing.	
BOTDA	High precision and spatial resolution, dynamic range, high accuracy	The system is more complex, pump laser and detection laser must be placed on both ends of the measured fiber, the practical application contains certain difficulties; It cannot be measured due to the existence of damaged sensing points; Application conditions are limited; Stress and temperature changes caused by more difficult to distinguish	Stress and temperature monitoring
ROTDR	Improve the system's	The return of the signal is very weak;	Temperature monitoring

	relative sensitivity and temperature measurement accuracy, expand the system's functionality and reduce costs	High requirement on light source.

Distributed fiber optics technologies based on OFDR mainly contains three different types: OFDR (based on Rayleigh scattering), ROFDR (based on Raman scattering) and BOFDA (based on Brillouin scattering). Optical frequency domain reflection (OFDR) systems[87-92] has drawn the attention from many research institutes with aiming to obtain the goal of short spatial resolutions and cost-effectiveness. In order to obtain the sensors with high spatial resolution by taking advantage of OTDR technique, a very narrow pulse of light is needed, leading to the proportion of backscatter signal in a level. Therefore, the noise level is also expected to increase in order to detect the small changes from backscatter signals due to strain and temperature is almost impossible. These combined factors make OTDR-based distributed fiber optics with the high spatial resolution become very expensive, which stimulates the development of the research on OFDR-based distributed fiber optics.

The strongest mode of scattering in the fiber is Rayleigh scattering, which is about -45db of the incident light. Rayleigh scattering is an inherent property of the fiber. During the process of pulling the fiber from the molten state to the solidified state, the inhomogeneity of the silica is caused by the random fluctuation of the refractive index of the core. The experimental and theoretical results show that the temperature sensitivity of the Rayleigh scattering coefficient is extremely weak for the glass fiber. Therefore, the solid-fiber distribution system on monitoring temperature based on Rayleigh scattering is difficult to achieve and the temperature resolution is rather low.

The distributed optical fiber temperature sensor based on optical

frequency domain Raman scattering technique is used to analyze the frequency domain signal by network analyzer according to the principle of Raman scattering effect, so as to determine the fiber complex baseband transfer function and achieve the distributed measurement on temperature.

The distributed fiber-optic sensors based on Brillouin frequency-domain analysis is similar to that of Raman scattering principle, also through the network analyzer to measure the complex fiber baseband transfer function, and then temperature information can be extracted from the amplitude and phase information of complex baseband transmission function, which results in the temperature of the distributed measurement.

This section gives a detailed description of OTDR and OFDR distributed fiber optics. And compared to OTDR, OFDR sensors have the distinctive advantage that OFDR sensors have higher sensitivity and spatial resolution. And Table. 1-2 shows the detailed configuration of diverse distributed fiber optics. It should be noted that FBGs can be achieved as quasi-distributed sensors.

Table. 1-2 Specification of different distributed fiber optic sensors (adapted from [93])

Sensing technology	**Transducer type**	**Sensing range**	**Spatial resolution**	**Measurands**
Raman OTDR	Distributed	1km 37km	1cm 17m	Temperature
BOTDR	Distributed	20-50km	1m	Temperature, Strain
BOTDA	Distributed	150-200km	2cm(2km) 2m(150km)	Temperature, Strain
Rayleigh OFDR	Distributed	50-70m	1mm	Temperature, Strain
FBG	Quasi-distributed	100 channels	2mm	Temperature, Strain and Displacement

1.4.2 SHM applications on distributed fiber optics

The majority of the photons sensing technology has been applied widely in the field of civil engineering application such as discrete FBG sensors. The topics about applications on infrastructures during the past few decades have been widely discussed in the various publications of [94-99]. Considering the scope of the most advanced papers, only the use of optical fibers based on distributed sensing technology has been reviewed in this section.

Currently distributed fiber optic sensors are more attractive in the SHM practice due to its excellent performance, compared to more traditional sensors. Despite their cost is expensive, they are still the best candidates that are more adaptable to diverse challenging environmental conditions. Although there are many advantages for distributed fiber optics, there still exist some limitations and challenges needs to be understood as follows:(1) Sensor package and installation; (2) Optical loss; (3) Fiber break; (4) Temperature range of the cable; (5) Quite limit of sampling frequency; (6) Lack of anti-aliasing filter. However, it is still being developing, since few applications on SHM projects based on distributed fiber optics have been come true. Anyway, in the past two decades, a variety of civil, mechanical and aerospace engineering structures, such as bridges, dams, tunnels and composite materials, etc. have been applied with distributed fiber optics. More detailed application descriptions are given here.

Inspection and maintenance of existing infrastructures is the most urgent task for national infrastructure managers. Because of higher quality inspection method which can offer more reliable bridge assessment to determine the maintenance strategy, and structural health monitoring system, and identify the early abnormal statement, so as to reduce the costs. For example, the rehabilitated RC girder bridges strengthened the simply supported RC T-beam has been installed health monitoring system by using BODTR sensors and FBG sensors in order to carry out a series of static and dynamic loading test and obtain the monitoring data. The configuration of health monitoring system is shown in Fig. 1-8[100].

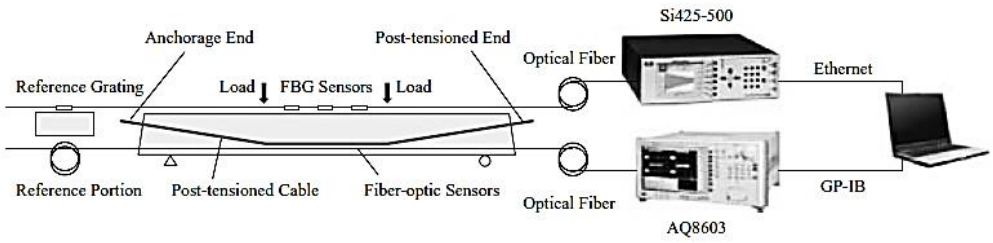

Fig. 1-8 Configuration of health monitoring system (adapted from [100])

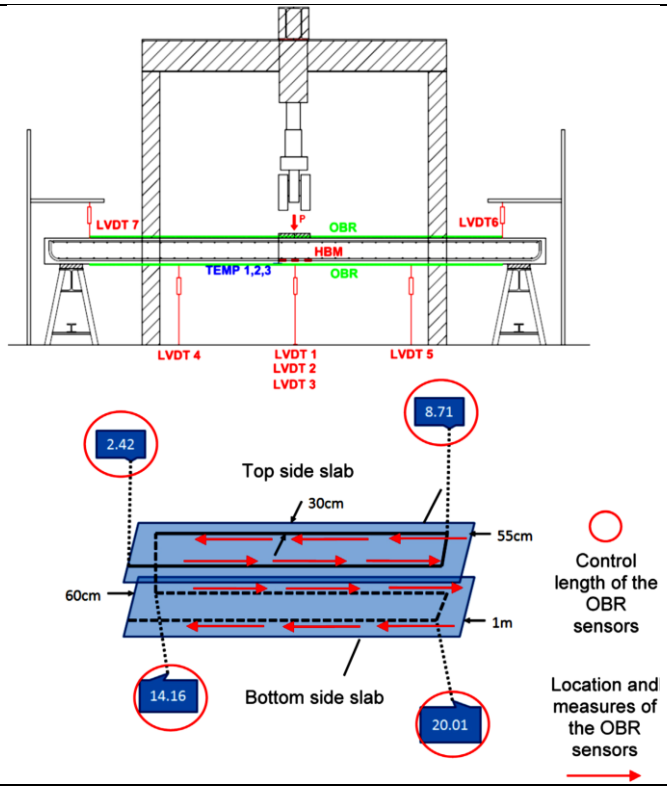

Fig. 1-9 Configuration of health monitoring system (adapted from [101])

The distributed fiber optic sensors based on backscattering reflectometer have been used in reinforced concrete slab successfully in order to identify the crack through monitoring strain along the fiber continuously[101].

More recently, a prototype of 13.5 meters of wind turbine blades has

been designed in order to develop the methodology for embedding several different types of sensors, FBG, OBR and traditional strain gauges respectively, into the structure during the manufacturing process, aiming to detect the damage after performing the static loadings[102].
Besides, more practical applications can be found in the publications[103-107].

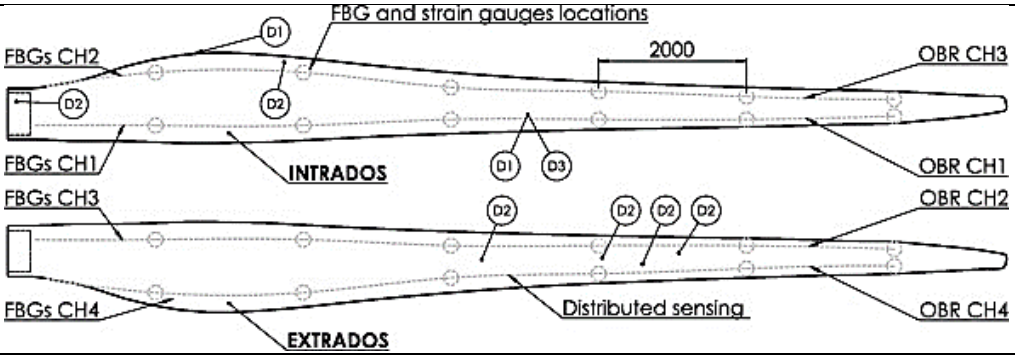

Fig. 1-10 Configuration of sensors and damage locations in blade prototype. The units in mm (adapted from [102])

1.5 Research objective and scope

Structural health monitoring has drawn a lot of attention from many researchers due to the fact that since along with the accumulation of damage gradually time by time, the security of structures is becoming risky. Therefore, the need of structural health monitoring seems essential and necessary, and damage detection is the vital part of it.
So far structural damage identification is still a coral and challenging research topic in structural health monitoring field. Existing research mainly focuses on identification and detection of linear damage in structures using modal parameters. There exists a variety of vibration-based methodologies applied into damage detection: based on the change of natural frequency, based on the change of mode shape, based on the change of frequency response function and based on the change of transmissibility function, and so on. Among the above methodologies, transmissibility function embodies its particular characteristics that it doesn't need any prior information about specific forms of loading and it

expresses more sensitive to local damage.

During my research, I aim to develop damage detection algorithm based on transmissibility function. The transmissibility is traditionally defined as the ratio of the spectra of two different system outputs, it has been comprehensively studied and it is widely used for damage detection and fault diagnosis. During the recent decades, more damage indicators based on transmissibility function have been proposed and applied into damage detection effectively due to its inherent characteristics. It is more capable to detect local change compared to the FRF and the corresponding sensitivity of transmissibility function in terms of damage, and it points out the significance of poles and zeros to localize damage in the dynamic system. More recently, the authors Christof Devriendt et have proposed that the convergence of transmissibility functions when frequency goes closely to system's poles is equal to ratio of mode shape between two different measurement points. They also pointed out that by using only a small frequency band around the resonance frequencies of structures, the outcomes of damage identification are more reliable and independent from the force location.

Although the methodologies based on transmissibility functions seem quite effective practically, most objective structures are considered as bearing linear damage which rarely happens in real engineering structures. And many researches mainly concentrate on linear damage case that damage can be considered as the linear reduction of mass and stiffness, which has been proved to be insensitive in terms of nonlinear damage. Few researches concentrate on the nonlinear damage situation based on the conception of transmissibility so far. It is worthy to mention that Timothy J. Johnson introduced nonlinear component in MDOF system by utilizing cubic nonlinear stiffness on the spring. Hence it is worth citing a recent study on the extension of the concept of transmissibility for non-linear systems using the concept of "non-linear output frequency response functions" (NOFRF) which is proposed by Lang.

In my thesis, OFDR-based distributed fiber optics, as a novel measurement technique, has been adopted. Since the evaluation on damage detection relies on the number of measurement sensors, distributed fiber optics is capable to offer an excellent strategy regarding the sensing spatial solution. The methodologies for linear damage

detection and nonlinear damage detection have been put forward respectively based on transmissibility function by using OFDR-based distributed fiber optics.

1.6 Outline of the thesis

In general, the thesis has been organized as four chapters initially starting with introduction which contains the background of structural health monitoring, vibration-based structural damage identification methods, fiber optics development history and detailed demonstration on distributed fiber optics.

Chapter 2 demonstrates a new conception and application of strain transmissibility function on linear damage identification by using distributed fiber optics. The conception of traditional transmissibility function and its damage indicators have been reviewed at the beginning, and sensitivity analysis of strain transmissibility proves its higher sensitivity compared to traditional transmissibility in terms of damage. In addition, distributed fiber optics is capable to offer loads of sensors that is helpful to locate the damage more precisely. The relative simulations and experiments have been performed.

Chapter 3 puts forward the methodologies of detecting and locating single or multiple nonlinear components under general input for MDOF system respectively. Nonlinear damage here is considered as breathing crack. Firstly, nonlinear output frequency response function (NOFRF) has been given a short review. Then nonlinear damage identification methods by using NOFRF-based and Output-based transmissibility under general input have been demonstrated in details. Moreover, distributed fiber optics is still applied into the beam structure as a dense measurement tool. A series of simulations and experiments have been carried out which could validate the effectiveness of the proposed methodologies.

Chapter 4 summaries the significant achievements which have been discussed in previous chapters. In addition, future research suggestion and prospective regarding to the research scope of this work have been provided.

CHAPTER 2

Linear damage identification method

2.1 Overview

Damage detection performed on modal parameters (natural frequency, mode shape and damping) has many advantages compared to other methods mainly due to the fact that modal parameters merely depend on the characteristics of structures themselves[108]. Since structural vibration characteristics depend on structural physical parameters, a change of the physical parameters due to a linear damage, for instance a stiffness reduction, will inevitably cause a change of the structural dynamic response.
Modal parameters identification during a continuous monitoring is usually performed by using only output measurement data and operational modal analysis. However, this could be a troublesome point in some cases, because the a priori hypothesis about independency of the modal parameters on the excitation level and the requirement of a flat spectrum of the driving force is not always respected. Among the operational feature that can be estimated from the structure response,

transmissibility function drew the attention of many researchers, because it does not require any prior knowledge of the exciting force and no modal identification is needed.
Transmissibility is conventionally defined as the ratio of the spectra of two different outputs of the system and it was proposed as damage feature firstly in[60]. The damage feature is usually the difference among the transmissibility functions of the health structure and an unknown scenario. As a fact that strain is more sensitive regarding to damage in comparison with displacement, strain transmissibility has been studied. In addition, the accuracy of damage localisation, based on the aforementioned transmissibility function, relies on the number of sensors as well. When dynamic test is performed on large structures such as bridges, tunnels and buildings, conventional sensors are extremely difficult to cover the entire target. Usually the number of sensors needed to do this is too big and then the idea is impracticable mainly for economic reasons. Fortunately, distributed fiber optics techniques have kept developing rather maturely and they have been applied into various domains [83], [109] and [110]. Distributed fiber optic sensors can measure continuously strain and temperature along the structure layout and in some cases they can also be embedded into concrete for checking the internal health status.
This chapter demonstrates the development of strain transmissibility function and its corresponding damage indicator by using distributed fiber optic sensor. A short review of damage detection based on traditional transmissibility function algorithm is described at the beginning. And then the conception of strain transmissibility has been proposed and its sensitivity analysis has been performed compared to that of traditional transmissibility. Corresponding simulation and experiment activities have been carried out respectively.

2.2 Traditional transmissibility and strain transmissibility

Transmissibility function is traditionally defined as the ratio of two different output spectra. As for a MDOF system, let $F_k(s)$ be driving force at DOF k, then the transmissibility function $T_{ij(k)}(s)$ can be calculated as:

$$T_{ij(k)}(s)=\frac{X_{ik}(s)}{X_{jk}(s)}=\frac{H_{ik}(s)F_k(s)}{H_{jk}(s)F_k(s)} \quad (2\text{-}3)$$

where $X_{ik}(s)$ and $X_{jk}(s)$ are the system outputs at DOF i and DOF j respectively; $H_{ik}(s)$ and $H_{jk}(s)$ are the frequency response functions at DOF i and DOF j respectively.

Similarly, transmissibility functions can also be defined in the same way between the same pair DOF i and DOF j when there is damage in the structure:

$$T^{D}_{ij(k)}(s)=\frac{X^{D}_{ik}(s)}{X^{D}_{jk}(s)}=\frac{H^{D}_{ik}(s)F_k(s)}{H^{D}_{jk}(s)F_k(s)} \quad (2\text{-}4)$$

where superscript D stands for the damaged status of the structure.

Usually, traditional transmissibility function (TTF) is calculated by acquiring acceleration, velocity or displacement measurement data. In this paper strain data are considered as base for a new transmissibility function, named Strain Transmissibility Function (STF). The aim of this work is to prove that STF is more sensitive to damage compared to TTF, based on the research achievement of TM Whalen, who has proved that higher order mode shape derivatives (e.g., modal curvature, third derivatives, and fourth derivatives) show better performance in terms of damage than the mode shape for beam-like structures[111].

The strain frequency response function between the loading point k and measurement point i can be written as:

$$H^{\varepsilon}_{ik}(\omega)=\frac{X^{\varepsilon}_{i}(\omega)}{F_k(\omega)}=\sum_{r=1}^{N}\frac{\delta_{ir}\varphi_{kr}}{M_r(\omega_r^2-\omega^2+2j\xi_r\omega_r\omega)} \quad (2\text{-}5)$$

Where δ_{ir} and φ_{kr} are the rth order strain mode shape and displacement mode shape respectively while ω_r is the resonance frequency. Variable k and i represent loading point and measurement output point respectively. Then the strain transmissibility function (STF) between two strain frequency response functions becomes:

$$T_{ik}^{\varepsilon}(\omega)=\frac{H_{ik}^{\varepsilon}(\omega)}{H_{jk}^{\varepsilon}(\omega)}=\frac{\sum_{r=1}^{N}\frac{\delta_{ir}\varphi_{kr}}{M_r(\omega_r^2-\omega^2+2j\xi_r\omega_r\omega)}}{\sum_{r=1}^{N}\frac{\delta_{jr}\varphi_{kr}}{M_r(\omega_r^2-\omega^2+2j\xi_r\omega_r\omega)}} \quad (2\text{-}6)$$

2.3 Damage indicators

Johnson[64] proposed the following damage indicator based on transmissibility function:

$$DI_{ij(k)}=\left|\sum_{\omega}\left(\frac{TP_{ij(k)}^{D}(\omega)-TP_{ij(k)}(\omega)}{TP_{ij(k)}(\omega)}\right)\right| \quad (2\text{-}7)$$

Where $TP_{ij(k)}(\omega)=\left|\log(T_{ij(k)}(\omega))\right|$

Additionally, literature also proposes a damage indicator based on occurrences that seems to provide more reliable and robust results according to the authors[112]. It can be briefly explained that an occurrence is counted for each frequency step at the location where the difference between intact and damaged transmissibility is maximum. Hence, the result of occurrence relies on the frequency band that you choose. The corresponding equation is

$$O_{ij(k)}(\omega)=Count(\max_{\omega}\left|TP_{ij(k)}^{D}(\omega)-TP_{ij(k)}(\omega)\right|) \quad (2\text{-}8)$$

From equation(2-8), it is shown that damage element could correspond to the maximum value of damage indicator integrated over a range of frequency band. The paper also demonstrates that the integration of frequency band could be applied to a small frequency band around the resonance frequencies of the structure under different loading conditions.

Similarly, the damage indicators for strain transmissibility can be written as follows:

$$DI_{ij(k)} = \left| \sum_{\omega} \left(\frac{TP^{\varepsilon D}_{ij(k)}(\omega) - TP^{\varepsilon}_{ij(k)}(\omega)}{TP^{\varepsilon}_{ij(k)}(\omega)} \right) \right| \quad (2\text{-}9)$$

$$O_{ij(k)}(\omega) = Count(\max_{\omega} \left| TP^{\varepsilon D}_{ij(k)}(\omega) - TP^{\varepsilon}_{ij(k)}(\omega) \right|) \quad (2\text{-}10)$$

Where $TP^{\varepsilon}_{ij(k)}(\omega) = \left| \log(T^{\varepsilon}_{ij(k)}(\omega)) \right|$

2.4 Strain transmissibility sensitivity analysis

The limit value of the transmissibility function equation(2-3), when variable *s* (the generic pole) approaches the system's poles, depends only on the mode shapes[113]:

$$\lim_{s \to \lambda_m} T_{ij(k)}(s) = \frac{\phi_{im}}{\phi_{jm}} \quad (2\text{-}11)$$

Where ϕ_{im} and ϕ_{jm} are the scalar mode-shape values.

It is obvious to observe that the limit value of transmissibility function is independent from the location and nature of the force. The variable *k* here defines the specific loading position. Therefore, the following equation is established:

$$\lim_{s \to \lambda_m} T_{ij(k)}(s) = \lim_{s \to \lambda_m} T_{ij(l)}(s) \quad (2\text{-}12)$$

Damage indicator can be calculated by using the difference between intact and damage transmissibility under integrating a small range around resonance frequencies independently from the forcing location[112].

when the variable *s* approaches to the resonance frequencies, the limit value can be obtained according to STF definition equation(2-6).

$$\lim_{\omega\to\omega_r} T_{ik}^{\varepsilon}(\omega) = \lim_{\omega\to\omega_r} \frac{\sum_{r=1}^{N} \frac{\delta_{ir}\varphi_{kr}}{M_r(\omega_r^2-\omega^2+2j\xi_r\omega_r\omega)}}{\sum_{r=1}^{N} \frac{\delta_{jr}\varphi_{kr}}{M_r(\omega_r^2-\omega^2+2j\xi_r\omega_r\omega)}} = \lim_{\omega\to\omega_r} \left. \frac{\frac{\delta_{ir}\varphi_{kr}}{M_r(\omega_r^2-\omega^2+2j\xi_r\omega_r\omega)}}{\frac{\delta_{jr}\varphi_{kr}}{M_r(\omega_r^2-\omega^2+2j\xi_r\omega_r\omega)}} \right|_r = \frac{\delta_{ir}}{\delta_{jr}} \quad (2\text{-}13)$$

It is known that FRFs can be decomposed into SDOF in modal space. When ω_r approaches to resonance frequencies, the corresponding mode will dominate the whole FRF. Similar to equation(2-11), (2-12) and (2-13), it demonstrates the limit value of STF in system poles is strain mode shape ratio.
Besides, it is known that the relationship between strain and bending moment according to beam's elastic theory:

$$\varepsilon = \frac{M}{EI} \cdot h_{\max} \quad (2\text{-}14)$$

Where M is the section moment, EI is bending stiffness, is the distance from the measurement point to the neutral axis.
However, bending curvature has the following relationship:

$$C = \frac{1}{\rho} = \frac{M}{EI} = \frac{d^2y}{dx^2} \quad (2\text{-}15)$$

Where C is the curvature, is the radius of curvature, y is the displacement normal to the neutral beam axis.
Therefore, the relationship between strain and displacement can be shown as:

$$\varepsilon = \frac{d^2y}{dx^2} \cdot h_{\max} \quad (2\text{-}16)$$

The dynamic displacement of beam structure at any position x and at any time t can be redefined as the product of space function and time function by applying separation variable method:

$$y(x,t)=\sum_{i=1}^{N}\phi_i(x)\eta_i(t) \tag{2-17}$$

Where $\phi_i(x)$ and $\eta_i(t)$ are mode shape and modal coordinate respectively.

Therefore, substitute equation(2-17) into (2-16), strain can be rewritten as:

$$\begin{aligned}\varepsilon(x,t)=\frac{d^2y(x,t)}{dx^2}\cdot h_{\max} &= h_{\max}\cdot\sum_{i=1}^{N}\phi_i''(x)\eta_i(t)\\ &=h_{\max}\cdot\sum_{i=1}^{N}\delta_i(x)\eta_i(t)\end{aligned} \tag{2-18}$$

Where $\delta_i(x)$ is strain mode shape.

According to equation(2-16), strain is equal to the product between the second derivative of displacement and a constant which is the distance from the measurement point to neutral axis. By combing this final statement with the conclusion proposed by TM Whalen, that second mode shape derivatives are better damage indicator compared to the mode shape in terms of beam-like structures[111], it is possible to declare that strain mode shape is more sensitive than displacement mode shape to damage. Therefore, the assumption that STF in correspondence of system's poles is more sensitive to damage than traditional TTF can be established.

2.5 Simulation study

In order to validate the effectiveness of the proposed assumption, harmonic response analysis has been performed on a simulated beam structure. Both displacement FRFs and strain FRFs have been extracted and used to calculate TTF and STF.

2.5.1 FEM modelling of the beam

A clamped- clamped steel beam structure has been simulated by means of the commercial software ANSYS©. The dimensions are 1.5 m × 0.04 m × 0.015 m. The beam is meshed with 25 beam elements and 26 nodes. Damage is simulated by adding a point mass (0.23kg, approximately 3% of the total mass, black block shown in Fig. 1) on element 19, which could be considered as linear damage that only changes the element mass between node 19 and node 20. Dynamic analysis is conducted for both intact and damaged beam, displacement responses and strain responses of all nodes have been acquired for both beams under two different scenarios. F1 and F2 are two impulse input forces on different node positions (node 3 and node 21 respectively) based on the fact that the intersections of two transmissibility functions on one specific measurement point under different loading situation corresponds to the natural frequencies of the system [18]. If there is damage, the intersections of those transmissibility functions are not coincidence with system's natural frequencies anymore and the damage indexes should reveal this fact.

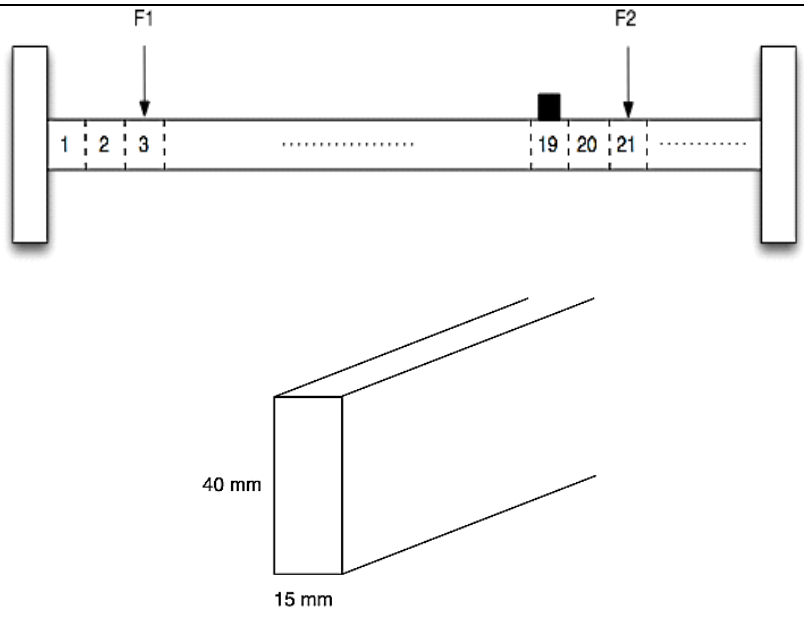

Fig. 2-11 The whole beam frame of FEM model and beam cross-section

2.5.2 Damage identification of numerical beam

F1 and F2 have been imposed on the intact beam as shown in Fig. 2-11. According to equation(2-11), it is well known that the intersection of strain transmissibility functions under two different loading positions should be in accordance with systems' poles. Fig. 2-12 shows the STFs acquired from 10th beam node and 11th
node of the intact beam under the loadings F1(3th beam node) and F2 (21th beam node) respectively.

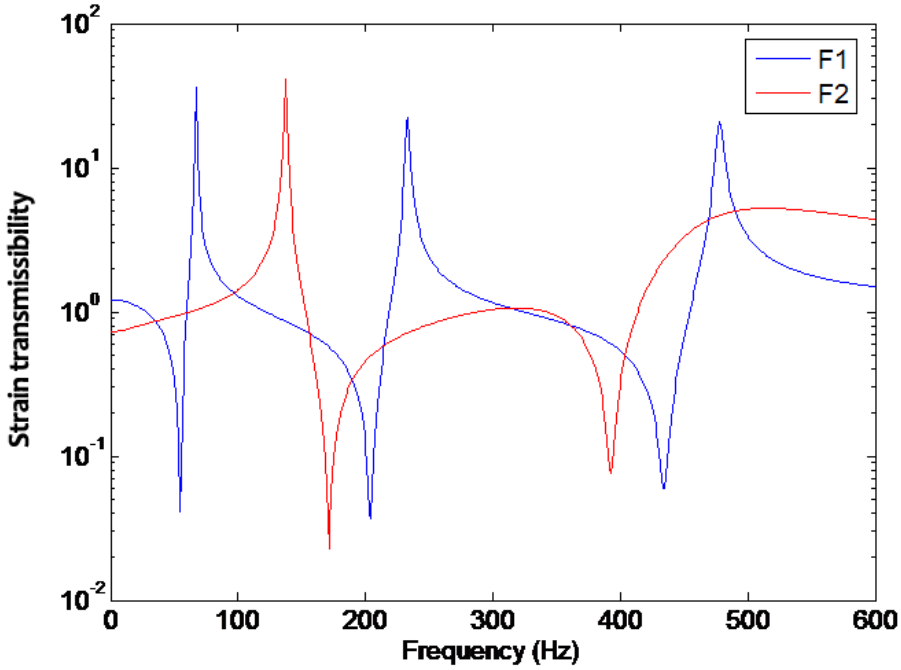

Fig. 2-12 10th measurement point STFs of intact beam for two different loading points

The following conclusion can be obtained from equation(2-11), (2-12) and (2-13), the limited value of transmissibility is independent of the location of the input. Consequently, the subtraction of two transmissibility functions under two different input DOFs when the variable converges to the systems' poles is equal to zero.

$$\lim_{\omega \to \omega_r} \left(T^{\varepsilon}_{ij(k)}(\omega) - T^{\varepsilon}_{ij(l)}(\omega) \right) = \frac{\delta_{ir}}{\delta_{jr}} - \frac{\delta_{ir}}{\delta_{jr}} = 0 \quad (2\text{-}19)$$

Therefore, the intersection points of two transmissibility under different input DOFs with the same output DOFs are corresponding to systems' poles shown in Fig. 2-12.

Zoom in the intersection area, and resonance frequencies from the 1st order to the 4th order are demonstrated in Fig. 2-13-Fig. 2-16.

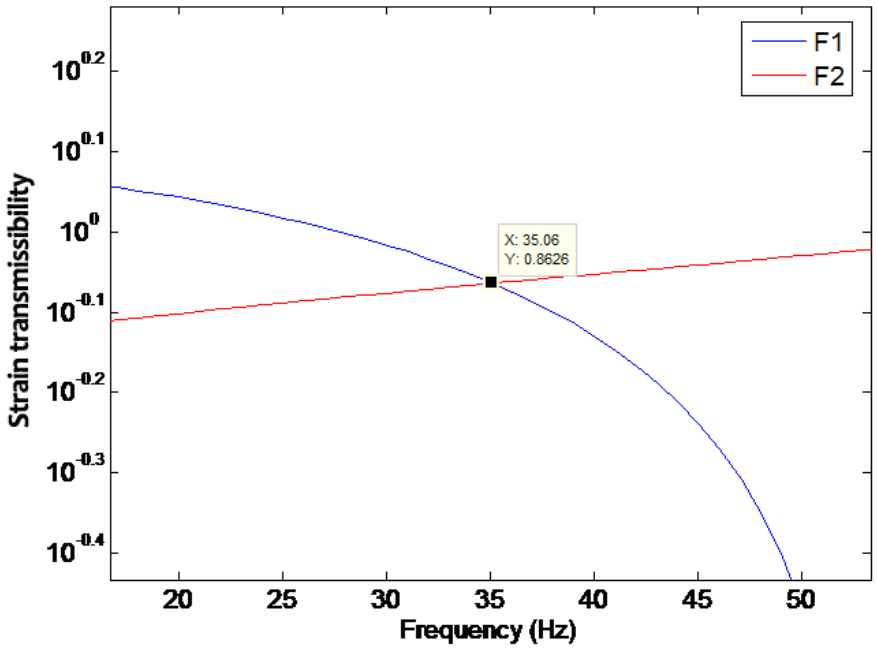

Fig. 2-13 The 1st order resonance frequency 35.06Hz

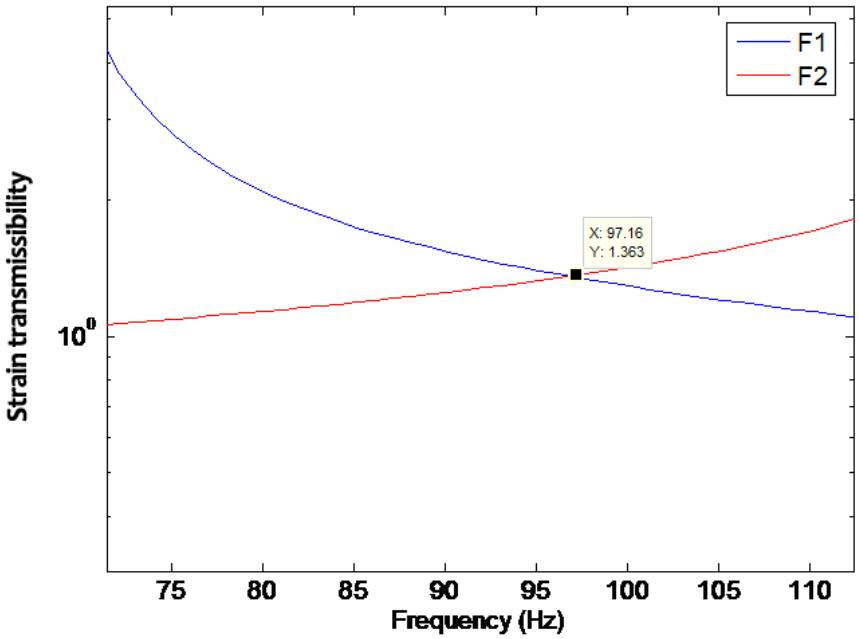

Fig. 2-14 The 2nd order resonance frequency 97.16Hz

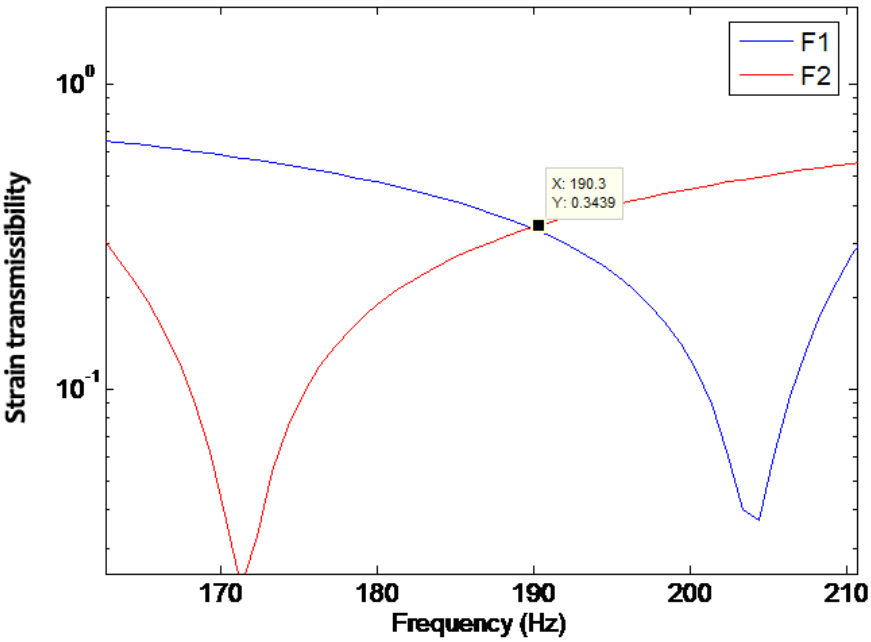

Fig. 2-15 The 3rd order resonance frequency 190.3Hz

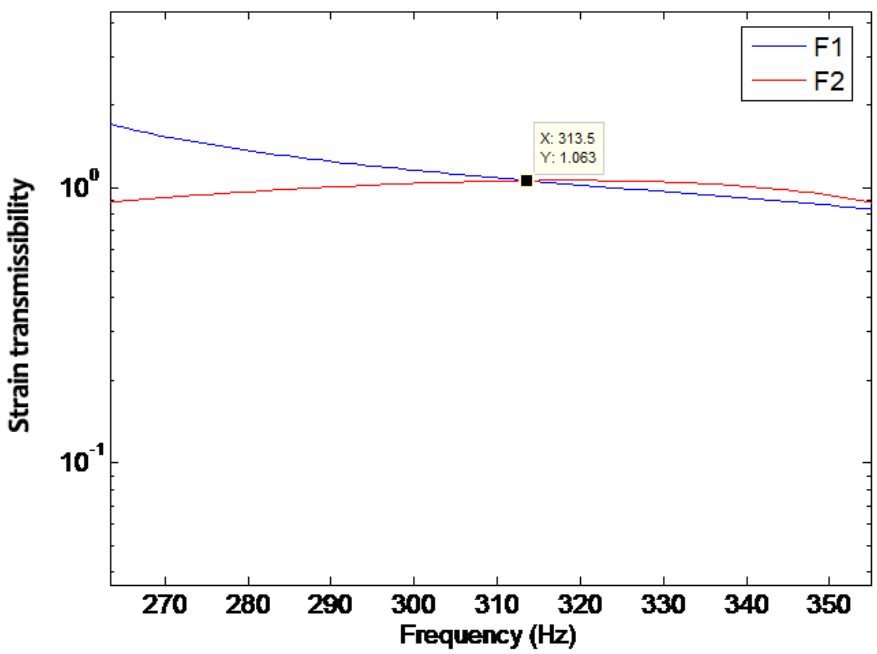

Fig. 2-16 The 4th order resonance frequency 313.5Hz

If a damage is introduced to this beam structure, the intersection points are not corresponding to the resonance frequencies any more due to the reason that the convergence value of transmissibility for damaged beam structure is not equal to the convergence value of transmissibility for intact beam structure. A derivation will occur between the intersection points from intact beam and those from damaged beam. Fig. 2-17-Fig. 2-20 Fig present the intersection points under two different input DOFs with the same output DOFs, but one transmissibility is acquired from 10th and 11th intact beam nodes and another one is from 10th and 11th damaged beam nodes.

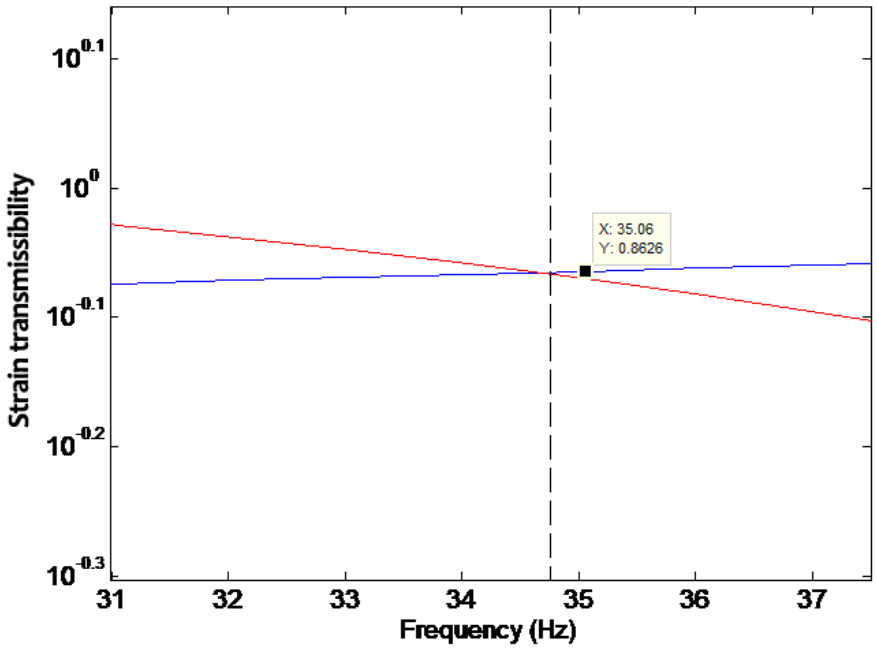

Fig. 2-17 The 1st order resonance frequency 34.70Hz

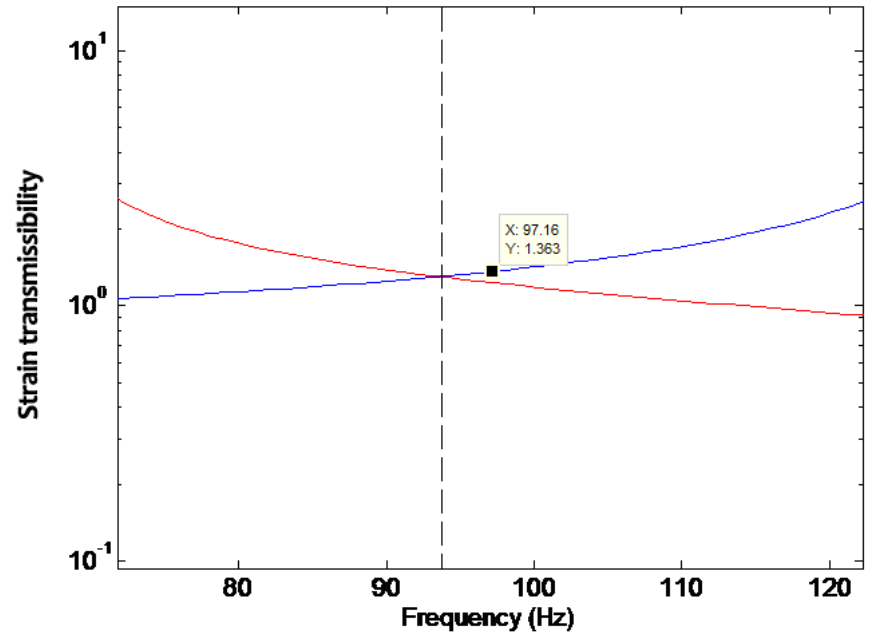

Fig. 2-18 The 2nd order resonance frequency 94.0Hz

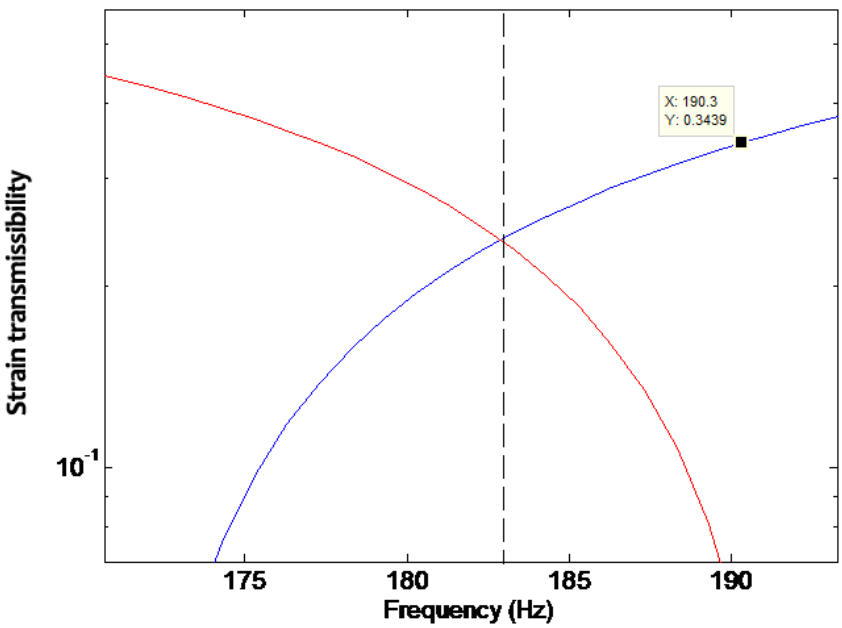

Fig. 2-19 The 3rd order resonance frequency 182.88Hz

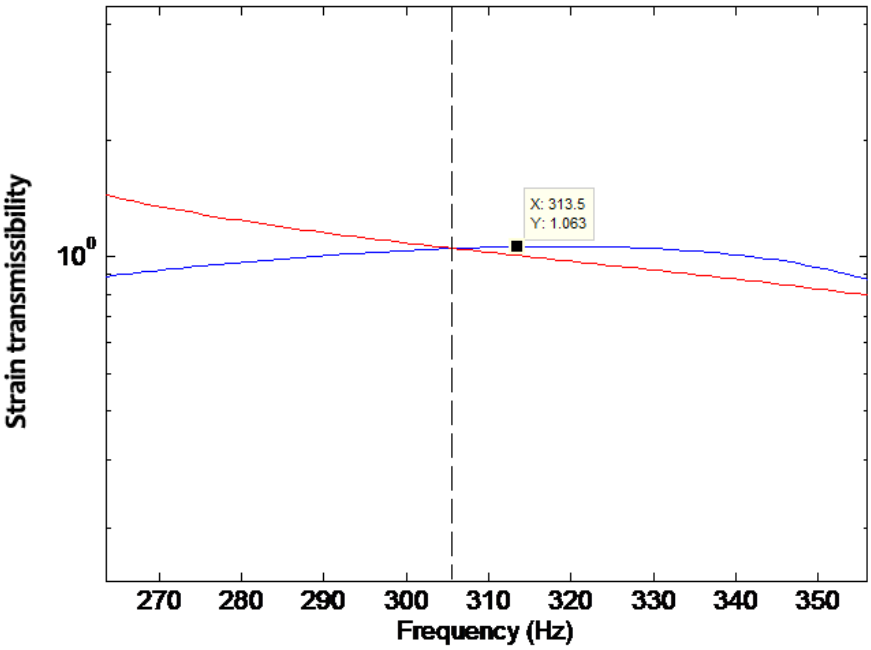

Fig. 2-20 The 4th order resonance frequency 305.50Hz

The small deviations are caused by damage, hence, damage indicator can be calculated by selecting the frequency range around the resonance frequencies connected to the system characteristics directly. If there is no damage, the damage indicators obtained should be zeros, otherwise, the maximum value could be recognized as damage location.
In order to locate damage properly, TTFs and STFs are estimated on pairs of consecutive measurement points to calculate both intact and damaged beam structures. Applying equations(2-3) to (2-10), damage features could be obtained for TTFs and STFs. In this case, a small frequency band around the first resonance frequency of the intact beam (35.06Hz) is selected to calculate the damage indicators by computing the difference between intact and damaged beam structure. The frequency band is fixed between 34-36Hz around the first mode.

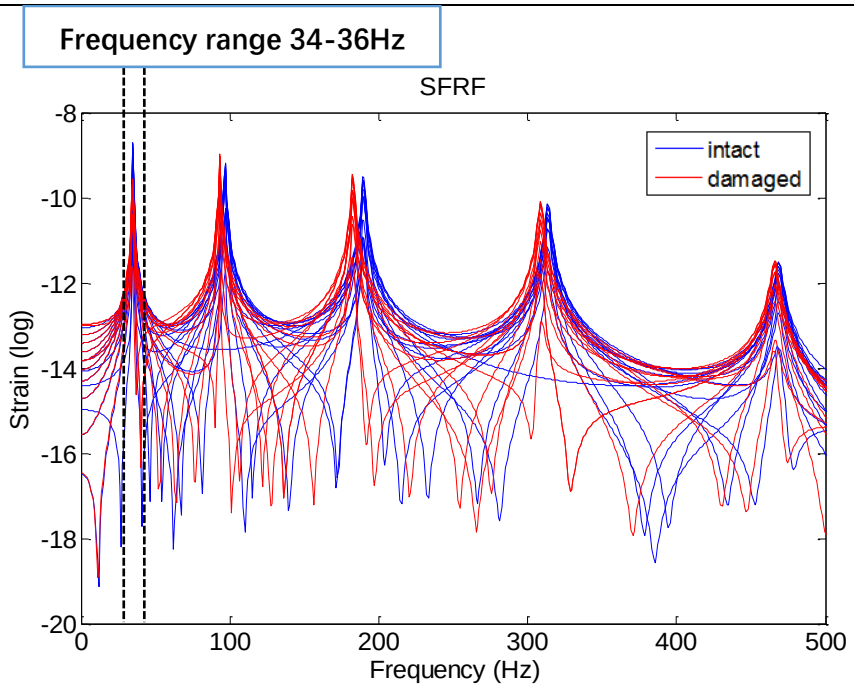

Fig. 2-21 The choice of frequency band

Table 2-3 shows the natural frequencies before and after damage, from the column of relative difference, small frequency change occurs which

means, only small amount of damage has been introduced. In addition, the change of modal masses for the first modes is listed as Table 2-4.

Table 2-3 The change of natural frequencies

Natural frequency	**Intact**	**Damaged**	**Relative difference**
1st order	35.06 Hz	34.53 Hz	1.51%
2nd order	97.16 Hz	92.97 Hz	4.31%
3rd order	190.30 Hz	184.47 Hz	3.06%
4th order	313.50 Hz	311.96 Hz	0.50%

Table 2-4 The change of modal masses

Modal mass	**Intact**	**Damaged**	**Relative difference**
1st order	2.8205	2.9203	3.54%
2nd order	3.1208	3.2362	3.70%
3rd order	3.1098	3.0290	2.60%
4th order	3.0940	2.8047	9.35%

Fig. 2-22 and Fig. 2-4 show the damage indicator DI by using TTFs and STFs respectively.

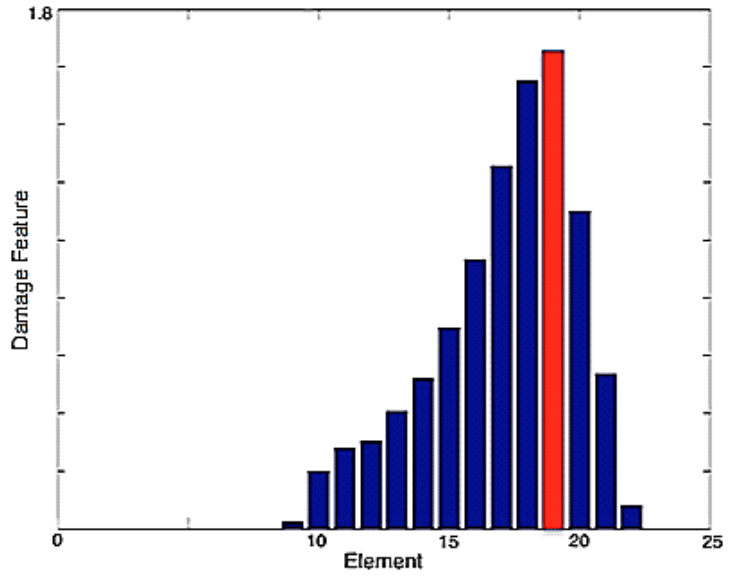

Fig. 2-22 Damage feature by using TTFs

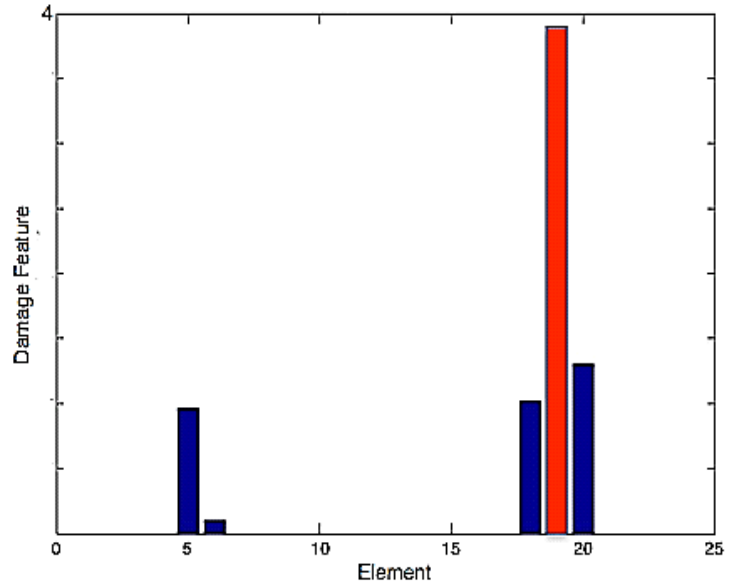

Fig. 2-23 Damage feature by using STFs

The red bars point out the damage location, apparently both damage indicators are able to figure out the correct damage location 19th element. One more interesting thing needs to be noticed, damage

indicator calculated by STFs seems more explicit compared to the one from TTFs. Basically, the maximum damage feature could correspond to the true damage location which localizes at 19th element shown in Fig. 2-22, however, the difference between 18th and 19th beam element is quite small in terms of damage indicator, which might make the result ambiguous. In contrast, damage indicator by using STFs in Fig. 2-23 shows a very clear result since there is only one high value at the19th beam element obviously.

The simulated data were also processed by the damage feature based on occurrences to test its performance. Fig. 2-24 and Fig. 2-25 show the results from occurrences and analogous conclusions to the previous case can be drawn. Both the measurements (displacement and strain) indicate precisely the damage location. Moreover, occurrences in Fig. 2-25 demonstrates that STFs are more sensitive than TTFs in terms of damage detection since only one damaged bar is shown.

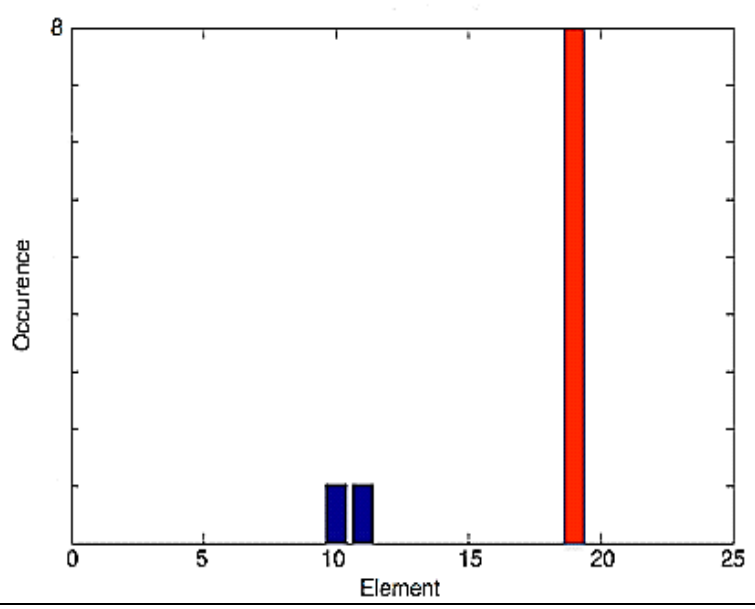

Fig. 2-24 Occurrence by using TTFs

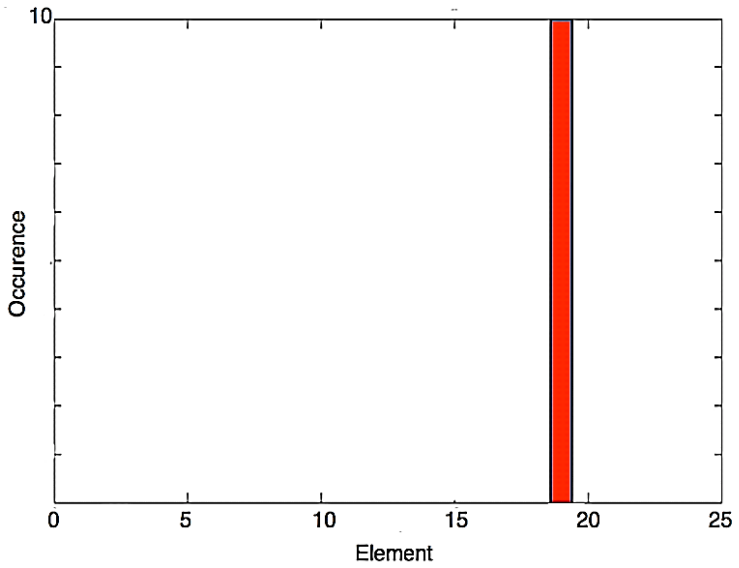

Fig. 2-25 Occurrence by using STFs

Apparently, occurrence is able to locate damage in a more robust and effective way, though damage indicator by using difference between intact and damaged TFs is able to work properly. Besides, no matter which the damage feature is used, it has shown that STFs have better performance on damage identification with respect to TTFs.

2.6 Experimental study

Since damage localisation depends on the number of sensing points, distributed fiber optics sensor has been applied for strain measurement because it is capable to provide numerous sensing points. Therefore, LUNA ODiSI-B optical distributed sensor interrogator has been adopted; which uses optical frequency domain reflectometry technique to measure strain along one single fiber.

2.6.1 Brief introduction of ODiSI-B

Optical distributed sensor interrogator (Model ODiSI-B in Fig. 2-26) provides a paramount industrial solution for applications in many fields with outstanding spatial resolution. LUNA's ODiSI B is capable to cover more than 10 meters of dynamic measurement range with a high density

of measurement points. ODiSI B can simultaneously demodulate thousands sensing points over a single optical fiber at a frequency of 100Hz. 10 m maximum sensing distance and spatial resolution of 2.56 mm make ODiSI B an extremely important tool as for strain and temperature sensing applications. Fig. 2-27 shows the operational interface of data acquisition software for ODiSI-B.

Fig. 2-26 Model ODiSI-B

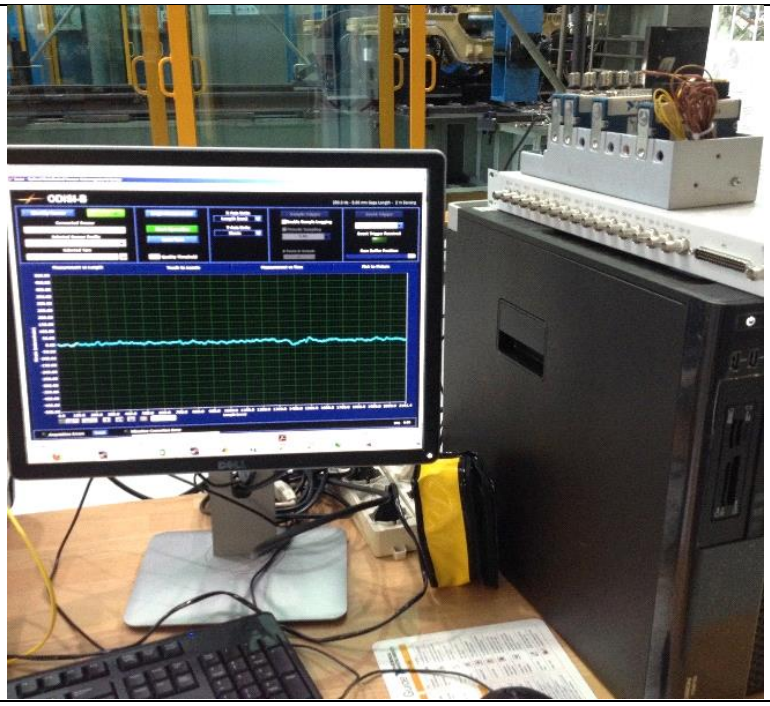

Fig. 2-27 Interface of DAQ system

There are several specifications for the distributed fiber optics based on ODiSi-B shown in Fig. 2-28.

PARAMETER	SPECIFICATION				UNITS
Performance					
Standoff	50				meters
Wavelength Accuracy[1,2]	1.5				pm
Strain Range[3]	± 10,000				µStrain
Temperature Range[4,5]	-268 to 900				°C
Mode of Operation[6]	**Standard**	**High-Speed**	**High-Resolution**	**Extended Length**	
Maximum Sensing Length	10	2	10	20	meters
Acquisition Rate	100	250	23.8	50	Hz
Sensor Spacing	2.56	2.56	0.64	2.56	mm
Gage Length	5.12	5.12	1.28	5.12	mm
Strain Repeatability (Single-scan)	± 5	± 5	± 20	± 10	µStrain
Temperature Repeatability (Single-scan)	± 0.4	± 0.4	± 1.6	± 0.8	°C

Fig. 2-28 Different specification for various modes of operation

2.6.2 Experimental setup description of the beam

A clamped-clamped steel beam has been utilized with dimension 1.5 m × 0.04 m × 0.015 m. In order to attach the fiber optics firmly, the steel beam surfaces were polished and then a specific glue was used to attach the fiber optics as shown in Fig. 2-29.

Fig. 2-29 Beam attached with fiber optic

Fig. 2-30 shows the whole frame of beam structure. Magnets are attached to the surface of the beam in order to increase the weight of beam itself, which is able to simulate linear damage situation due to the change of dynamic characteristic (Fig. 2-31). The weight of the magnets is about 0.23kg over 7.1kg of the beam.

Fig. 2-30 Beam experiment setup

Fig. 2-31 Magnets added into beam

2.6.3 Damage identification of experimental beam

The fiber optic we chose is 2 meters long and covers the full length of the beam, with sampling frequency 100 Hz and sensing space 2.6125 mm. Two damage scenarios are performed by placing the magnetics at two different locations (285mm left and 1170mm left respectively). A small range 38-42 Hz around the 1st resonant frequency is chosen to estimate the damage features. Since sampling frequency is 100 Hz, the maximum frequency component can be observed at 50 Hz. Within the frequency range of 0-50 Hz, only the first strain mode is correctly acquired. Along this 2m single fiber optic, 100 strain sensors with nearly 15 mm spacing are chosen. Fig. 2-32 shows the auto-spectra of the 100 strain sensing measurement points for intact beam.

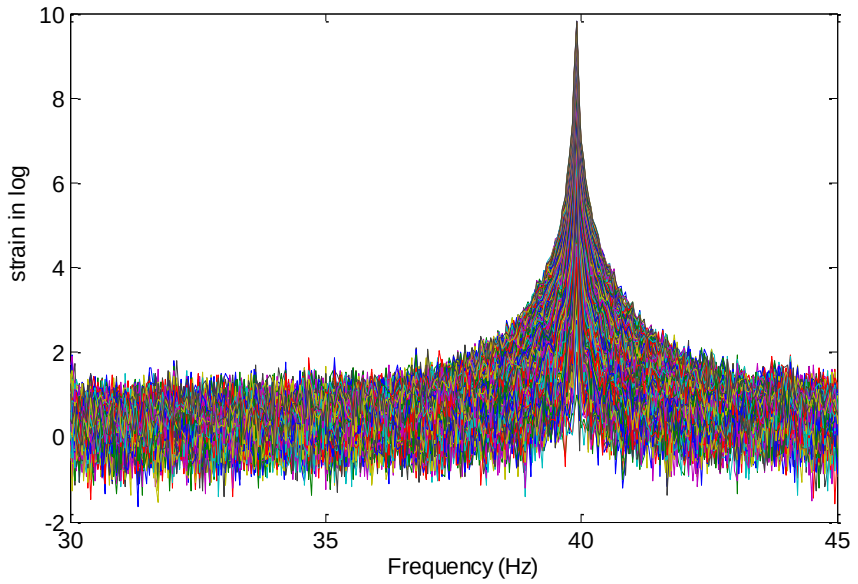

Fig. 2-32 Autospectra from 100 fiber optic sensors for intact beam

The damage identification process can be organized as the shown flow chart. A brief description is given: strain response signals are acquired from distributed fiber optics, and Fourier transform has been applied into the signals in order to get the corresponding spectra, which aims to calculate strain transmissibility. On account of the influence of noise and modal nodes, strain transmissibility coherence function has been considered so as to eliminate the unreliable transmissibility data. Then make a sentence on the value of strain transmissibility coherence, if the value is equal or larger 0.9, then it can be regarded as reliable data, otherwise, it would be discarded.

Case 1: Scenario 1 is adding magnetics on the left side of the beam, and its configuration is shown in Fig. 2-33.

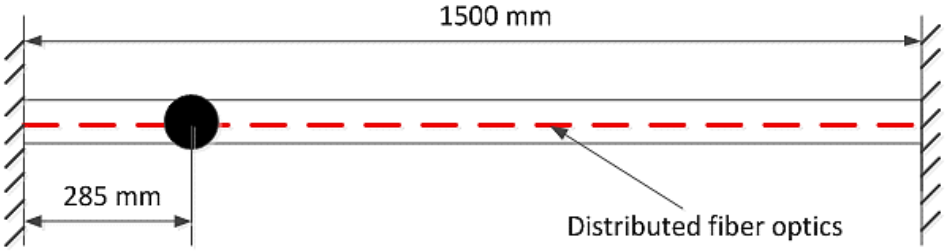

Fig. 2-33 Configuration of scenario 1

In Fig. 2-34, red bar revealed the damage location at 19th beam element based on the damage index from equation(2-9) which is in accordance with the true location of additional magnets at 285mm. Seemingly to simulations, the damage indicator in 19th element is prominent in comparison with others, which is easy to be recognized as damage component.

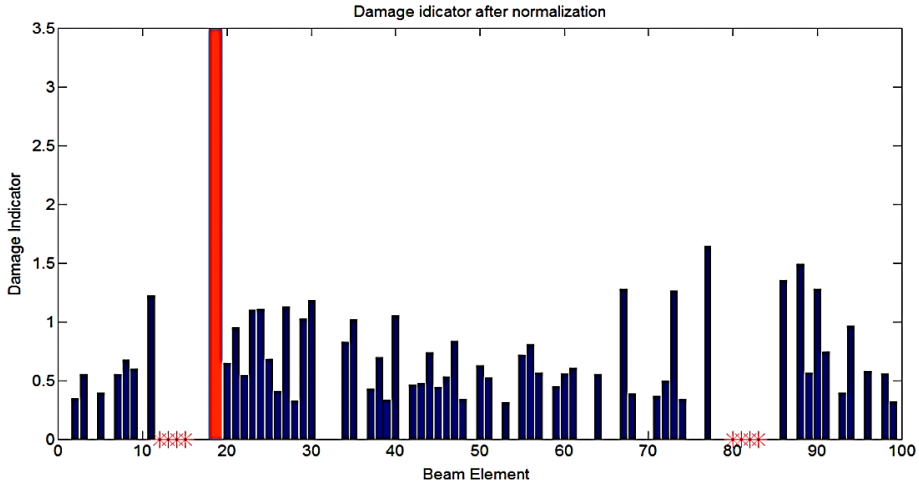

Fig. 2-34 Damage indicator of scenario 1

Occurrence damage feature has been taken into consideration as well and the identification result is shown in Fig. 2-35. Apparently, occurrence shows a clear recognition of the damage element in contrast with damage indicator of Fig. 2-34. Only one nonzero value can be seen at the 19th beam element where the magnets are placed.

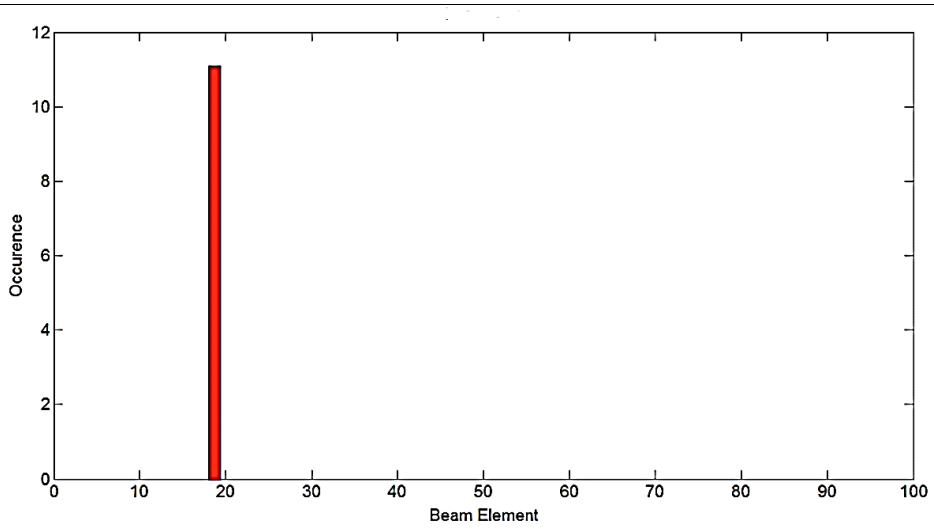

Fig. 2-35 Occurrence of scenario 1

Case 2: Scenario 2 is made by adding magnetics on the right side of the beam.

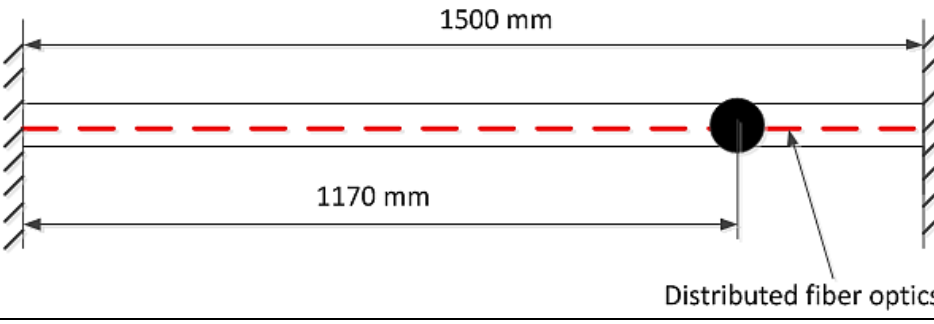

Fig. 2-36 Configuration of scenario 2

In scenario 2, red bar indicates the location of additional magnets which appears at 78th beam element in Fig. 2-36. The damage identification result is in correspondence of the true location where the magnets are placed. Fig. 2-37 shows the result of occurrence that points out correctly the damage location. Even though there are two small non-zero values at element 19th and element 67th but they can be neglected compared to element 78th.

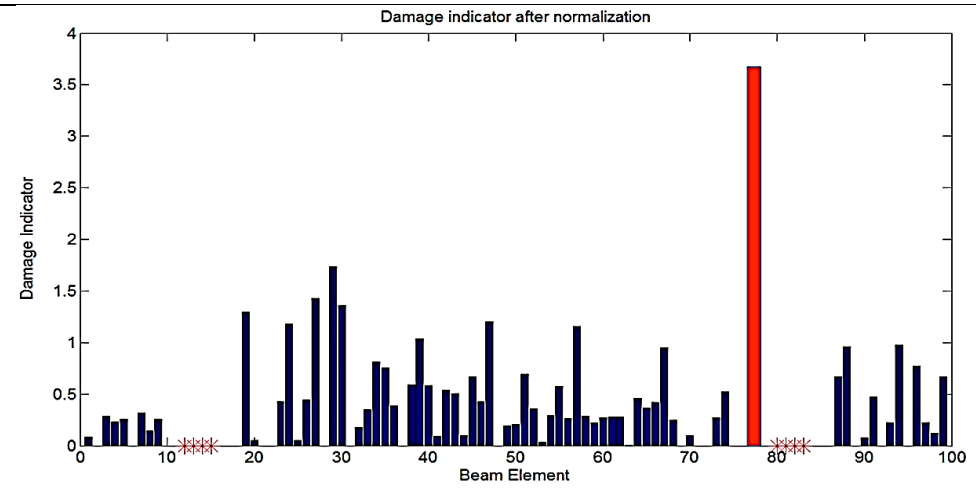

Fig. 2-37 Damage indicator of scenario 2

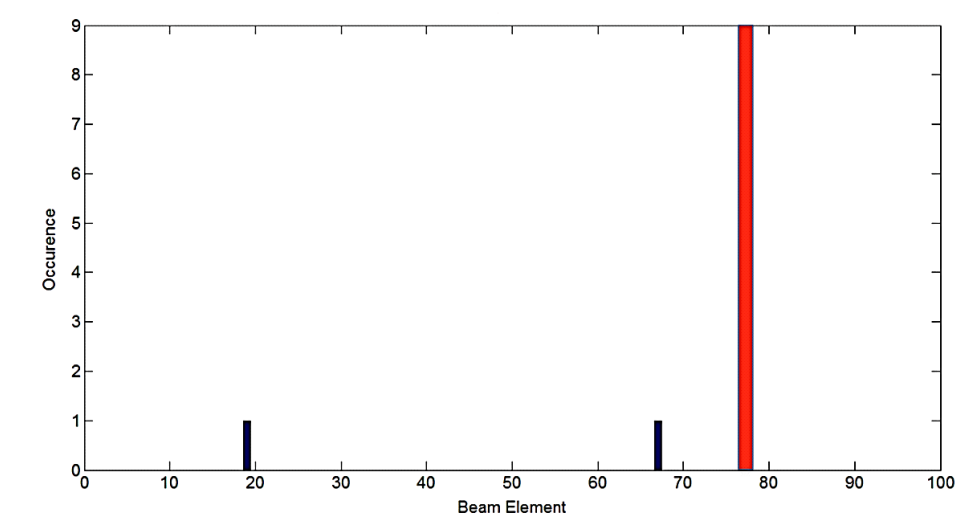

Fig. 2-38 Occurrence of scenario 2

Asterisks marked in Fig. 2-34 and Fig. 2-37 indicate the area where the damage feature is unreliable. This is due to the fact that those sensing points along the fiber are inside the area of strain nodes for the 1st strain mode which is basically equal to the curvature of the 1st mode shape of a clamped-clamped beam.

Transmissibility coherence function has been calculated in order to discard the unreliable damage indicators. It can be defined as follows:

$$C_{T_i^{\varepsilon},T_{i+1}^{\varepsilon}}(f)=\frac{\left|G_{T_i^{\varepsilon},T_{i+1}^{\varepsilon}}(f)\right|^2}{G_{T_i^{\varepsilon},T_i^{\varepsilon}}(f)G_{T_{i+1}^{\varepsilon},T_{i+1}^{\varepsilon}}(f)} \quad (2\text{-}20)$$

Where $G_{T_i^{\varepsilon},T_{i+1}^{\varepsilon}}(f)$ the cross spectral density between *i*th STF and *i+1*th STF, $G_{T_i^{\varepsilon},T_i^{\varepsilon}}(f)$ and $G_{T_{i+1}^{\varepsilon},T_{i+1}^{\varepsilon}}(f)$ are auto spectral density of *i*th STF and *i+1*th STF respectively. The value of $C_{T_i^{\varepsilon},T_{i+1}^{\varepsilon}}(f)$ is always between 0 and 1 which reflects the extent of linearity between two consecutive nodes.

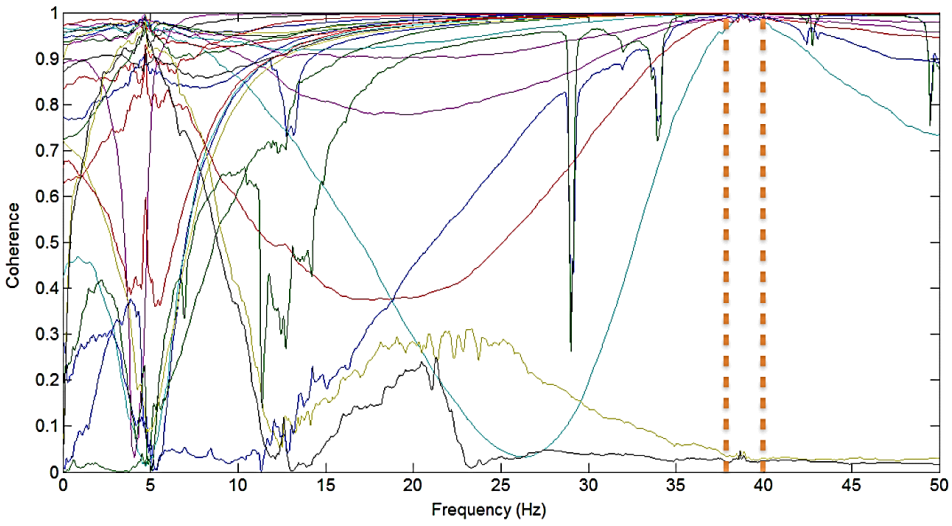

Fig. 2-39 Strain transmissibility coherence function

Fig. 2-39 shows the result of coherence function among the points used to estimate the transmissibility function. In this figure, 25 beam elements (sensors) have been selected evenly from the entire 100 sensors and corresponding strain transmissibility coherence functions have been calculated. The 1st resonance frequency is located in the area between two dash lines. In order to discard the unreliable ones, threshold for coherence function is set as 0.9. If the coherence values are closer to 1 means the corresponding STFs are reliable. Since we are interested in the area around resonance frequency, it is easy to observe that there are two coherence functions under the threshold 0.9, actually lower than 0.1. Hence, these two corresponding damage indicators should be discarded. This gives an explanation for the results of Fig. 2-39 where the sensors

placed near or at strain mode nodes are flagged as unreliable data.

Fig. 2-40 demonstrates the whole flow chart of damage identification process: Strain data acquired from distributed fiber optics, and then Fast Fourier transform (FFT) has been applied into strain data in order to obtain its spectra in frequency domain, used to calculate strain transmissibility. Strain transmissibility coherence function is established aiming to eliminate the unreliable data caused by noise and other interferences. Finally, damage location could be found according to the display of damage indicators.

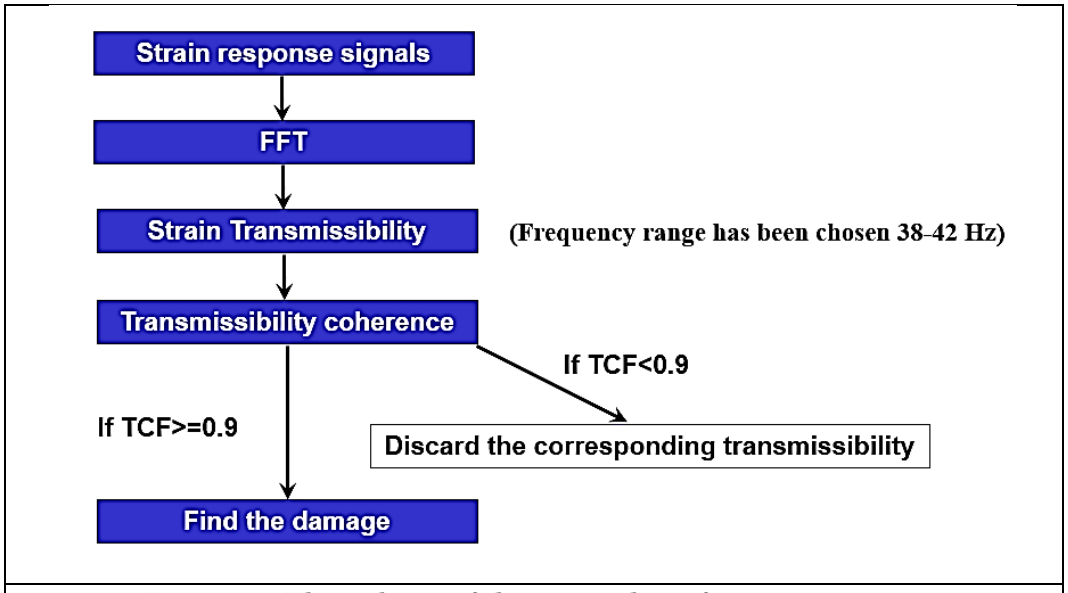

Fig. 2-40 Flow chart of damage identification process

2.6.4 Aliasing issue of distributed fiber optics

The A / D conversion places the signal at discrete levels, allows to know the value of the same signal only in well-defined time intervals, giving the fact the enormous information content is presented in the original signal. Of course, there are several types of sampling that allow you to save at least the important information while other information will be lost, unfortunately irreversible. It recalls that a non-recoverable and sampling error retrospectively because the lost information cannot be recovered.

Overlap phenomenon occurred in the signal after sampling, that the

frequency components higher than half the sampling frequency will be reconstructed into less than half the sampling frequency of the signal, this is called the aliasing effect (Aliasing Effect). The reconstructed signal is called the aliasing of the original signal, since the two signals have the same sample value.
There is the issue by referring to Fig. 2-41: in this figure x-axis you have the frequencies of the original signal, the analog signal is sampled, while the y-axis has the "apparent" frequencies, namely those resulting from the observation signal. The plot consists of a series of segments oriented alternately to +45° and -45°. The diagram is used in the following manner: it enters the abscissa with the frequency of the real signal and, the point at which it intersects the curve is reflected into y-axis and read as the mirrored frequency component due to aliasing.

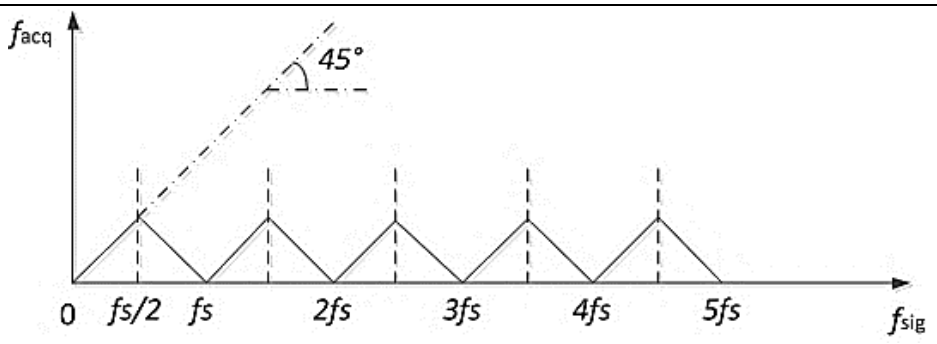

Fig. 2-41 The aliasing effect in the frequency domain

Due to the lack of anti-aliasing filter in the used distributed fiber optics, aliasing phenomenon occurred into the acquired signal. The sampling frequency of LUNA ODiSI-B is 100 Hz, therefore, the maximum frequency observed is 50Hz. Since the resonance frequencies are beyond the range of 50Hz apart from the 1st resonance frequency which is about 39.5Hz. Fig. 2-42 shows the spectra of strain FRF from simulation.

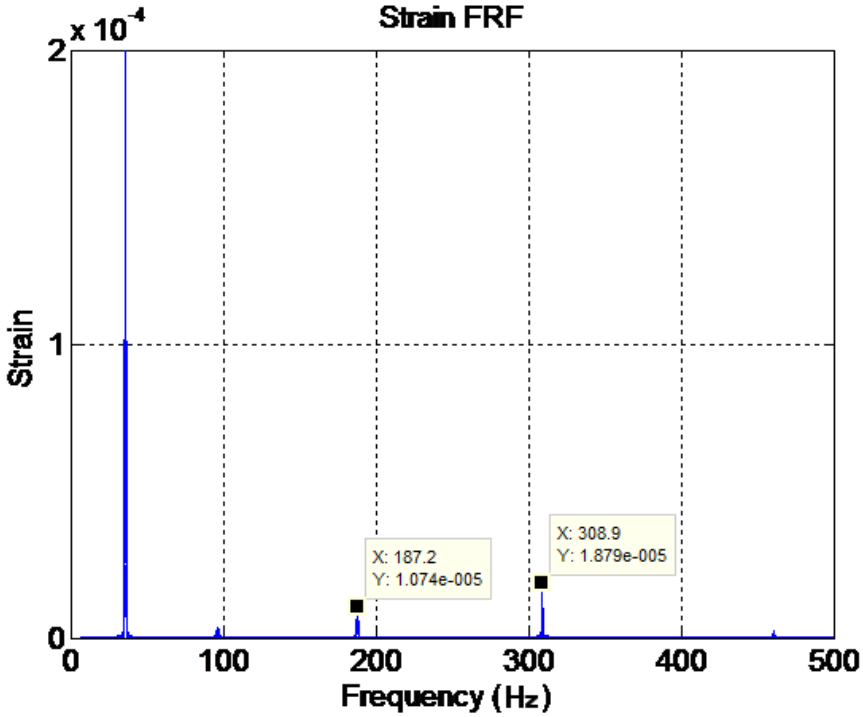

Fig. 2-42 Strain FRF

Aliasing occurred into the acquired signal from distributed fiber optics presented in Fig. 2-43.

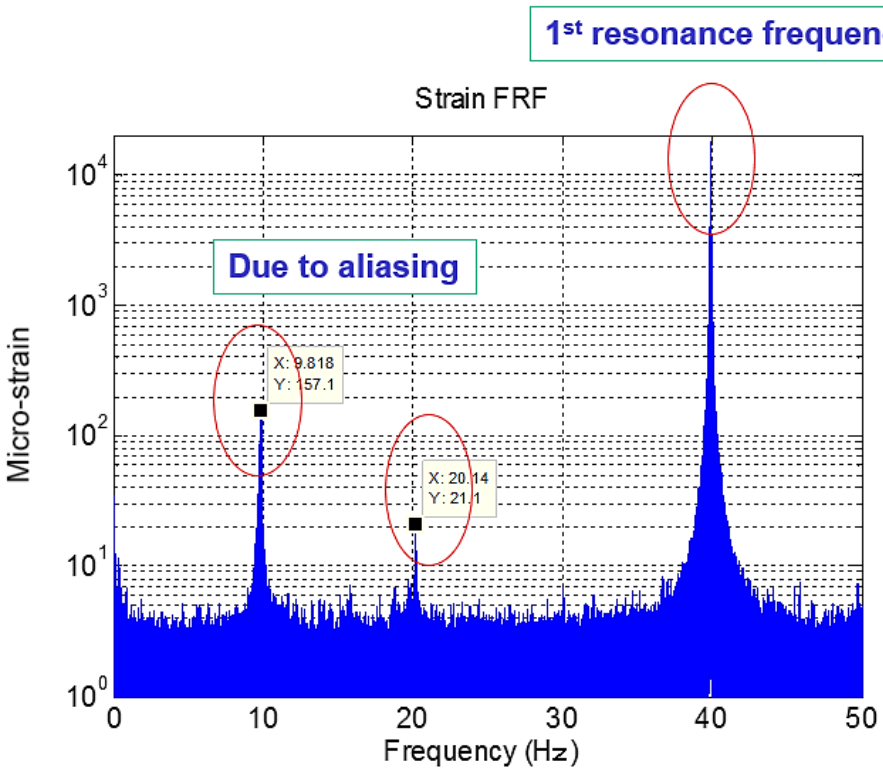

Fig. 2-43 Strain FRF from experiment data

2.7 Conclusion

In this chapter, the conception of strain transmissibility function has been proposed into damage identification based on the fact that strain can be acquired directly from distributed fiber optics. Its sensitivity analysis has been performed through the approach that the convergence value of STFs into system poles is equal to the ratio of strain mode instead of the ratio of displacement mode regarding to TTFs, which has been proved its higher sensitivity compared to TTFs in terms of damage. Both displacement data and strain data have been extracted from a simulated beam structure model, aiming to the calculation of TTFs and STFs respectively. The results show the effectiveness and feasibility of the methodology based on both transmissibility data, however, the damage identification results based on STFs demonstrate the higher sensitivity to damage.

On account of precise localisation of damage, distributed fiber optics has been applied which could provide a considerable amount of sensors along one single fiber. A steel beam has been made covered by a 2meters distributed fiber optics, and an additional magnetic mass is considered as damage (Mass change). Both dynamic strain data have been acquired from the intact and damaged beam so as to obtain the strain transmissibility. And the experimental results validate the effectiveness of proposed strain transmissibility and the excellent performance of distributed fiber optics.

And one thing needs to be noted that since there is no anti-aliasing filter during the measurement process, other frequency components will be reconstructed into the range within the analysed maximum frequency. Thus it is necessary to make clear that whether the reconstructed frequency components are mixed into the selected frequency range used to calculate damage indicators.

CHAPTER 3

Nonlinear damage identification method

3.1 Overview

Damage scenarios in engineering structures are manifested as nonlinear behaviors in many cases such as breathing crack and structural bulking failures which could be deemed as potential security hazard. Chapter 2 has proposed an approach on damage detection based on strain transmissibility conception, which is based on a linear system. Therefore, all the proposed methods based on the above assume behave linearly. However, certain types of damage in MDOF systems behave nonlinearly instead of linear damage, such as breathing crack (Bilinear stiffness), post-buckled structures (Duffing nonlinearity) and rattling joints (The system with discontinuity), etc. Therefore, the study on nonlinear damage identification is of great significance.

Recently, a new conception of Nonlinear Output Frequency Response Function (NOFRF) has been proposed by Lang *et al.* [66], which is able to clearly describe and understand a nonlinear system in separate order similar to frequency response function of linear system. Also the methodology based on Nonlinear output frequency response function (NOFRF) of MDOF system under single harmonic excitation has been

proposed by Lang et al., aiming to identify the nonlinear components. Moreover, Zhao *et al.* [69] proposed more convenient approach on nonlinearity identification by using super harmonics based on NOFRF. However, due to the fact that general input, namely bandlimited signal here, contains broader frequency band compared to single harmonic input, in this chapter, NOFRF-based transmissibility function under general input has been studied and the important properties of the proposed methodology has been derived accordingly for MDOF system with nonlinear components. In addition, the relationship between NOFRF-based transmissibility functions and Output-based transmissibility functions has been revealed. On account of the existence of single nonlinear component and multiple nonlinear components resulting in a change of system solution, two corresponding methodologies for nonlinear components identification have been presented respectively. Furthermore, it also has discussed the approach considering nonlinear components identification under multiple points excitation. The feasibility and effectiveness of the proposed methods will be validated by relative simulation work and experiments.

3.2 Nonlinear output frequency response function

3.2.1 Conception of NOFRFs

If a nonlinear system is stable at zero equilibrium which can be expressed in a mathematical way by using Volterra series[114]

$$y(t)=\sum_{n=1}^{N}\int_{-\infty}^{\infty}\cdots\int_{-\infty}^{\infty}h_n(\tau_1,\ldots,\tau_n)\prod_{i=1}^{n}u(t-\tau_i)d\tau_i \qquad (3\text{-}1)$$

In equation(3-1), $h_n(\tau_1,\ldots,\tau_n)$ is Volterra kernel function, $u(t)$ is input in time domain and the maximum nonlinear order of this system is N. Equation(3-1) demonstrates the output of this class of nonlinear system in time domain subjected to general input. And Lang and Billings in 1990 have derived the output in frequency domain corresponding to equation(3-1), namely nonlinear output frequency response, as the following expression:

$$\begin{cases} Y(j\omega)=\sum_{n=1}^{N}Y_n(j\omega) \quad for\ \forall\omega \\ Y_n(j\omega)=\dfrac{1/\sqrt{n}}{(2\pi)^{n-1}}\int_{\omega_1+\cdots+\omega_n}H_n(j\omega_1,\ldots,j\omega_n)\prod_{i=1}^{n}U(j\omega_i)d\sigma_{n\omega} \end{cases} \quad (3\text{-}2)$$

Where $Y_n(j\omega)$ is the nth order output spectra. $U(j\omega)$ and $Y(j\omega)$ are the system input and output spectra equation(3-2) states the relationship between the nth order output frequency response and input spectrum, and it states that the output frequency response is the summation of N different order output frequency response. Here $H_n(j\omega_1,\ldots,j\omega_n)$ is nth order GFRF (Generalized frequency response function), which is the multidimensional Fourier transform of $h_n(\tau_1,\ldots,\tau_n)$ [114]. It is defined as:

$$H_n(j\omega_1,\ldots,j\omega_n)=\int_{-\infty}^{\infty}\cdots\int_{-\infty}^{\infty}h_n(\tau_1,\ldots,\tau_n)\times e^{-(\omega_1\tau_1+\cdots+\omega_n\tau_n)j}d\tau_1\cdots d\tau_n \quad (3\text{-}3)$$

In terms of linear system, input and output signal contain the same frequency band. Whiles the frequency band of system output are wider compared to that of system input for nonlinear system. A general equation(3-4) can be used to reveal the relationship between output and input frequencies.

$$f_Y=\bigcup_{n=1}^{N}f_{Y_n} \quad (3\text{-}4)$$

Where f_Y stands for the overall output non-negative frequency components, and f_{Y_n} is the frequency components due to the nth order nonlinearity. Lang and Billings have derived an explicit expression for f_{Y_n} in 1997. More details can be found in[114].

Based on the conception and characteristics of nonlinear output frequency response explained in this section, nonlinear output frequency response function (NOFRF), as a new conception proposed by Lang *et al.*, has been reviewed in the following in order to represent a clearer and

deeper insight into the frequency response function due to nonlinear systems.

Lang and Billings[114] have recently proposed a new method to describe the phenomenon of nonlinear system named nonlinear output frequency function (NOFRF), which is defined as:

$$G_n(j\omega)=\frac{\int_{\omega_1+\cdots+\omega_n=\omega} H_n(j\omega_1,\ldots,j\omega_n)\prod_{i=1}^{n}U(j\omega_i)\,d\sigma_{n\omega}}{\int_{\omega_1+\cdots+\omega_n=\omega}\prod_{i=1}^{n}U(j\omega_i)\,d\sigma_{n\omega}} \tag{3-5}$$

Where equation(3-5) must satisfy the condition

$$U_n(j\omega)=\int_{\omega_1+\cdots+\omega_n=\omega}\prod_{i=1}^{n}U(j\omega_i)\,d\sigma_{n\omega}\neq 0 \tag{3-6}$$

Therefore, equation(3-2) can be rewritten by introducing the conception of NOFRF:

$$Y(j\omega)=\sum_{n=1}^{N}Y_n(j\omega)=\sum_{n=1}^{N}G_n(j\omega)U_n(j\omega) \tag{3-7}$$

Equation(3-7) is another expression for to a general class of nonlinear systems, which reveals the relationship between input and output of nonlinear systems. It shows the output is composed of a combined contribution from different order NOFRFs $G_n(j\omega)\ n=1,...,N$ and input $U_n(j\omega)\ n=1,...,N$ which can be regarded as the linear combination of output frequency response for linear system. Fig. 3-1 describes the input and output in frequency domain of linear system. Fig. 3-2 illustrates the relationship between input and output in frequency domain of nonlinear system which is the graphic expression of equation(3-7). The distinct merit of NOFRFs is that it is more convenient to implement the analysis of nonlinear system, since it is one-dimensional function of frequency compared to GFRFs $H_n\ (n=1,...,N)$ which is multi-dimensional and complexed to be interpreted.

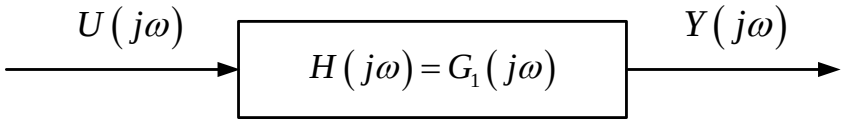

Fig. 3-1 The output frequency response for linear systems

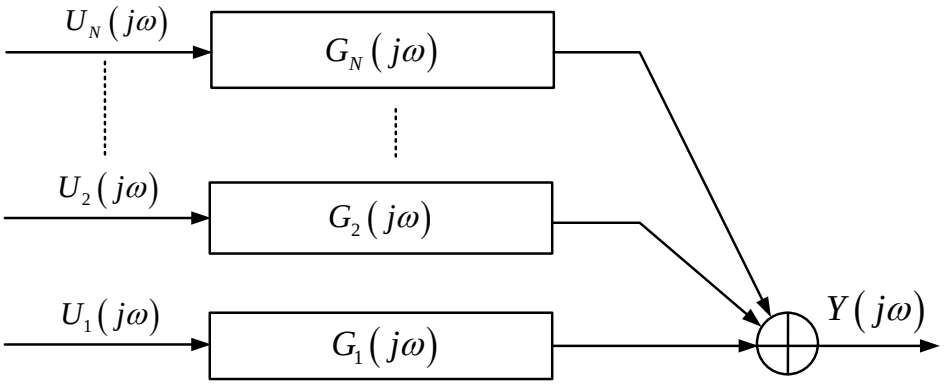

Fig. 3-2 The output frequency response for nonlinear systems

3.2.2 Estimation of NOFRFs

Equation(3-7) can be represented by using the product of two matrices:

$Y(j\omega)=\left[U_1(j\omega),\ldots,U_N(j\omega)\right]\left[G_1(j\omega),\ldots,G_N(j\omega)\right]^T$	(3-8)

Suppose the case that input is $u(t)=\alpha\cdot u^*(t)$ where α is a constant and $u^*(t)$ is the base input signal, therefore the expression of nth order input signal in frequency domain can be rewritten as:

$U_n(j\omega)=\dfrac{1/\sqrt{n}}{(2\pi)^{n-1}}\int_{\omega_1+\cdots+\omega_n=\omega}\prod_{i=1}^{n}U(j\omega_i)\,d\sigma_{n\omega}$ $=\alpha^n\dfrac{1/\sqrt{n}}{(2\pi)^{n-1}}\int_{\omega_1+\cdots+\omega_n=\omega}\prod_{i=1}^{n}U^*(j\omega_i)\,d\sigma_{n\omega}=\alpha^n U_n^*(j\omega)$	(3-9)

Hence equation(3-8) can be rewritten by substituting equation(3-9):

$$Y(j\omega)=\left[\alpha U_1^*(j\omega),\ldots,\alpha^N U_N^*(j\omega)\right]\left[G_1^*(j\omega),\ldots,G_N^*(j\omega)\right]^T \quad (3\text{-}10)$$

Here $\left[G_1^*(j\omega),\ldots,G_N^*(j\omega)\right]^T$ are the NOFRFs to be evaluated.

In order to excite the system $\bar{N}$ times, it is need to adopt $\bar{N}$ different value for α. All α_i $i=1,\ldots,\bar{N}$ are constant and

$$\bar{N}\geq N \quad (3\text{-}11)$$

Meanwhile, the following relationship should be established: $\alpha_{\bar{N}}>\alpha_{\bar{N}-1}>\cdots>\alpha_1>0$.

Consider $\bar{N}$ times excitation for the system, the NOFRFs can be estimated as:

$$\left[Y^1(j\omega),\ldots,Y^{\bar{N}}(j\omega)\right]^T=\begin{bmatrix}\alpha_1 U_1^*(j\omega),\ldots,\alpha_1^N U_N^*(j\omega)\\ \vdots \\ \alpha_{\bar{N}} U_1^*(j\omega),\ldots,\alpha_{\bar{N}}^N U_N^*(j\omega)\end{bmatrix} *\left[G_1^*(j\omega),\ldots,G_N^*(j\omega)\right]^T \quad (3\text{-}12)$$

Therefore, NOFRFs $\left[G_1^*(j\omega),\ldots,G_N^*(j\omega)\right]^T$ can be estimated by applying least square approach:

$$\left[G_1^*(j\omega),\ldots,G_N^*(j\omega)\right]^T=\left(\begin{bmatrix}\alpha_1 U_1^*(j\omega),\ldots,\alpha_1^N U_N^*(j\omega)\\ \vdots \\ \alpha_{\bar{N}} U_1^*(j\omega),\ldots,\alpha_{\bar{N}}^N U_N^*(j\omega)\end{bmatrix}^T\begin{bmatrix}\alpha_1 U_1^*(j\omega),\ldots,\alpha_1^N U_N^*(j\omega)\\ \vdots \\ \alpha_{\bar{N}} U_1^*(j\omega),\ldots,\alpha_{\bar{N}}^N U_N^*(j\omega)\end{bmatrix}\right)^{-1} *\begin{bmatrix}\alpha_1 U_1^*(j\omega),\ldots,\alpha_1^N U_N^*(j\omega)\\ \vdots \\ \alpha_{\bar{N}} U_1^*(j\omega),\ldots,\alpha_{\bar{N}}^N U_N^*(j\omega)\end{bmatrix}^T\left[Y^1(j\omega),\ldots,Y^{\bar{N}}(j\omega)\right]^T \quad (3\text{-}13)$$

3.3 Transmissibility of MDOF nonlinear structural system under general input

General input has been reckoned bandlimited input in this chapter which contains a broader frequency band compared to single harmonic input, and it can be considered approximately as a superposition of a succession of sinusoid signals. It starts from the transmissibility of MDOF nonlinear structural system.

3.3.1 MDOF Nonlinear structural system description

Consider a linear MDOF system which contains n degree of freedom. The input force, considered single point excitation, is applied on the Jth mass. The system of nonlinear MDOF is shown in Fig. 3-3. The governing motion equation is given as:

$$\boldsymbol{M}\ddot{\boldsymbol{y}}(t)+\boldsymbol{C}\dot{\boldsymbol{y}}(t)+\boldsymbol{K}\boldsymbol{y}(t)=\boldsymbol{F}(t) \tag{3-14}$$

Where: $\boldsymbol{M}$, $\boldsymbol{C}$, $\boldsymbol{K}$, $\boldsymbol{F}$ and $\boldsymbol{y}$ are the system mass matrix, damping matrix, stiffness matrix, force vector and response displacement vector respectively.

$$\boldsymbol{M}=\begin{bmatrix} m_1 & 0 & \cdots & 0 \\ 0 & m_2 & \cdots & 0 \\ \vdots & \vdots & \ddots & \vdots \\ 0 & 0 & 0 & m_n \end{bmatrix}$$

$$\boldsymbol{C}=\begin{bmatrix} c_1+c_2 & -c_2 & 0 & \cdots & 0 \\ -c_2 & c_2+c_3 & -c_3 & \ddots & \vdots \\ 0 & \ddots & \ddots & \ddots & \vdots \\ \vdots & \ddots & -c_{n-1} & c_{n-1}+c_n & -c_n \\ 0 & 0 & 0 & -c_n & c_n+c_{n+1} \end{bmatrix}$$

$$\boldsymbol{K}=\begin{bmatrix} k_1+k_2 & -k_2 & 0 & \cdots & 0 \\ -k_2 & k_2+k_3 & -k_3 & \ddots & \vdots \\ 0 & \ddots & \ddots & \ddots & \vdots \\ \vdots & \ddots & -k_{n-1} & k_{n-1}+k_n & -k_n \\ 0 & 0 & 0 & -k_n & k_n+k_{n+1} \end{bmatrix}$$

$$\boldsymbol{F}(t)=\begin{bmatrix} \overbrace{0 \ \cdots \ 0}^{J-1} & u(t) & \overbrace{0 \ \cdots \ 0}^{n-J} \end{bmatrix}^T$$

$$\boldsymbol{y}(t)=\begin{bmatrix} y_1(t) & \cdots & y_n(t) \end{bmatrix}^T$$

Assume there are $\bar{L}(\bar{L}\geq 1)$ nonlinear components (spring or damping) located between L_i-1 and L_i masses, where $i=1,2,...,\bar{L}$. The corresponding nonlinear restoring forces can be estimated as polynomial function of deformation and derivatives of deformation. These functions are assumed to be continuous, which can be approximated by a polynomial with its nonlinear part represented by (3-15).

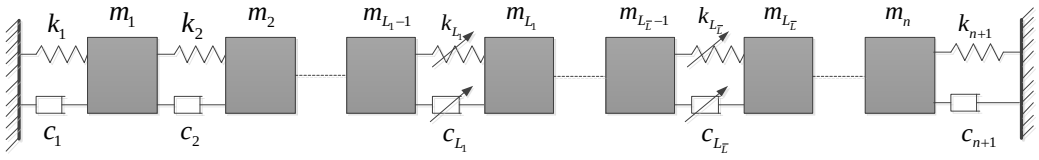

Fig. 3-3 MDOF nonlinear system

Denote nonlinear restoring forces as:

$$NonF_{L_i}=\sum_{l=1}^{N}\alpha_{(L_i,l)}(y_{L_i}(t)-y_{L_i-1}(t))^l+\sum_{l=1}^{\bar{N}}\beta_{(L_i,l)}(\dot{y}_{L_i}(t)-\dot{y}_{L_i-1}(t))^l \qquad (3\text{-}15)$$

Where $\alpha_{(L_i,l)}$ and $\beta_{(L_i,l)}$ are nonlinear coefficients of polynomial functions.
Therefore,

$$nf_i(t)=\left[\overbrace{0\ \cdots\ 0}^{L_i-2}\quad -NonF_{L_i}\quad NonF_{L_i}\quad \overbrace{0\ \cdots\ 0}^{n-L_i}\right]^T \tag{3-16}$$

The nonlinear force vector can be written as

$$\boldsymbol{NF}(t)=\sum_{i=1}^{L} nf_i(t) \tag{3-17}$$

So the nonlinear MDOF system can be defined as

$$\boldsymbol{M}\ddot{\boldsymbol{y}}(t)+\boldsymbol{C}\dot{\boldsymbol{y}}(t)+\boldsymbol{K}\boldsymbol{y}(t)=\boldsymbol{F}(t)+\boldsymbol{NF}(t) \tag{3-18}$$

Equation(3-14) represents a typical MDOF moving equation. The term *NF* is nonlinear spring or damping. If there is only one input term *F*, it is SIMO system, otherwise it is MIMO system.
In this chapter, a more effective approach aiming at nonlinear components identification on single and multiple nonlinear components situations has been studied, regarding SIMO and MIMO system respectively.

3.3.2 Output frequency range of MDOF Nonlinear structural systems under general input

This part shows the calculation of output frequency range for nonlinear system. One of the most important properties is the output frequency range of nonlinear system is much richer than the input, which is distinctly different with the case of linear system that the output frequency range is the same as the input. Lang and Billings[114] gave an explicit explanation of output frequency range of nonlinear system, and also proposed a set of formulas to calculate the output frequency range of nonlinear system.
Now consider the situation when the system is excited under a general input, namely bandlimited signal, $\omega=[a,b]\ b>a\geq 0$.

$$U(j\omega)\begin{cases}\neq 0 & \omega\in[a,b]\\ =0 & \omega\notin[a,b]\end{cases} \qquad (3\text{-}19)$$

Where $U(j\omega)$ is the input spectrum.

Lang and Billings have derived an approach to calculate output frequency range for nonlinear system when subjected to a general input expressed as (3-19).

The output frequency range can be expressed as

$$f_Y = f_{Y_N} \cup f_{Y_{N-(2p^*-1)}}$$

$$f_{Y_n} = \begin{cases} \bigcup_{k=0}^{i^*-1} I_k & \text{when } \dfrac{nb}{(a+b)} - \left[\dfrac{na}{(a+b)}\right] < 1 \\ \bigcup_{k=0}^{i^*} I_k & \text{when } \dfrac{nb}{(a+b)} - \left[\dfrac{na}{(a+b)}\right] \geq 1 \end{cases} \qquad (3\text{-}20)$$

$$i^* = \left[\frac{na}{(a+b)}\right] + 1 \text{ where } [.] \text{ means to take the integer part}$$

$$I_k = (na - k(a+b), nb - k(a+b)) \text{ for } k = 0,...,i^* - 1,$$

$$I_{i^*} = (0, nb - i^*(a+b))$$

In equation(3-20), p^* can be taken values from 1, 2, …, [N/2] which relies on the nonlinear system.

In order to better explain the use of (3-20), here consider an example of output frequency range calculation for each NOFRF order. The frequency of input is belonging to [a, b] which a=7 Hz, b=10 Hz. Since we only consider first fourth orders NOFRFs, each different NOFRF has its corresponding output frequency range. Only the first 4 order system nonlinearity is considered.

1) When n=1

$$i^* = \left[\frac{na}{a+b}\right] + 1 = \left[\frac{7}{7+10}\right] + 1 = 1$$

$$\frac{nb}{a+b} - \left[\frac{na}{a+b}\right] = \frac{10}{7+10} - \left[\frac{7}{7+10}\right] < 1$$

So $f_{Y_n} = f_{Y_1} = \bigcup_{k=0}^{i^*-1} I_k = I_0 = [na, nb] = [7,10]$

2) When n=2

$$i^* = \left[\frac{na}{a+b}\right] + 1 = \left[\frac{2*7}{7+10}\right] + 1 = 1$$

$$\frac{nb}{a+b} - \left[\frac{na}{a+b}\right] = \frac{2*10}{7+10} - \left[\frac{2*7}{7+10}\right] > 1$$

So $f_{Y_n} = f_{Y_2} = \bigcup_{k=0}^{i^*} I_k = I_0 + I_1 = [na, nb] \bigcup [0, nb-(a+b)] = [0,3] \bigcup [14,20]$

3) When n=3

$$i^* = \left[\frac{na}{a+b}\right] + 1 = \left[\frac{3*7}{7+10}\right] + 1 = 2$$

$$\frac{nb}{a+b} - \left[\frac{na}{a+b}\right] = \frac{3*10}{7+10} - \left[\frac{3*7}{7+10}\right] < 1$$

So

$$f_{Y_n} = f_{Y_3} = \bigcup_{k=0}^{i^*} I_k = I_0 + I_1 = [na, nb] \bigcup [na-(a+b), nb-(a+b)] = [4,13] \bigcup [21,30]$$

4) When n=4

$$i^* = \left[\frac{na}{a+b}\right] + 1 = \left[\frac{4*7}{7+10}\right] + 1 = 2$$

$$\frac{nb}{a+b} - \left[\frac{na}{a+b}\right] = \frac{4*10}{7+10} - \left[\frac{4*7}{7+10}\right] > 1$$

So

$$f_{Y_n} = f_{Y_4} = \bigcup_{k=0}^{i^*} I_k = I_0 + I_1 + I_2 = [na, nb] \bigcup [na-(a+b), nb-(a+b)] \bigcup \left[0, nb - i^* * (a+b)\right]$$

$$= [0,6] \bigcup [11,23] \bigcup [28,40]$$

3.3.3 NOFRF-based transmissibility of MDOF Nonlinear structural systems under general input

The nonlinear system output can also be defined in frequency domain:

$$
\begin{aligned}
y(t) &= \sum_{n=1}^{N} y_n(t) \\
&= \sum_{n=1}^{N} \int_{-\infty}^{\infty} \cdots \int_{-\infty}^{\infty} h_n(\tau_1, \ldots, \tau_n) \prod_{i=1}^{n} u(t-\tau_i) d\tau_i \\
&= \frac{1}{(2\pi)^n} \sum_{n=1}^{N} \int_{-\infty}^{\infty} \cdots \int_{-\infty}^{\infty} H_n(j\omega_1, \ldots, j\omega_n) \prod_{i=1}^{n} U(j\omega_i) d\omega_i \\
&= \frac{1}{(2\pi)^n} \sum_{n=1}^{N} \int_{-\infty}^{\infty} \cdots \int_{-\infty}^{\infty} Y_n(j\omega_1, \ldots, j\omega_n) e^{j(\omega_1 + \cdots + \omega_n)t} d\omega_1 \ldots d\omega_n \\
&= \frac{1}{2\pi} \sum_{n=1}^{N} \int_{-\infty}^{\infty} Y_n(j\omega) e^{j\omega t} d\omega \\
&= \frac{1}{2\pi} \sum_{n=1}^{N} \int_{-\infty}^{\infty} G_n(j\omega) U_n(j\omega) e^{j\omega t} d\omega
\end{aligned}
\qquad (3\text{-}21)
$$

Where $Y_n(j\omega_1, \ldots, j\omega_n) = H_n(j\omega_1, \ldots, j\omega_n) \prod_{i=1}^{n} U(j\omega_i)$ and $\omega = \omega_1 + \cdots + \omega_n$ with $\omega_i \in [-b, -a]$ or $[a, b], i = 1, 2, ..., n$, and $n = 1, 2, ..., \bar{N}; \bar{N}$ is the maximum analyzed nonlinear order.

Starting from the first row of the system matrix (3-18),

$$
m_1 \ddot{y}_1(t) + (c_1 + c_2)\dot{y}_1(t) - c_2 \dot{y}_2(t) + (k_1 + k_2) y_1(t) - k_2 y_2(t) = 0 \qquad (3\text{-}22)
$$

By inserting the variable of (3-21) into (3-22),

$$m_1\frac{1}{2\pi}\sum_{n=1}^{N}\int_{-\infty}^{\infty}(j\omega)^2G_{(1,n)}(j\omega)U_n(j\omega)e^{j\omega t}d\omega+(c_1+c_2)\frac{1}{2\pi}\sum_{n=1}^{N}\int_{-\infty}^{\infty}(j\omega)G_{(1,n)}(j\omega)U_n(j\omega)e^{j\omega t}d\omega$$
$$-c_2\frac{1}{2\pi}\sum_{n=1}^{N}\int_{-\infty}^{\infty}(j\omega)G_{(2,n)}(j\omega)U_n(j\omega)e^{j\omega t}d\omega+(k_1+k_2)\frac{1}{2\pi}\sum_{n=1}^{N}\int_{-\infty}^{\infty}G_{(1,n)}(j\omega)U_n(j\omega)e^{j\omega t}d\omega$$
$$-k_2\frac{1}{2\pi}\sum_{n=1}^{N}\int_{-\infty}^{\infty}G_{(2,n)}(j\omega)U_n(j\omega)e^{j\omega t}d\omega=0 \qquad (3\text{-}23)$$

The expansion of equation(3-22) into different nonlinear order is shown in (3-23) by offsetting $U_n(j\omega)$

$$m_1\frac{1}{2\pi}\left(\begin{array}{l}\int_{-\infty}^{\infty}(j\omega)^2G_{(1,1)}(j\omega)e^{j\omega t}d\omega\Big|_{\omega=\omega_1}+\int_{-\infty}^{\infty}(j\omega)^2G_{(1,2)}(j\omega)e^{j\omega t}d\omega\Big|_{\omega=\omega_1+\omega_2}+\\ \cdots+\int_{-\infty}^{\infty}(j\omega)^2G_{(1,n)}(j\omega)e^{j\omega t}d\omega\Big|_{\omega=\omega_1+\cdots+\omega_{\bar{N}}}\end{array}\right)+$$
$$(c_1+c_2)\frac{1}{2\pi}\left(\begin{array}{l}\int_{-\infty}^{\infty}(j\omega)G_{(1,1)}(j\omega)e^{j\omega t}d\omega\Big|_{\omega=\omega_1}+\int_{-\infty}^{\infty}(j\omega)G_{(1,2)}(j\omega)e^{j\omega t}d\omega\Big|_{\omega=\omega_1+\omega_2}+\\ \cdots+\int_{-\infty}^{\infty}(j\omega)G_{(1,n)}(j\omega)e^{j\omega t}d\omega\Big|_{\omega=\omega_1+\cdots+\omega_{\bar{N}}}\end{array}\right)$$
$$-c_2\frac{1}{2\pi}\left(\begin{array}{l}\int_{-\infty}^{\infty}(j\omega)G_{(2,1)}(j\omega)e^{j\omega t}d\omega\Big|_{\omega=\omega_1}+\int_{-\infty}^{\infty}(j\omega)^2G_{(2,2)}(j\omega)e^{j\omega t}d\omega\Big|_{\omega=\omega_1+\omega_2}+\\ \cdots+\int_{-\infty}^{\infty}(j\omega)G_{(2,n)}(j\omega)e^{j\omega t}d\omega\Big|_{\omega=\omega_1+\cdots+\omega_{\bar{N}}}\end{array}\right)$$
$$+(k_1+k_2)\frac{1}{2\pi}\left(\begin{array}{l}\int_{-\infty}^{\infty}G_{(1,1)}(j\omega)e^{j\omega t}d\omega\Big|_{\omega=\omega_1}+\int_{-\infty}^{\infty}G_{(1,2)}(j\omega)e^{j\omega t}d\omega\Big|_{\omega=\omega_1+\omega_2}+\\ \cdots+\int_{-\infty}^{\infty}G_{(1,n)}(j\omega)e^{j\omega t}d\omega\Big|_{\omega=\omega_1+\cdots+\omega_{\bar{N}}}\end{array}\right)$$
$$-k_2\frac{1}{2\pi}\left(\begin{array}{l}\int_{-\infty}^{\infty}G_{(2,1)}(j\omega)e^{j\omega t}d\omega\Big|_{\omega=\omega_1}+\int_{-\infty}^{\infty}G_{(2,2)}(j\omega)e^{j\omega t}d\omega\Big|_{\omega=\omega_1+\omega_2}+\\ \cdots+\int_{-\infty}^{\infty}G_{(2,n)}(j\omega)e^{j\omega t}d\omega\Big|_{\omega=\omega_1+\cdots+\omega_{\bar{N}}}\end{array}\right)=0 \qquad (3\text{-}24)$$

Rewrite equation(3-24) as:

$$\begin{pmatrix} m_1\frac{1}{2\pi}\int_{-\infty}^{\infty}(j\omega)^2 G_{(1,1)}(j\omega)e^{j\omega t}d\omega\Big|_{\omega=\omega_1}+(c_1+c_2)\frac{1}{2\pi}\int_{-\infty}^{\infty}(j\omega)G_{(1,1)}(j\omega)e^{j\omega t}d\omega\Big|_{\omega=\omega_1} \\ -c_2\frac{1}{2\pi}\int_{-\infty}^{\infty}(j\omega)G_{(2,1)}(j\omega)e^{j\omega t}d\omega\Big|_{\omega=\omega_1}+(k_1+k_2)\frac{1}{2\pi}\int_{-\infty}^{\infty}G_{(1,1)}(j\omega)e^{j\omega t}d\omega\Big|_{\omega=\omega_1} \\ -k_2\frac{1}{2\pi}\int_{-\infty}^{\infty}G_{(2,1)}(j\omega)e^{j\omega t}d\omega\Big|_{\omega=\omega_1} \end{pmatrix}+$$

$$\begin{pmatrix} m_1\frac{1}{2\pi}\int_{-\infty}^{\infty}(j\omega)^2 G_{(1,2)}(j\omega)e^{j\omega t}d\omega\Big|_{\omega=\omega_1+\omega_2}+(c_1+c_2)\frac{1}{2\pi}\int_{-\infty}^{\infty}(j\omega)G_{(1,2)}(j\omega)e^{j\omega t}d\omega\Big|_{\omega=\omega_1+\omega_2} \\ -c_2\frac{1}{2\pi}\int_{-\infty}^{\infty}(j\omega)G_{(2,2)}(j\omega)e^{j\omega t}d\omega\Big|_{\omega=\omega_1+\omega_2}+(k_1+k_2)\frac{1}{2\pi}\int_{-\infty}^{\infty}G_{(1,2)}(j\omega)e^{j\omega t}d\omega\Big|_{\omega=\omega_1+\omega_2} \\ -k_2\frac{1}{2\pi}\int_{-\infty}^{\infty}G_{(2,2)}(j\omega)e^{j\omega t}d\omega\Big|_{\omega=\omega_1+\omega_2} \end{pmatrix}+\cdots+$$

$$\begin{pmatrix} m_1\frac{1}{2\pi}\int_{-\infty}^{\infty}(j\omega)^2 G_{(1,n)}(j\omega)e^{j\omega t}d\omega\Big|_{\omega=\omega_1+\cdots+\omega_{\bar{N}}}+(c_1+c_2)\frac{1}{2\pi}\int_{-\infty}^{\infty}(j\omega)G_{(1,n)}(j\omega)e^{j\omega t}d\omega\Big|_{\omega=\omega_1+\cdots+\omega_{\bar{N}}} \\ -c_2\frac{1}{2\pi}\int_{-\infty}^{\infty}(j\omega)G_{(2,n)}(j\omega)e^{j\omega t}d\omega\Big|_{\omega=\omega_1+\cdots+\omega_{\bar{N}}}+(k_1+k_2)\frac{1}{2\pi}\int_{-\infty}^{\infty}G_{(1,n)}(j\omega)e^{j\omega t}d\omega\Big|_{\omega=\omega_1+\cdots+\omega_{\bar{N}}} \\ -k_2\frac{1}{2\pi}\int_{-\infty}^{\infty}G_{(2,n)}(j\omega)e^{j\omega t}d\omega\Big|_{\omega=\omega_1+\cdots+\omega_{\bar{N}}} \end{pmatrix}=0 \quad (3\text{-}25)$$

Equation(3-25) should always hold, therefore, the equation relationship can hold for each nonlinear order as well

$$
\begin{pmatrix}
m_1 \frac{1}{2\pi}\int_{-\infty}^{\infty}(j\omega)^2 G_{(1,1)}(j\omega)e^{j\omega t}d\omega\Big|_{\omega=\omega_1} + (c_1+c_2)\frac{1}{2\pi}\int_{-\infty}^{\infty}(j\omega)G_{(1,1)}(j\omega)e^{j\omega t}d\omega\Big|_{\omega=\omega_1} \\
-c_2\frac{1}{2\pi}\int_{-\infty}^{\infty}(j\omega)G_{(2,1)}(j\omega)e^{j\omega t}d\omega\Big|_{\omega=\omega_1} + (k_1+k_2)\frac{1}{2\pi}\int_{-\infty}^{\infty}G_{(1,1)}(j\omega)e^{j\omega t}d\omega\Big|_{\omega=\omega_1} \\
-k_2\frac{1}{2\pi}\int_{-\infty}^{\infty}G_{(2,1)}(j\omega)e^{j\omega t}d\omega\Big|_{\omega=\omega_1}
\end{pmatrix} = 0
$$

$$
\begin{pmatrix}
m_1 \frac{1}{2\pi}\int_{-\infty}^{\infty}(j\omega)^2 G_{(1,2)}(j\omega)e^{j\omega t}d\omega\Big|_{\omega=\omega_1+\omega_2} + (c_1+c_2)\frac{1}{2\pi}\int_{-\infty}^{\infty}(j\omega)G_{(1,2)}(j\omega)e^{j\omega t}d\omega\Big|_{\omega=\omega_1+\omega_2} \\
-c_2\frac{1}{2\pi}\int_{-\infty}^{\infty}(j\omega)G_{(2,2)}(j\omega)e^{j\omega t}d\omega\Big|_{\omega=\omega_1+\omega_2} + (k_1+k_2)\frac{1}{2\pi}\int_{-\infty}^{\infty}G_{(1,2)}(j\omega)e^{j\omega t}d\omega\Big|_{\omega=\omega_1+\omega_2} \\
-k_2\frac{1}{2\pi}\int_{-\infty}^{\infty}G_{(2,2)}(j\omega)e^{j\omega t}d\omega\Big|_{\omega=\omega_1+\omega_2}
\end{pmatrix} = 0
$$

…

$$
\begin{pmatrix}
m_1 \frac{1}{2\pi}\int_{-\infty}^{\infty}(j\omega)^2 G_{(1,n)}(j\omega)e^{j\omega t}d\omega\Big|_{\omega=\omega_1+\cdots+\omega_{\tilde{N}}} + (c_1+c_2)\frac{1}{2\pi}\int_{-\infty}^{\infty}(j\omega)G_{(1,n)}(j\omega)e^{j\omega t}d\omega\Big|_{\omega=\omega_1+\cdots+\omega_{\tilde{N}}} \\
-c_2\frac{1}{2\pi}\int_{-\infty}^{\infty}(j\omega)G_{(2,n)}(j\omega)e^{j\omega t}d\omega\Big|_{\omega=\omega_1+\cdots+\omega_{\tilde{N}}} + (k_1+k_2)\frac{1}{2\pi}\int_{-\infty}^{\infty}G_{(1,n)}(j\omega)e^{j\omega t}d\omega\Big|_{\omega=\omega_1+\cdots+\omega_{\tilde{N}}} \\
-k_2\frac{1}{2\pi}\int_{-\infty}^{\infty}G_{(2,n)}(j\omega)e^{j\omega t}d\omega\Big|_{\omega=\omega_1+\cdots+\omega_{\tilde{N}}}
\end{pmatrix} = 0
\tag{3-26}
$$

Then, the 2nd row of the system matrix (3-18) can be expended as a series of equations below:

$$
\begin{pmatrix}
m_2\frac{1}{2\pi}\int_{-\infty}^{\infty}(j\omega)^2 G_{(2,1)}(j\omega)e^{j\omega t}d\omega\Big|_{\omega=\omega_1}+(c_2+c_3)\frac{1}{2\pi}\int_{-\infty}^{\infty}(j\omega)G_{(2,1)}(j\omega)e^{j\omega t}d\omega\Big|_{\omega=\omega_1}\\
-c_3\frac{1}{2\pi}\int_{-\infty}^{\infty}(j\omega)G_{(3,1)}(j\omega)e^{j\omega t}d\omega\Big|_{\omega=\omega_1}-c_2\frac{1}{2\pi}\int_{-\infty}^{\infty}(j\omega)G_{(1,1)}(j\omega)e^{j\omega t}d\omega\Big|_{\omega=\omega_1}\\
+(k_2+k_3)\frac{1}{2\pi}\int_{-\infty}^{\infty}G_{(2,1)}(j\omega)e^{j\omega t}d\omega\Big|_{\omega=\omega_1}-k_3\frac{1}{2\pi}\int_{-\infty}^{\infty}G_{(3,1)}(j\omega)e^{j\omega t}d\omega\Big|_{\omega=\omega_1}\\
-k_2\frac{1}{2\pi}\int_{-\infty}^{\infty}G_{(1,1)}(j\omega)e^{j\omega t}d\omega\Big|_{\omega=\omega_1}
\end{pmatrix}=0
$$

$$
\begin{pmatrix}
m_2\frac{1}{2\pi}\int_{-\infty}^{\infty}(j\omega)^2 G_{(2,2)}(j\omega)e^{j\omega t}d\omega\Big|_{\omega=\omega_1+\omega_2}+(c_2+c_3)\frac{1}{2\pi}\int_{-\infty}^{\infty}(j\omega)G_{(2,2)}(j\omega)e^{j\omega t}d\omega\Big|_{\omega=\omega_1+\omega_2}\\
-c_3\frac{1}{2\pi}\int_{-\infty}^{\infty}(j\omega)G_{(3,2)}(j\omega)e^{j\omega t}d\omega\Big|_{\omega=\omega_1+\omega_2}-c_2\frac{1}{2\pi}\int_{-\infty}^{\infty}(j\omega)G_{(1,2)}(j\omega)e^{j\omega t}d\omega\Big|_{\omega=\omega_1+\omega_2}\\
+(k_2+k_3)\frac{1}{2\pi}\int_{-\infty}^{\infty}G_{(2,2)}(j\omega)e^{j\omega t}d\omega\Big|_{\omega=\omega_1+\omega_2}-k_3\frac{1}{2\pi}\int_{-\infty}^{\infty}G_{(3,2)}(j\omega)e^{j\omega t}d\omega\Big|_{\omega=\omega_1+\omega_2}\\
-k_2\frac{1}{2\pi}\int_{-\infty}^{\infty}G_{(1,2)}(j\omega)e^{j\omega t}d\omega\Big|_{\omega=\omega_1+\omega_2}
\end{pmatrix}=0
$$

…

$$
\begin{pmatrix}
m_2\frac{1}{2\pi}\int_{-\infty}^{\infty}(j\omega)^2 G_{(2,\bar{N})}(j\omega)e^{j\omega t}d\omega\Big|_{\omega=\omega_1+\cdots+\omega_{\bar{N}}}+(c_2+c_3)\frac{1}{2\pi}\int_{-\infty}^{\infty}(j\omega)G_{(2,\bar{N})}(j\omega)e^{j\omega t}d\omega\Big|_{\omega=\omega_1+\cdots+\omega_{\bar{N}}}\\
-c_3\frac{1}{2\pi}\int_{-\infty}^{\infty}(j\omega)G_{(3,\bar{N})}(j\omega)e^{j\omega t}d\omega\Big|_{\omega=\omega_1+\cdots+\omega_{\bar{N}}}-c_2\frac{1}{2\pi}\int_{-\infty}^{\infty}(j\omega)G_{(1,\bar{N})}(j\omega)e^{j\omega t}d\omega\Big|_{\omega=\omega_1+\cdots+\omega_{\bar{N}}}\\
+(k_2+k_3)\frac{1}{2\pi}\int_{-\infty}^{\infty}G_{(2,\bar{N})}(j\omega)e^{j\omega t}d\omega\Big|_{\omega=\omega_1+\cdots+\omega_{\bar{N}}}-k_3\frac{1}{2\pi}\int_{-\infty}^{\infty}G_{(3,\bar{N})}(j\omega)e^{j\omega t}d\omega\Big|_{\omega=\omega_1+\cdots+\omega_{\bar{N}}}\\
-k_2\frac{1}{2\pi}\int_{-\infty}^{\infty}G_{(1,\bar{N})}(j\omega)e^{j\omega t}d\omega\Big|_{\omega=\omega_1+\cdots+\omega_{\bar{N}}}
\end{pmatrix}=0
\tag{3-27}
$$

Similarly, the rth ($r<\min(L_i-1,L_i,J)$ or $r>\max(L_i-1,L_i,J)$, $i=1,2,...,\bar{L}$) row of the system matrix can be redefined as a series of equations below:

$$
\begin{pmatrix}
m_r \frac{1}{2\pi}\int_{-\infty}^{\infty}(j\omega)^2 G_{(r,1)}(j\omega)e^{j\omega t}d\omega\Big|_{\omega=\omega_1} + (c_r + c_{r+1})\frac{1}{2\pi}\int_{-\infty}^{\infty}(j\omega)G_{(r,1)}(j\omega)e^{j\omega t}d\omega\Big|_{\omega=\omega_1} \\
-c_{r+1}\frac{1}{2\pi}\int_{-\infty}^{\infty}(j\omega)G_{(r+1,1)}(j\omega)e^{j\omega t}d\omega\Big|_{\omega=\omega_1} - c_r\frac{1}{2\pi}\int_{-\infty}^{\infty}(j\omega)G_{(r-1,1)}(j\omega)e^{j\omega t}d\omega\Big|_{\omega=\omega_1} \\
+(k_r + k_{r+1})\frac{1}{2\pi}\int_{-\infty}^{\infty}G_{(r,1)}(j\omega)e^{j\omega t}d\omega\Big|_{\omega=\omega_1} - k_{r+1}\frac{1}{2\pi}\int_{-\infty}^{\infty}G_{(r+1,1)}(j\omega)e^{j\omega t}d\omega\Big|_{\omega=\omega_1} \\
-k_2\frac{1}{2\pi}\int_{-\infty}^{\infty}G_{(r-1,1)}(j\omega)e^{j\omega t}d\omega\Big|_{\omega=\omega_1}
\end{pmatrix} = 0
$$

$$
\begin{pmatrix}
m_r \frac{1}{2\pi}\int_{-\infty}^{\infty}(j\omega)^2 G_{(r,2)}(j\omega)e^{j\omega t}d\omega\Big|_{\omega=\omega_1+\omega_2} + (c_r + c_{r+1})\frac{1}{2\pi}\int_{-\infty}^{\infty}(j\omega)G_{(r,2)}(j\omega)e^{j\omega t}d\omega\Big|_{\omega=\omega_1+\omega_2} \\
-c_{r+1}\frac{1}{2\pi}\int_{-\infty}^{\infty}(j\omega)G_{(r+1,2)}(j\omega)e^{j\omega t}d\omega\Big|_{\omega=\omega_1+\omega_2} - c_r\frac{1}{2\pi}\int_{-\infty}^{\infty}(j\omega)G_{(r-1,2)}(j\omega)e^{j\omega t}d\omega\Big|_{\omega=\omega_1+\omega_2} \\
+(k_r + k_{r+1})\frac{1}{2\pi}\int_{-\infty}^{\infty}G_{(r,2)}(j\omega)e^{j\omega t}d\omega\Big|_{\omega=\omega_1+\omega_2} - k_{r+1}\frac{1}{2\pi}\int_{-\infty}^{\infty}G_{(r+1,2)}(j\omega)e^{j\omega t}d\omega\Big|_{\omega=\omega_1+\omega_2} \\
-k_r\frac{1}{2\pi}\int_{-\infty}^{\infty}G_{(r-1,2)}(j\omega)e^{j\omega t}d\omega\Big|_{\omega=\omega_1+\omega_2}
\end{pmatrix} = 0
$$

…

$$
\begin{pmatrix}
m_r \frac{1}{2\pi}\int_{-\infty}^{\infty}(j\omega)^2 G_{(r,\bar{N})}(j\omega)e^{j\omega t}d\omega\Big|_{\omega=\omega_1+\cdots+\omega_{\bar{N}}} + (c_r + c_{r+1})\frac{1}{2\pi}\int_{-\infty}^{\infty}(j\omega)G_{(r,\bar{N})}(j\omega)e^{j\omega t}d\omega\Big|_{\omega=\omega_1+\cdots+\omega_{\bar{N}}} \\
-c_{r+1}\frac{1}{2\pi}\int_{-\infty}^{\infty}(j\omega)G_{(r+1,\bar{N})}(j\omega)e^{j\omega t}d\omega\Big|_{\omega=\omega_1+\cdots+\omega_{\bar{N}}} - c_r\frac{1}{2\pi}\int_{-\infty}^{\infty}(j\omega)G_{(r-1,\bar{N})}(j\omega)e^{j\omega t}d\omega\Big|_{\omega=\omega_1+\cdots+\omega_{\bar{N}}} \\
+(k_r + k_{r+1})\frac{1}{2\pi}\int_{-\infty}^{\infty}G_{(r,\bar{N})}(j\omega)e^{j\omega t}d\omega\Big|_{\omega=\omega_1+\cdots+\omega_{\bar{N}}} - k_{r+1}\frac{1}{2\pi}\int_{-\infty}^{\infty}G_{(r+1,\bar{N})}(j\omega)e^{j\omega t}d\omega\Big|_{\omega=\omega_1+\cdots+\omega_{\bar{N}}} \\
-k_r\frac{1}{2\pi}\int_{-\infty}^{\infty}G_{(r-1,\bar{N})}(j\omega)e^{j\omega t}d\omega\Big|_{\omega=\omega_1+\cdots+\omega_{\bar{N}}}
\end{pmatrix} = 0
$$

(3-28)

When the mass is connected to the left side of L_i th spring, the row of the system matrix can be redefined as below:

$$m_{L_i-1}\frac{1}{2\pi}\sum_{n=1}^{N}\int_{-\infty}^{\infty}(j\omega)^2 G_{(L_i-1,n)}(j\omega)U_n(j\omega)e^{j\omega t}d\omega - c_{L_i-1}\frac{1}{2\pi}\sum_{n=1}^{N}\int_{-\infty}^{\infty}(j\omega)G_{(L_i-2,n)}(j\omega)U_n(j\omega)e^{j\omega t}d\omega$$
$$+(c_{L_i-1}+c_{L_i})\frac{1}{2\pi}\sum_{n=1}^{N}\int_{-\infty}^{\infty}(j\omega)G_{(L_i-1,n)}(j\omega)U_n(j\omega)e^{j\omega t}d\omega - c_{L_i}\frac{1}{2\pi}\sum_{n=1}^{N}\int_{-\infty}^{\infty}(j\omega)G_{(L_i,n)}(j\omega)U_n(j\omega)e^{j\omega t}d\omega$$
$$-k_{L_i-1}\frac{1}{2\pi}\sum_{n=1}^{N}\int_{-\infty}^{\infty}G_{(L_i-2,n)}(j\omega)U_n(j\omega)e^{j\omega t}d\omega + (k_{L_i-1}+k_{L_i})\frac{1}{2\pi}\sum_{n=1}^{N}\int_{-\infty}^{\infty}G_{(L_i-1,n)}(j\omega)U_n(j\omega)e^{j\omega t}d\omega$$
$$-k_{L_i}\frac{1}{2\pi}\sum_{n=1}^{N}\int_{-\infty}^{\infty}G_{(L_i,n)}(j\omega)U_n(j\omega)e^{j\omega t}d\omega = -NonF_{L_i}$$

$i=1,2,...,\bar{L}$ (3-29)

Here equation(3-29) cannot be expanded as (3-28) and $U_n(j\omega)$ cannot be cancelled, due to the existence of nonlinear force on the right side. Similarly, the mass is connected to the right side of L_i th spring, the row of the system matrix can be rewritten as below:

$$m_{L_i}\frac{1}{2\pi}\sum_{n=1}^{N}\int_{-\infty}^{\infty}(j\omega)^2 G_{(L_i,n)}(j\omega)U_n(j\omega)e^{j\omega t}d\omega - c_{L_i}\frac{1}{2\pi}\sum_{n=1}^{N}\int_{-\infty}^{\infty}(j\omega)G_{(L_i-1,n)}(j\omega)U_n(j\omega)e^{j\omega t}d\omega$$
$$+(c_{L_i}+c_{L_i+1})\frac{1}{2\pi}\sum_{n=1}^{N}\int_{-\infty}^{\infty}(j\omega)G_{(L_i,n)}(j\omega)U_n(j\omega)e^{j\omega t}d\omega - c_{L_i+1}\frac{1}{2\pi}\sum_{n=1}^{N}\int_{-\infty}^{\infty}(j\omega)G_{(L_i+1,n)}(j\omega)U_n(j\omega)e^{j\omega t}d\omega$$
$$-k_{L_i}\frac{1}{2\pi}\sum_{n=1}^{N}\int_{-\infty}^{\infty}G_{(L_i-1,n)}(j\omega)U_n(j\omega)e^{j\omega t}d\omega + (k_{L_i}+k_{L_i+1})\frac{1}{2\pi}\sum_{n=1}^{N}\int_{-\infty}^{\infty}G_{(L_i,n)}(j\omega)U_n(j\omega)e^{j\omega t}d\omega$$
$$-k_{L_i+1}\frac{1}{2\pi}\sum_{n=1}^{N}\int_{-\infty}^{\infty}G_{(L_i+1,n)}(j\omega)U_n(j\omega)e^{j\omega t}d\omega = NonF_{L_i}$$

$i=1,2,...,\bar{L}$ (3-30)

Expend the *J*th row of the system(3-18) where the input is loaded at *J*th mass as below:

$$
\begin{aligned}
&m_J \frac{1}{2\pi}\sum_{n=1}^{N}\int_{-\infty}^{\infty}(j\omega)^2 G_{(J,n)}(j\omega)U_n(j\omega)e^{j\omega t}d\omega - c_J \frac{1}{2\pi}\sum_{n=1}^{N}\int_{-\infty}^{\infty}(j\omega)G_{(J-1,n)}(j\omega)U_n(j\omega)e^{j\omega t}d\omega \\
&+(c_J + c_{J+1})\frac{1}{2\pi}\sum_{n=1}^{N}\int_{-\infty}^{\infty}(j\omega)G_{(J,n)}(j\omega)U_n(j\omega)e^{j\omega t}d\omega - c_{J+1}\frac{1}{2\pi}\sum_{n=1}^{N}\int_{-\infty}^{\infty}(j\omega)G_{(J+1,n)}(j\omega)U_n(j\omega)e^{j\omega t}d\omega \\
&-k_J \frac{1}{2\pi}\sum_{n=1}^{N}\int_{-\infty}^{\infty}G_{(J-1,n)}(j\omega)U_n(j\omega)e^{j\omega t}d\omega + (k_J + k_{J+1})\frac{1}{2\pi}\sum_{n=1}^{N}\int_{-\infty}^{\infty}G_{(J,n)}(j\omega)U_n(j\omega)e^{j\omega t}d\omega \\
&-k_{J+1}\frac{1}{2\pi}\sum_{n=1}^{N}\int_{-\infty}^{\infty}G_{(J+1,n)}(j\omega)U_n(j\omega)e^{j\omega t}d\omega = \frac{1}{2\pi}\int_a^b U(j\omega)e^{j\omega t}d\omega
\end{aligned}
\tag{3-31}
$$

For the (*n-1*)th row of the system,

$$
\begin{aligned}
&\left(\begin{aligned}
&m_{n-1}\frac{1}{2\pi}\int_{-\infty}^{\infty}(j\omega)^2 Y_{(n-1,1)}(j\omega)e^{j\omega t}d\omega\Big|_{\omega=\omega_1} + (c_{n-1}+c_n)\frac{1}{2\pi}\int_{-\infty}^{\infty}(j\omega)Y_{(n-1,1)}(j\omega)e^{j\omega t}d\omega\Big|_{\omega=\omega_1} \\
&-c_n\frac{1}{2\pi}\int_{-\infty}^{\infty}(j\omega)Y_{(n,1)}(j\omega)e^{j\omega t}d\omega\Big|_{\omega=\omega_1} - c_{n-1}\frac{1}{2\pi}\int_{-\infty}^{\infty}(j\omega)Y_{(n-2,1)}(j\omega)e^{j\omega t}d\omega\Big|_{\omega=\omega_1} \\
&+(k_{n-1}+k_n)\frac{1}{2\pi}\int_{-\infty}^{\infty}Y_{(n-1,1)}(j\omega)e^{j\omega t}d\omega\Big|_{\omega=\omega_1} - k_n\frac{1}{2\pi}\int_{-\infty}^{\infty}Y_{(r+1,1)}(j\omega)e^{j\omega t}d\omega\Big|_{\omega=\omega_1} \\
&-k_{n-1}\frac{1}{2\pi}\int_{-\infty}^{\infty}Y_{(n-2,1)}(j\omega)e^{j\omega t}d\omega\Big|_{\omega=\omega_1}
\end{aligned}\right) = 0 \\
&\left(\begin{aligned}
&m_r\frac{1}{2\pi}\int_{-\infty}^{\infty}(j\omega)^2 Y_{(r,2)}(j\omega)e^{j\omega t}d\omega\Big|_{\omega=\omega_1+\omega_2} + (c_{n-1}+c_n)\frac{1}{2\pi}\int_{-\infty}^{\infty}(j\omega)Y_{(n-1,2)}(j\omega)e^{j\omega t}d\omega\Big|_{\omega=\omega_1+\omega_2} \\
&-c_n\frac{1}{2\pi}\int_{-\infty}^{\infty}(j\omega)Y_{(n,2)}(j\omega)e^{j\omega t}d\omega\Big|_{\omega=\omega_1+\omega_2} - c_{n-1}\frac{1}{2\pi}\int_{-\infty}^{\infty}(j\omega)Y_{(n-2,2)}(j\omega)e^{j\omega t}d\omega\Big|_{\omega=\omega_1+\omega_2} \\
&+(k_{n-1}+k_n)\frac{1}{2\pi}\int_{-\infty}^{\infty}Y_{(n-1,2)}(j\omega)e^{j\omega t}d\omega\Big|_{\omega=\omega_1+\omega_2} - k_n\frac{1}{2\pi}\int_{-\infty}^{\infty}Y_{(n,2)}(j\omega)e^{j\omega t}d\omega\Big|_{\omega=\omega_1+\omega_2} \\
&-k_r\frac{1}{2\pi}\int_{-\infty}^{\infty}Y_{(n-2,2)}(j\omega)e^{j\omega t}d\omega\Big|_{\omega=\omega_1+\omega_2}
\end{aligned}\right) = 0 \\
&\cdots \\
&\left(\begin{aligned}
&m_{n-1}\frac{1}{2\pi}\int_{-\infty}^{\infty}(j\omega)^2 Y_{(n-1,\bar{N})}(j\omega)e^{j\omega t}d\omega\Big|_{\omega=\omega_1+\cdots+\omega_{\bar{N}}} + (c_{n-1}+c_n)\frac{1}{2\pi}\int_{-\infty}^{\infty}(j\omega)Y_{(n-1,\bar{N})}(j\omega)e^{j\omega t}d\omega\Big|_{\omega=\omega_1+\cdots+\omega_{\bar{N}}} \\
&-c_n\frac{1}{2\pi}\int_{-\infty}^{\infty}(j\omega)Y_{(n,\bar{N})}(j\omega)e^{j\omega t}d\omega\Big|_{\omega=\omega_1+\cdots+\omega_{\bar{N}}} - c_{n-1}\frac{1}{2\pi}\int_{-\infty}^{\infty}(j\omega)Y_{(n-2,\bar{N})}(j\omega)e^{j\omega t}d\omega\Big|_{\omega=\omega_1+\cdots+\omega_{\bar{N}}} \\
&+(k_{n-1}+k_n)\frac{1}{2\pi}\int_{-\infty}^{\infty}Y_{(n-1,\bar{N})}(j\omega)e^{j\omega t}d\omega\Big|_{\omega=\omega_1+\cdots+\omega_{\bar{N}}} - k_n\frac{1}{2\pi}\int_{-\infty}^{\infty}Y_{(n,\bar{N})}(j\omega)e^{j\omega t}d\omega\Big|_{\omega=\omega_1+\cdots+\omega_{\bar{N}}} \\
&-k_{n-1}\frac{1}{2\pi}\int_{-\infty}^{\infty}Y_{(n-2,\bar{N})}(j\omega)e^{j\omega t}d\omega\Big|_{\omega=\omega_1+\cdots+\omega_{\bar{N}}}
\end{aligned}\right) = 0
\end{aligned}
\tag{3-32}
$$

It has been known that equation(3-26) is the expression in time domain, therefore, equation(3-33) can be expressed in frequency domain.

$$
\begin{aligned}
&-m_1\omega^2 G_{(1,1)}(j\omega)\big|_{\omega=\omega_1} + j\omega(c_1+c_2)G_{(1,1)}(j\omega)\big|_{\omega=\omega_1} - j\omega c_2 G_{(2,1)}(j\omega)\big|_{\omega=\omega_1} \\
&+(k_1+k_2)G_{(1,1)}(j\omega)\big|_{\omega=\omega_1} - k_2 G_{(2,1)}(j\omega)\big|_{\omega=\omega_1} = 0 \\
&-m_1\omega^2 G_{(2,1)}(j\omega)\big|_{\omega=\omega_1+\omega_2} + j\omega(c_1+c_2)(j\omega)G_{(1,2)}(j\omega)\big|_{\omega=\omega_1+\omega_2} - j\omega c_2 G_{(2,2)}(j\omega)\big|_{\omega=\omega_1+\omega_2} \\
&+(k_1+k_2)G_{(1,2)}(j\omega)\big|_{\omega=\omega_1+\omega_2} - k_2 G_{(2,2)}(j\omega)\big|_{\omega=\omega_1+\omega_2} = 0 \\
&\cdots \\
&-m_1\omega^2 G_{(1,\bar{N})}(j\omega)\big|_{\omega=\omega_1+\cdots+\omega_{\bar{N}}} + j\omega(c_1+c_2)G_{(1,\bar{N})}(j\omega)\big|_{\omega=\omega_1+\cdots+\omega_{\bar{N}}} - j\omega c_2 G_{(2,\bar{N})}(j\omega)\big|_{\omega=\omega_1+\cdots+\omega_{\bar{N}}} \\
&+(k_1+k_2)G_{(1,\bar{N})}(j\omega)\big|_{\omega=\omega_1+\cdots+\omega_{\bar{N}}} - k_2 G_{(1,\bar{N})}(j\omega)\big|_{\omega=\omega_1+\cdots+\omega_{\bar{N}}} = 0
\end{aligned}
\tag{3-33}
$$

Define NOFRF-based transmissibility function as $\lambda_{i,i+1}^{j}(j\omega)=\dfrac{G_{(i,j)}(j\omega)}{G_{(i+1,j)}(j\omega)}$ (i=1,...,n-1; j=1,...,$\bar{N}$) , and substitute into equation(3-33).
Therefore,

$$
\begin{aligned}
\lambda_{1,2}^{1}(j\omega) &= \left.\frac{k_2+j\omega c_2}{-m_1\omega^2+j\omega(c_1+c_2)+k_1+k_2}\right|_{\omega=\omega_1} \\
\lambda_{1,2}^{2}(j\omega) &= \left.\frac{k_2+j\omega c_2}{-m_1\omega^2+j\omega(c_1+c_2)+k_1+k_2}\right|_{\omega=\omega_1+\omega_2} \\
&\cdots \\
\lambda_{1,2}^{\bar{N}}(j\omega) &= \left.\frac{k_2+j\omega c_2}{-m_1\omega^2+j\omega(c_1+c_2)+k_1+k_2}\right|_{\omega=\omega_1+\omega_2+\cdots+\omega_{\bar{N}}}
\end{aligned}
\tag{3-34}
$$

Similarly, NOFRF-based transmissibility between mass 2 and mass 3 from equation(3-27) can be obtained as equation(3-35) shown below

$$\lambda_{2,3}^{1}(j\omega)=\left.\frac{k_3+j\omega c_3}{-m_2\omega^2+j\omega(c_2+c_3)+k_2+k_3-(j\omega c_2+k_2\lambda_{1,2}^{1})(j\omega)}\right|_{\omega=\omega_1}$$

$$\lambda_{2,3}^{2}(j\omega)=\left.\frac{k_3+j\omega c_3}{-m_2\omega^2+j\omega(c_2+c_3)+k_2+k_3-(j\omega c_2+k_2\lambda_{1,2}^{2})(j\omega)}\right|_{\omega=\omega_1+\omega_2} \quad (3\text{-}35)$$

…

$$\lambda_{2,3}^{\bar{N}}(j\omega)=\left.\frac{k_3+j\omega c_3}{-m_2\omega^2+j\omega(c_2+c_3)+k_2+k_3-(j\omega c_2+k_2\lambda_{1,2}^{\bar{N}})(j\omega)}\right|_{\omega=\omega_1+\omega_2+\cdots+\omega_{\bar{N}}}$$

Through iteratively calculation, NOFRF-based transmissibility between mass *r* and mass *r+1* from equation(3-28) can be obtained as equation (34)

$$\lambda_{r,r+1}^{1}(j\omega)=\left.\frac{k_{r+1}+j\omega c_{r+1}}{-m_r\omega^2+j\omega(c_r+c_{r+1})+k_r+k_{r+1}-(j\omega c_r+k_r\lambda_{r-1,r}^{1})(j\omega)}\right|_{\omega=\omega_1}$$

$$\lambda_{r,r+1}^{2}(j\omega)=\left.\frac{k_{r+1}+j\omega c_{r+1}}{-m_r\omega^2+j\omega(c_r+c_{r+1})+k_r+k_{r+1}-(j\omega c_r+k_r\lambda_{r-1,r}^{1})(j\omega)}\right|_{\omega=\omega_1+\omega_2} \quad (3\text{-}36)$$

…

$$\lambda_{r,r+1}^{\bar{N}}(j\omega)=\left.\frac{k_{r+1}+j\omega c_{r+1}}{-m_r\omega^2+j\omega(c_r+c_{r+1})+k_r+k_{r+1}-(j\omega c_r+k_r\lambda_{r-1,r}^{1})(j\omega)}\right|_{\omega=\omega_1+\omega_2+\cdots+\omega_{\bar{N}}}$$

$$(r<\min(L_i-1,L_i,J)\ \text{or}\ r>\max(L_i-1,L_i,J),\quad i=1,2,...,\bar{L})$$

Transmissibility between mass L_i-1 and mass L_i can be defined from equation(3-29) into equation(3-37) shown below

$$\lambda^{1}_{L_i-1,L_i}(j\omega)=\left.\frac{k_{L_i}+j\omega c_{L_i}-\dfrac{P_1(NonF_{L_i}(j\omega))}{G_{(L_i,1)}(j\omega)U_1(j\omega)}}{-m_{L_i-1}\omega^2+j\omega(c_{L_i-1}+c_{L_i})+k_{L_i-1}+k_{L_i}-(j\omega c_{L_i-1}+k_r\lambda^{1}_{L_i-2,L_i-1})(j\omega)}\right|_{\omega=\omega_1}$$

$$\lambda^{2}_{L_i-1,L_i}(j\omega)=\left.\frac{k_{L_i}+j\omega c_{L_i}-\dfrac{P_2(NonF_{L_i}(j\omega))}{G_{(L_i,2)}(j\omega)U_2(j\omega)}}{-m_{L_i-1}\omega^2+j\omega(c_{L_i-1}+c_{L_i})+k_{L_i-1}+k_{L_i}-(j\omega c_{L_i-1}+k_{L_i-1}\lambda^{2}_{L_i-2,L_i-1})(j\omega)}\right|_{\omega=\omega_1+\omega_2}$$

…

$$\lambda^{\bar{N}}_{L_i-1,L_i}(j\omega)=\left.\frac{k_{L_i}+j\omega c_{L_i}-\dfrac{P_{\bar{N}}(NonF_{L_i}(j\omega))}{G_{(L_i,\bar{N})}(j\omega)U_{\bar{N}}(j\omega)}}{-m_{L_i-1}\omega^2+j\omega(c_{L_i-1}+c_{L_i})+k_{L_i-1}+k_{L_i}-(j\omega c_{L_i-1}+k_{L_i-1}\lambda^{\bar{N}}_{L_i-2,L_i-1})(j\omega)}\right|_{\omega=\omega_1+\omega_2+\cdots+\omega_{\bar{N}}}$$

$i=1,2,...,\bar{L}$ (3-37)

And

$$P_1(NonF_{L_i})+P_2(NonF_{L_i})+\cdots+P_{\bar{N}}(NonF_{L_i})=NonF_{L_i} \quad (3\text{-}38)$$

Equation(3-37) reveals the fact that the relationship like (3-25) and (3-26) cannot be held for (3-37), because of the nonzero value on the right side of (3-29). In order to construct a similar expression for (3-29), using $P_1(NonF_{L_i}),P_2(NonF_{L_i}),...,P_{\bar{N}}(NonF_{L_i})$ to represent corresponding nonlinear force for each nonlinear order. Obviously, they should satisfy the condition of (3-38) and are not constant terms. In a similar way, equation (3-29) can be derived based on (3-30) for the masses which are connected to the right side of the nonlinear springs or dampers.

$$\lambda^{1}_{L_i,L_i+1}(j\omega)=\left.\frac{k_{L_i+1}+j\omega c_{L_i+1}-\dfrac{P_1(NonF_{L_i+1}(j\omega))}{G_{(L_i+1,1)}(j\omega)U_1(j\omega)}}{-m_{L_i}\omega^2+j\omega(c_{L_i}+c_{L_i+1})+k_{L_i}+k_{L_i+1}-(j\omega c_{L_i}+k_{L_i}\lambda^{1}_{L_i-1,L_i})(j\omega)}\right|_{\omega=\omega_1}$$

$$\lambda^{2}_{L_i,L_i+1}(j\omega)=\left.\frac{k_{L_i+1}+j\omega c_{L_i+1}+\dfrac{P_2(NonF_{L_i+1}(j\omega))}{G_{(L_i+1,2)}(j\omega)U_2(j\omega)}}{-m_{L_i}\omega^2+j\omega(c_{L_i}+c_{L_i+1})+k_{L_i}+k_{L_i+1}-(j\omega c_{L_i}+k_{L_i}\lambda^{2}_{L_i-1,L_i})(j\omega)}\right|_{\omega=\omega_1+\omega_2}$$

…

$$\lambda^{\bar{N}}_{L_i,L_i+1}(j\omega)=\left.\frac{k_{L_i+1}+j\omega c_{L_i+1}+\dfrac{P_{\bar{N}}(NonF_{L_i+1}(j\omega))}{G_{(L_i+1,\bar{N})}(j\omega)U_{\bar{N}}(j\omega)}}{-m_{L_i}\omega^2+j\omega(c_{L_i}+c_{L_i+1})+k_{L_i}+k_{L_i+1}-(j\omega c_{L_i}+k_{L_i}\lambda^{\bar{N}}_{L_i-1,L_i})(j\omega)}\right|_{\omega=\omega_1+\omega_2+\cdots+\omega_{\bar{N}}}$$

$i=1,2,...,\bar{L}$ (3-39)

Accordingly, the transmissibility between mass J and mass $J+1$ from equation(3-31) can be calculated as equation

$$\lambda^{1}_{J,J+1}(j\omega)=\left.\frac{k_{J+1}+j\omega c_{J+1}+\dfrac{P_1(U(j\omega))}{G_{(J+1,1)}(j\omega)U_1(j\omega)}}{-m_J\omega^2+j\omega(c_J+c_{J+1})+k_J+k_{J+1}-(j\omega c_J+k_J\lambda^{1}_{J-1,J})(j\omega)}\right|_{\omega=\omega_1}$$

$$\lambda^{2}_{J,J+1}(j\omega)=\left.\frac{k_{J+1}+j\omega c_{J+1}+\dfrac{P_2(U(j\omega))}{G_{(J+1,2)}(j\omega)U_2(j\omega)}}{-m_J\omega^2+j\omega(c_J+c_{J+1})+k_J+k_{J+1}-(j\omega c_J+k_J\lambda^{2}_{J-1,J})(j\omega)}\right|_{\omega=\omega_1+\omega_2}$$

…

$$\lambda^{\bar{N}}_{J,J+1}(j\omega)=\left.\frac{k_{J+1}+j\omega c_{J+1}+\dfrac{P_{\bar{N}}(U(j\omega))}{G_{(J+1,\bar{N})}(j\omega)U_{\bar{N}}(j\omega)}}{-m_J\omega^2+j\omega(c_J+c_{J+1})+k_J+k_{J+1}-(j\omega c_J+k_J\lambda^{\bar{N}}_{J-1,J})(j\omega)}\right|_{\omega=\omega_1+\omega_2+\cdots+\omega_{\bar{N}}}$$

(3-40)

where $P_1(U)+P_2(U)+\cdots+P_{\bar{N}}(U)=U$

One interesting thing needs to be mentioned that $U(j\omega)$ is zero when frequency is out of range [a,b], which could make an diverse solution for the system. It will be discussed during the later sections.

It can be easily deduced the similar expression of transmissibility between mass n-1 and mass n for equation(3-32).

$$\lambda_{n-1,n}^{1}(j\omega)=\left.\frac{k_n+j\omega c_n}{-m_{n-1}\omega^2+j\omega(c_{n-1}+c_n)+k_{n-1}+k_n-(j\omega c_{n-1}+k_{n-1}\lambda_{n-2,n-1}^{1})(j\omega)}\right|_{\omega=\omega_1}$$

$$\lambda_{n-1,n}^{2}(j\omega)=\left.\frac{k_n+j\omega c_n}{-m_{n-1}\omega^2+j\omega(c_{n-1}+c_n)+k_{n-1}+k_n-(j\omega c_{n-1}+k_{n-1}\lambda_{n-2,n-1}^{2})(j\omega)}\right|_{\omega=\omega_1+\omega_2}$$

…

$$\lambda_{n-1,n}^{\bar{N}}(j\omega)=\left.\frac{k_n+j\omega c_n}{-m_{n-1}\omega^2+j\omega(c_{n-1}+c_n)+k_{n-1}+k_n-(j\omega c_{n-1}+k_{n-1}\lambda_{n-2,n-1}^{\bar{N}})(j\omega)}\right|_{\omega=\omega_1+\omega_2+\cdots+\omega_{\bar{N}}} \quad (3\text{-}41)$$

Staring from equation(3-41), it is easily to know that $\lambda_{n,n-1}(j\omega)=\dfrac{1}{\lambda_{n-1,n}(j\omega)}$

$$\lambda_{n,n-1}^{1}(j\omega)=\left.\frac{k_n+j\omega c_n}{-m_n\omega^2+j\omega(c_n+c_{n+1})+k_n+k_{n+1}}\right|_{\omega=\omega_1}$$

$$\lambda_{n,n-1}^{2}(j\omega)=\left.\frac{k_n+j\omega c_n}{-m_n\omega^2+j\omega(c_n+c_{n+1})+k_n+k_{n+1}}\right|_{\omega=\omega_1+\omega_2} \quad (3\text{-}42)$$

…

$$\lambda_{n,n-1}^{\bar{N}}(j\omega)=\left.\frac{k_n+j\omega c_n}{-m_n\omega^2+j\omega(c_n+c_{n+1})+k_n+k_{n+1}}\right|_{\omega=\omega_1+\omega_2+\cdots+\omega_{\bar{N}}}$$

So the expression for $\lambda_{n-1,n-2}(j\omega)$ can be derived as (41),

$$\lambda_{n-1,n-2}^{1}(j\omega)=\left.\frac{k_{n-1}+j\omega c_{n-1}}{-m_{n-1}\omega^{2}+j\omega(c_{n-1}+c_{n})+k_{n-1}+k_{n}-(j\omega c_{n}+k_{n}\lambda_{n,n-1}^{1})(j\omega)}\right|_{\omega=\omega_{1}}$$

$$\lambda_{n-1,n-2}^{2}(j\omega)=\left.\frac{k_{n-1}+j\omega c_{n-1}}{-m_{n-1}\omega^{2}+j\omega(c_{n-1}+c_{n})+k_{n-1}+k_{n}-(j\omega c_{n}+k_{n}\lambda_{n,n-1}^{2})(j\omega)}\right|_{\omega=\omega_{1}+\omega_{2}}$$

…

$$\lambda_{n-1,n-2}^{\bar{N}}(j\omega)=\left.\frac{k_{n-1}+j\omega c_{n-1}}{-m_{n-1}\omega^{2}+j\omega(c_{n-1}+c_{n})+k_{n-1}+k_{n}-(j\omega c_{n}+k_{n}\lambda_{n,n-1}^{\bar{N}})(j\omega)}\right|_{\omega=\omega_{1}+\omega_{2}+\cdots+\omega_{\bar{N}}}$$

(3-43)

Through iteratively calculation from equations(3-22)-(3-32), it can be easily to deduce that the following relationship can be established for the masses which are not connected to the nonlinear masses and the *J*th spring.

$$\lambda_{i,i-1}^{1}(j\omega)=\left.\frac{k_{i}+j\omega c_{i}}{-m_{i}\omega^{2}+j\omega(c_{i}+c_{i+1})+k_{i}+k_{i+1}-(j\omega c_{i+1}+k_{i+1}\lambda_{i+1,i}^{1})(j\omega)}\right|_{\omega=\omega_{1}}$$

$$\lambda_{i,i-1}^{2}(j\omega)=\left.\frac{k_{i}+j\omega c_{i}}{-m_{i}\omega^{2}+j\omega(c_{i}+c_{i+1})+k_{i}+k_{i+1}-(j\omega c_{i+1}+k_{i+1}\lambda_{i+1,i}^{2})(j\omega)}\right|_{\omega=\omega_{1}+\omega_{2}}$$

…

$$\lambda_{i,i-1}^{\bar{N}}(j\omega)=\left.\frac{k_{i}+j\omega c_{i}}{-m_{i}\omega^{2}+j\omega(c_{i}+c_{i+1})+k_{i}+k_{i+1}-(j\omega c_{i+1}+k_{i+1}\lambda_{i+1,i}^{\bar{N}})(j\omega)}\right|_{\omega=\omega_{1}+\omega_{2}+\cdots+\omega_{\bar{N}}}$$

(3-44)

Where $2\le i\le n,\ i\ne L_{i}-1, L_{i}, J,\ i=1,...,\bar{L}$

For the relationship among the masses connected to the left side of the nonlinear components can be rewritten as

$$\lambda^{1}_{L_i-1,L_i-2}(j\omega)=\left.\frac{k_{L_i-1}+j\omega c_{L_i-1}-\dfrac{P_1(NonF_{L_i}(j\omega))}{G_{(L_i-2,1)}(j\omega)U_1(j\omega)}}{-m_{L_i-1}\omega^2+j\omega(c_{L_i-1}+c_{L_i})+k_{L_i-1}+k_{L_i}-(j\omega c_{L_i}+k_{L_i}\lambda^{1}_{L_i,L_i-1})(j\omega)}\right|_{\omega=\omega_1}$$

$$\lambda^{2}_{L_i-1,L_i-2}(j\omega)=\left.\frac{k_{L_i-1}+j\omega c_{L_i-1}-\dfrac{P_1(NonF_{L_i}(j\omega))}{G_{(L_i-2,2)}(j\omega)U_2(j\omega)}}{-m_{L_i-1}\omega^2+j\omega(c_{L_i-1}+c_{L_i})+k_{L_i-1}+k_{L_i}-(j\omega c_{L_i}+k_{L_i}\lambda^{2}_{L_i,L_i-1})(j\omega)}\right|_{\omega=\omega_1+\omega_2}$$

…

$$\lambda^{\bar{N}}_{L_i-1,L_i-2}(j\omega)=\left.\frac{k_{L_i-1}+j\omega c_{L_i-1}-\dfrac{P_1(NonF_{L_i}(j\omega))}{G_{(L_i-2,N)}(j\omega)U_{\bar{N}}(j\omega)}}{-m_{L_i-1}\omega^2+j\omega(c_{L_i-1}+c_{L_i})+k_{L_i-1}+k_{L_i}-(j\omega c_{L_i}+k_{L_i}\lambda^{\bar{N}}_{L_i,L_i-1})(j\omega)}\right|_{\omega=\omega_1+\omega_2+\cdots+\omega_{\bar{N}}}$$

$i=1,2,...,\bar{L}$	(3-45)

where $P_1(NonF_{L_i})+P_2(NonF_{L_i})+\cdots+P_{\bar{N}}(NonF_{L_i})=NonF_{L_i}$

For the relationship among the masses connected to the right side of the nonlinear components can be rewritten as

$$\lambda^{1}_{L_i,L_i-1}(j\omega)=\left.\frac{k_{L_i}+j\omega c_{L_i}+\dfrac{P_1(NonF_{L_i}(j\omega))}{G_{(L_i-1,1)}(j\omega)U_1(j\omega)}}{-m_{L_i}\omega^2+j\omega(c_{L_i}+c_{L_i+1})+k_{L_i}+k_{L_i+1}-(j\omega c_{L_i+1}+k_{L_i+1}\lambda^{1}_{L_i+1,L_i})(j\omega)}\right|_{\omega=\omega_1}$$

$$\lambda^{2}_{L_i,L_i-1}(j\omega)=\left.\frac{k_{L_i}+j\omega c_{L_i}+\dfrac{P_1(NonF_{L_i}(j\omega))}{G_{(L_i-1,2)}(j\omega)U_2(j\omega)}}{-m_{L_i}\omega^2+j\omega(c_{L_i}+c_{L_i+1})+k_{L_i}+k_{L_i+1}-(j\omega c_{L_i+1}+k_{L_i+1}\lambda^{2}_{L_i+1,L_i})(j\omega)}\right|_{\omega=\omega_1+\omega_2}$$

…

$$\lambda^{\bar{N}}_{L_i,L_i-1}(j\omega)=\left.\frac{k_{L_i}+j\omega c_{L_i}+\dfrac{P_1(NonF_{L_i}(j\omega))}{G_{(L_i-1,\bar{N})}(j\omega)U_{\bar{N}}(j\omega)}}{-m_{L_i}\omega^2+j\omega(c_{L_i}+c_{L_i+1})+k_{L_i}+k_{L_i+1}-(j\omega c_{L_i+1}+k_{L_i+1}\lambda^{\bar{N}}_{L_i+1,L_i})(j\omega)}\right|_{\omega=\omega_1+\omega_2+\cdots+\omega_{\bar{N}}}$$

$i=1,2,...,\bar{L}$	(3-46)

For the Jth mass where the force is located, the relationship can be given as following

$$\lambda_{J,J-1}^{1}(j\omega)=\left.\frac{k_J+j\omega c_J+\dfrac{P_1(U(j\omega))}{G_{(J-1,1)}(j\omega)U_1(j\omega)}}{-m_J\omega^2+j\omega(c_J+c_{J+1})+k_J+k_{J+1}-(j\omega c_{J+1}+k_{J+1}\lambda_{J+1,J}^{1})(j\omega)}\right|_{\omega=\omega_1}$$

$$\lambda_{J,J-1}^{2}(j\omega)=\left.\frac{k_J+j\omega c_J+\dfrac{P_1(U(j\omega))}{G_{(J-1,2)}(j\omega)U_2(j\omega)}}{-m_J\omega^2+j\omega(c_J+c_{J+1})+k_J+k_{J+1}-(j\omega c_{J+1}+k_{J+1}\lambda_{J+1,J}^{2})(j\omega)}\right|_{\omega=\omega_1+\omega_2}$$

…

$$\lambda_{J,J-1}^{\bar{N}}(j\omega)=\left.\frac{k_J+j\omega c_J+\dfrac{P_1(U(j\omega))}{G_{(J-1,\bar{N})}(j\omega)U_{\bar{N}}(j\omega)}}{-m_J\omega^2+j\omega(c_J+c_{J+1})+k_J+k_{J+1}-(j\omega c_{J+1}+k_{J+1}\lambda_{J+1,J}^{\bar{N}})(j\omega)}\right|_{\omega=\omega_1+\omega_2+\cdots+\omega_{\bar{N}}}$$

(3-47)

where $P_1(U)+P_2(U)+\cdots+P_{\bar{N}}(U)=U$

From Equations(3-14)-(3-47) the relationships about output spectra ratio for each order between two consecutive masses have been illustrated in two different perspectives.

3.3.4 Output-based transmissibility of MDOF Nonlinear structural systems under general input

According to the definition of NOFRFs in equation(3-7), the following relationship can be derived:

$$Y_{(i,j)}(j\omega)=G_{(i,j)}(j\omega)U_j(j\omega)\quad\left(1\le i\le n;\ 1\le j\le\bar{N}\right)\tag{3-48}$$

Where subscript i means the output point, and j means the nonlinear order; when j=1, it means linear output.

Therefore, Output-based transmissibility can be defined as

$$\lambda_{i,i+1}^{j}(j\omega)=\frac{G_{(i,j)}(j\omega)}{G_{(i+1,j)}(j\omega)}=\frac{G_{(i,j)}(j\omega)U_j(j\omega)}{G_{(i+1,j)}(j\omega)U_j(j\omega)}=\frac{Y_{(i,j)}(j\omega)}{Y_{(i+1,j)}(j\omega)} \quad (i=1,\ldots,n\text{-}1;\ j=1,\ldots,\bar{N}) \tag{3-49}$$

Substitute equation(3-48) into equation(3-26) and calculate interactively through Equations(3-26)-(3-32), for the masses which are not connected with nonlinear components and the Jth spring,

$$\begin{pmatrix} -m_r\omega^2 Y_{(r,1)}(j\omega)\big|_{\omega=\omega_1}+j\omega(c_r+c_{r+1})Y_{(r,1)}(j\omega)\big|_{\omega=\omega_1}-j\omega c_{r+1}Y_{(r+1,1)}(j\omega)\big|_{\omega=\omega_1} \\ -j\omega c_r Y_{(r,1)}(j\omega)\big|_{\omega=\omega_1}+(k_r+k_{r+1})Y_{(r,1)}(j\omega)\big|_{\omega=\omega_1}-k_{r+1}Y_{(r+1,1)}(j\omega)\big|_{\omega=\omega_1}-k_r G_{(r,1)}(j\omega)\big|_{\omega=\omega_1} \end{pmatrix}=0$$

$$\begin{pmatrix} -m_r\omega^2 Y_{(r+1,2)}(j\omega)\big|_{\omega=\omega_1+\omega_2}+j\omega(c_r+c_{r+1})(j\omega)Y_{(r,2)}(j\omega)\big|_{\omega=\omega_1+\omega_2} \\ -j\omega c_{r+1}Y_{(r+1,2)}(j\omega)\big|_{\omega=\omega_1+\omega_2}-j\omega c_r Y_{(r,2)}(j\omega)\big|_{\omega=\omega_1+\omega_2}+(k_r+k_{r+1})Y_{(r,2)}(j\omega)\big|_{\omega=\omega_1+\omega_2} \\ -k_{r+1}Y_{(r+1,2)}(j\omega)\big|_{\omega=\omega_1+\omega_2}-k_r Y_{(r,2)}(j\omega)\big|_{\omega=\omega_1+\omega_2} \end{pmatrix}=0$$

…

$$\begin{pmatrix} -m_r\omega^2 Y_{(r,\bar{N})}(j\omega)\big|_{\omega=\omega_1+\cdots+\omega_{\bar{N}}}+j\omega(c_r+c_{r+1})Y_{(r,\bar{N})}(j\omega)\big|_{\omega=\omega_1+\cdots+\omega_{\bar{N}}} \\ -j\omega c_{r+1}Y_{(r+1,\bar{N})}(j\omega)\big|_{\omega=\omega_1+\cdots+\omega_{\bar{N}}}-j\omega c_r Y_{(r,\bar{N})}(j\omega)\big|_{\omega=\omega_1+\cdots+\omega_{\bar{N}}}+(k_r+k_{r+1})Y_{(r,\bar{N})}(j\omega)\big|_{\omega=\omega_1+\cdots+\omega_{\bar{N}}} \\ -k_{r+1}Y_{(r+1,\bar{N})}(j\omega)\big|_{\omega=\omega_1+\cdots+\omega_{\bar{N}}}-k_r Y_{(r,\bar{N})}(j\omega)\big|_{\omega=\omega_1+\cdots+\omega_{\bar{N}}} \end{pmatrix}=0$$

$$r<\min(L_i-1,L_i,J)\quad\text{or}\quad r>\max(L_i-1,L_i,J) \tag{3-50}$$

It reveals that the transmissibility functions based on NOFRFs are independent of force. Through Equations(3-48)-(3-50), it can be concluded that transmissibility based on NOFRFs are the same as the ones based on output response under each nonlinear order. The derivation of the transmissibility based on output response (3-34)-(3-47) is also suitable for the transmissibility based on NOFRFs. The following parts will illustrate the important properties of aforementioned two types of transmissibility functions and their interactive relationships.

3.3.5 Some important properties of NOFRF-based transmissibility and Output-based transmissibility of nonlinear MDOF system under general input

Transmissibility functions are strongly frequency-dependent due to the fact that the input signal is general input (bandlimited).

$$U(j\omega)\begin{cases}\neq 0 & \omega\in[a,b]\\ =0 & \omega\notin[a,b]\end{cases} \tag{3-51}$$

If $\omega\notin[a,b]$, $U(j\omega)$ in Equations(3-31), (3-40) and (3-47) are nonzero value; on the contrary when $\omega\notin[a,b]$, $U(j\omega)$ in Equations(3-31), (3-40) and (3-47) are becoming zero. Therefore, the Equations(3-34)-(3-47) contain different solution concerning the choice of analyzed frequency range.

A. When analyzed frequency $\omega\in[a,b]$ under single point input

Without loss of generality, assume that the system contains $L_i\left(\mathrm{i}=1,2,...,\bar{\mathrm{L}},\ \bar{\mathrm{L}}\geq 1\right)$ nonlinear components, and it meets the condition $L_1<L_2<\cdots<L_{\bar{L}}$, then the following properties of transmissibility functions based on output response under general input can be obtained for MDOF systems with multiple nonlinear components.

1) If $J\leq L_1$,then the NOFRF-based transmissibility between two consecutive masses ($1\leq i\leq J-1$ and $L_{\bar{L}}\leq i<n$), the following relationship holds

$$\frac{G_{(i,1)}(j\omega)}{G_{(i+1,1)}(j\omega)}=\frac{G_{(i,2)}(j\omega)}{G_{(i+1,2)}(j\omega)}=\cdots=\frac{G_{(i,\bar{N})}(j\omega)}{G_{(i+1,\bar{N})}(j\omega)} \tag{3-52}$$

2) If $J\leq L_1$,then the NOFRF-based transmissibility between two consecutive masses ($J\leq i<L_{\bar{L}}$), the following relationship holds

$$\frac{G_{(i,1)}(j\omega)}{G_{(i+1,1)}(j\omega)} \neq \frac{G_{(i,2)}(j\omega)}{G_{(i+1,2)}(j\omega)} \neq \cdots \neq \frac{G_{(i,\bar{N})}(j\omega)}{G_{(i+1,\bar{N})}(j\omega)} \quad (3\text{-}53)$$

3) If $L_1 \le J \le L_{\bar{L}}$,then the NOFRF-based transmissibility between two consecutive masses ($1 \le i < L_1 - 1$ and $L_{\bar{L}} \le i < n$), the following relationship holds

$$\frac{G_{(i,1)}(j\omega)}{G_{(i+1,1)}(j\omega)} = \frac{G_{(i,2)}(j\omega)}{G_{(i+1,2)}(j\omega)} = \cdots = \frac{G_{(i,\bar{N})}(j\omega)}{G_{(i+1,\bar{N})}(j\omega)} \quad (3\text{-}54)$$

4) If $L_1 \le J \le L_{\bar{L}}$,then the NOFRF-based transmissibility between two consecutive masses ($L_1 \le i < L_{\bar{L}}$), the following relationship holds

$$\frac{G_{(i,1)}(j\omega)}{G_{(i+1,1)}(j\omega)} \neq \frac{G_{(i,2)}(j\omega)}{G_{(i+1,2)}(j\omega)} \neq \cdots \neq \frac{G_{(i,\bar{N})}(j\omega)}{G_{(i+1,\bar{N})}(j\omega)} \quad (3\text{-}55)$$

5) If $J \ge L_{\bar{L}}$,then the NOFRF-based transmissibility between two consecutive masses ($1 \le i < L_1 - 1$ and $J \le i < n$), the following relationship holds

$$\frac{G_{(i,1)}(j\omega)}{G_{(i+1,1)}(j\omega)} = \frac{G_{(i,2)}(j\omega)}{G_{(i+1,2)}(j\omega)} = \cdots = \frac{G_{(i,\bar{N})}(j\omega)}{G_{(i+1,\bar{N})}(j\omega)} \quad (3\text{-}56)$$

6) If $J \ge L_{\bar{L}}$,then the NOFRF-based transmissibility between two consecutive masses ($L_1 - 1 \le i < J$), the following relationship holds

$$\frac{G_{(i,1)}(j\omega)}{G_{(i+1,1)}(j\omega)} \neq \frac{G_{(i,2)}(j\omega)}{G_{(i+1,2)}(j\omega)} \neq \cdots \neq \frac{G_{(i,\bar{N})}(j\omega)}{G_{(i+1,\bar{N})}(j\omega)} \quad (3\text{-}57)$$

Similarly, the following relationships for transmissibility functions based on output response of MDOF system with multiple nonlinear components can be established

7) If $J \le L_1$,then the Output-based transmissibility between two consecutive masses ($1 \le i < J-1$ and $L_{\bar{L}} \le i < n$), the following relationship holds

$$\frac{Y_{(i,1)}(j\omega)}{Y_{(i+1,1)}(j\omega)} = \frac{Y_{(i,2)}(j\omega)}{Y_{(i+1,2)}(j\omega)} = \cdots = \frac{Y_{(i,\bar{N})}(j\omega)}{Y_{(i+1,\bar{N})}(j\omega)} \quad (3\text{-}58)$$

8) If $J \le L_1$,then the Output-based transmissibility between two consecutive masses ($J-1 \le i < L_{\bar{L}}$), the following relationship holds

$$\frac{Y_{(i,1)}(j\omega)}{Y_{(i+1,1)}(j\omega)} \ne \frac{Y_{(i,2)}(j\omega)}{Y_{(i+1,2)}(j\omega)} \ne \cdots \ne \frac{Y_{(i,\bar{N})}(j\omega)}{Y_{(i+1,\bar{N})}(j\omega)} \quad (3\text{-}59)$$

9) If $L_1 \le J \le L_{\bar{L}}$,then the Output-based transmissibility between two consecutive masses ($1 \le i < L_1 - 1$ and $L_{\bar{L}} \le i < n$), the following relationship holds

$$\frac{Y_{(i,1)}(j\omega)}{Y_{(i+1,1)}(j\omega)} = \frac{Y_{(i,2)}(j\omega)}{Y_{(i+1,2)}(j\omega)} = \cdots = \frac{Y_{(i,\bar{N})}(j\omega)}{Y_{(i+1,\bar{N})}(j\omega)} \quad (3\text{-}60)$$

10) If $L_1 \le J \le L_{\bar{L}}$,then the Output-based transmissibility between two consecutive masses ($L_1 - 1 \le i < L_{\bar{L}}$), the following relationship holds

$$\frac{Y_{(i,1)}(j\omega)}{Y_{(i+1,1)}(j\omega)} \ne \frac{Y_{(i,2)}(j\omega)}{Y_{(i+1,2)}(j\omega)} \ne \cdots \ne \frac{Y_{(i,\bar{N})}(j\omega)}{Y_{(i+1,\bar{N})}(j\omega)} \quad (3\text{-}61)$$

11) If $J \ge L_{\bar{L}}$,then the Output-based transmissibility between two consecutive masses ($1 \le i < L_1 - 1$ and $J \le i < n$), the following relationship holds

$$\frac{Y_{(i,1)}(j\omega)}{Y_{(i+1,1)}(j\omega)}=\frac{Y_{(i,2)}(j\omega)}{Y_{(i+1,2)}(j\omega)}=\cdots=\frac{Y_{(i,\bar{N})}(j\omega)}{Y_{(i+1,\bar{N})}(j\omega)} \quad (3\text{-}62)$$

12) If $J \geq L_{\bar{L}}$,then the Output-based transmissibility between two consecutive masses ($L_1 - 1 \leq i < J$), the following relationship holds

$$\frac{Y_{(i,1)}(j\omega)}{Y_{(i+1,1)}(j\omega)} \neq \frac{Y_{(i,2)}(j\omega)}{Y_{(i+1,2)}(j\omega)} \neq \cdots \neq \frac{Y_{(i,\bar{N})}(j\omega)}{Y_{(i+1,\bar{N})}(j\omega)} \quad (3\text{-}63)$$

B. When analyzed frequency $\omega \notin [a,b]$ (out of the range [a, b]) under single point input

When $\omega \notin [a,b]$, $U(j\omega)$=0, thus the Equations(3-31), (3-40) and (3-47) will become as the following Equations(3-64), (3-65) and (3-66).

$$\begin{aligned}
&m_J \frac{1}{2\pi}\sum_{n=1}^{N}\int_{-\infty}^{\infty}(j\omega)^2 G_{(J,n)}(j\omega)e^{j\omega t}d\omega - c_J \frac{1}{2\pi}\sum_{n=1}^{N}\int_{-\infty}^{\infty}(j\omega)G_{(J-1,n)}(j\omega)e^{j\omega t}d\omega \\
&+(c_J + c_{J+1})\frac{1}{2\pi}\sum_{n=1}^{N}\int_{-\infty}^{\infty}(j\omega)G_{(J,n)}(j\omega)e^{j\omega t}d\omega - c_{J+1}\frac{1}{2\pi}\sum_{n=1}^{N}\int_{-\infty}^{\infty}(j\omega)G_{(J+1,n)}(j\omega)e^{j\omega t}d\omega \\
&-k_J \frac{1}{2\pi}\sum_{n=1}^{N}\int_{-\infty}^{\infty}G_{(J-1,n)}(j\omega)e^{j\omega t}d\omega + (k_J + k_{J+1})\frac{1}{2\pi}\sum_{n=1}^{N}\int_{-\infty}^{\infty}G_{(J,n)}(j\omega)e^{j\omega t}d\omega \\
&-k_{J+1}\frac{1}{2\pi}\sum_{n=1}^{N}\int_{-\infty}^{\infty}G_{(J+1,n)}(j\omega)e^{j\omega t}d\omega = 0
\end{aligned} \quad (3\text{-}64)$$

$$\lambda_{J,J+1}^{1}(j\omega)=\left.\frac{k_{J+1}+j\omega c_{J+1}}{-m_J\omega^2+j\omega(c_J+c_{J+1})+k_J+k_{J+1}-(j\omega c_J+k_J\lambda_{J-1,J}^{1})(j\omega)}\right|_{\omega=\omega_1}$$

$$\lambda_{J,J+1}^{2}(j\omega)=\left.\frac{k_{J+1}+j\omega c_{J+1}}{-m_J\omega^2+j\omega(c_J+c_{J+1})+k_J+k_{J+1}-(j\omega c_J+k_J\lambda_{J-1,J}^{2})(j\omega)}\right|_{\omega=\omega_1+\omega_2}$$

…

$$\lambda_{J,J+1}^{\bar{N}}(j\omega)=\left.\frac{k_{J+1}+j\omega c_{J+1}}{-m_J\omega^2+j\omega(c_J+c_{J+1})+k_J+k_{J+1}-(j\omega c_J+k_J\lambda_{J-1,J}^{\bar{N}})(j\omega)}\right|_{\omega=\omega_1+\omega_2+\cdots+\omega_{\bar{N}}}$$

(3-65)

$$\lambda_{J,J-1}^{1}(j\omega)=\left.\frac{k_J+j\omega c_J}{-m_J\omega^2+j\omega(c_J+c_{J+1})+k_J+k_{J+1}-(j\omega c_{J+1}+k_{J+1}\lambda_{J+1,J}^{1})(j\omega)}\right|_{\omega=\omega_1}$$

$$\lambda_{J,J-1}^{2}(j\omega)=\left.\frac{k_J+j\omega c_J}{-m_J\omega^2+j\omega(c_J+c_{J+1})+k_J+k_{J+1}-(j\omega c_{J+1}+k_{J+1}\lambda_{J+1,J}^{2})(j\omega)}\right|_{\omega=\omega_1+\omega_2}$$

…

$$\lambda_{J,J-1}^{\bar{N}}(j\omega)=\left.\frac{k_J+j\omega c_J}{-m_J\omega^2+j\omega(c_J+c_{J+1})+k_J+k_{J+1}-(j\omega c_{J+1}+k_{J+1}\lambda_{J+1,J}^{\bar{N}})(j\omega)}\right|_{\omega=\omega_1+\omega_2+\cdots+\omega_{\bar{N}}}$$

(3-66)

All the terms related to $U(j\omega)$ become zeros as a result of Equations(3-64)-(3-66). Based on this conclusion, Equations(3-22)-(3-32) can be rewritten as a matrix form

$$\Theta(j(\omega_1+\omega_2+\cdots+\omega_j))Y_n(j(\omega_1+\omega_2+\cdots+\omega_j))=\Delta_j(j(\omega_1+\omega_2+\cdots+\omega_j))$$

$j=1,2,...,\bar{N}$ (3-67)

Where

$$\Delta_j(j(\omega_1+\omega_2+\cdots+\omega_n))=\begin{cases}0 & \text{if } l\neq L_i-1, L_i,\ 1\le x\le L_{\bar{L}}\\ -P_j(NonF_{L_x}j(\omega_1+\omega_2+\cdots+\omega_j)) & \text{if } l=L_i-1,\ 1\le x\le L_{\bar{L}}\\ P_j(NonF_{L_x}j(\omega_1+\omega_2+\cdots+\omega_j)) & \text{if } l=L_i,\ 1\le x\le L_{\bar{L}}\end{cases}$$

So that

$$Y_j(j(\omega_1+\omega_2+\cdots+\omega_j))=\Theta^{-1}(j(\omega_1+\omega_2+\cdots+\omega_j))\Delta_j(j(\omega_1+\omega_2+\cdots+\omega_j)) \quad (3\text{-}68)$$

Define

$$\Theta^{-1}(j(\omega_1+\omega_2+\cdots+\omega_j))=Q(j(\omega_1+\omega_2+\cdots+\omega_j)) \quad (3\text{-}69)$$

Therefore, the *n*th order nonlinear output spectrum for each mass can be obtained from Equations(3-66)-(3-69).

$$Y_{i,j}(j(\omega_1+\omega_2+\cdots+\omega_n))=\sum_{x=1}^{L_T}\begin{pmatrix}Q_{i,L_x-1}(j(\omega_1+\omega_2+\cdots+\omega_j))\\ Q_{i,L_x}(j(\omega_1+\omega_2+\cdots+\omega_j))\end{pmatrix}^T\begin{pmatrix}-P_j(NonF_{L_x}j(\omega_1+\omega_2+\cdots+\omega_j))\\ P_j(NonF_{L_x}j(\omega_1+\omega_2+\cdots+\omega_j))\end{pmatrix}$$

$i=1,...,n-1$ (3-70)

Equation(3-70) reveals the relationship between the number of nonlinear components and *n*th order nonlinear output spectra. When there is only one nonlinear component, that is, $\bar{L}=1$,the *n*th order nonlinear output spectrum for each mass can be calculated as

$$\begin{aligned}Y_{i,j}(j(\omega_1+\omega_2+\cdots+\omega_j))=&-Q_{i,L_x-1}(j(\omega_1+\omega_2+\cdots+\omega_j))P_j(NonF_{L_x}j(\omega_1+\omega_2+\cdots+\omega_j))\\&+Q_{i,L_x}(j(\omega_1+\omega_2+\cdots+\omega_j))P_j(NonF_{L_x}j(\omega_1+\omega_2+\cdots+\omega_j))\end{aligned} \quad (3\text{-}71)$$

Then the transmissibility function for each consecutive masses

$$\begin{aligned}\lambda_{i,i+1}^{j}(j\omega)&=\frac{Y_{(i,j)}(j\omega)}{Y_{(i+1,j)}(j\omega)}\\&=\frac{-Q_{i,L_x-1}(j(\omega_1+\omega_2+\cdots+\omega_j))+Q_{i,L_x}(j(\omega_1+\omega_2+\cdots+\omega_j))}{-Q_{i+1,L_x-1}(j(\omega_1+\omega_2+\cdots+\omega_j))+Q_{i+1,L_x}(j(\omega_1+\omega_2+\cdots+\omega_j))}\end{aligned} \quad (3\text{-}72)$$

When there is more than one nonlinear component, that is, $\bar{L}>1$

$$\lambda_{i,i+1}^{j}(j\omega)=\frac{Y_{(i,j)}(j\omega)}{Y_{(i+1,j)}(j\omega)}=\frac{\sum_{x=1}^{L_{\bar{L}}}\begin{pmatrix}Q_{i,L_x-1}(j(\omega_1+\omega_2+\cdots+\omega_j))\\ Q_{i,L_x}(j(\omega_1+\omega_2+\cdots+\omega_j))\end{pmatrix}^{T}\begin{pmatrix}-P_j(NonF_{L_x}j(\omega_1+\omega_2+\cdots+\omega_j))\\ P_j(NonF_{L_x}j(\omega_1+\omega_2+\cdots+\omega_j))\end{pmatrix}}{\sum_{x=1}^{L_{\bar{L}}}\begin{pmatrix}Q_{i+1,L_x-1}(j(\omega_1+\omega_2+\cdots+\omega_j))\\ Q_{i+1,L_x}(j(\omega_1+\omega_2+\cdots+\omega_j))\end{pmatrix}^{T}\begin{pmatrix}-P_j(NonF_{L_x}j(\omega_1+\omega_2+\cdots+\omega_j))\\ P_j(NonF_{L_x}j(\omega_1+\omega_2+\cdots+\omega_j))\end{pmatrix}}$$

$i=1,...,n-1$ (3-73)

Equation(3-72) indicates that the transmissibility functions for each pair of consecutive masses are independent with nonlinear component, and only rely on the system's physical parameters. While the situation with more than one nonlinear component is entirely converse, that is, the transmissibility functions not only depend on the system's physical parameters but also the nonlinear restoring forces, observed from equation(3-73).

Based on the aforementioned derivation, if there is only one nonlinear component in the MDOF system, there is no significance of considering nonlinear output frequency range (out of [a, b]) due to the fact that the transmissibility function merely depends on system physical parameters. However, if two or more than two nonlinear components exist, nonlinear output frequency range should be an effective way to recognize the location of multiple nonlinear components through the similar iterative perspective in Equations(3-14)-(3-47) given that the terms related to input are zeros, the remaining terms on the right side are nonlinear restoring forces in Equations(3-32)-(3-47).

Therefore, the corresponding properties for identifying multiple nonlinear components can be obtained

13) For the Output-based transmissibility between two consecutive masses ($1\le i<L_1-1$ and $L_{\bar{L}}\le i<n$), the following relationship holds

$$\frac{Y_{(i,1)}(j\omega)}{Y_{(i+1,1)}(j\omega)}=\frac{Y_{(i,2)}(j\omega)}{Y_{(i+1,2)}(j\omega)}=\cdots=\frac{Y_{(i,\bar{N})}(j\omega)}{Y_{(i+1,\bar{N})}(j\omega)} \quad (3\text{-}74)$$

14) For the Output-based transmissibility between two consecutive masses ($L_1 - 1 \le i < L_{\bar{L}}$), the following relationship holds

$$\frac{Y_{(i,1)}(j\omega)}{Y_{(i+1,1)}(j\omega)} \neq \frac{Y_{(i,2)}(j\omega)}{Y_{(i+1,2)}(j\omega)} \neq \cdots \neq \frac{Y_{(i,\bar{N})}(j\omega)}{Y_{(i+1,\bar{N})}(j\omega)} \tag{3-75}$$

Similarly, the following relationships for transmissibility functions based on NOFRFs of MDOF system with multiple nonlinear components can be established

15) For the NOFRF-based transmissibility between two consecutive masses ($1 \le i < L_1 - 1$ and $L_{\bar{L}} \le i < n$), the following relationship holds

$$\frac{G_{(i,1)}(j\omega)}{G_{(i+1,1)}(j\omega)} = \frac{G_{(i,2)}(j\omega)}{G_{(i+1,2)}(j\omega)} = \cdots = \frac{G_{(i,\bar{N})}(j\omega)}{G_{(i+1,\bar{N})}(j\omega)} \tag{3-76}$$

16) For the transmissibility functions between two consecutive masses ($L_1 - 1 \le i < L_{\bar{L}}$), the following relationship holds

$$\frac{G_{(i,1)}(j\omega)}{G_{(i+1,1)}(j\omega)} \neq \frac{G_{(i,2)}(j\omega)}{G_{(i+1,2)}(j\omega)} \neq \cdots \neq \frac{G_{(i,\bar{N})}(j\omega)}{G_{(i+1,\bar{N})}(j\omega)} \tag{3-77}$$

C. When analyzed frequency $\omega \in [a,b]$ under multiple-point input

The above situations and properties are only considered that there is single point excitation. This short session will discuss the methodology under multiple points excitation.

First of all, analyzed frequency $\omega \in [a,b]$ has been considered, in order not to loss generality, then assume that each mass has been loaded one force which means there are *n* points excitations on the MDOF system. And all the *n* loading forces have the same frequency range [a, b], amplitudes and phases could be diverse. Through the iterative calculation as Equations(3-14)-(3-47), it indicates that each transmissibility function contains one term related to output response, which is directly connected to effect of nonlinear restoring force.

Therefore, for all masses, the following relationship can be established

$$\frac{Y_{(i,1)}(j\omega)}{Y_{(i+1,1)}(j\omega)} \neq \frac{Y_{(i,2)}(j\omega)}{Y_{(i+1,2)}(j\omega)} \neq \cdots \neq \frac{Y_{(i,\bar{N})}(j\omega)}{Y_{(i+1,\bar{N})}(j\omega)} \tag{3-78}$$

$$\frac{G_{(i,1)}(j\omega)}{G_{(i+1,1)}(j\omega)} \neq \frac{G_{(i,2)}(j\omega)}{G_{(i+1,2)}(j\omega)} \neq \cdots \neq \frac{G_{(i,\bar{N})}(j\omega)}{G_{(i+1,\bar{N})}(j\omega)} \tag{3-79}$$

D. When analyzed frequency $\omega \notin [a,b]$ (out of the range [a, b]) under multiple-point input

Consider if analyzed frequency $\omega \notin [a,b]$, even if there are n loading forces, because of zero values of input spectra, the term related to output response could be eliminated accordingly. Therefore, the properties under this condition could be the same as Equations(3-74)-(3-77). Also one note needs to be reminded, the properties of Equations(3-75)-(3-78) only can be established when there are two or more than two nonlinear components, no matter how many loading forces have been reckoned.

3.3.6 Damage detection and localization method

The properties aforementioned have explained the relationship of Output-based transmissibility function and NOFRF-based transmissibility function under each nonlinear order respectively. In the view of above-mentioned properties, the procedure for identifying single or multiple nonlinear components has been organized as follows.

Those properties are also suitable for the transmissibility functions based on merely total output response instead of output response under each separate nonlinear order or NOFRFs, which could make the identification process simpler. Take an example of property (3-52) and (3-53).

$$\begin{aligned}\lambda_{i,i+1}(j\omega) &= \frac{Y_i(j\omega)}{Y_{i+1}(j\omega)} \\ &= \frac{Y_{(i,1)}(j\omega)+Y_{(i,2)}(j\omega)+\cdots+Y_{(i,\bar{N})}(j\omega)}{Y_{(i+1,1)}(j\omega)+Y_{(i+1,2)}(j\omega)+\cdots+Y_{(i+1,\bar{N})}(j\omega)} \\ &= \frac{Y_{(i,1)}(j\omega)}{Y^1_{(i+1,1)}(j\omega)} = \frac{Y_{(i,2)}(j\omega)}{Y_{(i+1,2)}(j\omega)} = \cdots = \frac{Y_{(i,\bar{N})}(j\omega)}{Y_{(i+1,\bar{N})}(j\omega)}\end{aligned} \tag{3-80}$$

$$\begin{aligned}\lambda_{i,i+1}(j\omega) &= \frac{Y_i(j\omega)}{Y_{i+1}(j\omega)} \\ &= \frac{Y_{(i,1)}(j\omega)+Y_{(i,2)}(j\omega)+\cdots+Y_{(i,\bar{N})}(j\omega)}{Y_{(i+1,1)}(j\omega)+Y_{(i+1,2)}(j\omega)+\cdots+Y_{(i+1,\bar{N})}(j\omega)} \\ &\neq \frac{Y_{(i,1)}(j\omega)}{Y^1_{(i+1,1)}(j\omega)} \neq \frac{Y_{(i,2)}(j\omega)}{Y_{(i+1,2)}(j\omega)} \neq \cdots \neq \frac{Y_{(i,\bar{N})}(j\omega)}{Y_{(i+1,\bar{N})}(j\omega)}\end{aligned} \tag{3-81}$$

Therefore, the corresponding relationship between transmissibility based on total output and the one under each nonlinear order or NOFRFs can be deduced as the way (3-78) and (3-79). The coral idea of nonlinear components identification is on the account of that output response of nonlinear MDOF system depends on input including the frequency components and excitation intensity to a certain extent. Hence, two different loading forces with different excitation will be introduced. Still take the example of property (3-52) and (3-53) as an explanation.

In the equation(3-52),

$$\begin{aligned}\lambda^{f_1}_{i,i+1}(j\omega) &= \frac{Y^{f_1}_i(j\omega)}{Y^{f_1}_{i+1}(j\omega)} = \frac{Y^{f_1}_{(i,1)}(j\omega)}{Y^{f_1}_{(i+1,1)}(j\omega)} = \frac{Y^{f_1}_{(i,2)}(j\omega)}{Y^{f_1}_{(i+1,2)}(j\omega)} = \cdots = \frac{Y^{f_1}_{(i,\bar{N})}(j\omega)}{Y^{f_1}_{(i+1,\bar{N})}(j\omega)} \\ \lambda^{f_2}_{i,i+1}(j\omega) &= \frac{Y^{f_2}_i(j\omega)}{Y^{f_2}_{i+1}(j\omega)} = \frac{Y^{f_2}_{(i,1)}(j\omega)}{Y^{f_2}_{(i+1,1)}(j\omega)} = \frac{Y^{f_2}_{(i,2)}(j\omega)}{Y^{f_2}_{(i+1,2)}(j\omega)} = \cdots = \frac{Y^{f_2}_{(i,\bar{N})}(j\omega)}{Y^{f_2}_{(i+1,\bar{N})}(j\omega)}\end{aligned} \tag{3-82}$$

Where the superscripts f_1 and f_2 in equation(3-82) stand for two different inputs which contain the same frequency band [a, b] but

diverse excitation intensities.

Due to the reason that the transmissibility from equation(3-52) only rely on the physical parameters of the system. Therefore,

$$\lambda_{i,i+1}^{(1)}(j\omega)=\lambda_{i,i+1}^{(2)}(j\omega) \tag{3-83}$$

While in the equation(3-53),

$$\begin{aligned}\lambda_{i,i+1}^{f_1}(j\omega)&=\frac{Y_i^{f_1}(j\omega)}{Y_{i+1}^{f_1}(j\omega)}\neq\frac{Y_{(i,1)}^{f_1}(j\omega)}{Y_{(i+1,1)}^{f_1}(j\omega)}\neq\frac{Y_{(i,2)}^{f_1}(j\omega)}{Y_{(i+1,2)}^{f_1}(j\omega)}\neq\cdots\neq\frac{Y_{(i,\bar{N})}^{f_1}(j\omega)}{Y_{(i+1,\bar{N})}^{f_1}(j\omega)}\\ \lambda_{i,i+1}^{f_2}(j\omega)&=\frac{Y_i^{f_2}(j\omega)}{Y_{i+1}^{f_2}(j\omega)}\neq\frac{Y_{(i,1)}^{f_2}(j\omega)}{Y_{(i+1,1)}^{f_2}(j\omega)}\neq\frac{Y_{(i,2)}^{f_2}(j\omega)}{Y_{(i+1,2)}^{f_2}(j\omega)}\neq\cdots\neq\frac{Y_{(i,\bar{N})}^{f_2}(j\omega)}{Y_{(i+1,\bar{N})}^{f_2}(j\omega)}\end{aligned} \tag{3-84}$$

The transmissibility functions are associated with nonlinear restoring forces which could be changeable under different loading conditions. Therefore,

$$\lambda_{i,i+1}^{f_1}(j\omega)\neq\lambda_{i,i+1}^{f_2}(j\omega) \tag{3-85}$$

Through the above-mentioned analysis, the following conclusions can be derived.

3.3.6.1 When analyzed frequency $\omega\in[a,b]$ (within the range [a, b])

1) If $J\le L_1$,then the Output-based transmissibility between two consecutive masses ($1\le i\le J-1$ and $L_{\bar{L}}\le i<n$), the following relationship holds

$$\lambda_{i,i+1}^{f_1}(j\omega)=\lambda_{i,i+1}^{f_2}(j\omega) \tag{3-86}$$

The proof of (3-86) is demonstrated in the following.
Proof:

When analyzed frequency $\omega \in [a,b]$, from equation(3-34), it is easy to obtain the following relationship

$$\lambda_{1,2}^{1}(j\omega) = \lambda_{1,2}^{2}(j\omega) = \cdots = \lambda_{1,2}^{\bar{N}}(j\omega) \quad (3\text{-}87)$$

Then substitute (3-87) into equation(3-35), the following relationship can be derived

$$\lambda_{2,3}^{1}(j\omega) = \lambda_{2,3}^{2}(j\omega) = \cdots = \lambda_{2,3}^{\bar{N}}(j\omega) \quad (3\text{-}88)$$

Substitute iteratively until $i = J - 1$ based on the above approach, the same conclusion can be obtained.
Start from another prospective equation(3-42), it is known that

$$\lambda_{n,n-1}^{1}(j\omega) = \lambda_{n,n-1}^{2}(j\omega) = \cdots = \lambda_{n,n-1}^{\bar{N}}(j\omega) \quad (3\text{-}89)$$

Then substitute (3-89) into equation(3-44), the following relationship can be derived

$$\lambda_{n-1,n-2}^{1}(j\omega) = \lambda_{n-1,n-2}^{2}(j\omega) = \cdots = \lambda_{n-1,n-2}^{\bar{N}}(j\omega) \quad (3\text{-}90)$$

Substitute iteratively until $i = L_{\bar{L}} - 1$ based on the above approach, the property of (3-86) can be proved.

2) If $J \le L_1$,then the Output-based transmissibility between two consecutive masses ($J \le i < L_{\bar{L}}$), the following relationship holds

$$\lambda_{i,i+1}^{f_1}(j\omega) \neq \lambda_{i,i+1}^{f_2}(j\omega) \quad (3\text{-}91)$$

Proof:
The transmissibility between mass *J* and mass *J+1* is shown in equation(3-40), take an example of the first order transmissibility

$$\lambda_{J,J+1}^{1}(j\omega)=\left.\frac{k_{J+1}+j\omega c_{J+1}+\dfrac{P_1(U(j\omega))}{G_{(J,1)}(j\omega)U_1(j\omega)}}{-m_J\omega^2+j\omega(c_J+c_{J+1})+k_J+k_{J+1}-(j\omega c_J+k_J\lambda_{J-1,J}^{1})(j\omega)}\right|_{\omega=\omega_1} \tag{3-92}$$

From equation(3-92), it can be known that $\lambda_{J,J+1}^{1}(j\omega)$ not only depends on system physical parameters, but input and output that is closely related to nonlinear components. Also because

$$\frac{P_1(U(j\omega))}{G_{(J,1)}(j\omega)U_1(j\omega)}\neq\frac{P_2(U(j\omega))}{G_{(J,2)}(j\omega)U_2(j\omega)}\cdots\neq\frac{P_{\bar{N}}(U(j\omega))}{G_{(J,\bar{N})}(j\omega)U_{\bar{N}}(j\omega)} \tag{3-93}$$

Therefore, substitute (3-93) into equation(3-40), (3-94) can be obtained

$$\lambda_{J,J+1}^{1}(j\omega)\neq\lambda_{J,J+1}^{2}(j\omega)\neq\cdots\neq\lambda_{J,J+1}^{\bar{N}}(j\omega) \tag{3-94}$$

From another prospective, the transmissibility between mass $L_{\bar{L}}$ and mass $L_{\bar{L}}-1$ is shown in equation(3-46), due to the existence of nonlinear component in the express and

$$\frac{P_1(NonF_{L_{\bar{L}}}(j\omega))}{G_{(L_{\bar{L}}-1,1)}(j\omega)U_1(j\omega)}\neq\frac{P_2(NonF_{L_{\bar{L}}}(j\omega))}{G_{(L_{\bar{L}}-1,2)}(j\omega)U_2(j\omega)}\neq\cdots\neq\frac{P_{\bar{N}}(NonF_{L_{\bar{L}}}(j\omega))}{G_{(L_{\bar{L}}-1,\bar{N})}(j\omega)U_{\bar{N}}(j\omega)} \tag{3-95}$$

Hence, (3-96) can be proved

$$\lambda_{L_{\bar{L}},L_{\bar{L}}-1}^{1}(j\omega)\neq\lambda_{L_{\bar{L}},L_{\bar{L}}-1}^{2}(j\omega)\neq\cdots\neq\lambda_{L_{\bar{L}},L_{\bar{L}}-1}^{\bar{N}}(j\omega) \tag{3-96}$$

Until here, property of (3-91) has been proved.

3) If $L_1\le J\le L_{\bar{L}}$,then the Output-based transmissibility between two consecutive masses ($1\le i<L_1-1$ and $L_{\bar{L}}\le i<n$), the following relationship holds

$$\lambda_{i,i+1}^{f_1}(j\omega)=\lambda_{i,i+1}^{f_2}(j\omega) \tag{3-97}$$

4) If $L_1 \le J \le L_{\bar{L}}$,then the Output-based transmissibility between two consecutive masses ($L_1 - 1 \le i < L_{\bar{L}}$), the following relationship holds

$\lambda_{i,i+1}^{f_1}(j\omega) \ne \lambda_{i,i+1}^{f_2}(j\omega)$	(3-98)

Proof:

The similar proof process as the previous proofs has been demonstrated here, when analyzed frequency $\omega \in [a,b]$, from equation(3-34), the relationship (3-87) is obtained.

Then substitute (3-87) into equation(3-35), the relationship (3-88) can be derived. Substitute iteratively until $i = L_1 - 1$ based on the above approach, the same conclusion can be obtained.
Start from another prospective equation(3-42), the relationship (3-89) is obtained.

Then substitute (3-89) into equation(3-44), the relationship (3-90) can be derived. Substitute iteratively until $i = L_{\bar{L}} - 1$ based on the above approach, the property of (3-86) and (3-98) can be proved.
The following properties can be proved in a similar here, and the details are neglected here.

5) If $J \ge L_{\bar{L}}$,then the Output-based transmissibility between two consecutive masses ($1 \le i < L_1 - 1$ and $J \le i < n$), the following relationship holds

$\lambda_{i,i+1}^{f_1}(j\omega) = \lambda_{i,i+1}^{f_2}(j\omega)$	(3-99)

6) If $J \ge L_{\bar{L}}$,then the Output-based transmissibility functions between two consecutive masses ($L_1 - 1 \le i < J$), the following relationship holds

$\lambda_{i,i+1}^{f_1}(j\omega) \ne \lambda_{i,i+1}^{f_2}(j\omega)$	(3-

	100)

3.3.6.2 When analyzed frequency $\omega \notin [a,b]$ *(out of the range [a, b])*

1) For the transmissibility functions between two consecutive masses ($1 \le i < L_1 - 1$ and $L_{\bar{L}} \le i < n$), the following relationship holds

$\lambda_{i,i+1}^{f_1}(j\omega) = \lambda_{i,i+1}^{f_2}(j\omega)$	(3-101)

2) For the transmissibility functions between two consecutive masses ($L_1 - 1 \le i < L_{\bar{L}}$), the following relationship holds

$\lambda_{i,i+1}^{f_1}(j\omega) \neq \lambda_{i,i+1}^{f_2}(j\omega)$	(3-102)

Similarly, the following relationships for transmissibility functions based on NOFRFs of MDOF system with multiple nonlinear components can be established.

3) For the NOFRF-based transmissibility between two consecutive masses ($1 \le i < L_1 - 1$ and $L_{\bar{L}} \le i < n$), the following relationship holds

$\lambda_{i,i+1}^{f_1}(j\omega) = \lambda_{i,i+1}^{f_2}(j\omega)$	(3-103)

4) For the NOFRF-based transmissibility between two consecutive masses ($L_1 - 1 \le i < L_{\bar{L}}$), the following relationship holds

$\lambda_{i,i+1}^{f_1}(j\omega) \neq \lambda_{i,i+1}^{f_2}(j\omega)$	(3-104)

Through the transmissibility function analysis under general input for MDOF system with single or multiple nonlinear components, the following steps are concluded for recognizing nonlinear components.

3.3.6.3 CASE 1: Damage identification if there is only one nonlinear component

It has been concluded that only linear output frequency range $\omega \in [a,b]$ could be a useful choice for calculating transmissibility functions when only one nonlinear component exists in the system.

Step 1: Two single forces with the same bandlimited frequency range [a, b] can be loaded at one mass separately, which contains different excitation intensity. f_1, f_2

Because in the expression of transmissibility in Equations(3-44)-(3-45), outputs are included which significantly rely on input in terms of the nonlinear MDOF system. Hence, outputs under two different excitation intensities could be various.

Step 2: Calculate Output-based transmissibility function for each pair of consecutive masses.

$$\lambda_{i,i+1}^{f_1}(j\omega) = \frac{Y_i^{f_1}(j\omega)}{Y_{i+1}^{f_1}(j\omega)}$$
$$\lambda_{i,i+1}^{f_2}(j\omega) = \frac{Y_i^{f_2}(j\omega)}{Y_{i+1}^{f_2}(j\omega)} \quad (3\text{-}105)$$

Step 3: Calculate the damage index (Difference between $\lambda_{i,i+1}^{f_1}(j\omega)$ and $\lambda_{i,i+1}^{f_2}(j\omega)$)

$$DI_{i,i+1} = \int_{\omega_1}^{\omega_2} \left| \lambda_{i,i+1}^{f_1}(j\omega) - \lambda_{i,i+1}^{f_2}(j\omega) \right| d\omega \quad (3\text{-}106)$$

Where $a \le \omega_1 \le \omega_2 \le b$

Step 4: According to relationship of nonzero values of *DI* and force location, localize the nonlinear component by referring to the properties

[Equations(3-86)-(3-100)]. The boundary of force and nonlinear component could be found.

3.3.6.4 CASE 2: Damage identification if there are multiple nonlinear components under single point input

For this situation, it is necessary to choose nonlinear output frequency range $\omega \notin [a,b]$.

Step 1: Two single forces with the same bandlimited frequency range [a, b] can be loaded at one mass separately, which contains different excitation intensities. f_1, f_2

Step 2: Calculate Output-based transmissibility function for each pair of consecutive masses.

$$\lambda_{i,i+1}^{f_1}(j\omega) = \frac{Y_i^{f_1}(j\omega)}{Y_{i+1}^{f_1}(j\omega)}$$
$$\lambda_{i,i+1}^{f_2}(j\omega) = \frac{Y_i^{f_2}(j\omega)}{Y_{i+1}^{f_2}(j\omega)} \quad (3\text{-}107)$$

Step 3: Calculate the damage index (Difference between $\lambda_{i,i+1}^{f_1}(j\omega)$ and $\lambda_{i,i+1}^{f_2}(j\omega)$)

$$DI_{i,i+1} = \int_{\omega_1}^{\omega_2} \left| \lambda_{i,i+1}^{f_1}(j\omega) - \lambda_{i,i+1}^{f_2}(j\omega) \right| d\omega \quad (3\text{-}108)$$

Where $\omega_1 \le \omega_2$ and $\omega_1 \notin [a,b], \omega_2 \notin [a,b]$

Step 4: According to relationship of nonzero values of *DI* and, localize the nonlinear components by referring to properties [Equations(3-101)-(3-104)]. The area of nonlinear components could be found.

3.3.6.5 CASE 3: Damage identification if there are multiple nonlinear components under multiple-point input

More complicated situation that under multiple-point loading is considered here, the detailed analyzed process is demonstrated as follows.

Starting from MDOF system, $\boldsymbol{M}$, $\boldsymbol{C}$, $\boldsymbol{K}$, $\boldsymbol{F}$ and $\boldsymbol{y}$ are the system mass matrix, damping matrix, stiffness matrix, force vector and response displacement vector respectively.

$$\boldsymbol{M}=\begin{bmatrix} m_1 & 0 & \cdots & 0 \\ 0 & m_2 & \cdots & 0 \\ \vdots & \vdots & \ddots & \vdots \\ 0 & 0 & 0 & m_n \end{bmatrix}$$

$$\boldsymbol{C}=\begin{bmatrix} c_1+c_2 & -c_2 & 0 & \cdots & 0 \\ -c_2 & c_2+c_3 & -c_3 & \ddots & \vdots \\ 0 & \ddots & \ddots & \ddots & \vdots \\ \vdots & \ddots & -c_{n-1} & c_{n-1}+c_n & -c_n \\ 0 & 0 & 0 & -c_n & c_n \end{bmatrix} \tag{3-109}$$

$$\boldsymbol{K}=\begin{bmatrix} k_1+k_2 & -k_2 & 0 & \cdots & 0 \\ -k_2 & k_2+k_3 & -k_3 & \ddots & \vdots \\ 0 & \ddots & \ddots & \ddots & \vdots \\ \vdots & \ddots & -k_{n-1} & k_{n-1}+k_n & -k_n \\ 0 & 0 & 0 & -k_n & k_n \end{bmatrix}$$

$$\boldsymbol{F}(t)=\begin{bmatrix} u_1(t) & \cdots & u_n(t) \end{bmatrix}^T$$

Therefore, the moving equation of nonlinear MDOF system is defined as

$$\boldsymbol{M}\ddot{\boldsymbol{y}}(t)+\boldsymbol{C}\dot{\boldsymbol{y}}(t)+\boldsymbol{K}\boldsymbol{y}(t)=\boldsymbol{F}(t)+\boldsymbol{N}\boldsymbol{F}(t) \tag{3-110}$$

Here, *F(t)* contains multiple-point loadings u_1, u_2, …, u_n. *NF(t)* is nonlinear force matrix reckoned as the same as equation(3-18). Suppose all the inputs have the same frequency band *[a, b]*, that is

$Ui(j\omega)\begin{cases}\neq 0 & \omega\in[a,b]\\ =0 & \omega\notin[a,b]\end{cases}$ $i=1, 2, \ldots, n$	(3-111)

Starting from the first row of the new system matrix(3-110)

$m_1\ddot{y}_1(t)+(c_1+c_2)\dot{y}_1(t)-c_2\dot{y}_2(t)+(k_1+k_2)y_1(t)-k_2y_2(t)=u_1(t)$	(3-112)

The Output-based transmissibility function $\lambda_{1,2}(j\omega)$ can be calculated

$\lambda_{1,2}(j\omega)=\dfrac{k_2+j\omega c_2+\dfrac{U1(j\omega)}{Y_2(j\omega)}}{-m_1\omega^2+j\omega(c_1+c_2)+k_1+k_2}$	(3-113)

From equation(3-111), it can be known that if $\omega\in[a,b]$, $U1(j\omega)\neq 0$, therefore $\dfrac{U1(j\omega)}{Y_2(j\omega)}\neq 0$, and the value of this term will be changed accordingly if the input (Excitation intensity) has been changed, which means $\dfrac{U1^1(j\omega)}{Y_2^1(j\omega)}\neq\dfrac{U1^2(j\omega)}{Y_2^2(j\omega)}$. Therefore, $\lambda_{1,2}^{f_1}(j\omega)\neq\lambda_{1,2}^{f_2}(j\omega)$, which is different with the case under single point excitation.

if $\omega\notin[a,b]$, $U1(j\omega)=0$, so $\dfrac{U1(j\omega)}{Y_2(j\omega)}=0$. Therefore, $\lambda_{1,2}^{f_1}(j\omega)=\lambda_{1,2}^{f_2}(j\omega)$. In this case, the same conclusion could be obtained as the one under single point excitation.

The analyzed process is the same for NOFRF-based transmissibility, due to the fact that

$$\lambda_{1,2}(j\omega)=\frac{k_2+j\omega c_2+\dfrac{U1(j\omega)}{Y_2(j\omega)}}{-m_1\omega^2+j\omega(c_1+c_2)+k_1+k_2}=\frac{k_2+j\omega c_2+\dfrac{U1(j\omega)}{\sum_{i=1}^{\bar{N}}G_i(j\omega)U_i(j\omega)}}{-m_1\omega^2+j\omega(c_1+c_2)+k_1+k_2} \quad (3\text{-}114)$$

For the masses which are not connected to the nonlinear components.
$(r<\min(L_i-1,L_i,J)$ or $r>\max(L_i-1,L_i,J),i=1,...,\bar{L})$

$$\lambda_{r,r+1}(j\omega)=\frac{k_{r+1}+j\omega c_{r+1}+\dfrac{Ur(j\omega)}{Y_{r+1}(j\omega)}}{-m_r\omega^2+j\omega(c_r+c_{r+1})+k_r+k_{r+1}-(j\omega c_r+k_r\lambda^1_{r-1,r})(j\omega)} \quad (3\text{-}115)$$

If $\omega\in[a,b]$, $Ur(j\omega)\neq 0$. Therefore, $\dfrac{Ur^1(j\omega)}{Y^1_{r+1}(j\omega)}\neq\dfrac{Ur^2(j\omega)}{Y^2_{r+1}(j\omega)}$, and $\lambda^1_{r,r+1}(j\omega)\neq\lambda^2_{r,r+1}(j\omega)$.

if $\omega\notin[a,b]$, $Ur(j\omega)=0$. Therefore, $\dfrac{Ur^1(j\omega)}{Y^1_{r+1}(j\omega)}\neq\dfrac{Ur^2(j\omega)}{Y^2_{r+1}(j\omega)}$ and $\lambda^1_{r,r+1}(j\omega)=\lambda^2_{r,r+1}(j\omega)$, which is the same conclusion as the one under single point excitation.

For the masses which are connected to the nonlinear components, it can obtain the same conclusion as previous deduction.

Through this deduction, it indicates that the transmissibility functions under multiple points excitation will be the same compared to the situation under single point excitation when the analyzed frequency is belonging to nonlinear output frequency range, that is $\omega\notin[a,b]$. In other words, when $\omega\in[a,b]$, there is no feasible regular conclusion for damage detection, only when $\omega\notin[a,b]$, multiple nonlinear damages could be found.

Therefore, the detailed steps are given here

Step 1: Two single forces with the same bandlimited frequency range [a, b] can be loaded at one mass separately, which contains different excitation intensities. f_1, f_2

Step 2: Calculate Output-based transmissibility function for each pair of consecutive masses.

$$\lambda_{i,i+1}^{f_1}(j\omega) = \frac{Y_i^{f_1}(j\omega)}{Y_{i+1}^{f_1}(j\omega)}$$

$$\lambda_{i,i+1}^{f_2}(j\omega) = \frac{Y_i^{f_2}(j\omega)}{Y_{i+1}^{f_2}(j\omega)}$$

Step 3: Calculate the damage index (Difference between $\lambda_{i,i+1}^{f_1}(j\omega)$ and $\lambda_{i,i+1}^{f_2}(j\omega)$)

$$DI_{i,i+1} = \int_{\omega_1}^{\omega_2} \left| \lambda_{i,i+1}^{f_1}(j\omega) - \lambda_{i,i+1}^{f_2}(j\omega) \right| d\omega$$

Where $\omega_1 \le \omega_2$ and $\omega_1 \notin [a,b], \omega_2 \notin [a,b]$

Step 4: According to relationship of nonzero values of *DI* and, localize the nonlinear components by referring to properties [Equations(3-101)-(3-104)]. The area of nonlinear components could be found.

3.3.7 Effect of boundary conditions

The proposed theory is based on MDOF system, that means changes of boundary conditions do not change the obtained conclusions. Here illustrates an example of changing the system under fixed-fixed boundary condition shown in Fig. 3-3 into fixed-free shown in Fig. 3-4.

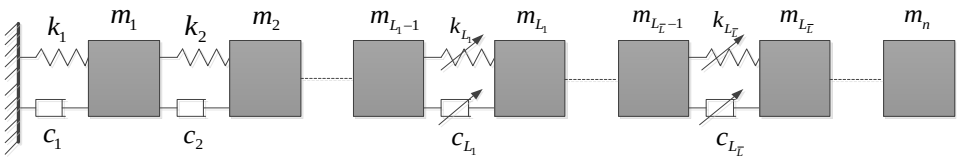

Fig. 3-4 Fixed-free MDOF nonlinear system

According to the new MDOF nonlinear system, it can be found subtle changes occur into the stiffness matrix and damping matrix by using k_n and c_n instead of $k_n + k_{n+1}$ and $c_n + c_{n+1}$ in the (2n, 2n)th element of K and C in the system(3-14) respectively.

$$\boldsymbol{M} = \begin{bmatrix} m_1 & 0 & \cdots & 0 \\ 0 & m_2 & \cdots & 0 \\ \vdots & \vdots & \ddots & \vdots \\ 0 & 0 & 0 & m_n \end{bmatrix}$$

$$\boldsymbol{C} = \begin{bmatrix} c_1 + c_2 & -c_2 & 0 & \cdots & 0 \\ -c_2 & c_2 + c_3 & -c_3 & \ddots & \vdots \\ 0 & \ddots & \ddots & \ddots & \vdots \\ \vdots & \ddots & -c_{n-1} & c_{n-1} + c_n & -c_n \\ 0 & 0 & 0 & -c_n & c_n \end{bmatrix}$$

$$\boldsymbol{K} = \begin{bmatrix} k_1 + k_2 & -k_2 & 0 & \cdots & 0 \\ -k_2 & k_2 + k_3 & -k_3 & \ddots & \vdots \\ 0 & \ddots & \ddots & \ddots & \vdots \\ \vdots & \ddots & -k_{n-1} & k_{n-1} + k_n & -k_n \\ 0 & 0 & 0 & -k_n & k_n \end{bmatrix}$$

That means let $k_{n+1} = 0$ and $c_{n+1} = 0$ in the equation(3-42), which doesn't make a change for the conclusions. Similarly, the boundary conditions could be changed into free-free.

3.3.8 Simulation study

In order to validate the proposed methodology, a 10 DOFs Mass-spring-damper system has been simulated and coded in Software Matlab® shown in Fig. 3-5. Damping is assumed to be proportional damping, e.g., $C=uK$

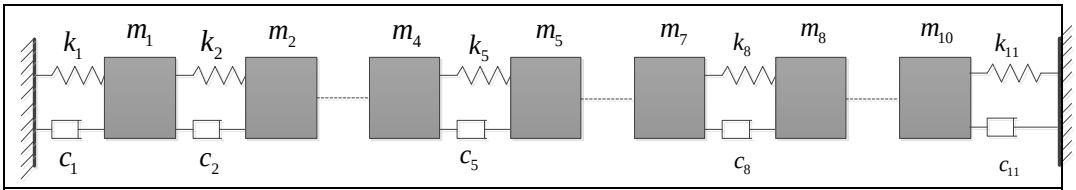

In order to validate the proposed methodology, a 10 DOFs Mass-spring-damper system has been simulated and coded in Software Matlab® shown in Fig. 3-5 10DOFs mass-spring-damper system

The detailed parameters are set as follows:

$m_1 = m_2 = ... = m_{10} = 1$

$k_1 = k_2 = k_3 = k_4 = k_5 = k_{10} = 3.6\times10^4$

$k_6 = k_7 = k_8 = 0.8k_1$

$k_9 = 0.9k_1$

$\mu = 0.01$

$C = \mu K$

And N=3 in equation(3-15)

$\alpha_{(L_i,2)} = 0.8k_1^2$

$\alpha_{(L_i,3)} = 0.4k_1^3$

$\beta_{(L_i,2)} = 0$

$\beta_{(L_i,3)} = 0$

Where $i = 1,2,...,\bar{L}$, $\bar{L}$ is the number of nonlinear components in the system.

In order to generate bandlimited input, the expression of input signal is given here:

$$u(t) = \frac{3\cdot(\sin(2\pi 10t) - \sin(2\pi 7t))}{2\pi t} \quad (3\text{-}116)$$

In equation(3-116), a bandlimited input signal has been generated as [7, 10Hz], with sampling frequency 100Hz and acquired time 100s, the time history and it spectrum are shown in Fig. 3-6 and Fig. 3-7. The input that considers when t<0 is to construct a better spectra, containing even energy at each frequency bin.

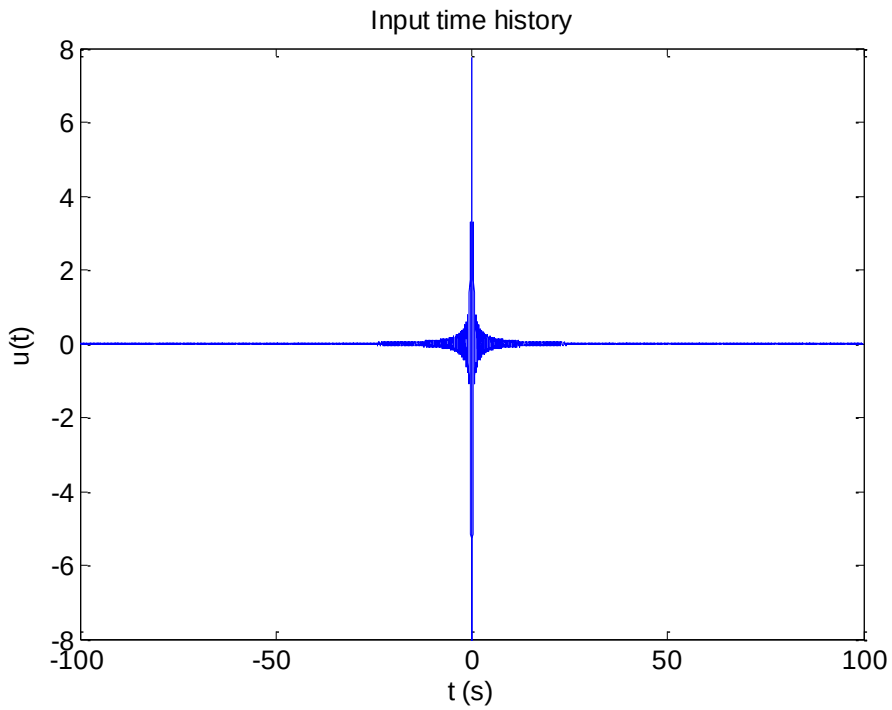

Fig. 3-6 Time history of the general input

.

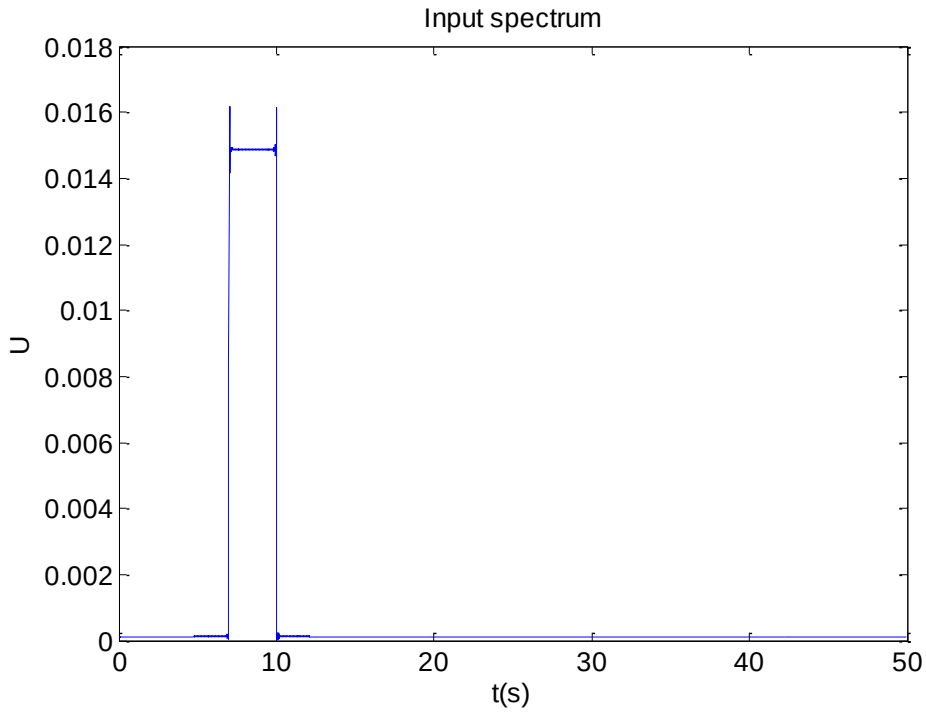

Fig. 3-7 The spectrum of the general input

3.3.8.1 Case study 1: one nonlinear component under single point loading

Loading position J=2

Number of nonlinear components $\bar{L}=1$ and the spring is considered to be nonlinear that $L_1=6$ (between mass 5 and mass 6)

When the system is linear, the output of the system can be obtained by using a fifth order Runge–Kutta simulation method, and the response is shown in Fig. 3-8.

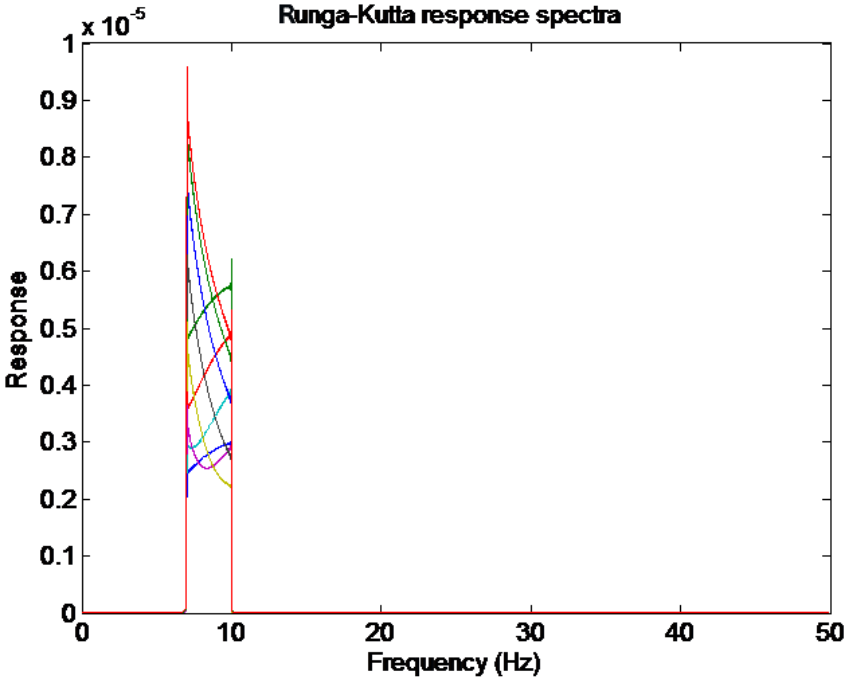

Fig. 3-8 Response spectra of 10-DOF linear system

From observing the results of Fig. 3-8, it is clear that the output frequency range is the same as the general input which is from 7Hz to 10Hz, because of linear system.
Following the process of single nonlinear component identification demonstrated in the section 3.3.6.3.

Step 1: Two single forces with the same bandlimited frequency range [7, 10Hz] can be loaded at one mass separately, which contains different excitation intensity. Here $f_1 = 1, f_2 = 10$

Considering adding the nonlinear component described in aforementioned parameters, the output in frequency domain can be obtained in Fig. 3-9 and Fig. 3-10 (in logarithms) when the excitation level is 10.
Compared to Fig. 3-8, the spectra of output transfer some energy from [7, 10Hz] into lower frequency [0, 7Hz], and into some higher frequency [10, 20Hz].

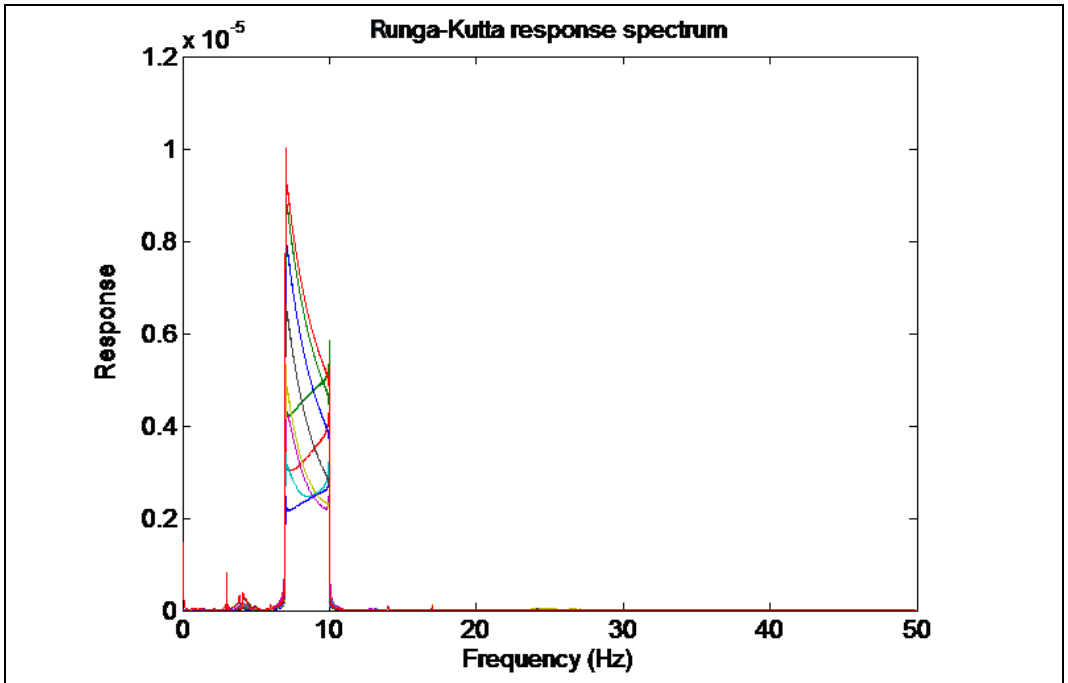

Fig. 3-9 Response spectra of 10-DOF nonlinear system

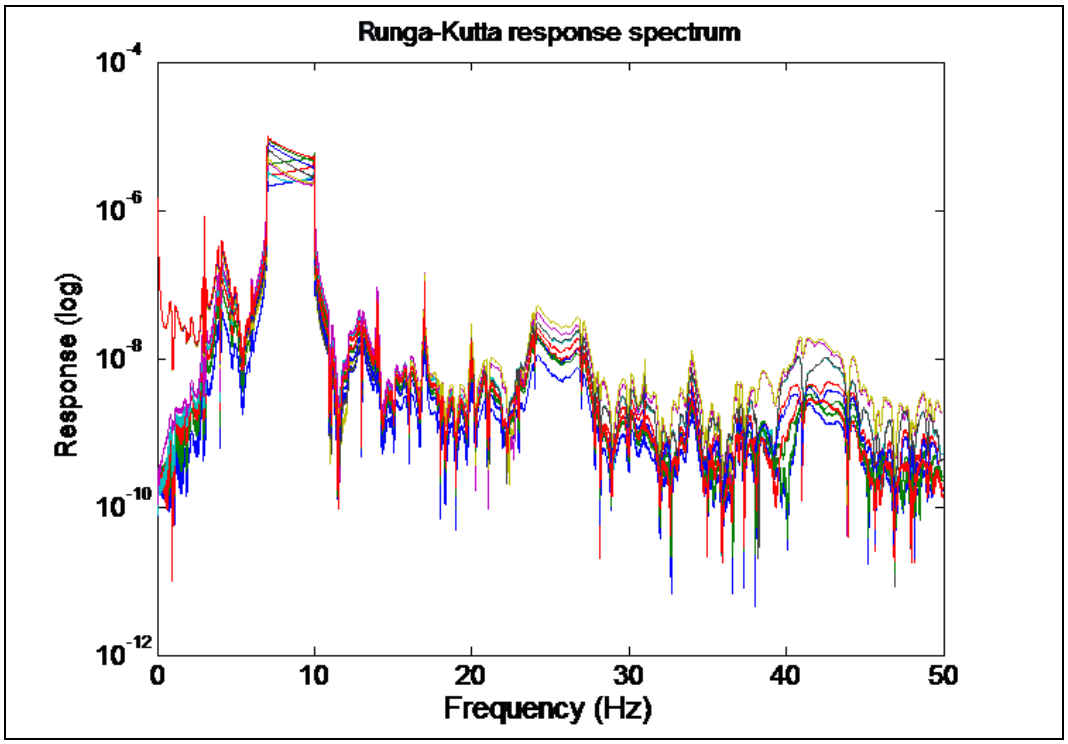

Fig. 3-10 Response spectra of 10-DOF nonlinear system

Step 2: Calculate Output-based transmissibility function for each pair of consecutive masses.

$$\lambda_{i,i+1}^{f_1}(j\omega)=\frac{Y_i^{f_1}(j\omega)}{Y_{i+1}^{f_1}(j\omega)}$$

$$\lambda_{i,i+1}^{f_2}(j\omega)=\frac{Y_i^{f_2}(j\omega)}{Y_{i+1}^{f_2}(j\omega)}$$

And the corresponding transmissibility functions between two consecutive masses under two different excitation levels could be obtained shown in Fig. 3-11-Fig. 3-19.

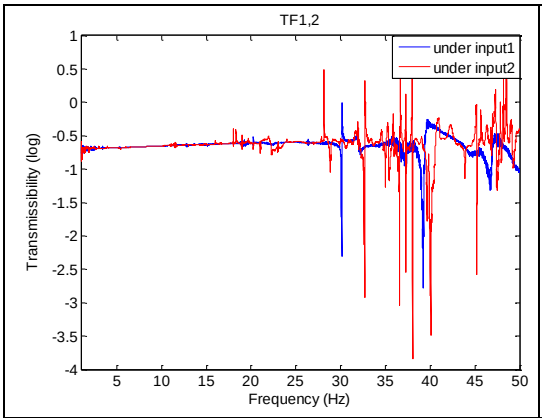

Fig. 3-11 TF between mass1 and mass2

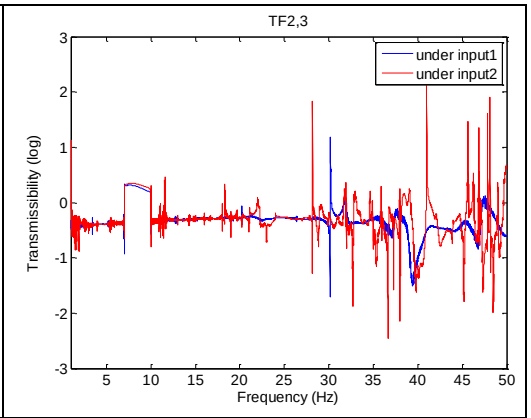

Fig. 3-12 TF between mass2 and mass3

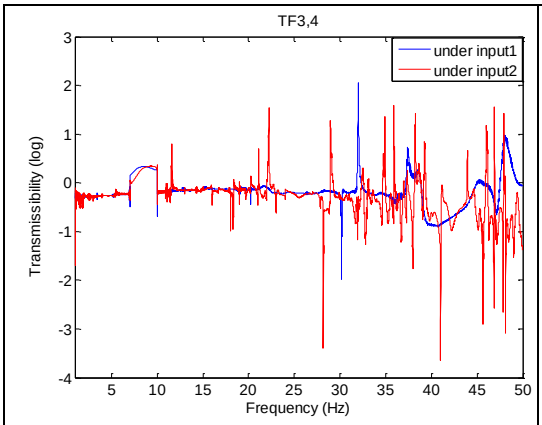

Fig. 3-13 TF
between mass3 and mass4

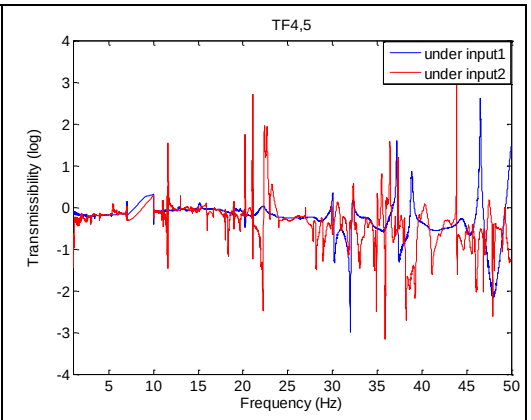

Fig. 3-14 TF
between mass4 and mass5

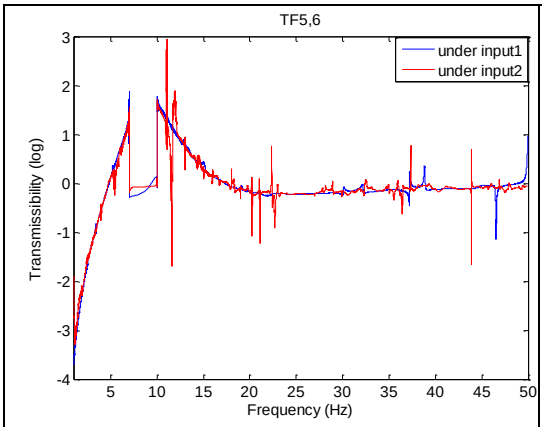

Fig. 3-15 TF
between mass5 and mass6

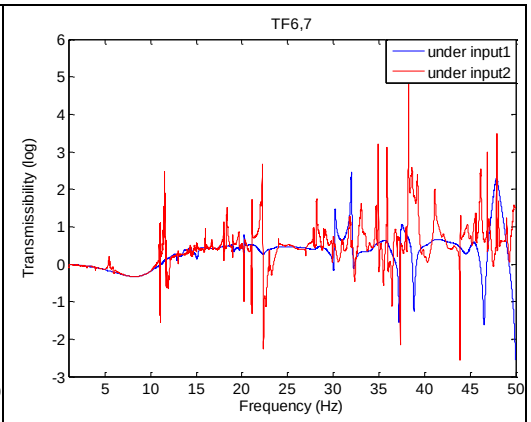

Fig. 3-16 TF
between mass6 and mass7

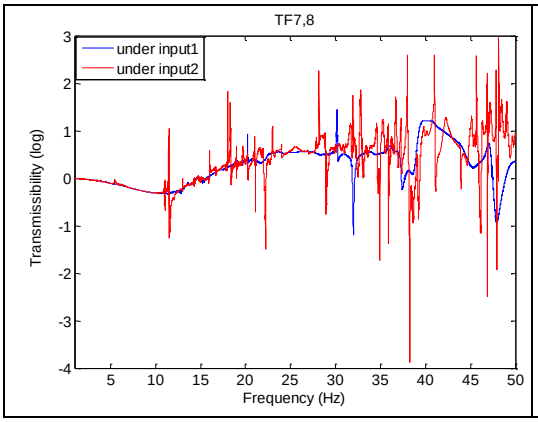

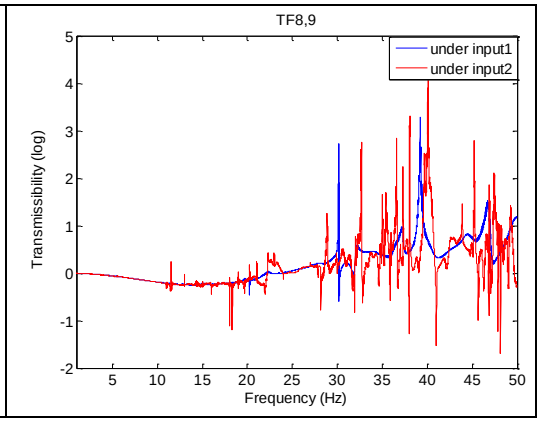

Fig. 3-17 TF between mass7 and mass8	Fig. 3-18 TF between mass8 and mass9

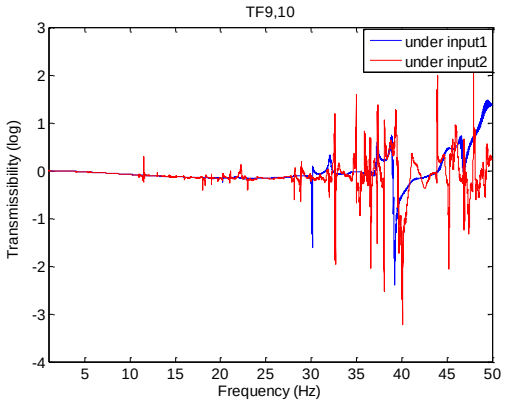

Fig. 3-19 TF
between mass9 and mass10

Step 3: Calculate the damage index (Difference between $\lambda_{i,i+1}^{f_1}(j\omega)$ and $\lambda_{i,i+1}^{f_2}(j\omega)$)

$$DI_{i,i+1} = \int_{\omega_1}^{\omega_2} \left| \lambda_{i,i+1}^{f_1}(j\omega) - \lambda_{i,i+1}^{f_2}(j\omega) \right| d\omega$$

Where $7Hz \le \omega_1 \le \omega_2 \le 10Hz$

Damage index is shown in Fig. 3-20.

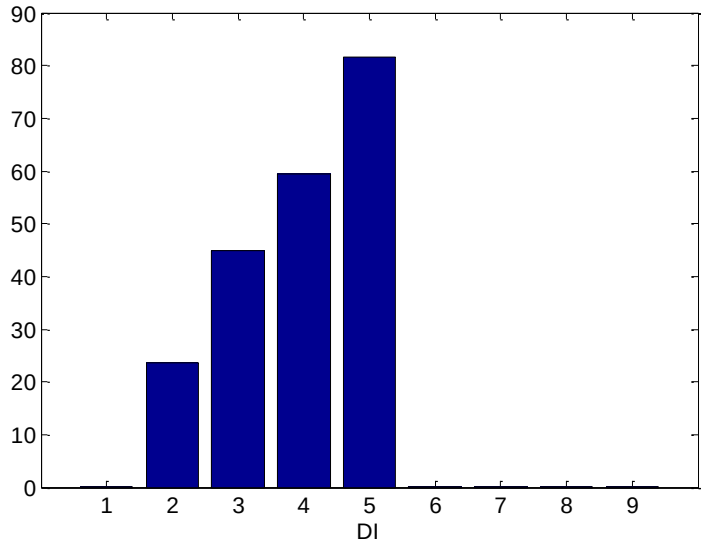

Fig. 3-20 Damage index of [7, 10Hz]

Considering changing the frequency band into [8, 9Hz], the same damage index result should be obtained due to the reason that [8, 9Hz] is belong to the frequency range [7, 10Hz], which is shown in Fig. 3-21.

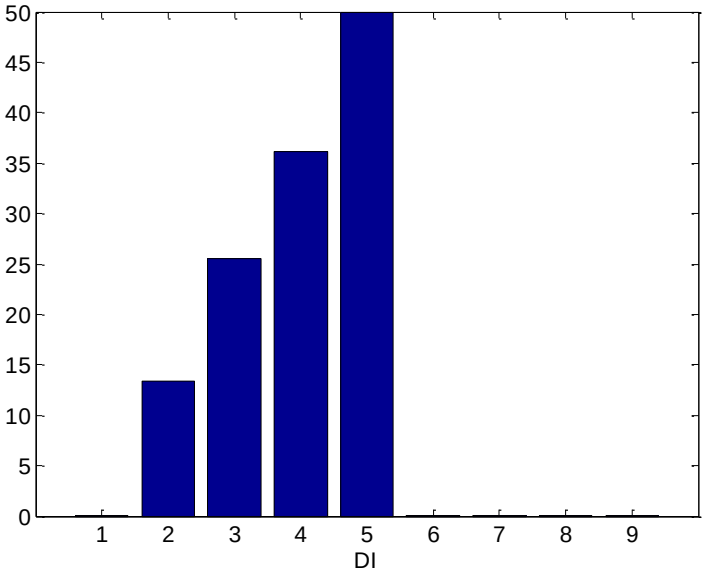

Fig. 3-21 Damage index of [8, 9Hz]

If the frequency ranges outside [7, 10Hz] has been taken into consider, such as [1, 3Hz] and [12, 15Hz], the results are shown in the Fig. 3-22 and Fig. 3-23.

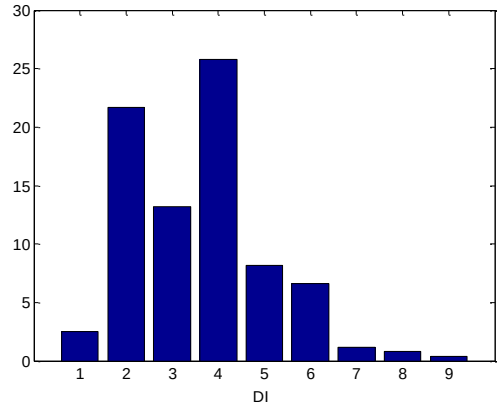

Fig. 3-22 Damage index of [1, 3Hz]

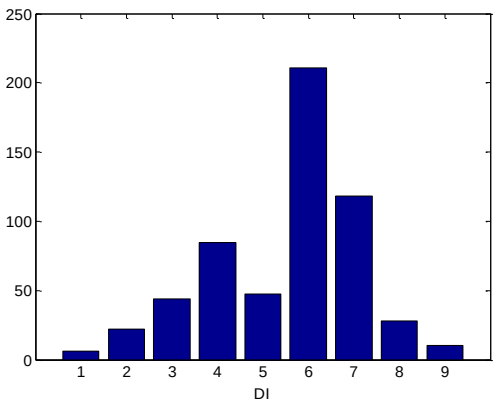

Fig. 3-23 Damage index of [12, 15Hz]

Step 4: According to relationship of nonzero values of *DI* and force location, localize the nonlinear component by referring to the properties [Equations(3-86)-(3-100)]. The boundary of force and nonlinear component could be found.

As the location of loading J=2 is already known, then using the conclusion of (3-86), it is known that the DIs will not be zeros for the area [J, L_1-1], since J=2, and L_1-1 can be read from Fig. 3-20 or Fig. 3-21, that is 5. Therefore, L_1=5+1=6, which is accordance with the description at the beginning. So the only one nonlinear component can be localized between mass5 and mass6.

3.3.8.2 Case study 2: one nonlinear component under single point loading

Loading position J=8

Number of nonlinear components $\bar{L}$ =1 and the spring is considered to be nonlinear that $L_1 = 5$ (between mass 4 and mass 5)

The process of nonlinear damage is the same as the previous damage scenario 3.3.7.1. The detailed procedure is neglected here, only the

identification result is shown in Fig. 3-24 Damage index of [7, 10Hz]. The frequency range [7, 10Hz] is considered in terms of damage indicator.

According to the conclusion (3-99) and (3-100), when the existence of nonzero values for DIs is only belonging to the area $[L_1-1,\ J-1]$. Since the nonzero value boundary can be read from the Fig. 3-24 Damage index of [7, 10Hz]is [4, 7], and location of loading J is already known as $J=8$. Therefore, $L_1-1=4$, and $L_1=5$, that means the nonlinear component is located between mass4 and mass5, which is in accordance with the provided description of damage scenario.

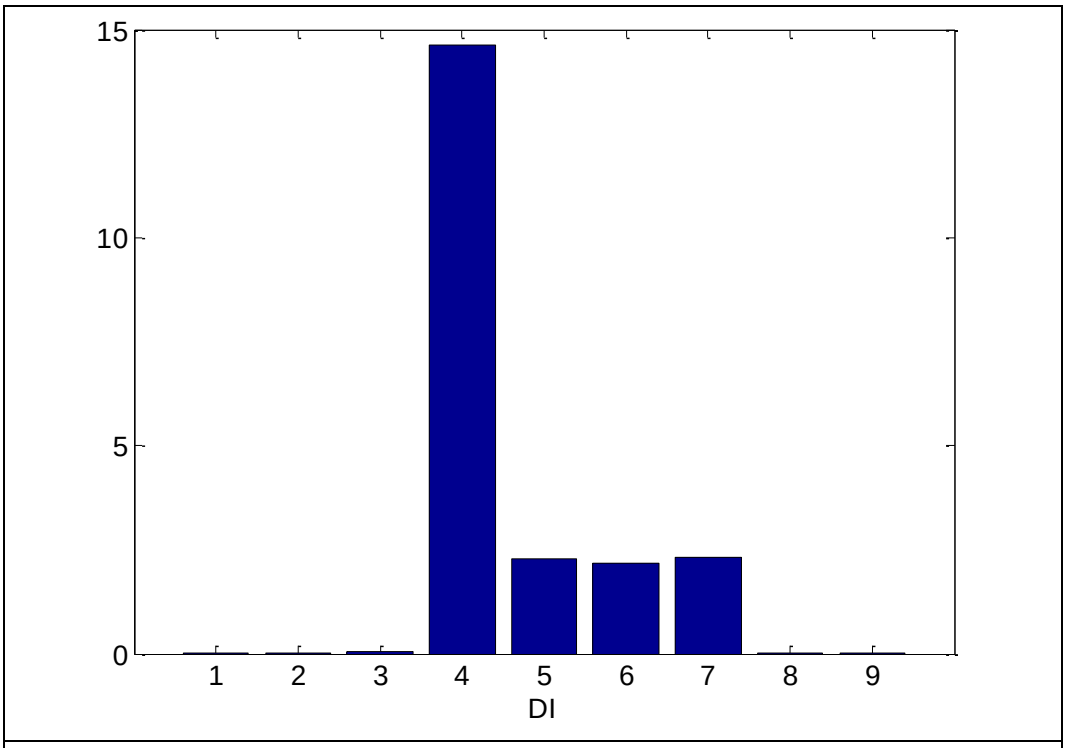

Fig. 3-24 Damage index of [7, 10Hz]

3.3.8.3 Case study 3: multiple nonlinear components under single point loading

Loading position J=2

Number of nonlinear components $\bar{L}$ =2 and the springs are considered to be nonlinear that $L_1 = 6$ (between mass 5 and mass 6) and $L_2 = 9$ (between mass 8 and mass 9).
The number of nonlinear components is more than 1, the damage identification procedure should be followed as the section 3.3.6.4, which is for multiple nonlinear damage identification under single point loading.

For this situation, it is necessary to choose nonlinear output frequency range $\omega \notin [7,10Hz]$.

Step 1: Two single forces with the same bandlimited frequency range [a, b] can be loaded at one mass separately, which contains different excitation intensities. $f_1 = 1, f_2 = 10$

The output spectra of 10-DOF under two different excitation levels are shown in Fig. 3-25 and Fig. 3-26.

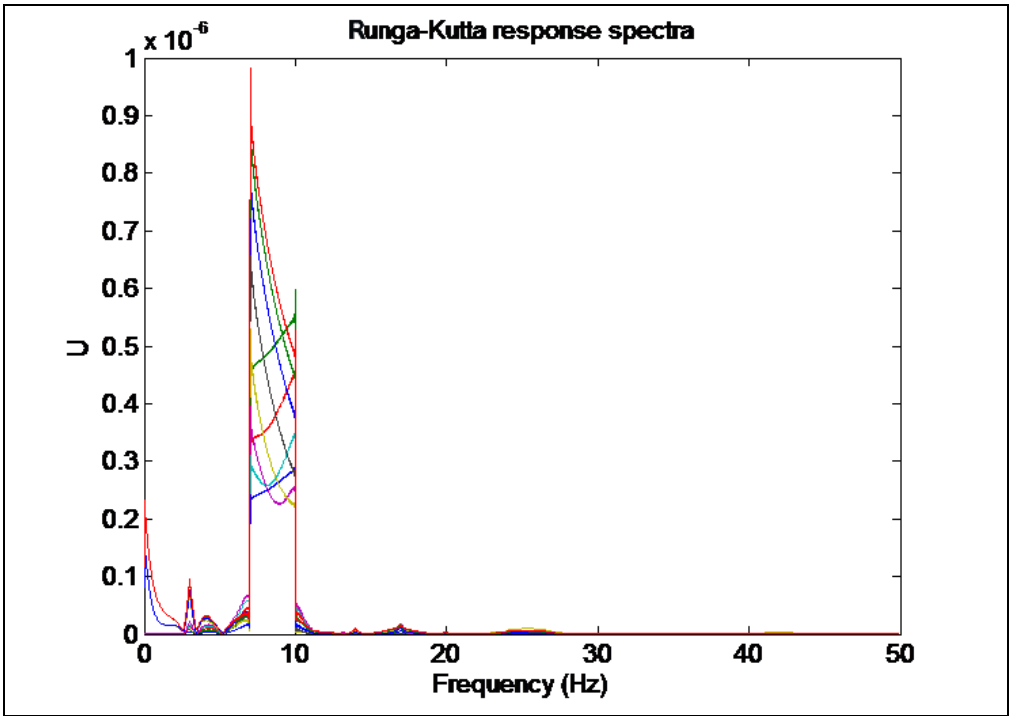

Fig. 3-25 Response spectra of 10-DOF nonlinear system under

excitation f1=1

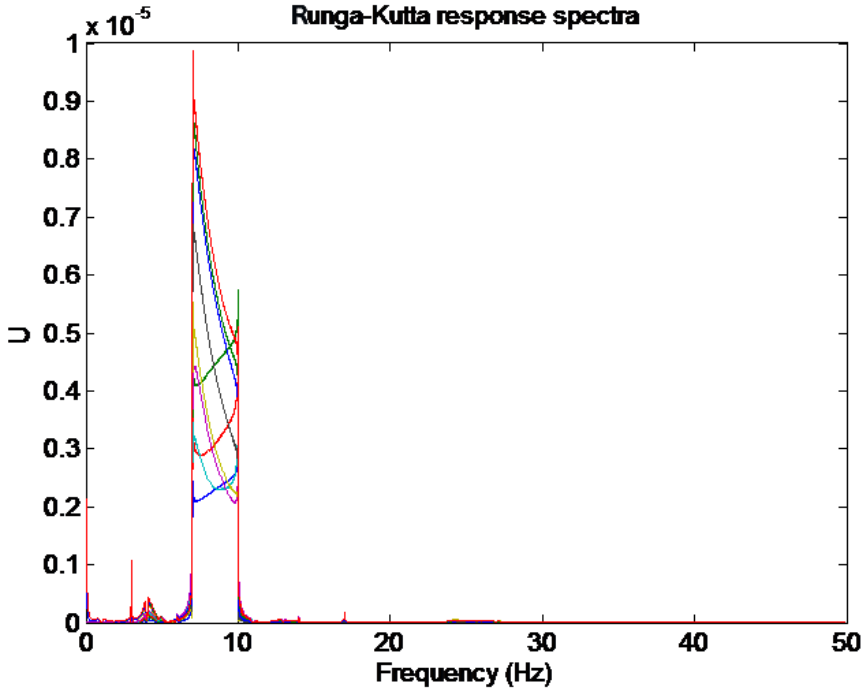

Fig. 3-26 Response spectra of 10-DOF nonlinear system under excitation f2=10

From Fig. 3-25 Response spectra of 10-DOF nonlinear system under excitation f1=1 and Fig. 3-26, it can be observed that part of energy is transferred from [7, 10Hz] into [0, 7Hz] and even [10, 30Hz] due to the existence of nonlinear components.

Step 2: Calculate Output-based transmissibility function for each pair of consecutive masses.

$$\lambda_{i,i+1}^{f_1}(j\omega) = \frac{Y_i^{f_1}(j\omega)}{Y_{i+1}^{f_1}(j\omega)}$$

$$\lambda_{i,i+1}^{f_2}(j\omega) = \frac{Y_i^{f_2}(j\omega)}{Y_{i+1}^{f_2}(j\omega)}$$

Step 3: Calculate the damage index (Difference between

$\lambda_{i,i+1}^{f_1}(j\omega)$ and $\lambda_{i,i+1}^{f_2}(j\omega)$)

$$DI_{i,i+1} = \int_{\omega_1}^{\omega_2} \left| \lambda_{i,i+1}^{f_1}(j\omega) - \lambda_{i,i+1}^{f_2}(j\omega) \right| d\omega \qquad (3\text{-}117)$$

Where $\omega_1 \le \omega_2$ and $\omega_1 \notin [7,10Hz], \omega_2 \notin [7,10Hz]$, here $\omega_1 = 12Hz, \omega_2 = 15Hz$

Here gives a detailed explanation about how to choose the calculated nonlinear frequency range. Because the output values are zeros or very small, which could result in a bigger error when calculating transmissibility between two tiny numbers.

According to the calculation rules of NOFRFs ($G_{i(J)}^{n}(j\omega)$,J=2, n=1,...,N, i=1,..,10) under general input which has been demonstrated in section 3.2.2. In this case only the first four NOFRFs are considered which are $G_{i(J)}^{1}(j\omega)$, $G_{i(J)}^{2}(j\omega)$, $G_{i(J)}^{3}(j\omega)$ and $G_{i(J)}^{4}(j\omega)$ (J=2, i=1,..,10). The condition for satisfying the least square approach, two different loading intensity are applied, which α in equation(3-9) are 1, 1.1, 1.2, 1.3, 1.4 and 1.5, which satisfies the condition of Least Square Calculation(3-11). The output frequency range can be obtained in Table 1 and its calculation process is shown in section3.3.2:

Table 1 Output frequency range for the first four orders

Output under different order NOFRFs	Frequency range
1st	(7Hz, 10Hz)
2nd	(0Hz, 3Hz) ∪ (14Hz, 20Hz)
3rd	(4Hz, 13Hz) ∪ (21Hz, 30Hz)
4th	(0Hz, 6Hz) ∪ (28Hz, 40Hz)

And the first NOFRFs are shown in the Fig. 3-27.

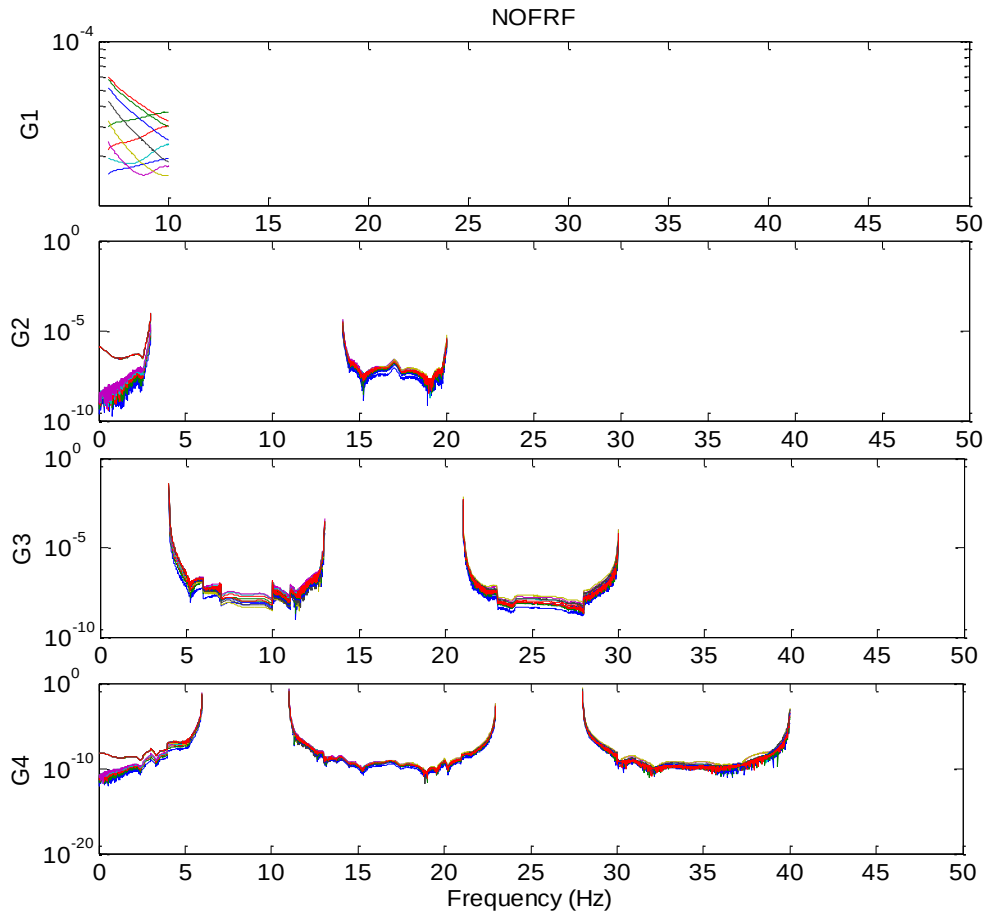

Fig. 3-27 The first four NOFRF functions

In order to evaluate the NOFRFs identification, Fig. 3-28 shows the estimated output spectrum and also the error regarding to the actual output spectrum from Runge–Kutta simulation. From the figure of estimated error, it can be known that the first four NOFRFs are enough to be considered because of the small error.

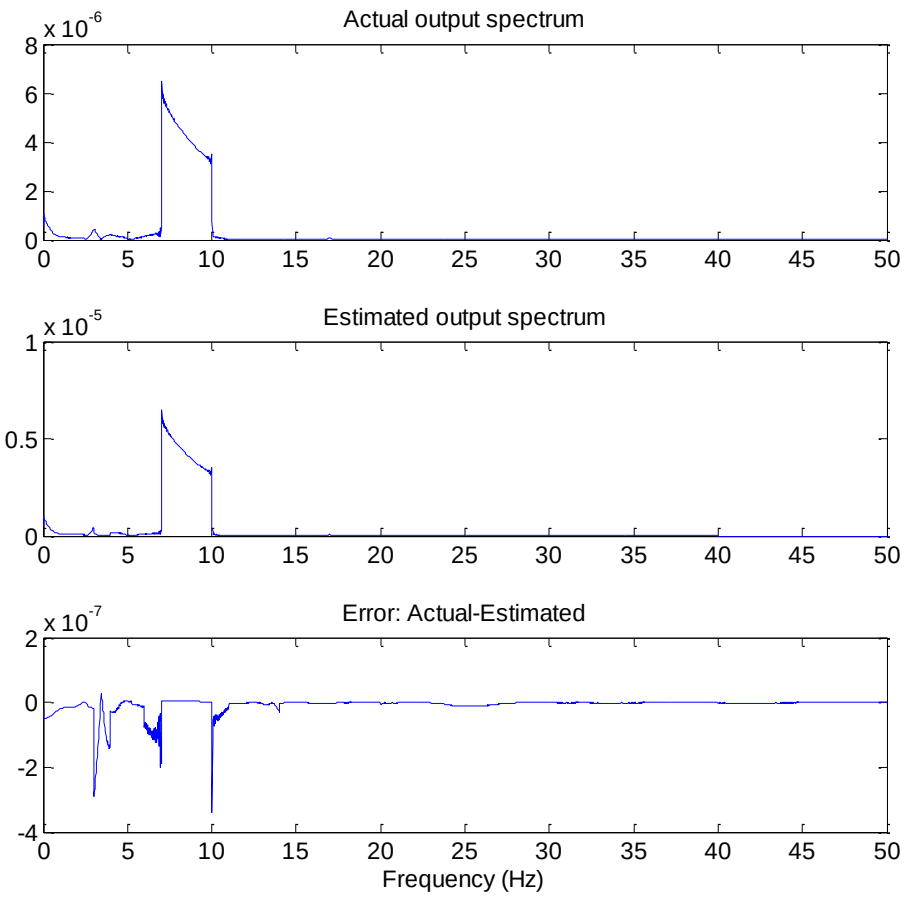

Fig. 3-28 The actual output spectrum, estimated output spectrum and the estimated error

It can be observed from Fig. 3-27 that there are some zero-gap values for each NOFRF due to the reason of the inherent characteristic of output frequency range of nonlinear system.

Therefore, the calculated nonlinear frequency range taken into damage indicator calculation in equation(3-117) should be chosen from [0,7Hz) and (10,40Hz].

Step 4: According to relationship of nonzero values of *DI* and, localize the nonlinear components by referring to properties [Equations(3-101)-

(3-104)]. The area of nonlinear components could be found.

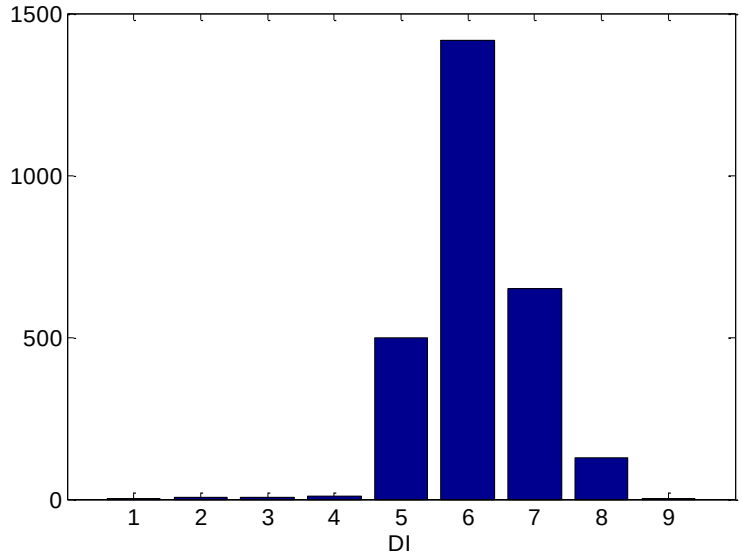

Fig. 3-29 Damage index of [12, 15Hz]

According to the conclusion [Equations(3-101)-(3-104)], the nonzero values of DI should be $L_1 - 1 \le i \le L_{\bar{L}} - 1$ and it doesn't associate with loads for the situation that there are multiple nonlinear components in the system. From Fig. 3-29, the nonlinear components boundary can be read as from DI5 to DI8. Therefore, by matching the result read from Fig. 3-29 and equation(3-101), it is easy to know, L_1=6, $L_2 = 9$.

If considering the frequency range within [7, 10Hz], such as [8, 9Hz], the damage indicator result is shown in Fig. 3-30. It can be observed that the nonlinear components' area is not accordance with the provided condition. Because the calculated frequency range is belonging into the input frequency range, therefore, the nonzero value outcome should be the boundary between the loading and the nonlinear component farthest away from the loading. So, J=2, $L_2 = 9$ is the information extracted from Fig. 3-30, according to conclusion (3-98).

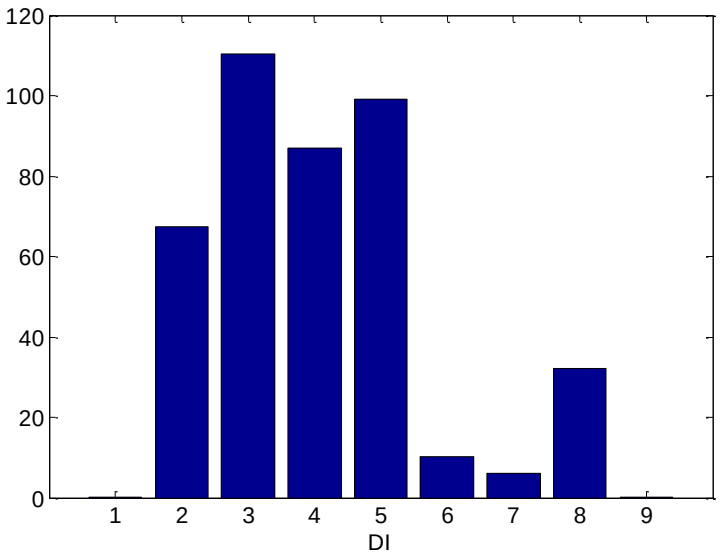

Fig. 3-30 Damage index of [8, 9Hz]

3.3.8.4 Case study 4: multiple nonlinear components under single point loading

Loading position *J*=8
Number of nonlinear components $\bar{L}$ =2 and the springs are considered to be nonlinear that $L_1 = 6$ (between mass 5 and mass 6) and $L_2 = 9$ (between mass 8 and mass 9).

In this case, the only changed condition is loading position from mass2 to mass8. The detailed recognized process is neglected here. Fig. 3-31 shows the identification result with choosing frequency range [12, 14Hz]. The correct nonlinear components' area has been identified which is $L_1 - 1 = 5$, $L_2 - 1 = 8$, therefore, $L_1 = 6$, $L_2 = 9$. It means nonlinear components are located between mass5 and mass8, which is in accordance with the provided description of damage scenario.

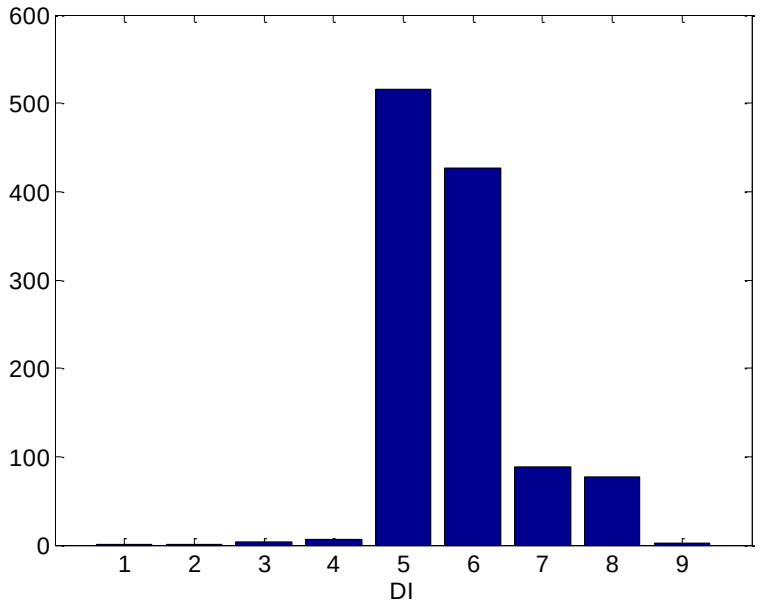

Fig. 3-31 Damage index of [12, 14Hz]

While Fig. 3-32 shows the identification result by choosing the frequency range [8, 9Hz] within input frequency range [7, 10Hz].

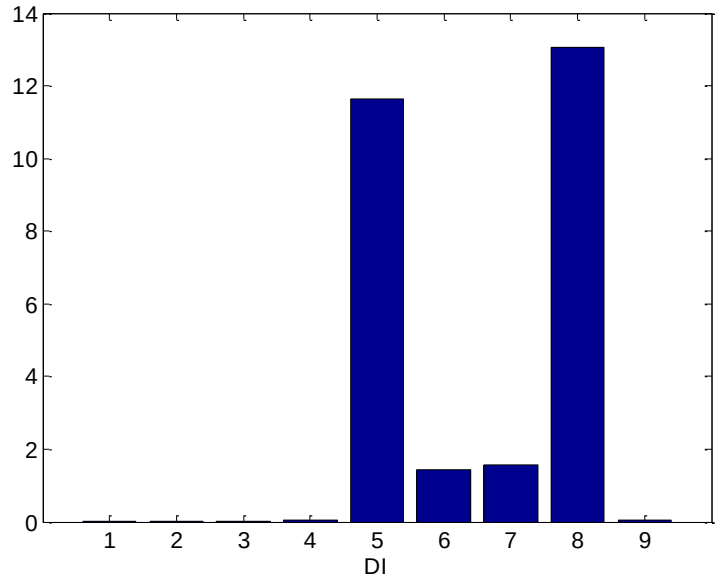

Fig. 3-32 Damage index of [8, 9Hz]

It can be seen that the recognized result is the same as the Fig. 3-31, that is because the loading position is between the two nonlinear components according to the conclusions(3-97) and (3-98).

3.3.8.5 Case study 5: multiple nonlinear components under multiple-point loading

Loading position $J_1 = 2$, $J_2 = 4$ and $J_3 = 8$

Number of nonlinear components $\bar{L}$ =3 and the springs are considered to be nonlinear that $L_1 = 6$ (between mass 5 and mass 6), $L_2 = 8$ (between mass 7 and mass 8) and $L_3 = 9$ (between mass 8 and mass 9)

This process should be followed as section 3.3.6.5 Case3.

Step 1: Two single forces with the same bandlimited frequency range [7, 10Hz] can be loaded at one mass separately, which contains different excitation intensities. $f_1 = 1, f_2 = 10$

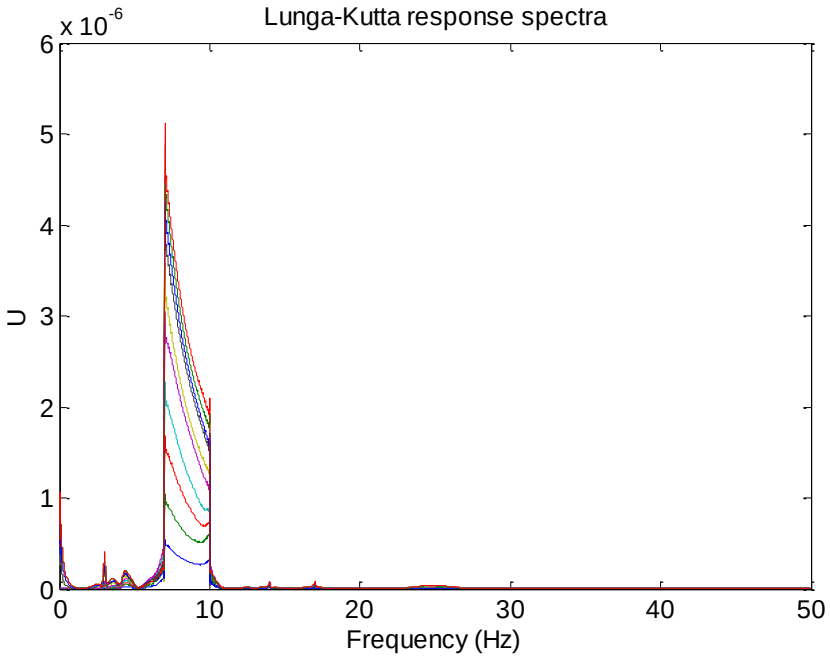

Fig. 3-33 Response spectra of 10-DOF nonlinear system under

excitation f1=1

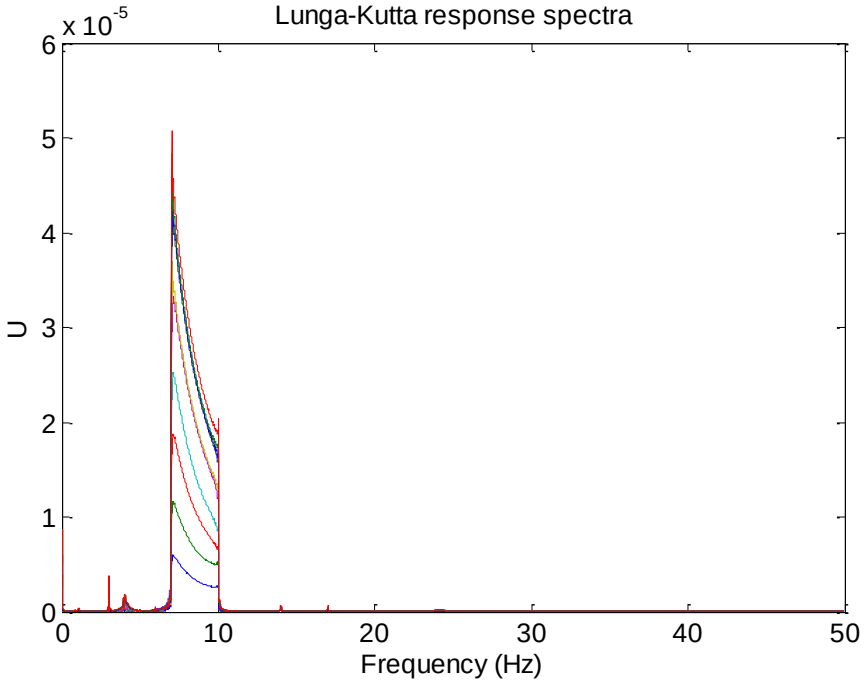

Fig. 3-34 Response spectra of 10-DOF nonlinear system under excitation f1=10

The output spectra of 10-DOF points are shown in the Fig. 3-33 and Fig. 3-34 under two different excitation levels.

Step 2: Calculate Output-based transmissibility function for each pair of consecutive masses.

$$\lambda_{i,i+1}^{f_1}(j\omega)=\frac{Y_i^{f_1}(j\omega)}{Y_{i+1}^{f_1}(j\omega)}$$

$$\lambda_{i,i+1}^{f_2}(j\omega)=\frac{Y_i^{f_2}(j\omega)}{Y_{i+1}^{f_2}(j\omega)}$$

Step 3: Calculate the damage index (Difference between $\lambda_{i,i+1}^{f_1}(j\omega)$ and $\lambda_{i,i+1}^{f_2}(j\omega)$)

$$DI_{i,i+1} = \int_{\omega_1}^{\omega_2} \left| \lambda_{i,i+1}^{f_1}(j\omega) - \lambda_{i,i+1}^{f_2}(j\omega) \right| d\omega$$

Step 4: According to relationship of nonzero values of *DI* and, localize the nonlinear components by referring to properties [Equations(3-101)-(3-104)]. The area of nonlinear components could be found.

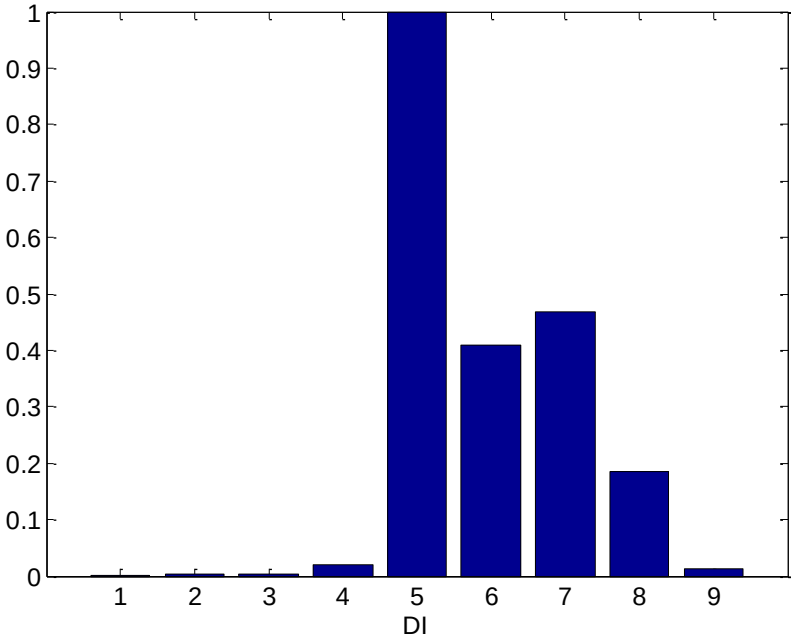

Fig. 3-35 Damage index of [12, 15Hz]

The nonlinear components' area can be read as DI5-DI8. That can be matched by using Equations(3-101)-(3-104) to find the nonlinear components' boundary which is $L_1 - 1 = 5$, $L_3 - 1 = 8$, therefore, $L_1 = 6$, $L_3 = 9$, and it means the nonlinear components are located between mass5 and mass9. Also it is accordance with the provided description of damage scenario.

3.3.8.6 Case study 6: multiple nonlinear components under uniform distributed loading

Loading position $J_i = i$,where i=1, 2, …,10

Number of nonlinear components $\bar{L}$ =3 and the springs are considered to be nonlinear that $L_1 = 6$ (between mass 5 and mass 6), $L_2 = 8$ (between mass 7 and mass 8) and $L_3 = 9$ (between mass 8 and mass 9)

As for distributed load, which should be considered as the same case as section 3.3.7.5 Case study 5. Hence, the direct identified result is shown in Fig. 3-36. According to Equations(3-101)-(3-104), nonlinear components' area could be found at the boundary $L_1 - 1 \le i \le L_3 - 1$, therefore, in comparison with the outcome shown in Fig. 3-36, it is easy to find that $L_1 - 1 = 5$, $L_3 - 1 = 8$. That is $L_1 = 6$ and $L_3 = 9$, it means the nonlinear components are located between mass5 and mass9, which is accordance with the provided damage condition.

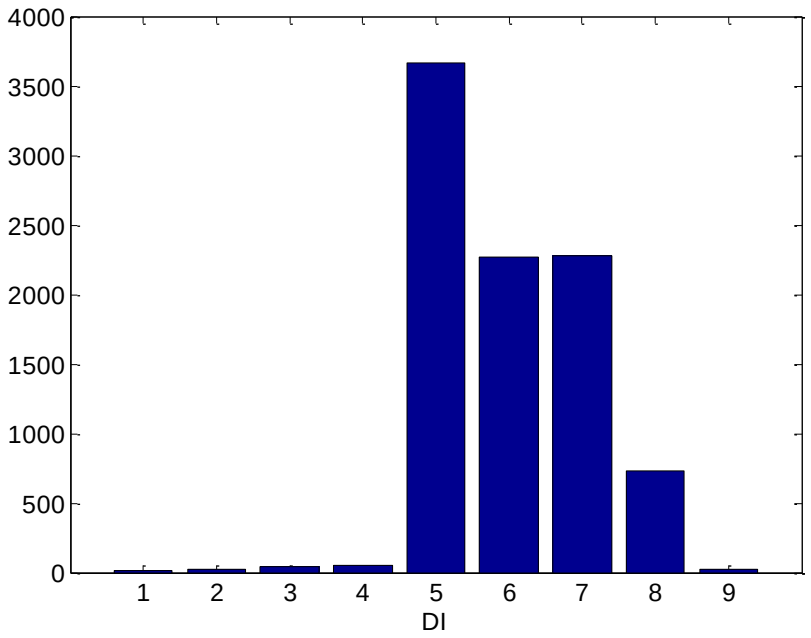

Fig. 3-36 Damage index of [12, 15Hz]

3.3.9 Experimental study

In order to verify the effectiveness of the proposed methodology, nonlinear damage detection should be performed not only in numerical simulation cases, but also under the real working condition. The experimental tests are organized into two different setups, which are blade and steel beam structures with cracks that behaviors nonlinearly.

3.3.9.1 Case study 1: Nonlinear damage identification on blade structure

The blade model is made by wood proportionally in terms of the shape of real blade structures, aiming to carry out experiments in lab conveniently. Four laser sensors have been applied as data acquisition ports, considered as non-contact measurement. The sensing unit is millimeter. The experimental setup is shown in Fig. 3-37. The blade was mounted on an actuator near sensor 4.

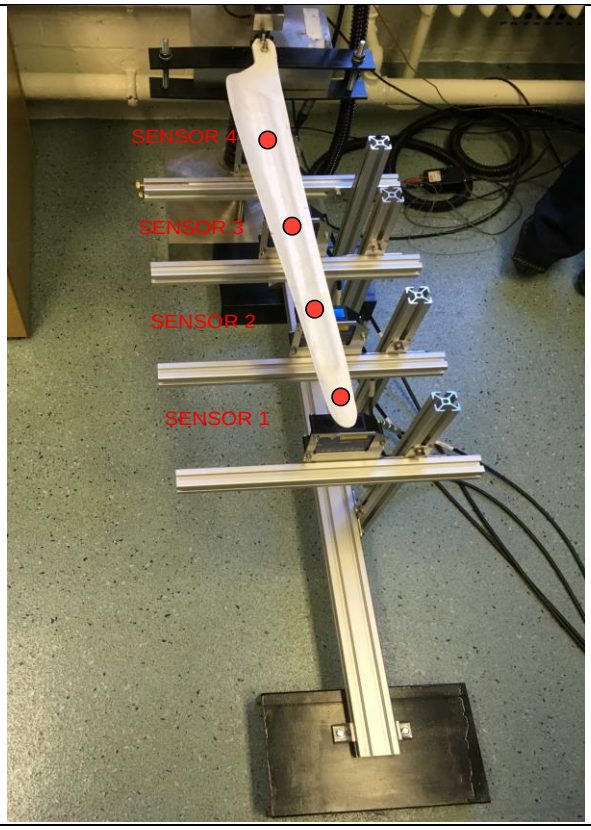

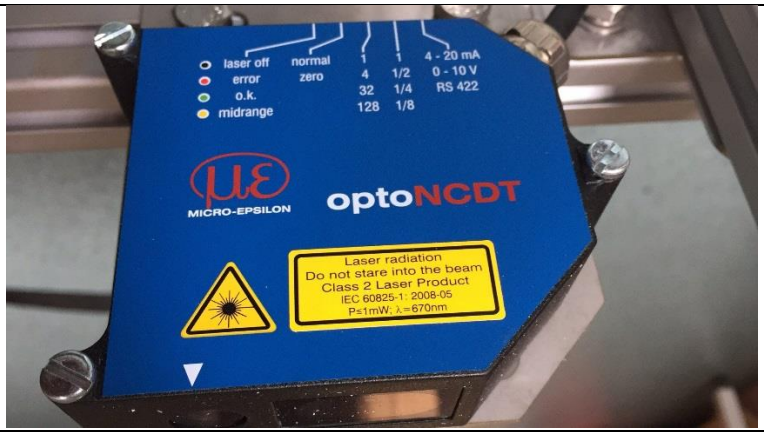

Fig. 3-37 Experimental setup: blade model and laser sensor

Two damage scenarios will be taken into consideration: single crack and two cracks (breathing crack here). The detailed experimental schedule is shown in Table 2.

Table 2. Experimental schedule

Input Amplitude / Bandlimited	A	B
3-7Hz	✓	✓
7-12Hz	✓	✓
10-15Hz	✓	✓

Three bandlimited input signals, here considered as white noise, are generated with different frequency band. In the meantime, two different excitation levels are taken into account. (A>B, adjusted by the power amplifier).

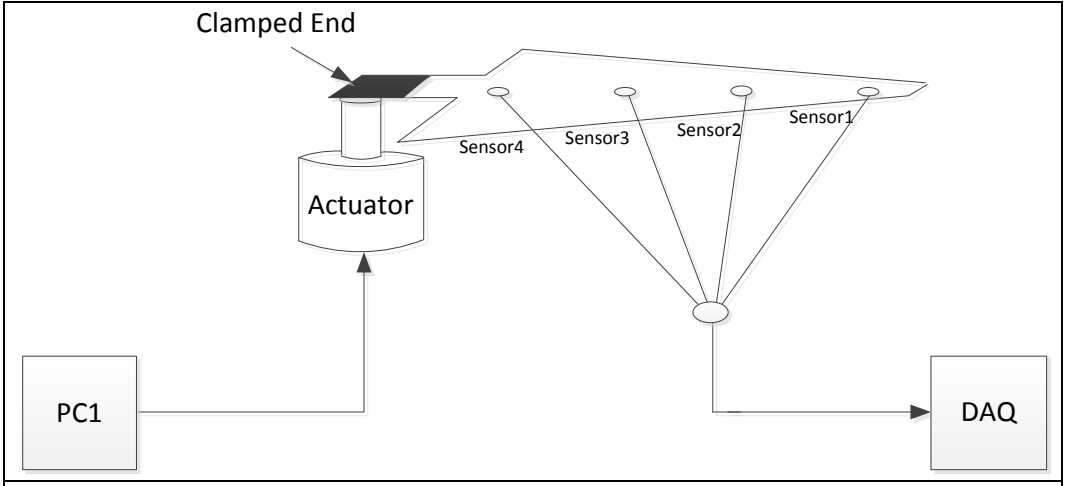

Fig. 3-38 Experimental setup configuration

a. blade model with one crack

The experimental configuration is shown in Fig. 3-38. The crack was made by using a very thin saw between laser sensor 1 and laser sensor 2, in order to make it behavior nonlinearly, shown in Fig. 3-39.

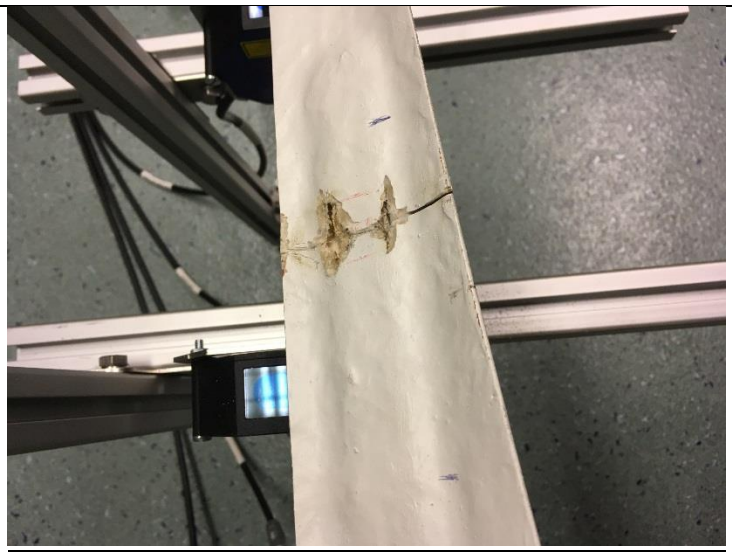

Fig. 3-39 Blade model with one crack

The laser sensors are capable to measure the displacement with sampling frequency 2500Hz, and the responses of the four laser sensors in time domain under input amplitude A is presented in Fig. 3-40. The

input frequency band is chosen as 3-7Hz.

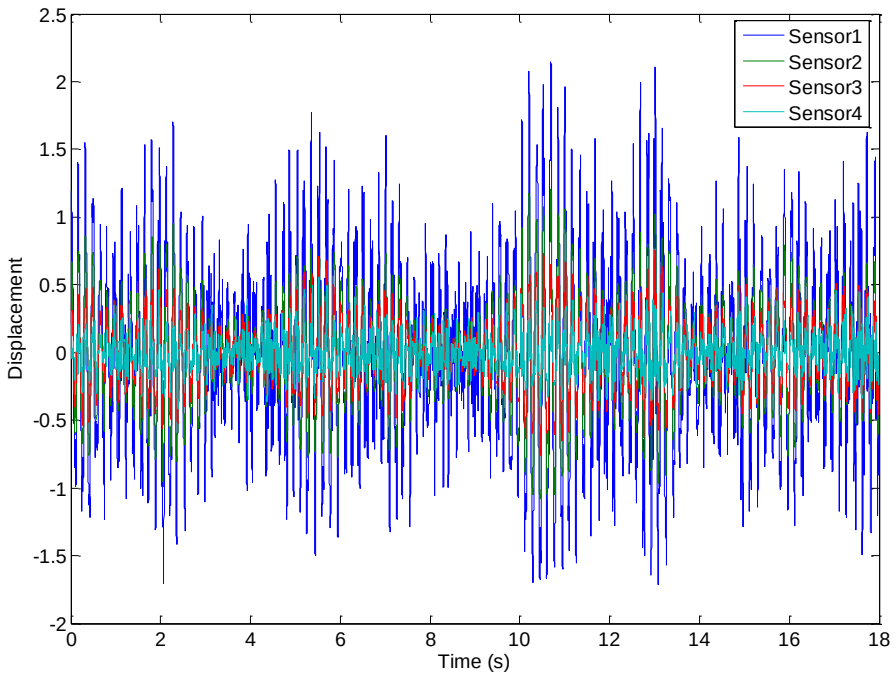

Fig. 3-40 The response of laser sensors in time domain under excitation amplitude A

In Fig. 3-40, it is apparent to observe that displacement acquired from sensor 1 has the maximum amplitude and the one acquired from sensor 4 has the minimum amplitude due to the fact that sensor 1 is mounted on the cantilevered end and sensor 4 is mounted on the clamped end. Fig. 3-41 shows the spectra of the four sensors.

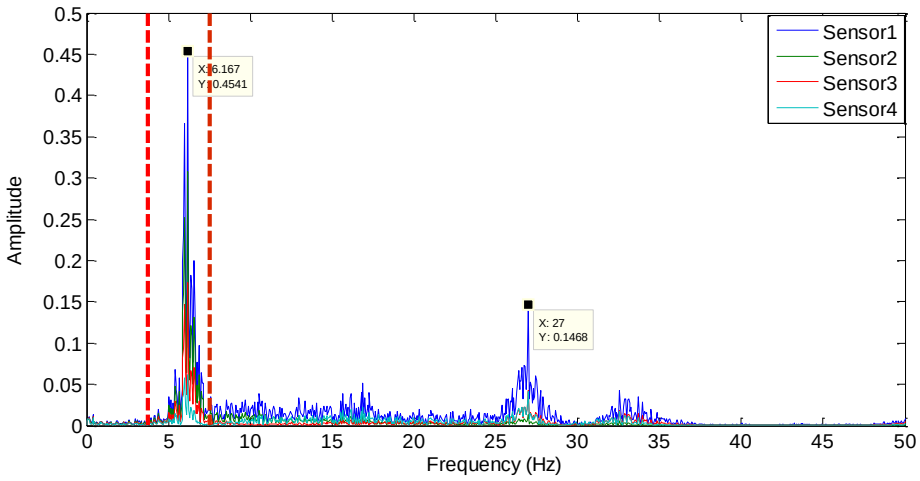

Fig. 3-41 Spectra of the four sensors under excitation amplitude A

From the Fig. 3-41 of response spectra, the area covered by two dash lines is the input frequency band [3-7Hz], due to the existence of crack, more frequency bands appear especially from 7-35Hz. Part of energy originally stored in the frequency band [3-7Hz] has been transferred into the frequency band [7-35Hz] because of the nonlinearity of the system. Also, two resonance frequencies could be detected obviously, that have been marked in the Fig. 3-41, they are 6.167Hz and 27Hz in accordance with the first and second modal frequency of the blade model.

In order to perform the nonlinear damage identification procedure, two different loading conditions should be considered. Therefore, the same process has been carried out under the input with a higher excitation amplitude B. The responses from the sensors in time domain and in frequency domain are shown in Fig. 3-42 and Fig. 3-43 respectively.

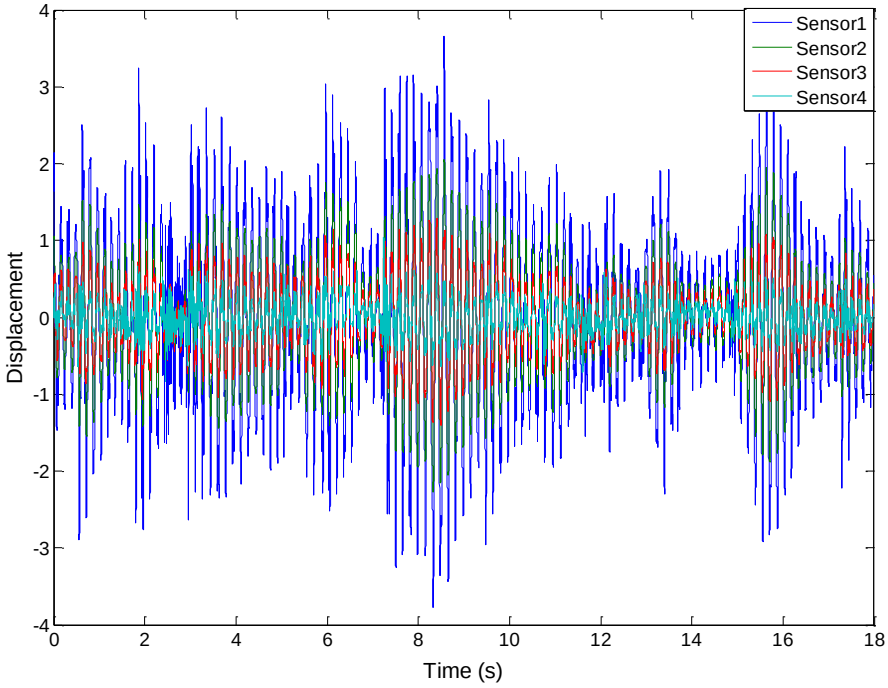

Fig. 3-42 The response of laser sensors in time domain under excitation amplitude B

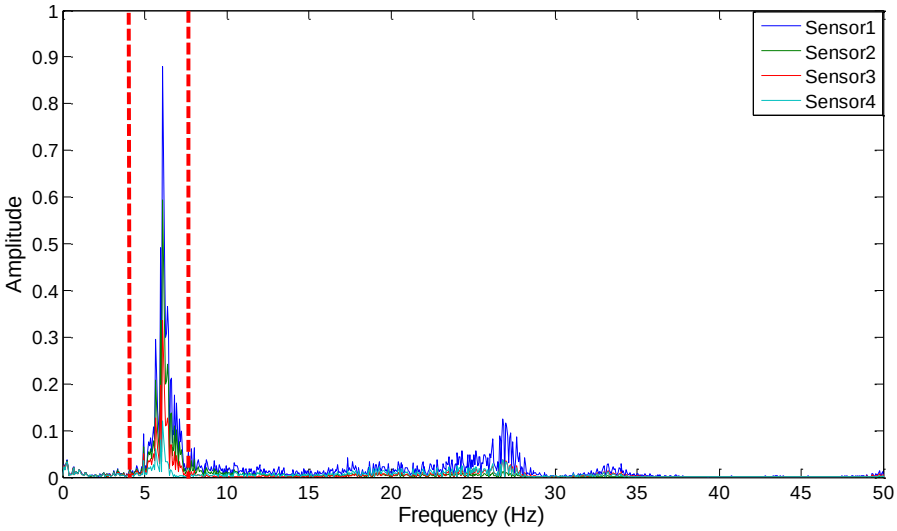

Fig. 3-43 Spectra of the four sensors under excitation amplitude B

Follow the nonlinear identification procedure from step1 to step4 in section 3.3.6.3, ω_1, ω_2 are valued as 3Hz and 7Hz in the equation(3-105) and equation(3-106). The procedure has been repeated for 5 times, and identified damage index can be reached by averaging the damage index obtained separately from those 5 times.

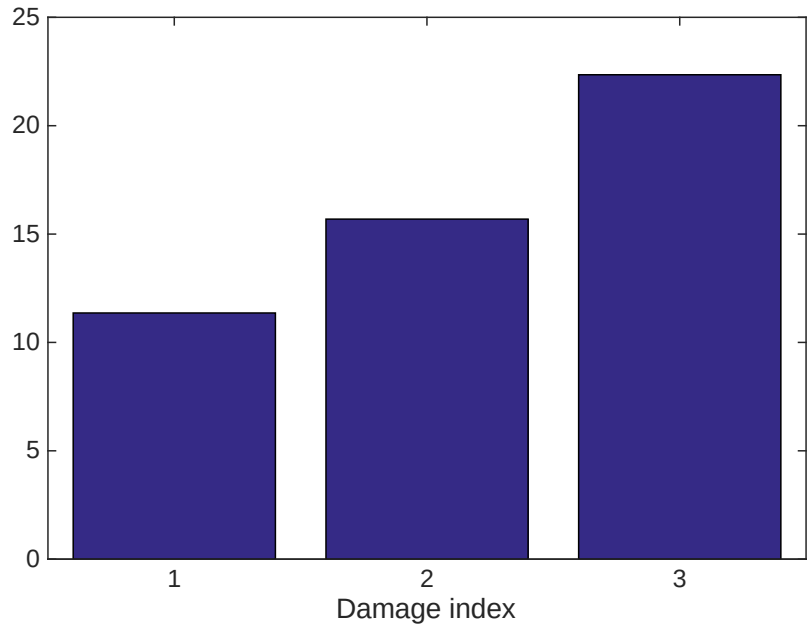

Fig. 3-44 Damage index under [3-7Hz]

Fig. 3-44 shows the damage index. According to the conclusion of the proposed method in the section 3.3.6.1, there exists nonzero values for all damage index $DI_{1,2}$ $DI_{2,3}$ and $DI_{3,4}$, in other words, $DI_{1,2} \neq 0$ $DI_{2,3} \neq 0,$ and $DI_{3,4} \neq 0$, which is in accordance with the identified result shown in Fig. 3-44..

Same identification procedures have been carried out for the other two scenarios that vary the frequency band of input [7-12Hz] and [10-15Hz]. The damage indexes for the case of [7-12Hz] and [10-15Hz] have been presented in the Fig. 3-45 and Fig. 3-46 respectively.

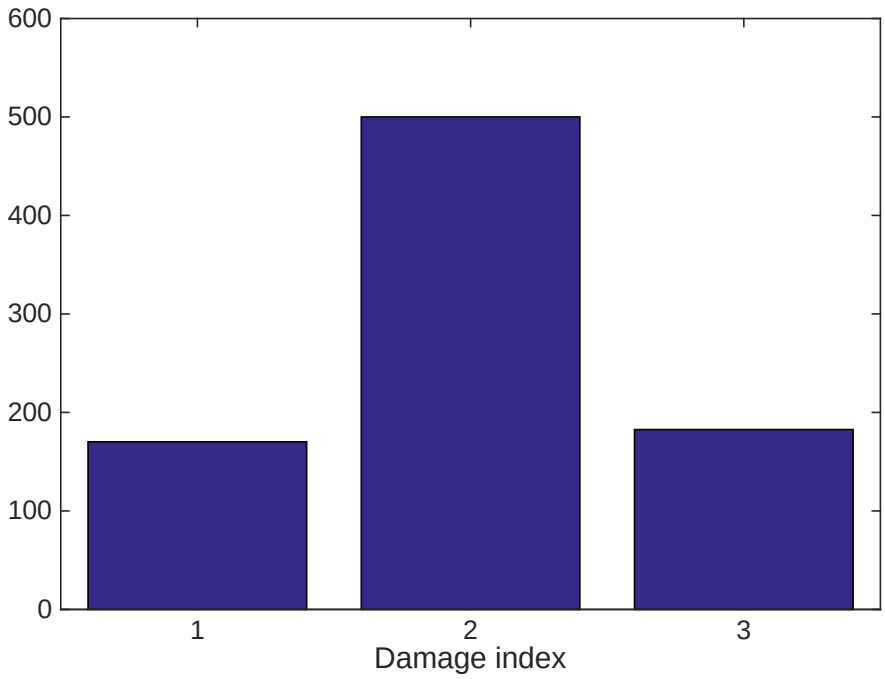

Fig. 3-45 Damage index under [7-12Hz]

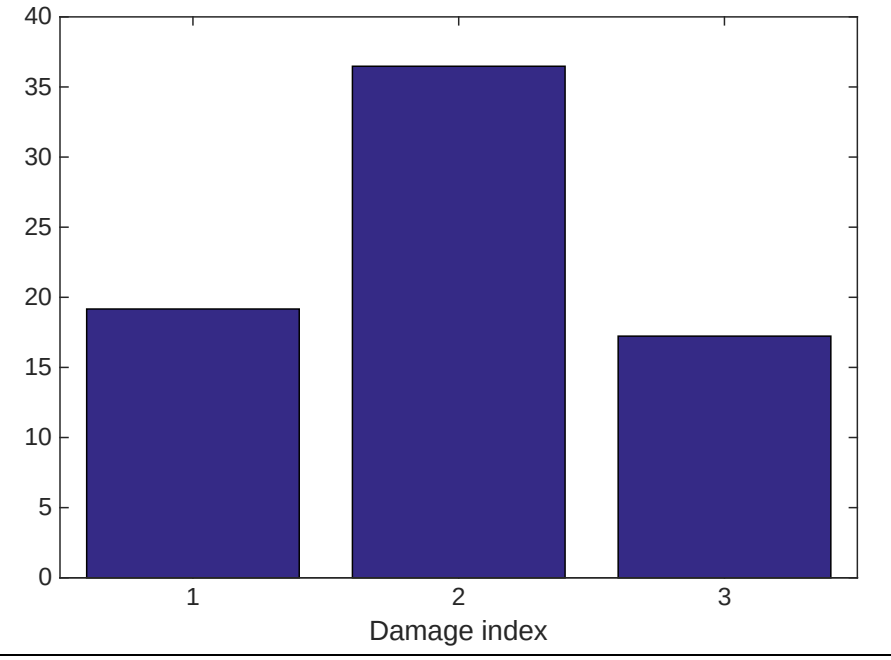

Fig. 3-46 Damage index under [10-15Hz]

Apparently, both identification results indicate the same conclusion regarding to the scenario under input with bandwidth [3-7Hz], that is $DI_{1,2} \neq 0, DI_{2,3} \neq 0,$ and $DI_{3,4} \neq 0$.

b. blade model with two cracks

Two cracks have been created, one is located between sensor 1 and sensor 2, the other is located between sensor 2 and sensor 3. The blade with two cracks is shown in Fig. 3-47.

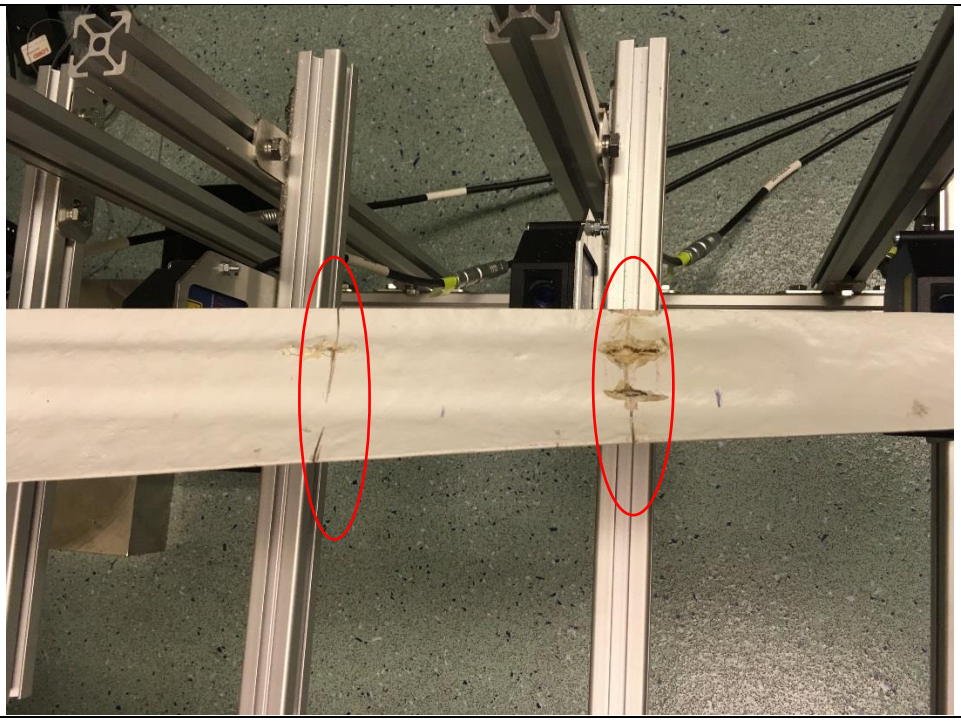

Fig. 3-47 Blade model with two cracks

The responses under bandlimited input with the frequency band [3-7Hz] obtained from the laser sensors in time domain and frequency domain have been shown in the Fig. 3-48 - Fig. 3-51, considering two excitation levels: amplitude A and B.

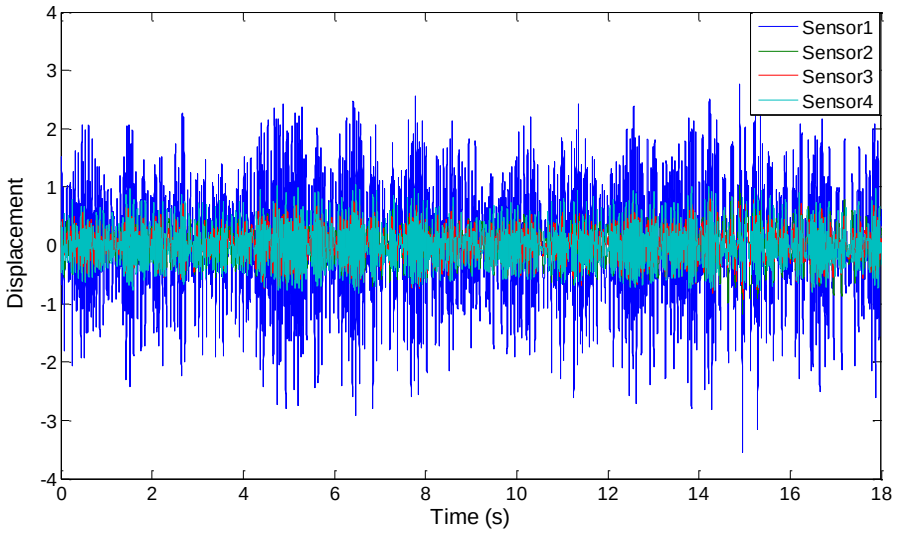

Fig. 3-48 The response of laser sensors in time domain under excitation amplitude A

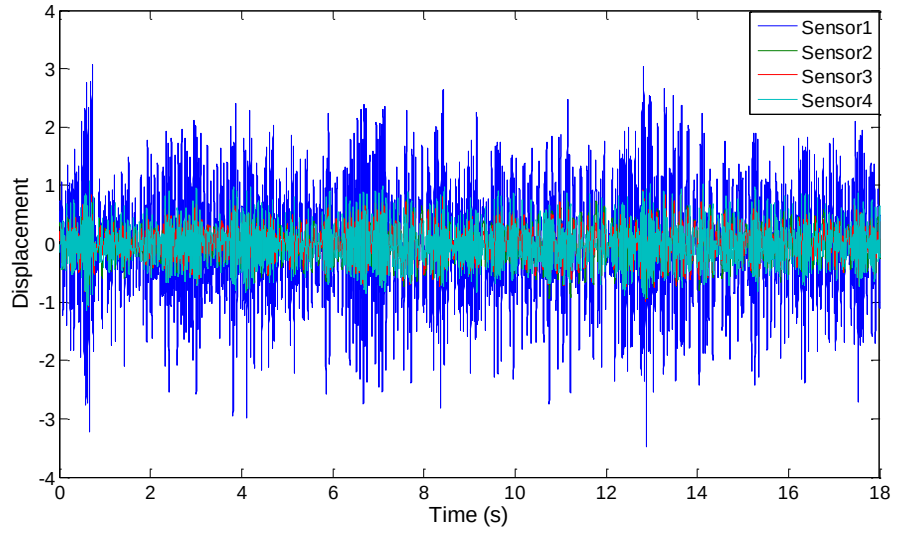

Fig. 3-49 The response of laser sensors in time domain under excitation amplitude B

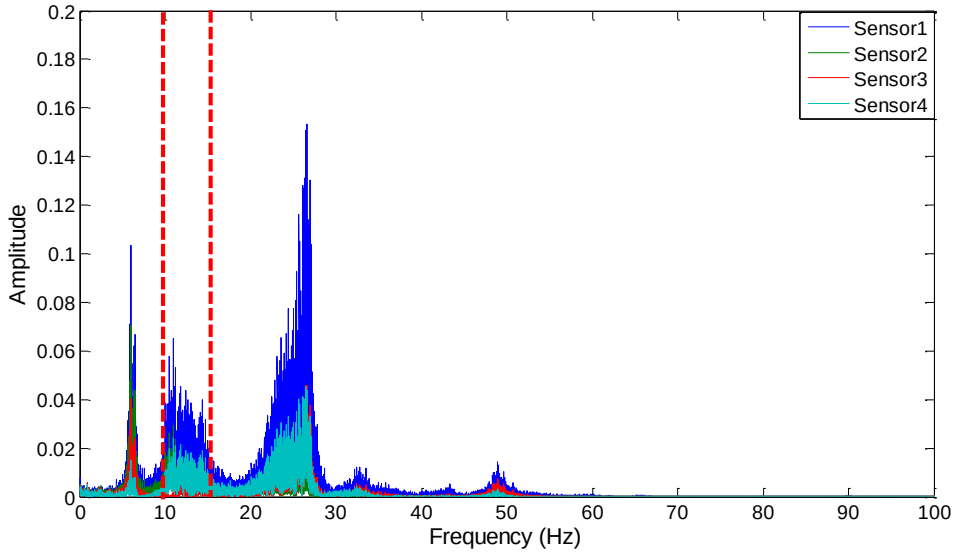

Fig. 3-50 Spectra of the four sensors under excitation amplitude A

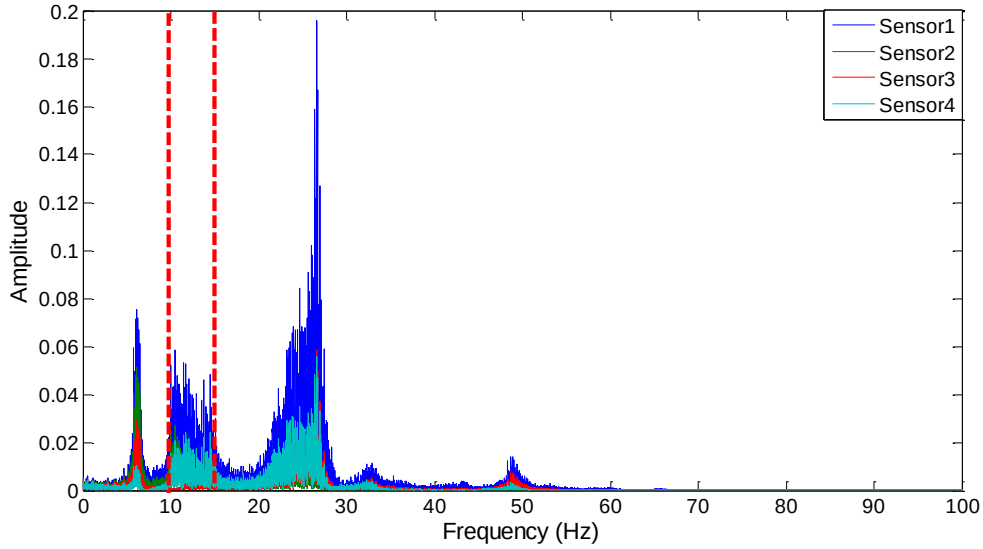

Fig. 3-51 Spectra of the four sensors under excitation amplitude B

From the Fig. 3-50 and Fig. 3-51, the occurrence of energy located within frequency range [5-8Hz], [20-35Hz] and [45-55Hz] can be clearly observed. Because the system output frequency response is the effect of a combination of the output frequency responses of the involved

homogeneous non-linear systems.

To confirm the effectiveness of proposed method for multiple nonlinear components identification, step1-step4 described in section 3.3.6.4 should be applied here. And ω_1 and ω_2 should be considered outside of range [10-15Hz], the frequency range [20-30Hz] made a great contribution to the system output which could be the good choice of ω_1 and ω_2, that is ω_1=20Hz $\omega_2 = 30\text{Hz}$.

The damage identification is shown in the Fig. 3-52. According to the proposition of section 3.3.6.2, there exists only nonzero values in $DI_{1,2}$ and $DI_{2,3}$, and other damage indexes should be zero. Considering the provided result below, it is correspondence with the description of that proposition, $DI_{1,2} \neq 0, DI_{2,3} \neq 0, DI_{3,4} = 0$. Actually, a small value can be observed from $DI_{3,4}$, which could be the result of noise and other source of interference, and it has been indicated by the red dash line.

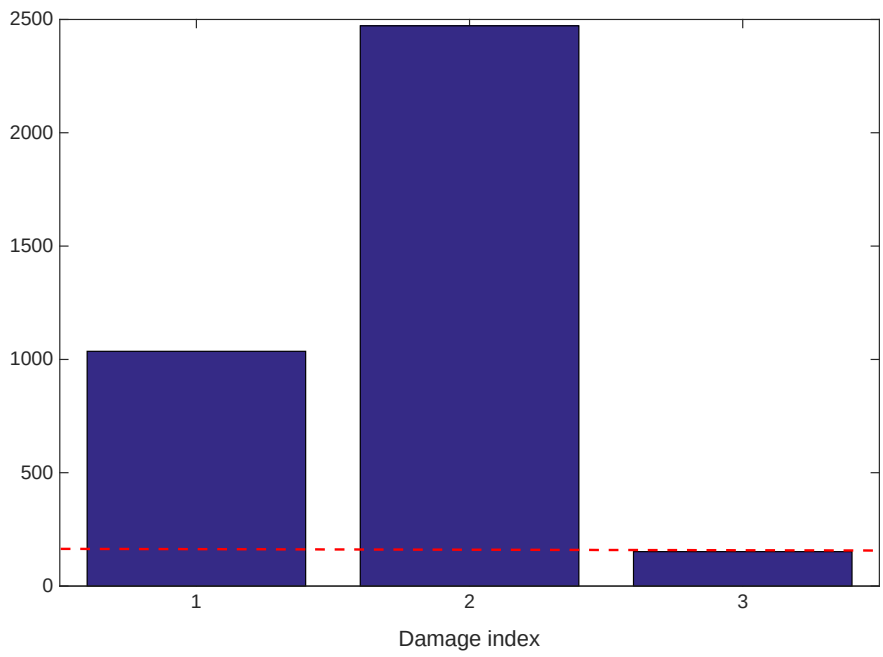

Fig. 3-52 Damage index under [10-15Hz]

Same operations for other scenarios: under input with bandwidth [3-7Hz] and [7-12Hz] have been performed, and their identification results are displayed in the Fig. 3-53 and Fig. 3-54 respectively. It can be clearly

understood that the same conclusions have been obtained in comparison with Fig. 3-52, which significantly verifies the feasibility of the proposed methodology.

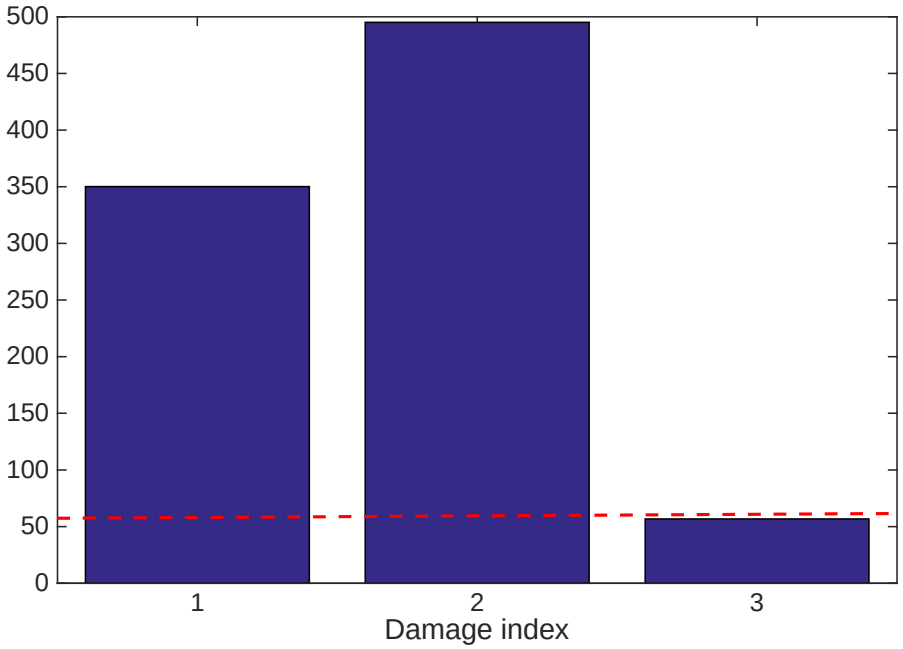

Fig. 3-53 Damage index under [3-7Hz]

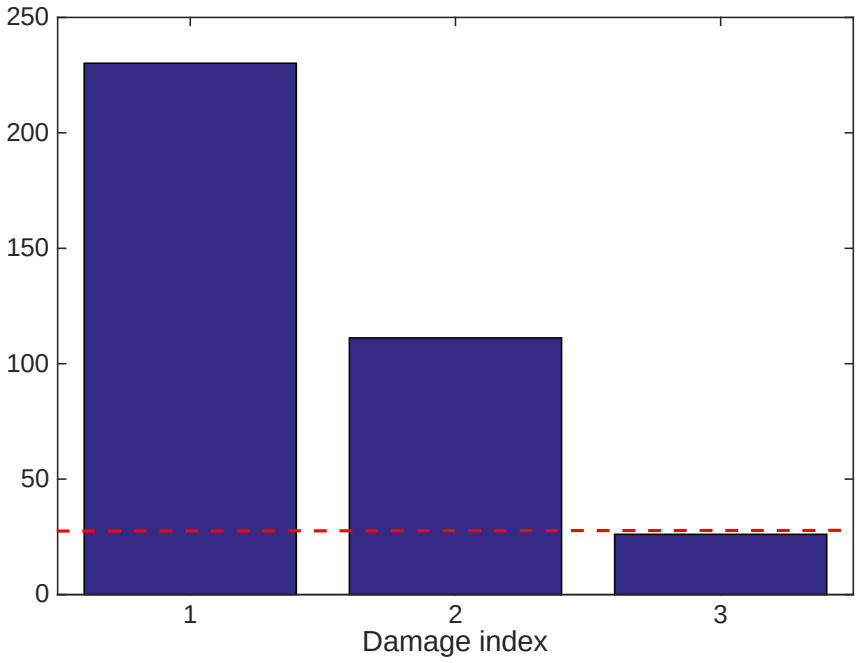

Fig. 3-54 Damage index under [7-12Hz]

The experimental procedures on damage identification are shown in the framework of Fig. 3-55. Note: A and B in the Fig. 3-55 stand for different excitation levels of input.

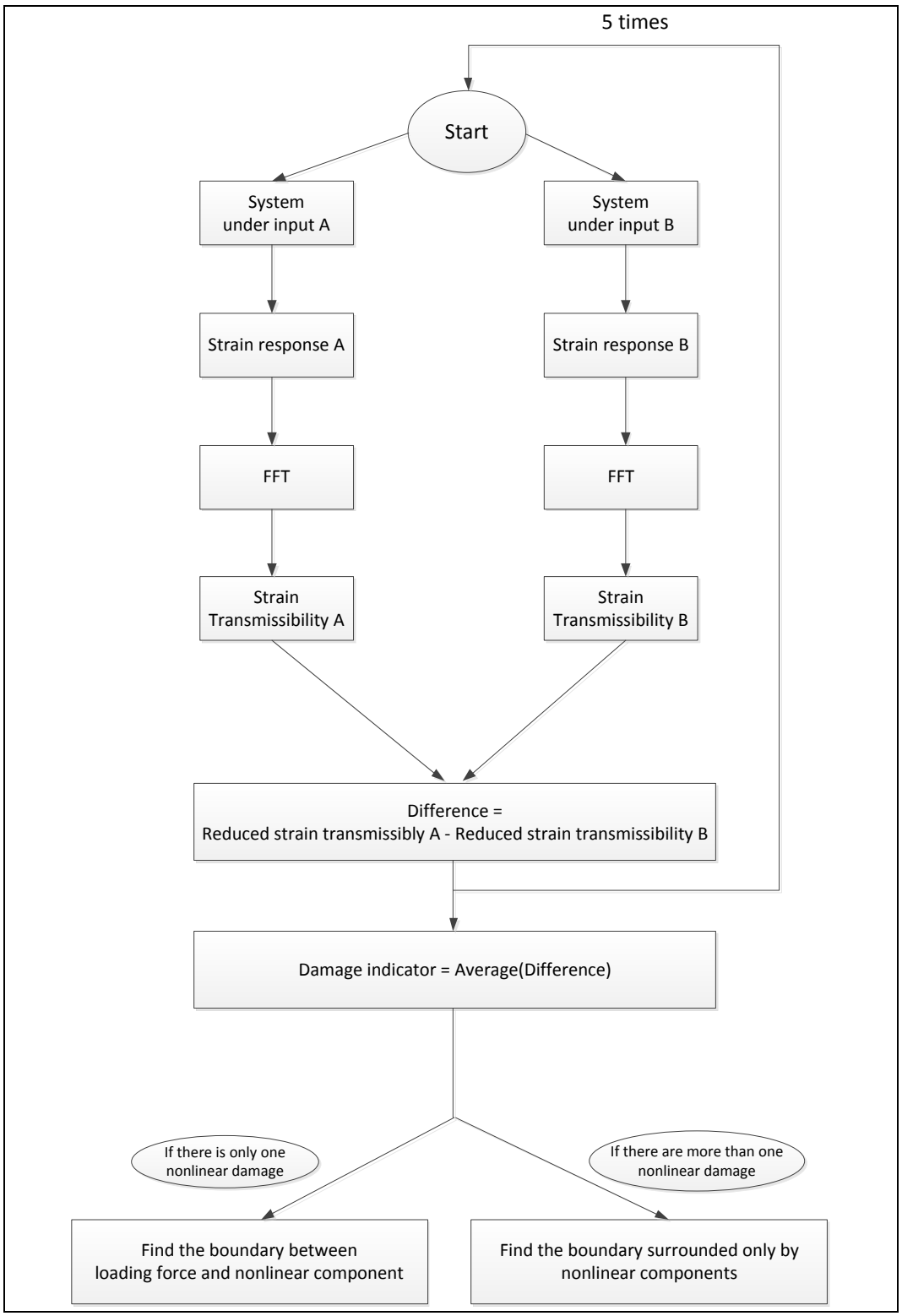
5 times
Start
System under input A
System under input B
Strain response A
Strain response B
FFT
FFT
Strain Transmissibility A
Strain Transmissibility B
Difference = Reduced strain transmissibly A - Reduced strain transmissibility B
Damage indicator = Average(Difference)
If there is only one nonlinear damage
If there are more than one nonlinear damage
Find the boundary between loading force and nonlinear component
Find the boundary surrounded only by nonlinear components

Fig. 3-55 Framework of experiments on nonlinear damage detection

3.3.9.2 Case study 2: Nonlinear damage identification on beam structure by using distributed fiber optics

Due to the limited number of sensors applied in case study 1, the cracks cannot be precisely localized based on scant information provided. In case study 2, a beam structure will be deeply studied with breathing cracks, and acquisition sensor will be substituted by using distributed fiber optics. The core idea of the research project is the use of huge amount of data, both in time and space, for damage detection. Traditional transducers can sense the vibrations of mechanical systems like vibration velocity, acceleration and displacement, etc. and convert into usable output signal. They can provide dynamic measurements (huge information in time domain) but are usually limited sensing points. Thanks to the dense measurement points provided by distributed fiber optics, the proposed work is to apply this new measurement device, LUNA Optical distributed sensor interrogator, to acquire vibrations in terms of dynamic strain.

In order to make breathing crack, fatigue experiments could be the best approach. However, in this case study, another way to create "breathing crack" has been applied which is more convenient to reach the target and able to save time. The details about crack creation are described as follows: A rectangular block gap has been cut with the dimension 40mm × 3mm × 2mm (length × width × thickness), and the removed block gap will be plugged with a steel block with the same width of removed gap by using the particular glue, resulting in breathing behavior when the beam is deforming under periodic loading. The configuration of this crack is displayed in Fig. 3-56.

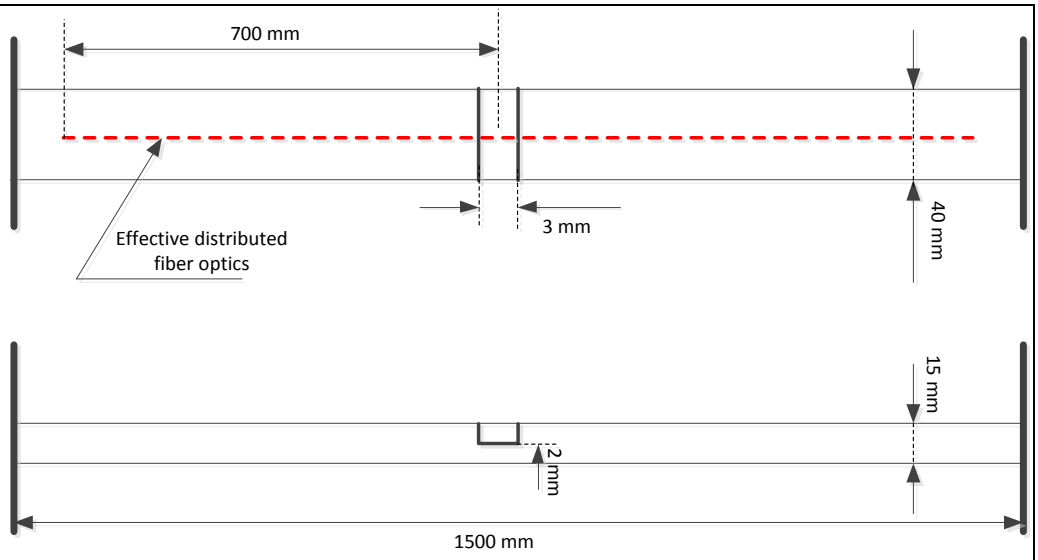

Fig. 3-56 Configuration of beam structure with crack and distributed fiber optics

A clamped-clamped steel beam has been utilized with dimension 1.5 m × 0.04 m × 0.015 m. Red dash line in the above figure indicates the installation configuration of distributed fiber optics. 2meters distributed fiber optics has been attached on the surface of the beam, only 1.28meters effective distributed fiber optics are taken into consideration due to the limitation of beam length. The block crack is located on the 700mm left regarding the initial effective part.

There are 497 sensors along the effective distributed fiber optics with the sampling frequency 250Hz and 2.6125mm sensing space. The crack is located around the 267th sensor, it can be calculated considering the distance and sensing space:
distance/sensing space=700mm/2.6125mm=267
The Fig. 3-57 shows the crack made in the beam.

Fig. 3-57 Crack in the beam

The description of system configuration is presented in Fig. 3-58. Bandlimited input signal is generated by using NI-MyDAQ, which is transferred into Power Amplifier and reached at the mini-Shake to create the input signal into the beam. Meanwhile, the strain dynamic responses are acquired through the attached distributed fiber optics, and the signals are demodulated by LUNA OSiDI-B into the display port PC2.

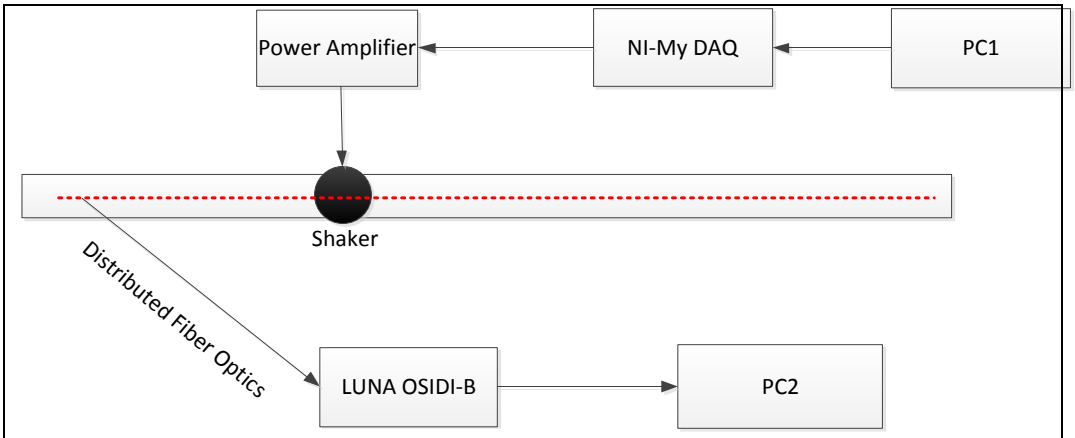

Fig. 3-58 System configuration

And Fig. 3-59 and Fig. 3-60 show the configuration of the corresponding experimental system.

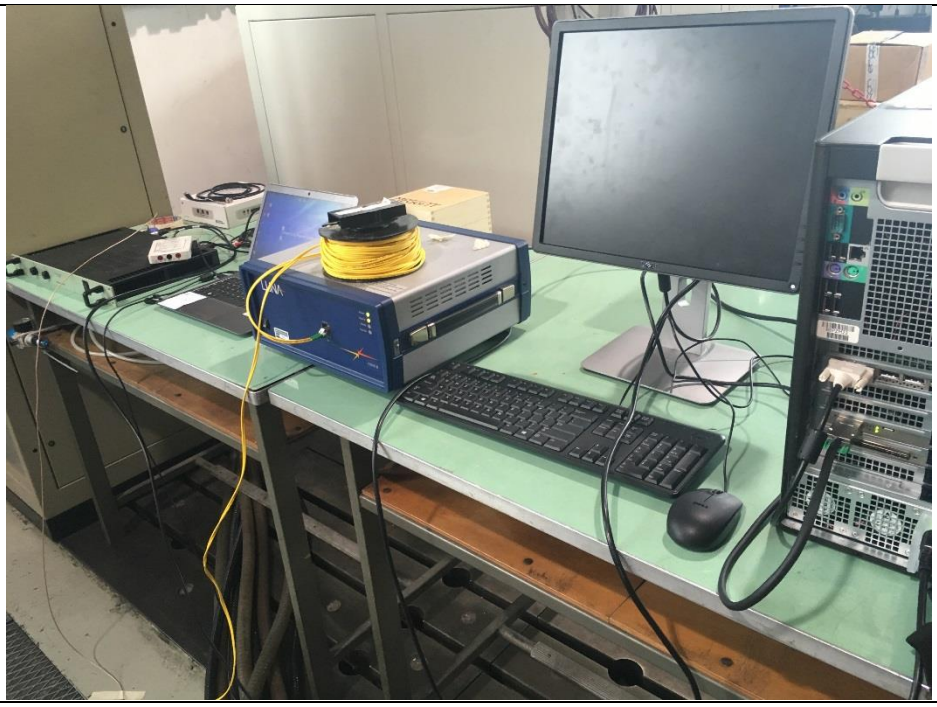

Fig. 3-59 Configuration of experimental system(A)

Fig. 3-60 Configuration of experimental system(B)

Two operational scenarios have been considered as following demonstration.

Case 1: Input on the left side of the beam, and its configuration is shown in Fig. 3-61.

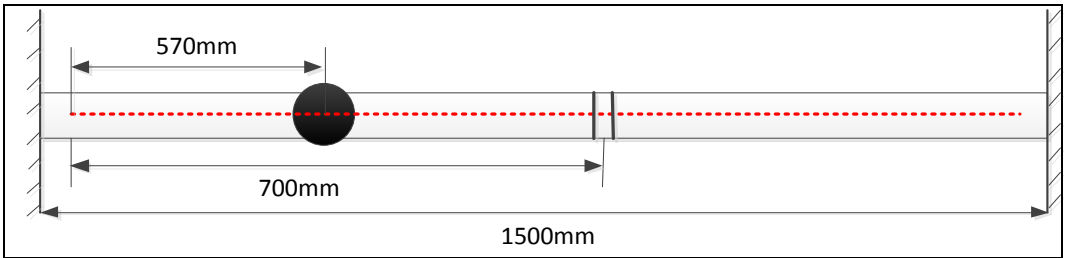

Fig. 3-61 Configuration of scenario 1

Input has been chosen as chirp signal, which contains bandwidth frequency band [25Hz,45Hz]. Two different excitation levels are taken into consideration, namely level A and level B, and they satisfy the condition: A>B. The chirp signal with bandwidth [25Hz,45Hz] under unit excitation amplitude in time domain and frequency domain is shown in Fig. 3-62 and Fig. 3-63.

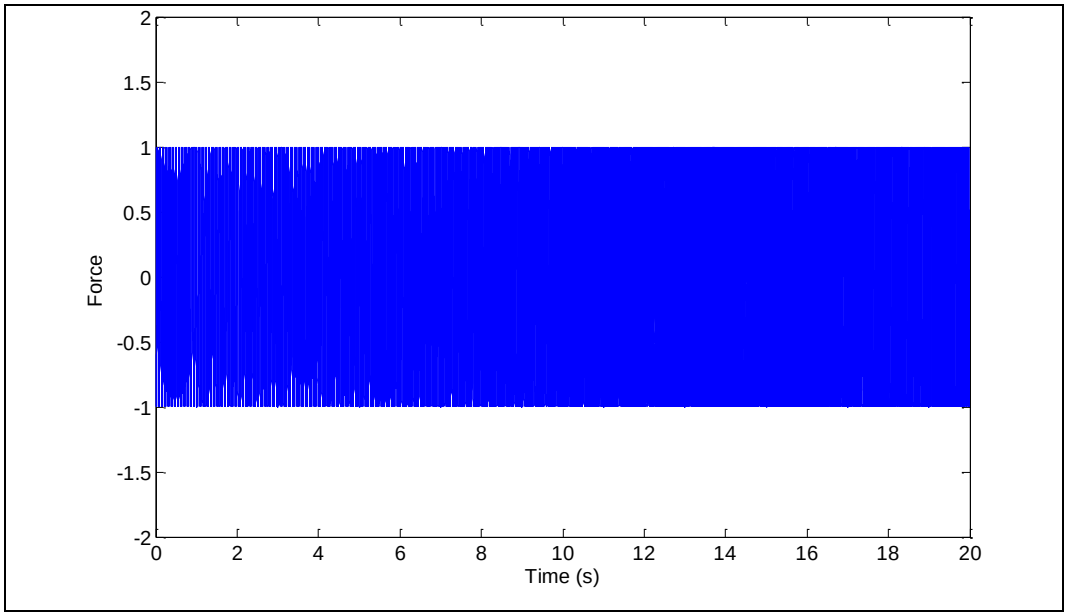

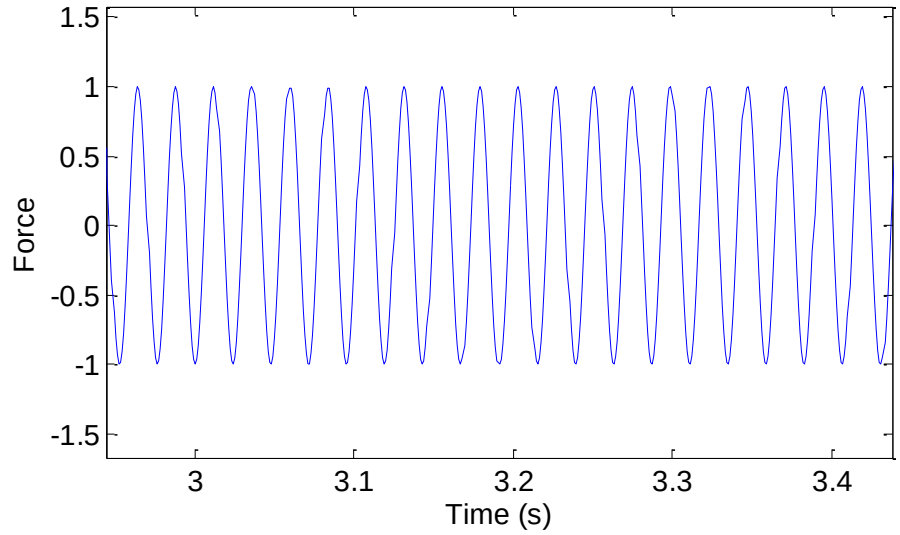

Fig. 3-62 Chirp input signal with bandwidth [25Hz,45Hz] in time domain (unit amplitude) and its partial enlarged drawing

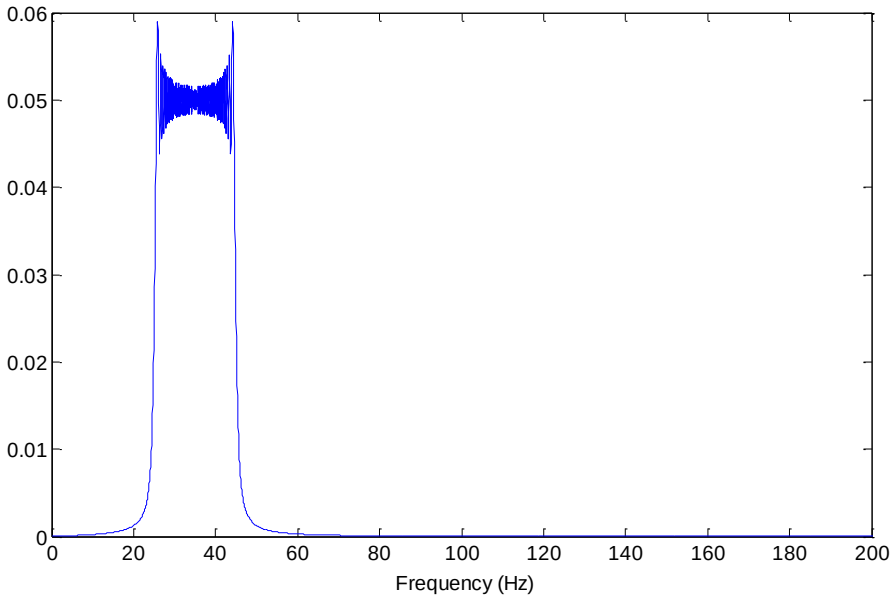

Fig. 3-63 Chirp input signal with bandwidth [25Hz,45Hz] in frequency domain

The input signal was generated by the mini-shaker, which is located at 570mm to the left side of the fiber optics, corresponding to the 219th

sensor. And the crack is located at 700mm to the left side of the fiber optics, corresponding to the 267th sensor.

The Fig. 3-64 and Fig. 3-65 show the strain responses of all the 497 sensors along with the distributed fiber optics under excitation level A and B in time domain respectively.

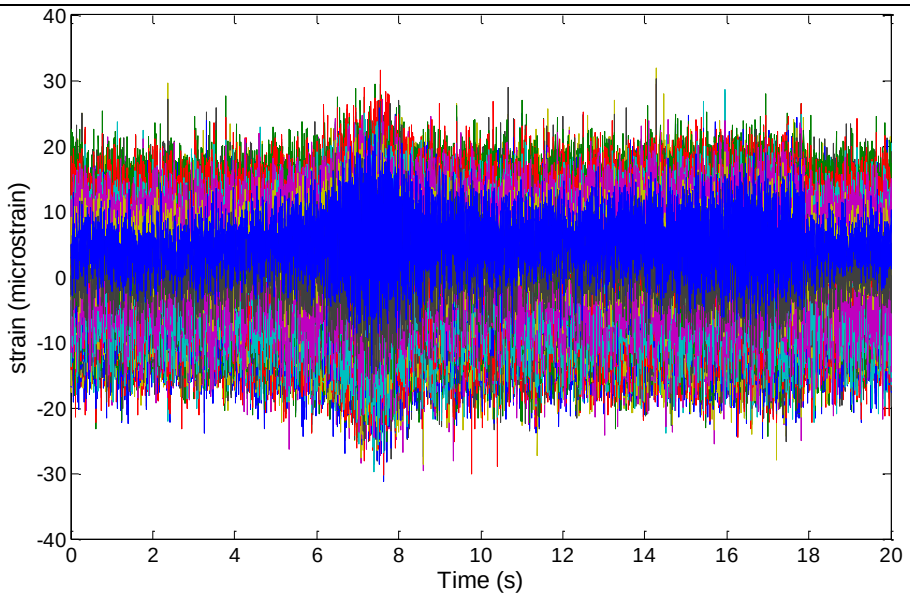

Fig. 3-64 Strain responses of the 497 sensors along with the distributed fiber optics under excitation level A in time domain

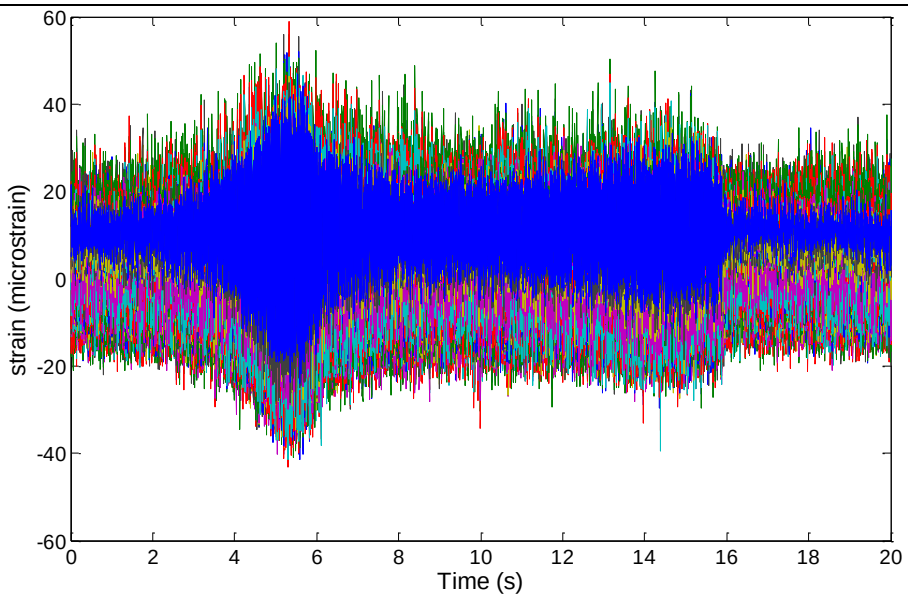

Fig. 3-65 Strain responses of the 497 sensors along with the distributed fiber optics under excitation level A in time domain

From the above figures, it can be noticed that the strain response in the Fig. 3-65 is bigger than that of Fig. 3-64 due to the two different excitation levels.

Meantime, the strain responses in frequency domain can be obtained by performing Fourier Transform, and they are shown in the Fig. 3-66 and Fig. 3-67.

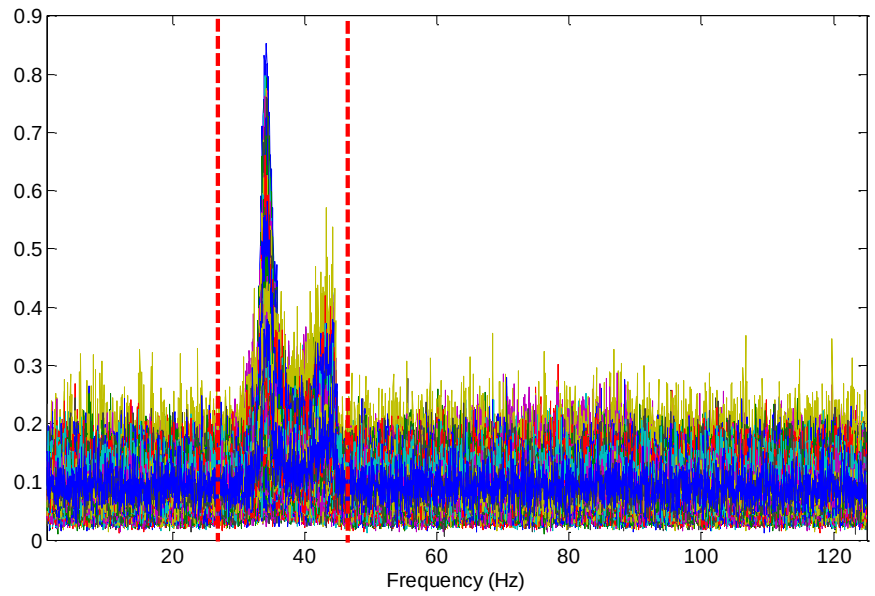

Fig. 3-66 Strain response spectra of the 497 sensors along with the distributed fiber optics under excitation level A

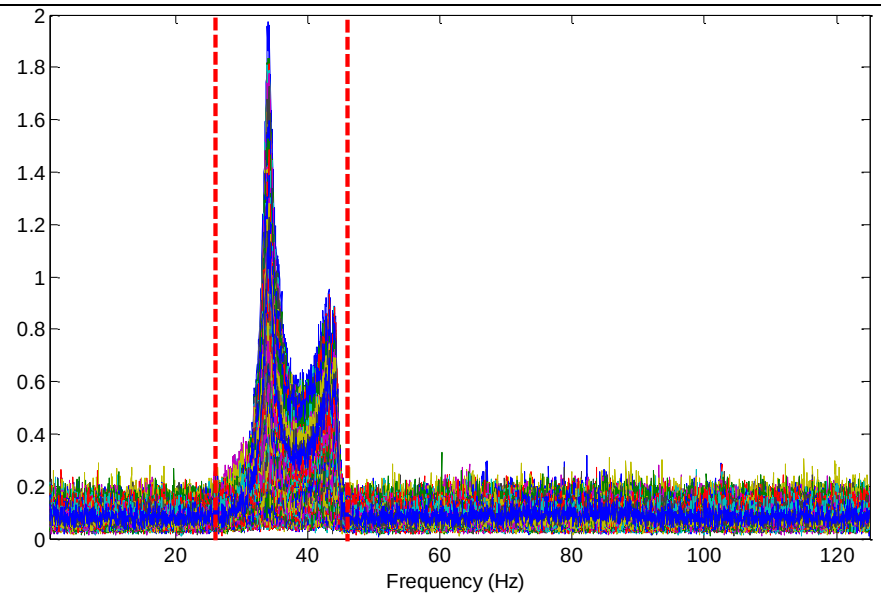

Fig. 3-67 Strain response spectra of the 497 sensors along with the distributed fiber optics under excitation level B

The areas covered by two red dash lines in the Fig. 3-66 and Fig. 3-67

indicate that the spectra concentrated on the frequency band [25Hz,45Hz] corresponds with input frequency range. And the peak within the frequency band remarks the 1st order resonance frequency, the bandwidth [25Hz,45Hz] has been chosen around resonance frequency in order to obtain more stable output response.
However, there exist two mode nodes during the first strain mode, which can be found in the Fig. 3-68.
The 1st unscaled mode shape of intact beam has been extracted by using the method[115] under hammer impact, it is shown in Fig. 3-68

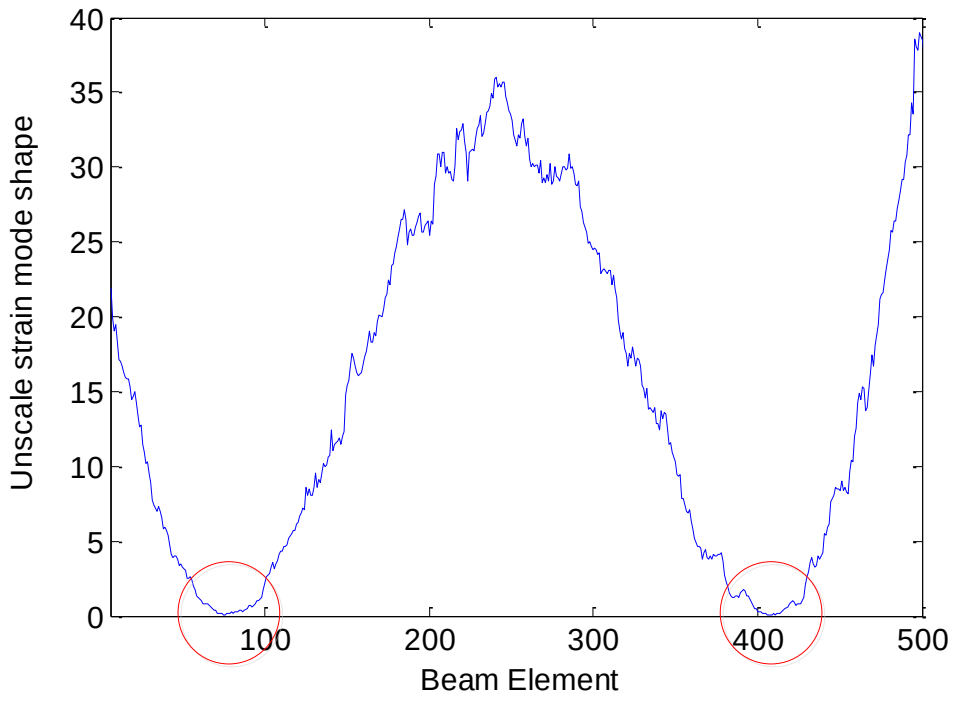

Fig. 3-68 Unscaled strain mode shape of intact beam

It can be observed that the values of two zeros marked by red circles in the Fig. 3-68 are very subtle, close to zero, which are corresponding to the 1st strain mode nodes.
Those beam elements nearby the mode nodes cannot be taken into damage identification procedure, therefore, transmissibility coherence function should be introduced here, as the same as the section 2.6 performed. And the threshold for eliminating the unreliable beam nodes has been selected as 0.8.

Fig. 3-69 shows the transmissibility coherence function under excitation level A, and the areas covered by the green dash lines are unreliable that are lower than 0.8. Hence the corresponding beam elements are not taken into account.

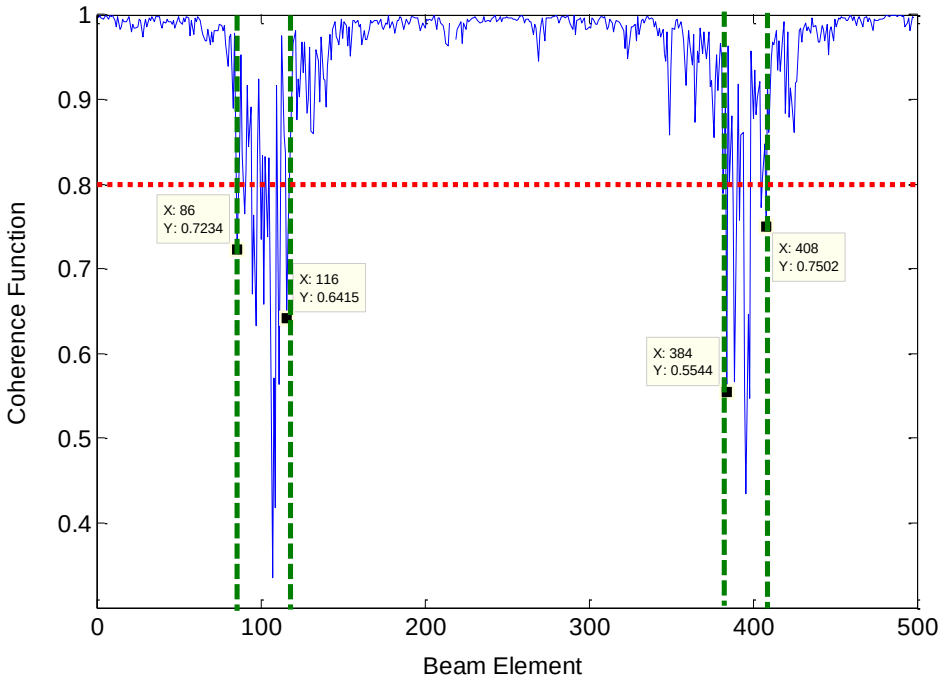

Fig. 3-69 Transmissibility coherence function under excitation level A

Aiming to nonlinear damage identification, the procedure step1 to step4 3.3.6.3 has been applied. And the frequency band here has been chosen as [25Hz,45Hz], which are the values of a and b in step1 in section 3.3.6.3.

Damage indicator can be obtained from equation(3-106) and it is shown in Fig. 3-70.

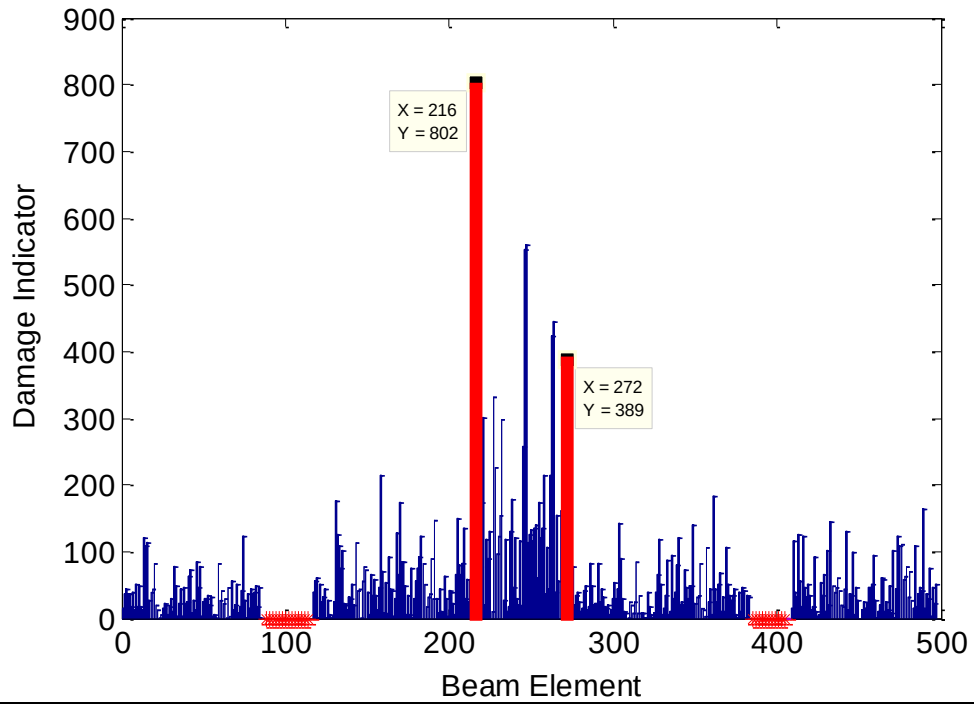

Fig. 3-70 Damage indicator of scenario 1

The asterisks in the Fig. 3-70 indicate the unreliable beam elements. According to the deduction (3-58) and (3-59), the boundary of the area composed by loading force and nonlinear component is $[J, L_1 - 1]$. In this scenario, $J = 219$ and $L_1 = 267$, therefore, the boundary should be [219,266]. In Fig. 3-70, the red bars are the identified boundary between loading force and nonlinear component which are 216 and 272 respectively. Given that the location of loading force could be considered as prior information, red bar at beam element 267 should be recognized as nonlinear component. Considering the small spatial resolution of the fiber optics and uncertainties of the installation of distributed fiber optics, noise effect and practical operations, the recognized boundary can be acceptable compared to the theoretical boundary.

Case 2: Input on the right side of the beam, and its configuration is shown in Fig. 3-71.

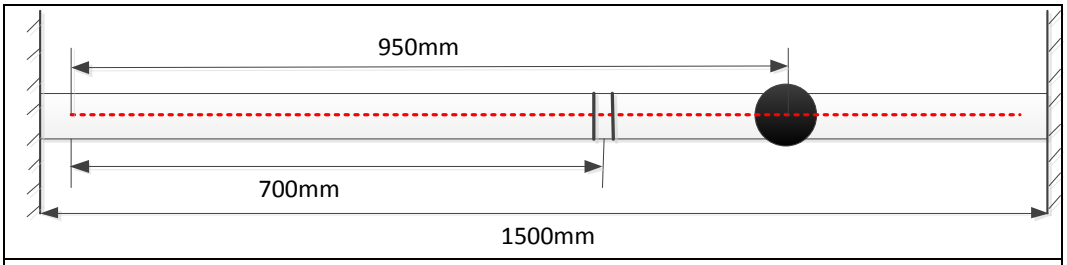

Fig. 3-71 Configuration of scenario 2

The input signal was generated by the mini-shaker, which is located at 950mm to the left side of the fiber optics, corresponding to the 364th sensor. And the crack is located at 700mm to the left side of the fiber optics, corresponding to the 267th sensor.

A chirp signal, as input, contains different bandwidth frequency band [25Hz,40Hz] instead of [25Hz,45Hz]. Also, two different excitation levels (level A and level B) are considered, and they satisfy the condition: A>B. The chirp signal with bandwidth [25Hz,40Hz] under unit excitation amplitude in time domain and frequency domain is shown in Fig. 3-72 and Fig. 3-73.

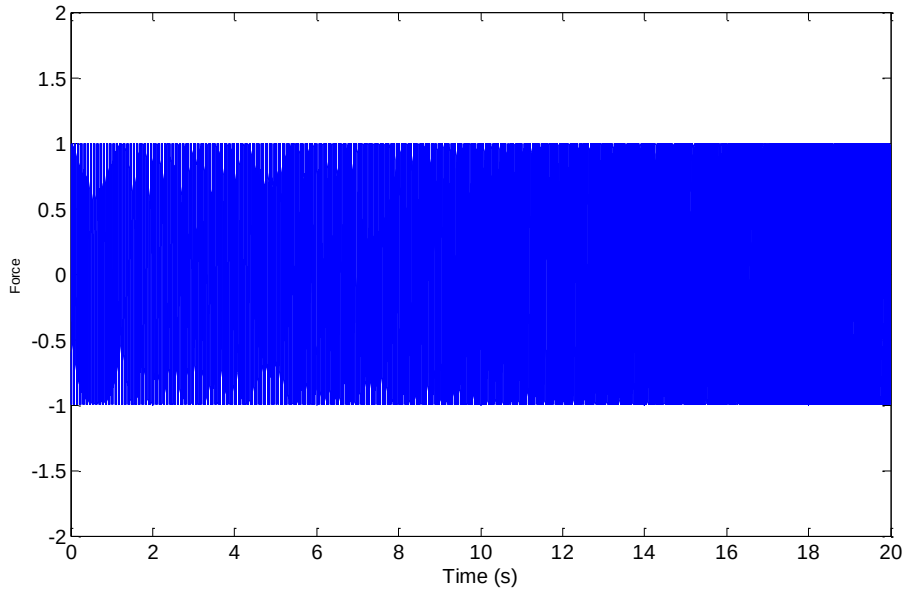

Fig. 3-72 Chirp input signal with bandwidth [25Hz,40Hz] in time domain (unit amplitude)

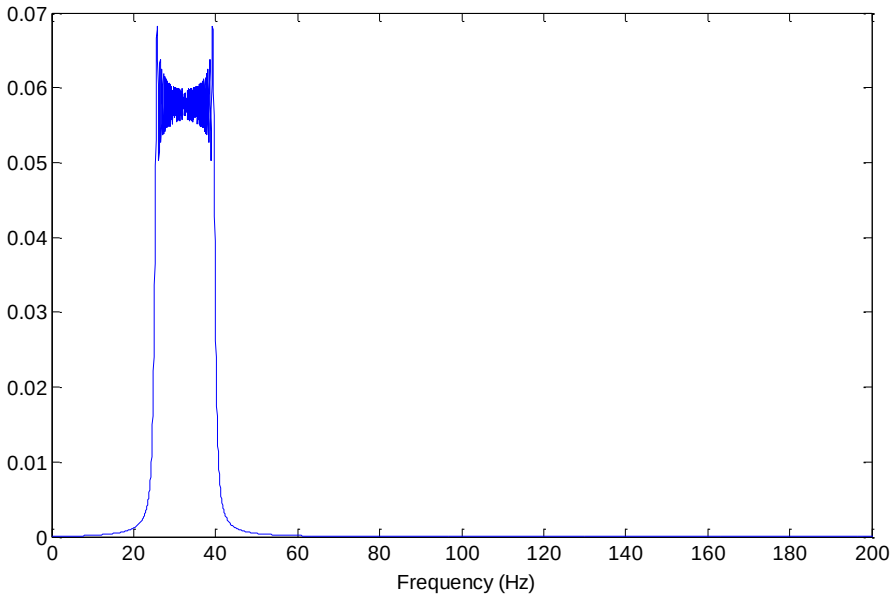

Fig. 3-73 Chirp input signal with bandwidth [25Hz,40Hz] in frequency domain

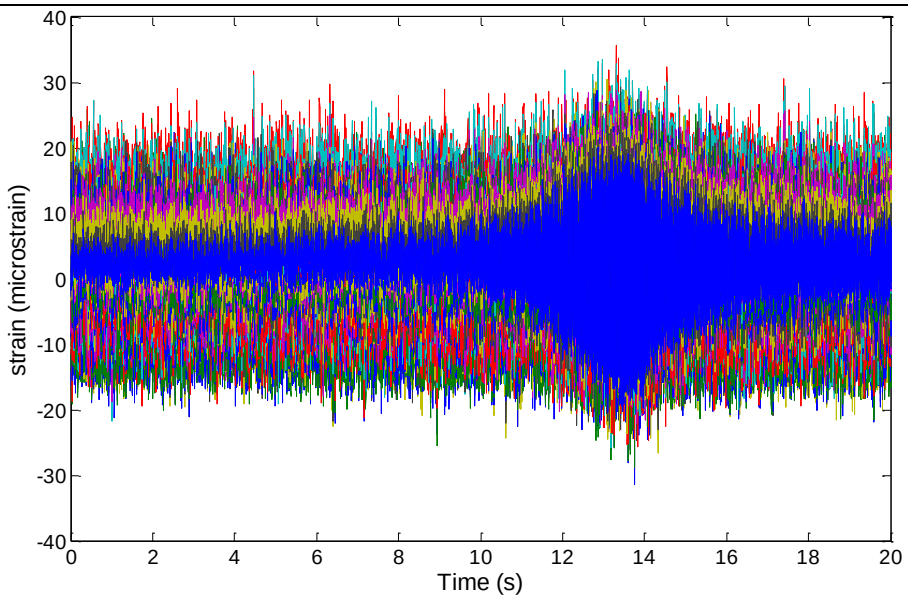

Fig. 3-74 Strain responses of the 497 sensors along with the distributed fiber optics under excitation level A in time domain

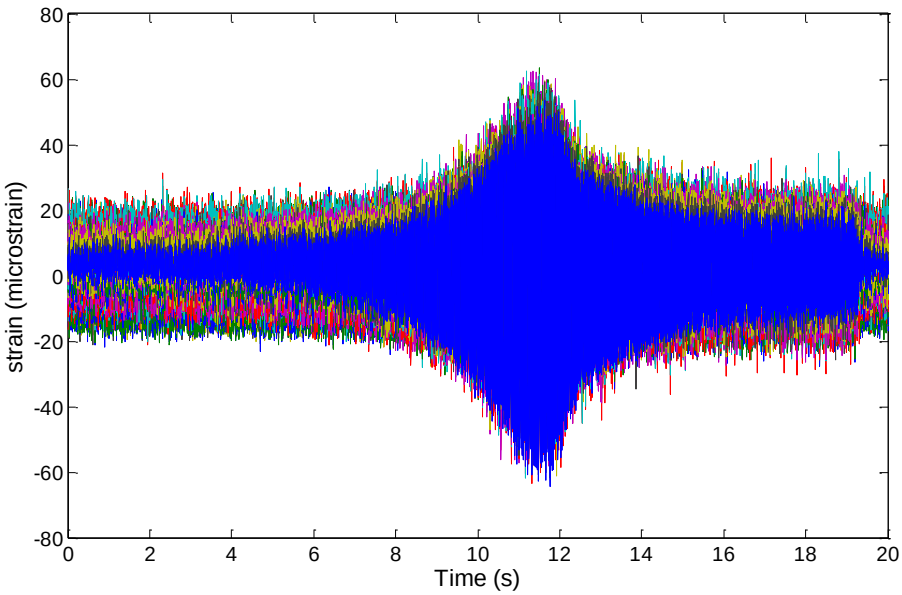

Fig. 3-75 Strain responses of the 497 sensors along with the distributed fiber optics under excitation level B in time domain

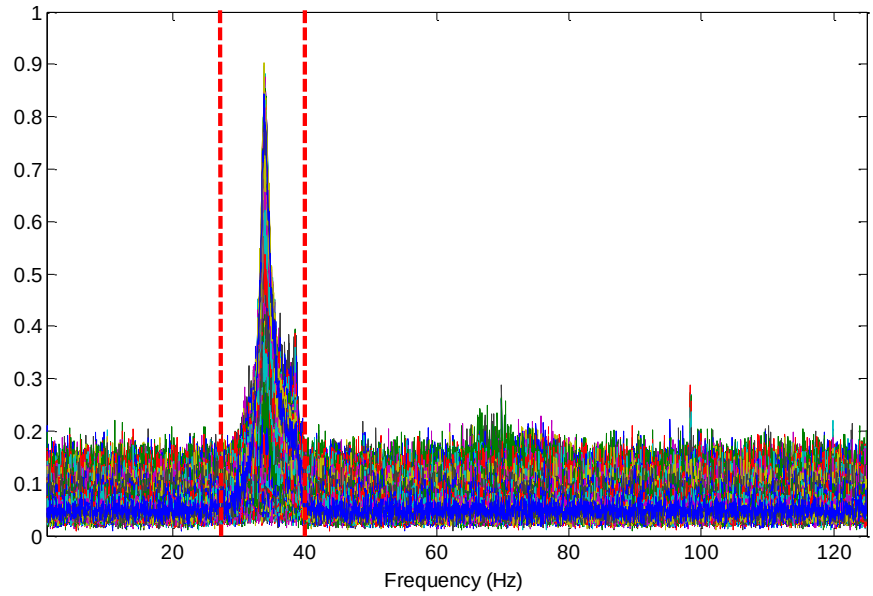

Fig. 3-76 Strain responses of the 497 sensors along with the distributed fiber optics under excitation level A in frequency domain

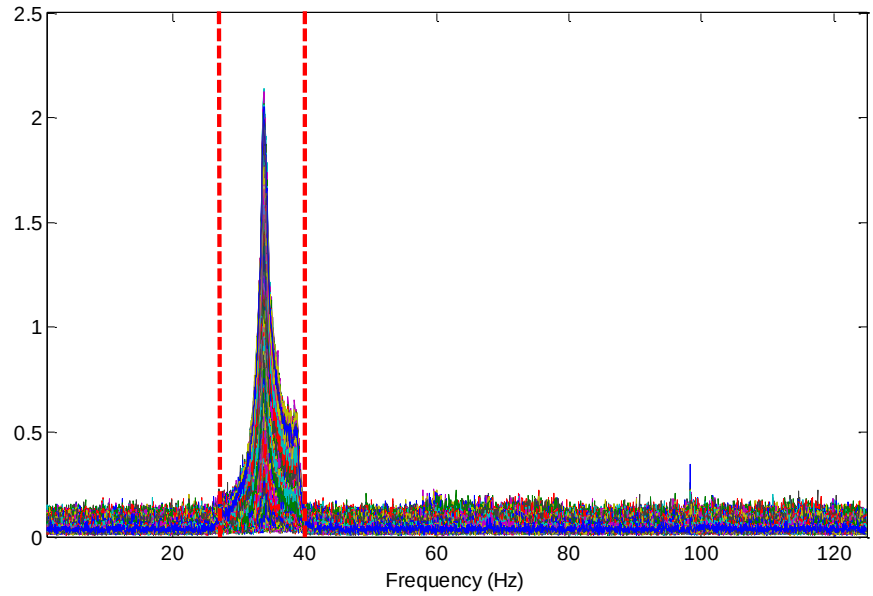

Fig. 3-77 Strain responses of the 497 sensors along with the distributed fiber optics under excitation level B in frequency domain

Each test is carried out for 5 times, aiming to noise reduction by averaging manipulation.

The marked two red dash lines indicate the correspondent frequency band of input [25Hz,40Hz] in Fig. 3-76 and Fig. 3-77. In order to discard the unreliable vibration response, transmissibility coherence function has been performed as well and shown in Fig. 3-78. The red dash line demonstrates the threshold 0.8 for the choice of reliable beam elements.

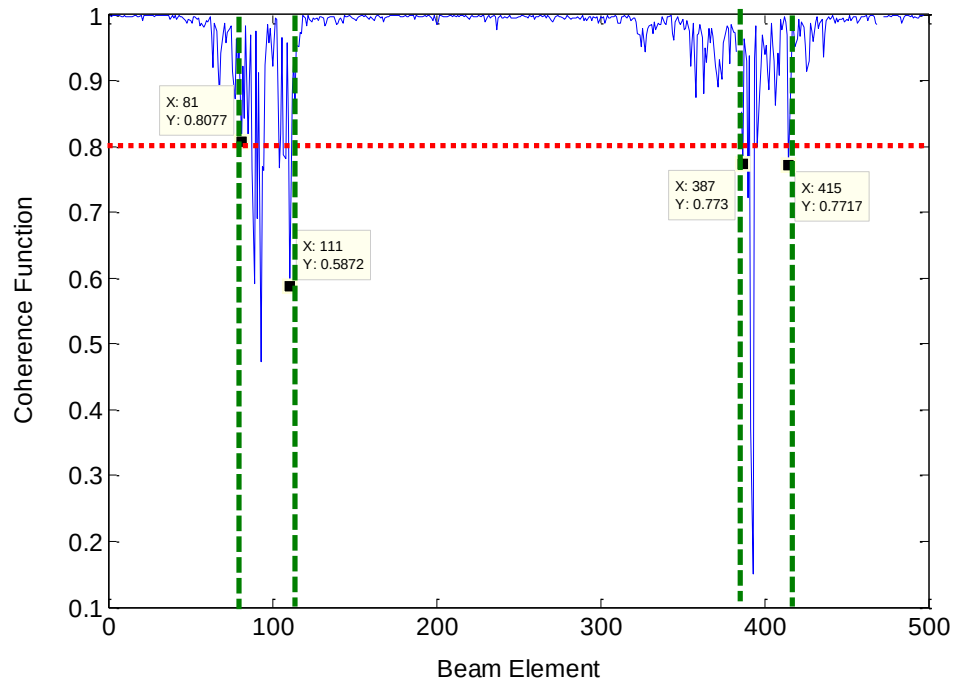

Fig. 3-78 Transmissibility coherence function under excitation level A

Same procedure step1 to step4 3.3.6.3 has been applied for identifying the boundary of loading force and nonlinear component. The frequency band here has been chosen as [25Hz,40Hz], which are the values of a and b in step1 in section 3.3.6.3.

Damage indicator can be obtained from equation(3-106) and it is shown in Fig. 3-79.

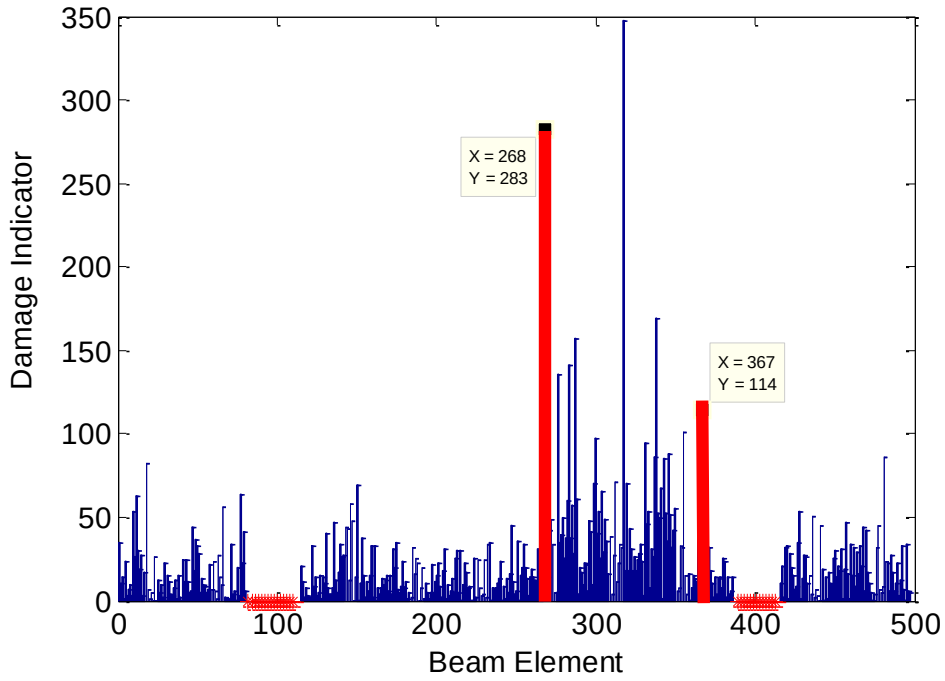

Fig. 3-79 Damage indicator of scenario 2

The asterisks in the Fig. 3-79 illustrate the discarded beam elements. From the deduction (3-62) and (3-63), the boundary of the area between loading force and nonlinear component is $[L_1-1, J-1]$. According to the real experimental configuration $L_1=267$ and $J=364$, therefore, the boundary between loading force and crack should be [266,363]. In Fig. 3-70, the red bars are the identified boundary of loading and nonlinear component which are 268 and 367. The recognized boundary is a little bit differentiated in terms of the real situation, considering the uncertainties of the system and operations.

This case study demonstrates the experiment process on identification of signal nonlinear component, here breathing crack, by means of distributed fiber optics. The framework of experiment process is shown in Fig. 3-80. Through the recognition of boundary covered by loading force and crack, crack could be localized based on the condition of known position of loading force. Otherwise, at least two different tests should be performed in order to find the coincidence boundary, which could be identified as nonlinear component.

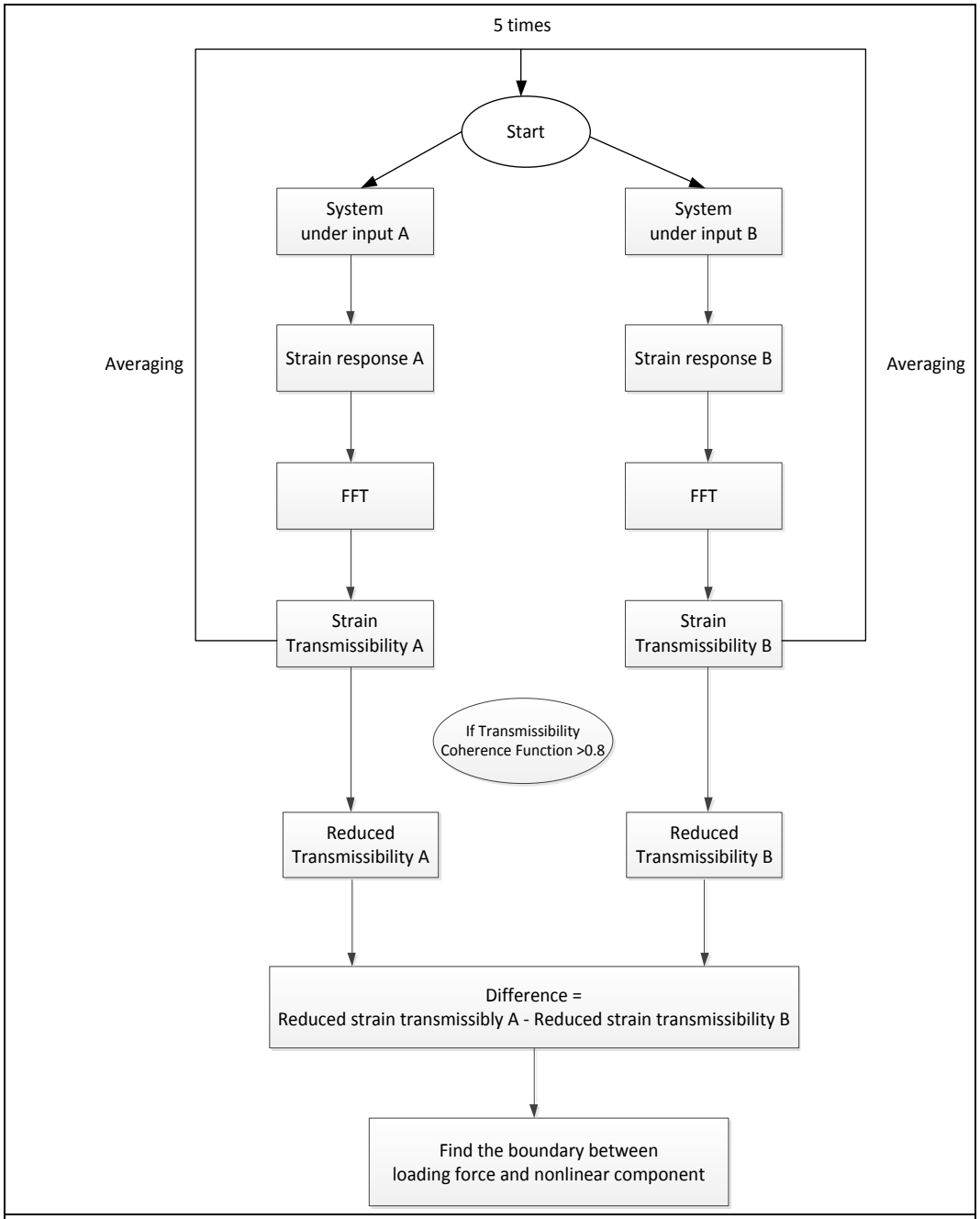

Fig. 3-80 Framework of experiments on nonlinear damage detection

3.4 Conclusion

The methodology about identifying single or multiple nonlinear components for MDOF system under general input has been put forward. The important properties of transmissibility functions based on different nonlinear order NOFRFs and output have been illustrated and it clearly figures out the relationship between transmissibility functions based on the total system output and the output under different nonlinear order or NOFRFs. According to the linear frequency range and nonlinear frequency range, different damage identification procedures are proposed respectively. Moreover, it is helpful to replenish the knowledge and application of NOFRFs on damage identification under general input. The conclusion finds that it is more convenient to use the Output-based transmissibility, which is derived from NOFRF-based transmissibility, in terms of nonlinear damage identification, regarding the fact that NOFRF-based transmissibility needs another complicated process of parameter identification of calculation, and Output-based transmissibility skips the errors caused by NOFRF identification.

In addition, a series of simulation studies have been carried out considering diverse situation:

1) Only existence of one nonlinear component;
2) Existence of multiple nonlinear components;
3) Only single point loading;
4) Existence of multiple-point loading;
5) Existence of uniform distributed loading.

All the simulation results have indicated the feasibility and effectiveness of proposed methodology.

As for the experiments, a wood blade model with cracks has been studied by using 4 laser sensors considering two damage situations: single crack and two cracks. The experimental results validate the effectiveness of proposed methodology, however, the damage location cannot be precisely localized due to the limited number of sensors applied. Based on this consideration, distributed fiber optics have been applied which is capable to provide huge number of sensors, hence another series of damage identification experiments on beam structure by means of distributed fiber optics have been conducted. Through the recognized damage indicator, rather good consequence could be achieved even if

there exists a small fluctuation, but within the range of tolerance.

CHAPTER 4

Conclusion and future research

Structural damage identification is crucial for engineering structures, but it is still a tough issue concerning the practical conduction and implementation. Correct and rapid identification of these damage is able to ensure the safe operation of the structures and to prevent accidents, which has an important significance. Currently the methods of damage detection are still in the state of development. In this thesis, a novel damage detection approach on linear damage and nonlinear damage based on transmissibility function has been mainly studied.

4.1 Conclusions

In this thesis, several damage identification methods have been reviewed shortly, and it points out that transmissibility could be the better damage indicators among those methods.

Due to the fact that strain could be the second derivative of displacement, which has been proved its better sensitivity in terms of damage in the paper[111], distributed fiber optics have been applied into this study, taking into account that it can directly measure strain data and it is capable to offer a huge number of sensors along one single fiber.

In chapter 2, based on study of strain data, strain transmissibility

function (STF) has been proposed and it has been verified more sensitive compared to traditional transmissibility functions (TTF) (displacement, acceleration and velocity), calculated through the approach that the convergence value of STFs into system poles is equal to the ratio of strain mode instead of the ratio of displacement mode from TTFs. Corresponding simulation studies have been performed in order to verify the outcome of higher sensitivity of STF compared to TTF. Moreover, its feasibility has also been validated based on experimental studies of beam structure by applying a distributed fiber optics.

All the proposed methods are based on the assumption that the system behavior of structure is linear. However, many damages in real engineering structures are manifested as nonlinear behaviors. Under this situation, the damage identification methods based on linear system are not so sensitive to nonlinear damage, even not working functionally. Considering that there is a few research on the topic of nonlinear damage identification by using transmissibility function. In chapter 3, the method based on transmissibility by using NOFRFs has been selected as a base study, with aiming to develop into more general applicable cases, since the proposed method for nonlinear damage identification is only applicable to the system under single harmonic excitation. Thus, transmissibility based on NOFRFs has been developed into adapt the system under general input, namely bandlimited input, which contains richer frequency components compared to signal harmonic input.

Therefore, this thesis puts forward the methodologies of detecting and locating single and multiple nonlinear components under general input for MDOF system respectively. Through the discovery of the relationship between NOFRF-based transmissibility and Output-based transmissibility under general input, it is proved that Output-based transmissibility contains exactly the same properties as NOFRF-based transmissibility. The main consequence is that Output-based transmissibility could be more convenient and manipulative for damage identification, because it skips the complicated mathematical computation process of NOFRFs. Moreover, the detailed identification procedure for nonlinear components has been proposed. A short review on frequency response function of nonlinear system and Conception of Nonlinear output frequency response function has been described in the beginning. And then it discusses the NOFRF-based transmissibility

functions under general input for MDOF system. The Output-based transmissibility has been studied which is derived from NOFRF-based transmissibility. Some important properties of NOFRF-based transmissibility and Output-based transmissibility have been concluded respectively, which offers the strategy for detecting and locating nonlinear components. In the end, it brings up the concrete steps for identifying single and multiple nonlinear components, concerning the loading conditions: single point excitation and multiple points excitation.

4.2 Contribution to knowledge

In this thesis, the contribution to knowledge can be listed as the following points.

For linear damage identification

1. Conception of strain transmissibility function (STF) has been proposed;
2. The feasibility and effectiveness of damage detection by using STF have been verified by a series of simulation studies and experimental studies.
3. Higher sensitivity of STF has been proved compared to TTF (Traditional transmissibility function) in terms of damage.
4. Distributed fiber optics based on OFDR technology has been successfully applied into damage identification of beam structures.

For nonlinear damage identification

1. Some important properties of NOFRF-based transmissibility of MDOF system under general input have been discovered;
2. The relationship between NOFRF-based and Output-based transmissibility of MDOF system under general input has been demonstrated clearly.
3. Accordingly, some important properties of NOFRF-based transmissibility of MDOF system under general input have been discovered;
4. The methodology for nonlinear damage identification based on NOFRF-based and Output-based transmissibility of MDOF system under general input has been proposed in details, considering

different working conditions which include the existence of single and multiple nonlinear components, the existence of single point loading, multiple-point loading and uniform distributed loading.
5. Since the method of nonlinear damage identification based on harmonic loading has been studied maturely already by Lang *et al*. This part of work has been contributed into development of NOFRF system theory.
6. Distributed fiber optics based on OFDR technology has been applied into nonlinear damage identification (breathing crack) successfully as well.

4.3 Future work prospects

Based on the aforementioned work of this thesis, here lists the recommendations for the future work.

1. The threshold for distinguishing the level of uncertainty while carrying out the experiments, which could be from mechanical operations, noise and other external disturbance.
2. Different fiber optic sensors should be applied in order to compare their corresponding performance.
3. Applications of damage detection on more complicated engineering structures based on strain transmissibility function should be practiced, such as bridges and high buildings.
4. More nonlinear damage behaviors, apart from breathing crack, and real engineering structures should be applied in order to verify the proposed nonlinear damage identification method.

Bibliography

1. Farrar, C.R. and K. Worden, *An introduction to structural health monitoring.* Philosophical Transactions of the Royal Society of London A: Mathematical, Physical and Engineering Sciences, 2007. **365**(1851): p. 303-315.
2. Wang, Y. and Z. Wang, *A Study on Software Framework of Structural Health Monitoring System Based on NEESit.*
3. Peeters, B., *System identification and damage detection in civil engineering.* Department of Civil Engineering, Katholieke Universiteit Leuven, Leuven, 2000: p. 233.
4. Ciang, C.C., J.-R. Lee, and H.-J. Bang, *Structural health monitoring for a wind turbine system: a review of damage detection methods.* Measurement Science and Technology, 2008. **19**(12): p. 122001.
5. Farrar, C.R., S.W. Doebling, and D.A. Nix, *Vibration–based structural damage identification.* Philosophical Transactions of the Royal Society of London A: Mathematical, Physical and Engineering Sciences, 2001. **359**(1778): p. 131-149.
6. Inman, D.J., et al., *Damage prognosis: for aerospace, civil and mechanical systems*. 2005: John Wiley & Sons.
7. Farrar, C.R. and N.A. Lieven, *Damage prognosis: the future of structural health monitoring.* Philosophical Transactions of the Royal Society of London A: Mathematical, Physical and Engineering Sciences, 2007. **365**(1851): p. 623-632.
8. Farrar, C.R., N.A. Lieven, and M.T. Bement, *An introduction to damage prognosis.* Damage Prognosis for Aerospace, Civil and Mechanical Systems, 2005: p. 1-12.
9. Venkatasubramanian, V., et al., *A review of process fault detection and diagnosis: Part I: Quantitative model-based methods.* Computers & chemical engineering, 2003. **27**(3): p. 293-311.
10. Venkatasubramanian, V., R. Rengaswamy, and S.N. Kavuri, *A review of process fault detection and diagnosis: Part II: Qualitative models and search strategies.* Computers & Chemical Engineering, 2003. **27**(3): p. 313-326.
11. Venkatasubramanian, V., et al., *A review of process fault detection and diagnosis: Part III: Process history based methods.* Computers & chemical engineering, 2003. **27**(3): p. 327-346.

12. Patton, R.J., *Robustness in model-based fault diagnosis: the 1995 situation.* Annual reviews in control, 1997. **21**: p. 103-123.
13. Gertler, J.J., *Survey of model-based failure detection and isolation in complex plants.* IEEE Control systems magazine, 1988. **8**(6): p. 3-11.
14. Falkenhainer, B. and K.D. Forbus, *Cmpositional modeling: finding the right model for the job.* Artificial intelligence, 1991. **51**(1-3): p. 95-143.
15. Grantham, S. and L. Ungar, *Comparative analysis of qualitative models when the model changes.* AIChE journal, 1991. **37**(6): p. 931-943.
16. Friswell, M.I., *Damage identification using inverse methods.* Philosophical Transactions of the Royal Society of London A: Mathematical, Physical and Engineering Sciences, 2007. **365**(1851): p. 393-410.
17. Montgomery, D.C., E.A. Peck, and G.G. Vining, *Introduction to linear regression analysis*. 2015: John Wiley & Sons.
18. Zhao, J., J.N. Ivan, and J.T. DeWolf, *Structural damage detection using artificial neural networks.* Journal of Infrastructure Systems, 1998. **4**(3): p. 93-101.
19. Szewczyk, Z.P. and P. Hajela, *Damage detection in structures based on feature-sensitive neural networks.* Journal of computing in civil engineering, 1994. **8**(2): p. 163-178.
20. Zang, C. and M. Imregun, *Structural damage detection using artificial neural networks and measured FRF data reduced via principal component projection.* Journal of Sound and Vibration, 2001. **242**(5): p. 813-827.
21. Oh, C.K. and H. Sohn, *Damage diagnosis under environmental and operational variations using unsupervised support vector machine.* Journal of Sound and Vibration, 2009. **325**(1): p. 224-239.
22. Widodo, A., B.-S. Yang, and T. Han, *Combination of independent component analysis and support vector machines for intelligent faults diagnosis of induction motors.* Expert systems with applications, 2007. **32**(2): p. 299-312.
23. Konar, P. and P. Chattopadhyay, *Bearing fault detection of induction motor using wavelet and Support Vector Machines (SVMs).* Applied Soft Computing, 2011. **11**(6): p. 4203-4211.
24. Pawar, P.M. and R. Ganguli, *Genetic fuzzy system for damage detection in beams and helicopter rotor blades.* Computer methods

in applied mechanics and engineering, 2003. **192**(16): p. 2031-2057.
25. da Silva, S., et al., *Structural damage detection by fuzzy clustering.* Mechanical Systems and Signal Processing, 2008. **22**(7): p. 1636-1649.
26. Chandrashekhar, M. and R. Ganguli, *Uncertainty handling in structural damage detection using fuzzy logic and probabilistic simulation.* Mechanical Systems and Signal Processing, 2009. **23**(2): p. 384-404.
27. Yang, Q., *Model-based and data driven fault diagnosis methods with applications to process monitoring*, 2004, Case Western Reserve University.
28. Sumitoro, S., et al. *Long span bridge health monitoring system in Japan.* in *6th Annual International Symposium on NDE for Health Monitoring and Diagnostics*. 2001. International Society for Optics and Photonics.
29. Kim, J.-T., et al., *Recent R&D activities on structural health monitoring in Korea.* 2016.
30. Chen, W., et al., *Theoretical and experimental modal analysis of the Guangzhou New TV Tower.* Engineering Structures, 2011. **33**(12): p. 3628-3646.
31. Rytter, A., *Vibrational based inspection of civil engineering structures.* 1993.
32. Cawley, P. and R. Adams, *The location of defects in structures from measurements of natural frequencies.* The Journal of Strain Analysis for Engineering Design, 1979. **14**(2): p. 49-57.
33. Hassiotis, S. and G. Jeong, *Assessment of structural damage from natural frequency measurements.* Computers & Structures, 1993. **49**(4): p. 679-691.
34. Messina, A., I. Jones, and E. Williams. *Damage detection and localization using natural frequency changes*. in *14th International Modal Analysis Conference*. 1996.
35. Nandwana, B. and S. Maiti, *Detection of the location and size of a crack in stepped cantilever beams based on measurements of natural frequencies.* Journal of Sound and Vibration, 1997. **203**(3): p. 435-446.
36. Morassi, A., *Identification of a crack in a rod based on changes in a pair of natural frequencies.* Journal of Sound and Vibration, 2001. **242**(4): p. 577-596.
37. Xu, G., W. Zhu, and B. Emory, *Experimental and numerical*

investigation of structural damage detection using changes in natural frequencies. Journal of vibration and acoustics, 2007. **129**(6): p. 686-700.

38. Pandey, A., M. Biswas, and M. Samman, *Damage detection from changes in curvature mode shapes.* Journal of sound and vibration, 1991. **145**(2): p. 321-332.
39. Ratcliffe, C.P., *Damage detection using a modified Laplacian operator on mode shape data.* Journal of Sound and Vibration, 1997. **204**(3): p. 505-517.
40. Shi, Z., S. Law, and L. Zhang, *Damage localization by directly using incomplete mode shapes.* Journal of Engineering Mechanics, 2000. **126**(6): p. 656-660.
41. Ndambi, J.-M., J. Vantomme, and K. Harri, *Damage assessment in reinforced concrete beams using eigenfrequencies and mode shape derivatives.* Engineering Structures, 2002. **24**(4): p. 501-515.
42. Parloo, E., P. Guillaume, and M. Van Overmeire, *Damage assessment using mode shape sensitivities.* Mechanical systems and signal Processing, 2003. **17**(3): p. 499-518.
43. Qiao, P., et al., *Curvature mode shape-based damage detection in composite laminated plates.* Composite Structures, 2007. **80**(3): p. 409-428.
44. Zhu, H., L. Li, and X.-Q. He, *Damage detection method for shear buildings using the changes in the first mode shape slopes.* Computers & Structures, 2011. **89**(9): p. 733-743.
45. West, W.M., *Illustration of the use of modal assurance criterion to detect structural changes in an orbiter test specimen.* 1986.
46. Pandey, A. and M. Biswas, *Damage detection in structures using changes in flexibility.* Journal of sound and vibration, 1994. **169**(1): p. 3-17.
47. Robinson, N., et al., *Damage detection in aircraft structures using dynamically measured static flexibility matrices*, 1996, Los Alamos National Lab., NM (United States).
48. Catbas, F.N., D.L. Brown, and A.E. Aktan, *Use of modal flexibility for damage detection and condition assessment: case studies and demonstrations on large structures.* Journal of Structural Engineering, 2006. **132**(11): p. 1699-1712.
49. Jaishi, B. and W.-X. Ren, *Damage detection by finite element model updating using modal flexibility residual.* Journal of sound and vibration, 2006. **290**(1): p. 369-387.
50. Duan, Z., et al., *Damage detection in ambient vibration using*

proportional flexibility matrix with incomplete measured DOFs. Structural Control and Health Monitoring, 2007. **14**(2): p. 186-196.
51. Tomaszewska, A., *Influence of statistical errors on damage detection based on structural flexibility and mode shape curvature.* Computers & structures, 2010. **88**(3): p. 154-164.
52. Toksoy, T. and A. Aktan, *Bridge-condition assessment by modal flexibility.* Experimental Mechanics, 1994. **34**(3): p. 271-278.
53. Yong-mei, L., *2, ZHOU Xi-yuan1, 3, GAO Xiang-yu1 (1. College of Civil Engineering and Architecture, Beijing University of Technology, Beijing 100124, China; 2. Key Laboratory of Urban Security and Disaster Engineering of Ministry of Education of China, Beijing University of Technology, Beijing 100124, China; 3. Beijing Key Laboratory of Earthquake Engineering Structural Retrofit, Beijing 100124, China); DETECTION INDICTOR OF STRUCTURAL NONDESTRUCTIVE DAMAGE BASED ON CURVATURE-FLEXIBILITY-DIFFERENCE MATRIX [J].* Engineering Mechanics, 2009. **2**.
54. Catbas, F., M. Gul, and J. Burkett, *Damage assessment using flexibility and flexibility-based curvature for structural health monitoring.* Smart materials and structures, 2007. **17**(1): p. 015024.
55. Wang, Z., R. Lin, and M. Lim, *Structural damage detection using measured FRF data.* Computer methods in applied mechanics and engineering, 1997. **147**(1-2): p. 187-197.
56. Thyagarajan, S., et al., *Detecting structural damage using frequency response functions.* Journal of Sound and Vibration, 1998. **210**(1): p. 162-170.
57. Park, N.-G. and Y.-S. Park, *Damage detection using spatially incomplete frequency response functions.* Mechanical Systems and Signal Processing, 2003. **17**(3): p. 519-532.
58. Maia, N., et al., *Damage detection in structures: from mode shape to frequency response function methods.* Mechanical systems and signal processing, 2003. **17**(3): p. 489-498.
59. Kessler, S.S., et al., *Damage detection in composite materials using frequency response methods.* Composites Part B: Engineering, 2002. **33**(1): p. 87-95.
60. Chen, Q., et al. *Structural fault detection using neural networks trained on transmissibility functions.* in *Proceedings of the International Conference on Vibration Engineering*. 1994.
61. Sampaio, R., et al. *On the use of transmissibility for damage*

detection and location. in *European COST F3 Conference on System Identification and Structural Health Monitoring, Madrid*. 2000.
62. Maia, N., J. Silva, and A. Ribeiro, *The transmissibility concept in multi-degree-of-freedom systems.* Mechanical Systems and Signal Processing, 2001. **15**(1): p. 129-137.
63. Sampaio, R., et al. *Transmissibility techniques for damage detection*. in *Proceedings of the International Modal Analysis Conference*. 2001.
64. Johnson, T.J., *Analysis of dynamic transmissibility as a feature for structural damage detection*, 2002, Purdue University.
65. Johnson, T.J. and D.E. Adams, *Transmissibility as a differential indicator of structural damage.* TRANSACTIONS-AMERICAN SOCIETY OF MECHANICAL ENGINEERS JOURNAL OF VIBRATION AND ACOUSTICS, 2002. **124**(4): p. 634-641.
66. Lang, Z.-Q., et al., *Transmissibility of non-linear output frequency response functions with application in detection and location of damage in MDOF structural systems.* International Journal of Non-Linear Mechanics, 2011. **46**(6): p. 841-853.
67. Maia, N.M., et al., *Damage detection and quantification using transmissibility.* Mechanical Systems and Signal Processing, 2011. **25**(7): p. 2475-2483.
68. Chesné, S. and A. Deraemaeker, *Damage localization using transmissibility functions: a critical review.* Mechanical systems and signal processing, 2013. **38**(2): p. 569-584.
69. Zhao, X.Y., et al., *A new transmissibility analysis method for detection and location of damage via nonlinear features in mdof structural systems.* IEEE/ASME transactions on mechatronics, 2015. **20**(4): p. 1933-1947.
70. SCHULZ, M.J., et al. *Detecting structural damage using transmittance functions*. in *Proceedings of SPIE, the International Society for Optical Engineering*. 1997. Society of Photo-Optical Instrumentation Engineers.
71. Grattan, K. and T. Sun, *Fiber optic sensor technology: an overview.* Sensors and Actuators A: Physical, 2000. **82**(1): p. 40-61.
72. Yin, S.S. and P. Ruffin, *Fiber optic sensors*. 2002: Wiley Online Library.
73. Jackson, D. and J. Jones, *Fibre optic sensors.* Journal of Modern Optics, 1986. **33**(12): p. 1469-1503.
74. Krohn, D.A., *Fiber optic sensors.* Social Studies of Science, 1986.

1.
75. Guo, H., et al., *Fiber optic sensors for structural health monitoring of air platforms.* Sensors, 2011. **11**(4): p. 3687-3705.
76. Culshaw, B., *Smart structures and materials, Artech House.* Inc., Norwood, MA, USA, 1996.
77. Hill, K.O. and G. Meltz, *Fiber Bragg grating technology fundamentals and overview.* Journal of lightwave technology, 1997. **15**(8): p. 1263-1276.
78. Rao, Y.-J., *In-fibre Bragg grating sensors.* Measurement science and technology, 1997. **8**(4): p. 355.
79. Wild, G. and S. Hinckley, *Acousto-ultrasonic optical fiber sensors: overview and state-of-the-art.* IEEE Sensors Journal, 2008. **8**(7): p. 1184-1193.
80. Gangopadhyay, T.K., *Prospects for fibre Bragg gratings and Fabry-Perot interferometers in fibre-optic vibration sensing.* Sensors and Actuators A: Physical, 2004. **113**(1): p. 20-38.
81. Shibata, N., R.G. Waarts, and R.P. Braun, *Brillouin-gain spectra for single-mode fibers having pure-silica, GeO 2-doped, and P 2 O 5-doped cores.* Optics letters, 1987. **12**(4): p. 269-271.
82. Shimizu, K., et al., *Coherent self-heterodyne Brillouin OTDR for measurement of Brillouin frequency shift distribution in optical fibers.* Journal of Lightwave Technology, 1994. **12**(5): p. 730-736.
83. Bao, X. and L. Chen, *Recent progress in distributed fiber optic sensors.* Sensors, 2012. **12**(7): p. 8601-8639.
84. Bussières, J., et al. *Load Monitoring using a Rayleigh Backscattering Fiber Optic System*. in *International conference of Adapative Structures and Technologies, Aruba*. 2013.
85. Oakley, L.H., et al., *Identification of organic materials in historic oil paintings using correlated extractionless surface-enhanced Raman scattering and fluorescence microscopy.* Analytical chemistry, 2011. **83**(11): p. 3986-3989.
86. Abalde-Cela, S., et al., *Surface-enhanced Raman scattering biomedical applications of plasmonic colloidal particles.* Journal of the Royal Society Interface, 2010. **7**(Suppl 4): p. S435-S450.
87. Eickhoff, W. and R. Ulrich, *Optical frequency domain reflectometry in single - mode fiber*. Applied Physics Letters, 1981. **39**(9): p. 693-695.
88. Nakayama, J., K. Iizuka, and J. Nielsen, *Optical fiber fault locator by the step frequency method.* Applied optics, 1987. **26**(3): p. 440-

443.
89. Yu, F., et al. *A novel distributed fiber sensor based on the Fourier spectrometer technique*. in *Proceedings of the OSA Annual Meeting, Dallas, TX, USA*. 1994.
90. Juškaitis, R., et al., *Distributed interferometric fiber sensor system*. Optics letters, 1992. **17**(22): p. 1623-1625.
91. Rathod, R., et al., *Distributed temperature-change sensor based on Rayleigh backscattering in an optical fiber*. Optics letters, 1994. **19**(8): p. 593-595.
92. Froggatt, M. and J. Moore, *High-spatial-resolution distributed strain measurement in optical fiber with Rayleigh scatter*. Applied Optics, 1998. **37**(10): p. 1735-1740.
93. Barrias, A., J.R. Casas, and S. Villalba, *A review of distributed optical fiber sensors for civil engineering applications*. Sensors, 2016. **16**(5): p. 748.
94. Xu, G. and D. Xiong, *Applications of fiber Bragg grating sensing technology in engineering*. Chin. Opt, 2013. **6**: p. 306-317.
95. Antunes, P., et al., *Optical fiber sensors for static and dynamic health monitoring of civil engineering infrastructures: Abode wall case study*. Measurement, 2012. **45**(7): p. 1695-1705.
96. Chan, T.H., et al., *Fiber Bragg grating sensors for structural health monitoring of Tsing Ma bridge: Background and experimental observation*. Engineering structures, 2006. **28**(5): p. 648-659.
97. Zhou, Z., et al., *Techniques of Advanced FBG sensors: fabrication, demodulation, encapsulation and their application in the structural health monitoring of bridges*. Pacific Science Review, 2003. **5**(1): p. 116-121.
98. Rao, Y.-J., *Recent progress in applications of in-fibre Bragg grating sensors*. Optics and lasers in Engineering, 1999. **31**(4): p. 297-324.
99. Li, H.-N., D.-S. Li, and G.-B. Song, *Recent applications of fiber optic sensors to health monitoring in civil engineering*. Engineering structures, 2004. **26**(11): p. 1647-1657.
100. Zhang, W., et al., *Health monitoring of rehabilitated concrete bridges using distributed optical fiber sensing*. Computer - Aided Civil and Infrastructure Engineering, 2006. **21**(6): p. 411-424.
101. Villalba, S. and J.R. Casas, *Application of optical fiber distributed sensing to health monitoring of concrete structures*. Mechanical

Systems and Signal Processing, 2013. **39**(1): p. 441-451.
102. Sierra-Pérez, J., M.A. Torres-Arredondo, and A. Güemes, *Damage and nonlinearities detection in wind turbine blades based on strain field pattern recognition. FBGs, OBR and strain gauges comparison.* Composite Structures, 2016. **135**: p. 156-166.
103. Glišić, B., D. Posenato, and D. Inaudi. *Integrity monitoring of old steel bridge using fiber optic distributed sensors based on Brillouin scattering*. in *The 14th International Symposium on: Smart Structures and Materials & Nondestructive Evaluation and Health Monitoring*. 2007. International Society for Optics and Photonics.
104. Glisic, B. and D. Inaudi, *Development of method for in-service crack detection based on distributed fiber optic sensors.* Structural Health Monitoring, 2012. **11**(2): p. 161-171.
105. Inaudi, D. and B. Glisic, *Distributed fiber optic strain and temperature sensing for structural health monitoring.* Proceedings of the IABMAS, 2006. **6**.
106. Juarez, J.C. and H.F. Taylor. *Distributed fiber optic intrusion sensor system for monitoring long perimeters*. in *Defense and Security*. 2005. International Society for Optics and Photonics.
107. Vogel, B., et al. *Leakage detection systems by using distributed fiber optical temperature measurement*. in *SPIE's 8th Annual International Symposium on Smart Structures and Materials*. 2001. International Society for Optics and Photonics.
108. Majumdar, A., et al., *Structural damage detection based on modal parameters using continuous ant colony optimization.* Advances in Civil Engineering, 2014. **2014**.
109. Abrate, S., *Structural Monitoring with Fiber Optic Technology.* Applied Mechanics Reviews, 2002. **55**: p. B10.
110. Hotate, K., *Distributed fiber sensing technology: Currents and challenges.* 2012.
111. Whalen, T.M., *The behavior of higher order mode shape derivatives in damaged, beam-like structures.* Journal of sound and vibration, 2008. **309**(3): p. 426-464.
112. Devriendt, C., et al., *Structural health monitoring in changing operational conditions using tranmissibility measurements.* Shock and Vibration, 2010. **17**(4-5): p. 651-675.
113. Sampaio, R., et al. *Damage detection using the transmissibility concept*. in *Proceedings of the 6th international congress on sound and vibration (ICSV 6), Copenhagen*. 1999.

114. Lang, Z.-Q. and S. Billings, *Output frequencies of nonlinear systems*. International Journal of Control, 1997. **67**(5): p. 713-730.
115. Cheng, L., G. Busca, and A. Cigada. *Experimental strain modal analysis for beam-like structure by using distributed fiber optics*. in *14th IMEKO TC10 Workshop on Technical Diagnostics 2016: New Perspectives in Measurements, Tools and Techniques for Systems Reliability, Maintainability and Safety*. 2016.